STATE OF THE CLIMATE IN 2019

GLOBAL CLIMATE

R. J. H. Dunn, D. M. Stanitski, N. Gobron, and K. M. Willett, Eds.

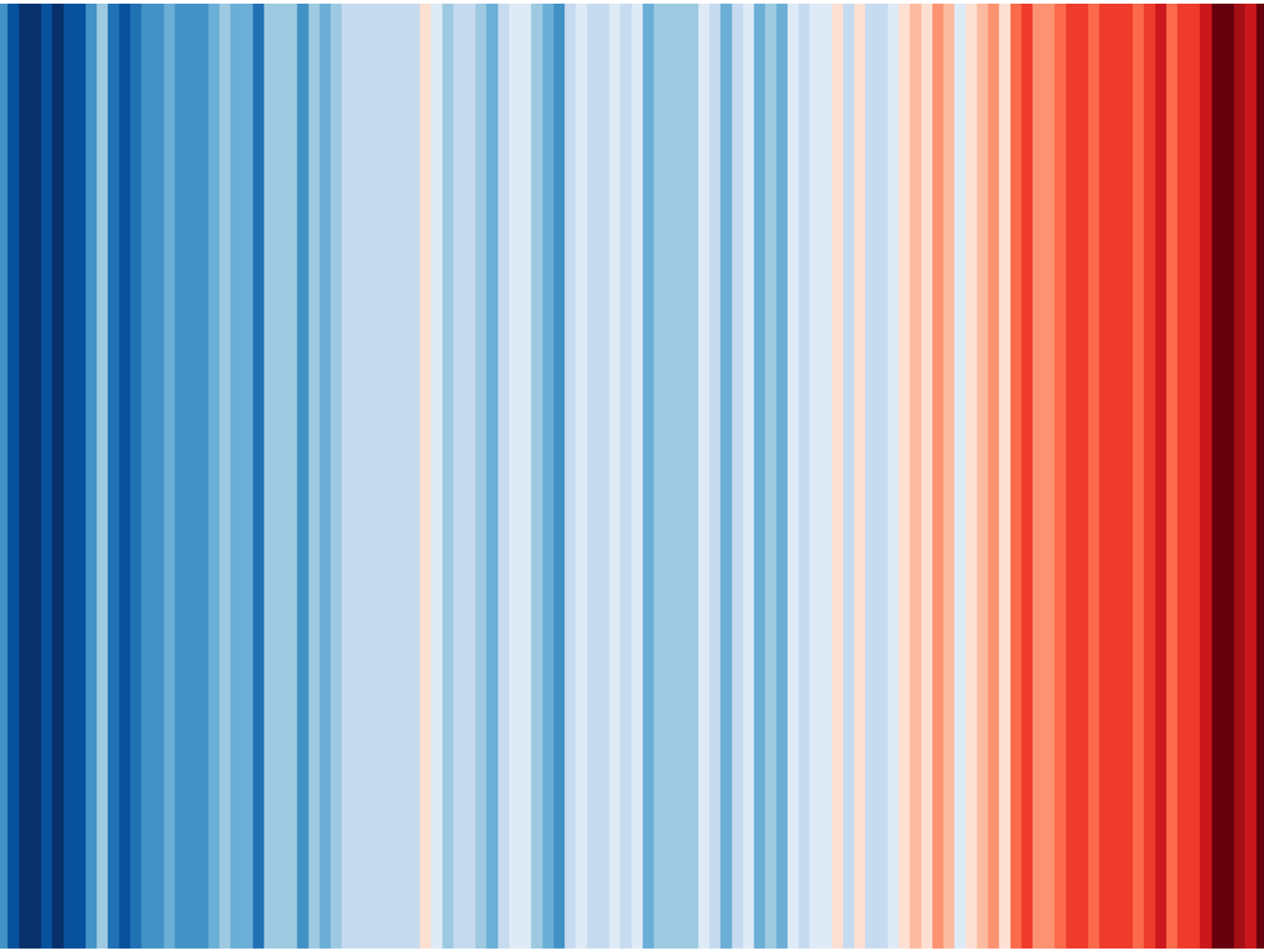

Special Online Supplement to the *Bulletin of the American Meteorological Society,* Vol.101, No. 8, August, 2020

https://doi.org/10.1175/BAMS-D-20-0104.1

Corresponding author: Robert Dunn / robert.dunn@metoffice.gov.uk

STATE OF THE CLIMATE IN 2019

Global Climate

Editors

Jessica Blunden
Derek S. Arndt

Chapter Editors

Peter Bissolli
Howard J. Diamond
Matthew L. Druckenmiller
Robert J. H. Dunn
Catherine Ganter
Nadine Gobron
Rick Lumpkin
Jacqueline A. Richter-Menge
Tim Li
Ademe Mekonnen
Ahira Sánchez-Lugo
Ted A. Scambos
Carl J. Schreck III
Sharon Stammerjohn
Diane M. Stanitski
Kate M. Willett

Technical Editor

Andrea Andersen

BAMS Special Editor for Climate

Richard Rosen

American Meteorological Society

Cover credit:
The cover shows a cropped image of the warming stripes (seen in full below), as developed by Ed Hawkins (Reading University, UK). Each vertical line shows the global average temperature of a whole year, starting at 1850 on the far left and ending with 2019 on the far right. The underlying data are from the HadCRUT4.6 dataset of the UK Met Office Hadley Centre. To create stripes of other regions and countries visit https://showyourstripes.info/. Image created on 23 June 2020 by https://showyourstripes.info/ under a CC BY 4.0 licence.

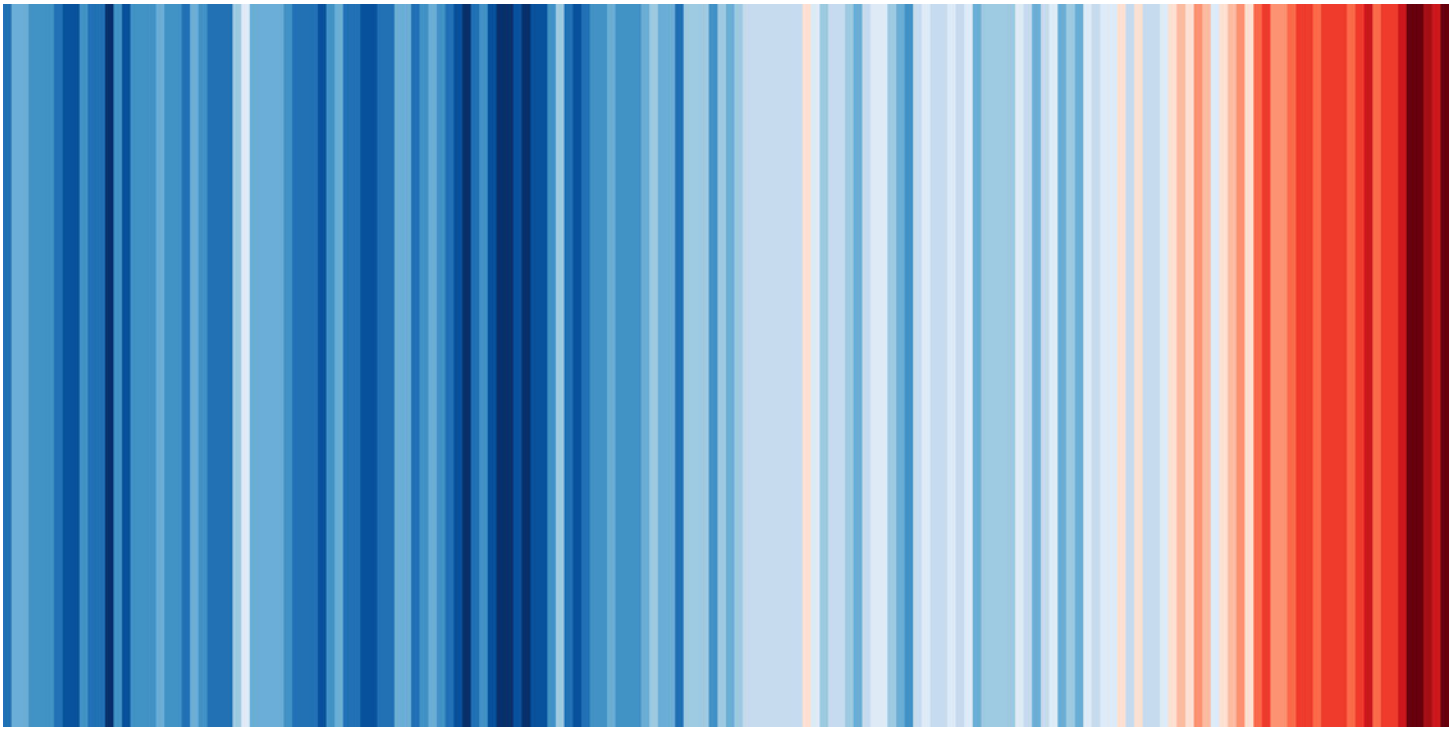

Global Climate is one chapter from the *State of the Climate in 2019* annual report and is available from https://doi.org/10.1175/BAMS-D-20-0104.1 Compiled by NOAA's National Centers for Environmental Information, *State of the Climate in 2019* is based on contributions from scientists from around the world. It provides a detailed update on global climate indicators, notable weather events, and other data collected by environmental monitoring stations and instruments located on land, water, ice, and in space.
The full report is available from https://doi.org/10.1175/2020BAMSStateoftheClimate.1.

How to cite this document:

Citing the complete report:
Blunden, J. and D. S. Arndt, Eds., 2020: State of the Climate in 2019. *Bull. Amer. Meteor.*, **101** (8), Si–S429 doi:10.1175/2020BAMSStateoftheClimate.1

Citing this chapter:
Dunn, R. J. H., D. M. Stanitski, N. Gobron, and K. M. Willett, Eds., 2020: Global Climate [in "State of the Climate in 2019"]. *Bull. Amer. Meteor.*, **101** (8), S9–S127, https://doi.org/10.1175/BAMS-D-20-0104.1

Citing a section (example):
Davis, M., K. H. Rosenlof, D. F. Hurst, H. Vömel, and H.B. Selkirk, 2020: Stratospheric water vapor [in "State of the Climate in 2019"]. *Bull. Amer. Meteor.*, **101** (8), S81–S83, https://doi.org/10.1175/BAMS-D-20-0104.1.

Editor and Author Affiliations (alphabetical by name)

Ades, M., European Centre for Medium-Range Weather Forecasts, Reading, United Kingdom
Adler, R., University of Maryland, College Park, Maryland
Allan, Rob, Met Office Hadley Centre, Exeter, United Kingdom
Allan, R. P., University of Reading, Reading, United Kingdom
Anderson, J., Department of Atmospheric and Planetary Science, Hampton University, Hampton, Virginia
Argüez, Anthony, NOAA/NESDIS National Centers for Environmental Information, Asheville, North Carolina
Arosio, C., University of Bremen, Bremen, Germany
Augustine, J. A., NOAA/OAR Earth System Research Laboratories, Boulder, Colorado
Azorin-Molina, C., Centro de Investigaciones sobre Desertificación – Spanish National Research Council, Moncada (Valencia), Spain; and Regional Climate Group, Department of Earth Sciences, University of Gothenburg, Gothenburg, Sweden
Barichivich, J., Instituto de Geografía, Pontificia Universidad Católica de Valparaíso, Valparaíso, Chile
Barnes, J., NOAA/OAR ESRL Global Monitoring Laboratory, Boulder, Colorado
Beck, H. E., Department of Civil and Environmental Engineering, Princeton University, Princeton, New Jersey
Becker, Andreas, Global Precipitation Climatology Centre, Deutscher Wetterdienst, Offenbach, Germany
Bellouin, Nicolas, University of Reading, Reading, United Kingdom
Benedetti, Angela, European Centre for Medium-Range Weather Forecasts, Reading, United Kingdom
Berry, David I., National Oceanography Centre, Southampton, United Kingdom
Blenkinsop, Stephen, School of Engineering, Newcastle University, Newcastle-upon-Tyne, United Kingdom
Bock, Olivier, Université de Paris, Institut de physique du globe de Paris, CNRS, IGN, Paris, France, and ENSG-Géomatique, IGN, Marne-la-Vallée, France
Bosilovich, Michael G., Global Modeling and Assimilation Office, NASA Goddard Space Flight Center, Greenbelt, Maryland
Boucher, Olivier, Sorbonne Université, Paris, France
Buehler, S. A., Universität Hamburg, Hamburg, Germany
Carrea, Laura, Department of Meteorology, University of Reading, Reading, United Kingdom
Christiansen, Hanne H., Geology Department, University Centre in Svalbard, Longyearbyen, Norway
Chouza, F., Jet Propulsion Laboratory, California Institute of Technology, Wrightwood, California
Christy, John R., The University of Alabama in Huntsville, Huntsville, Alabama
Chung, E.-S., IBS Center for Climate Physics, Busan, South Korea
Coldewey-Egbers, Melanie, German Aerospace Center (DLR) Oberpfaffenhofen, Wessling, Germany
Compo, Gil P., Cooperative Institute for Research in Environmental Sciences, University of Colorado Boulder, and Physical Sciences Division, NOAA/Earth System Research Laboratory, Boulder, Colorado
Cooper, Owen R., Cooperative Institute for Research in Environmental Sciences, University of Colorado Boulder, and NOAA/OAR Earth System Research Laboratories, Boulder, Colorado
Covey, Curt, Lawrence Livermore National Laboratory, Livermore, California
Crotwell, A., Cooperative Institute for Research in Environmental Sciences, University of Colorado, and NOAA/OAR Global Monitoring Division, Boulder, Colorado
Davis, Sean M., Cooperative Institute for Research in Environmental Sciences, University of Colorado Boulder, and NOAA/OAR Earth System Research Laboratory, Boulder, Colorado
de Eyto, Elvira, Marine Institute, Furnace, Newport, Ireland
de Jeu, Richard A. M., VanderSat B.V., Haarlem, the Netherlands
DeGasperi, Curtis L., King County Water and Land Resources Division, Seattle, Washington
Degenstein, Doug, University of Saskatchewan, Saskatoon, Saskatchewan, Canada
Di Girolamo, Larry, University of Illinois at Urbana-Champaign, Champaign, Illinois
Dokulil, Martin T., Research Department for Limnology, University of Innsbruck, Austria
Donat, Markus G., Barcelona Supercomputing Centre, Barcelona, Spain
Dorigo, Wouter A., Department of Geodesy and Geoinformation, TU Wien - Vienna University of Technology, Vienna, Austria
Dunn, Robert J. H., Met Office Hadley Centre, Exeter, United Kingdom
Durre, Imke, NOAA/NESDIS National Centers for Environmental Information, Asheville, North Carolina
Dutton, Geoff S., Cooperative Institute for Research in Environmental Sciences, University of Colorado Boulder, and NOAA/OAR Earth System Research Laboratories, Boulder, Colorado
Duveiller, G., European Commission, Joint Research Centre, Ispra, Italy
Elkins James W., NOAA/OAR Earth System Research Laboratories, Boulder, Colorado,
Fioletov, Vitali E., Environment and Climate Change Canada, Toronto, Canada
Flemming, Johannes, European Centre for Medum-Range Weather Forecasts, Reading, United Kingdom
Foster, Michael J., Cooperative Institute for Meteorological Satellite Studies, Space Science and Engineering Center, University of Wisconsin-Madison, Madison, Wisconsin
Frey, Richard A., Cooperative Institute for Meteorological Satellite Studies, Space Science and Engineering Center, University of Wisconsin-Madison, Madison, Wisconsin
Frith, Stacey M., Science Systems and Applications, Inc, Lanham, Maryland, NASA Goddard Space Flight Center, Greenbelt, Maryland
Froidevaux, Lucien, Jet Propulsion Laboratory, California Institute of Technology, Pasadena, California
Garforth, J., Woodland Trust, Grantham, United Kingdom
Gobron, Nadine, European Commission, Joint Research Centre, Ispra, Italy
Gupta, S. K., Science Systems and Applications, Inc., Hampton, Virginia
Haimberger, Leopold, Department of Meteorology and Geophysics, University of Vienna, Vienna, Austria
Hall, Brad D., NOAA/OAR Earth System Research Laboratories, Boulder, Colorado
Harris, Ian, National Centre for Atmospheric Science (NCAS), University of East Anglia, Norwich, United Kingdom and Climatic Research Unit, School of Environmental Sciences, University of East Anglia, Norwich, United Kingdom
Heidinger, Andrew K., NOAA/NESDIS/STAR University of Wisconsin - Madison, Madison, Wisconsin
Hemming, D. L., Met Office Hadley Centre, Exeter, United Kingdom; Birmingham Institute of Forest Research, Birmingham University, Birmingham, United Kingdom
Ho, Shu-peng (Ben), NOAA/NESDIS Center for Satellite Applications and Research, College Park, Maryland
Hubert, Daan, Royal Belgian Institute for Space Aeronomy (BIRA), Brussels, Belgium
Hurst, Dale F., Cooperative Institute for Research in Environmental Sciences, University of Colorado Boulder, and NOAA/OAR Earth System Research Laboratories, Boulder, Colorado
Hüser, I., Deutscher Wetterdienst, Offenbach, Germany
Inness, Antje, European Centre for Medium Range Weather Forecasts, Reading, United Kingdom

Editor and Author Affiliations (alphabetical by name)

Isaksen, K., Norwegian Meteorological Institute, Blindern, Oslo, Norway
John, Viju, EUMETSAT, Darmstadt, Germany
Jones, Philip D., Climatic Research Unit, School of Environmental Sciences, University of East Anglia, Norwich, United Kingdom
Kaiser, J. W., Deutscher Wetterdienst, Offenbach, Germany
Kelly, S., Dundalk Institute of Technology, Dundalk, Ireland
Khaykin, S., LATMOS/IPSL, UVSQ, Sorbonne Université, CNRS, Guyancourt, France
Kidd, R., Earth Observation Data Centre GmbH, Vienna, Austria
Kim, Hyungiun, Institite of Industrial Science, The University of Tokyo, Tokyo, Japan
Kipling, Z., European Centre for Medium-Range Weather Forecasts, Reading, United Kingdom
Kraemer, B. M., IGB Leibniz Institute for Freshwater Ecology and Inland Fisheries, Berlin, Germany
Kratz, D. P., NASA Langley Research Center, Hampton, Virginia
La Fuente, R. S., Dundalk Institute of Technology, Dundalk, Ireland
Lan, Xin, Cooperative Institute for Research in Environmental Sciences, University of Colorado Boulder, and NOAA/OAR Earth System Research Laboratories, Boulder, Colorado
Lantz, Kathleen O., NOAA/OAR Earth System Research Laboratory, and Cooperative Institute for Research in the Environmental Sciences, University of Colorado, Boulder, Colorado
Leblanc, T., Jet Propulsion Laboratory, California Institute of Technology, Wrightwood, California
Li, Bailing, Hydrological Sciences Laboratory, NASA Goddard Space Flight Center, Greenbelt, Maryland, USA; Earth System Science Interdisciplinary Center, University of Maryland, College Park, Maryland
Loeb, Norman G., NASA Langley Research Center, Hampton, Virginia
Long, Craig S., NOAA/NWS National Centers for Environmental Prediction, College Park, Maryland
Loyola, Diego, German Aerospace Center (DLR) Oberpfaffenhofen, Wessling, Germany
Marszelewski, Wlodzimierz, Department of Hydrology and Water Management, Nicolaus Copernicus University, Toruń, Poland
Martens, B., Hydro-Climate Extremes Lab (H-CEL), Ghent University, Ghent, Belgium
May, Linda, Centre for Ecology & Hydrology, Edinburgh, United Kingdom
Mayer, Michael, Department of Meteorology and Geophysics, University of Vienna, Austria; European Centre for Medium-Range Weather Forecasts, Reading, United Kingdom
McCabe, M. F., Division of Biological and Environmental Sciences and Engineering, King Abdullah University of Science and Technology, Thuwal, Saudi Arabia
McVicar, Tim R., CSIRO Land and Water, Canberra, Australian Capital Territory; and Australian Research Council Centre of Excellence for Climate Extremes, Sydney, New South Wales, Australia
Mears, Carl A., Remote Sensing Systems, Santa Rosa, California
Menzel, W. Paul, Space Science and Engineering Center, University of Wisconsin-Madison, Madison, Wisconsin
Merchant, Christopher J., Department of Meteorology, and National Centre for Earth Observation, University of Reading, Reading, United Kingdom
Miller, Ben R., Cooperative Institute for Research in Environmental Sciences, University of Colorado Boulder, and NOAA/OAR Earth System Research Laboratories, Boulder, Colorado
Miralles, Diego G., Hydro-Climate Extremes Lab (H-CEL), Ghent University, Ghent, Belgium
Montzka, Stephen A., NOAA/OAR Earth System Research Laboratories, Boulder, Colorado
Morice, Colin, Met Office Hadley Centre, Exeter, United Kingdom
Mühle, Jens, Scripps Institution of Oceanography, University of California, San Diego, La Jolla, California
Myneni, R., Department of Earth and Environment, Boston University, Boston, Massachusetts
Nicolas, Julien P., European Centre for Medium-Range Weather Forecasts, Reading, United Kingdom
Noetzli, Jeannette, WSL Institute for Snow and Avalanche Research SLF, Davos-Dorf, Switzerland
Osborn, Tim J., Climatic Research Unit, School of Environmental Sciences, University of East Anglia, Norwich, United Kingdom
Park, T., NASA Ames Research Center, and Bay Area Environmental Research Institute, Moffett Field, California
Pasik, A., Department of Geodesy and Geoinformation, TU Wien - Vienna University of Technology, Vienna, Austria
Paterson, Andrew M., Dorset Environmental Science Centre, Ontario Ministry of the Environment and Climate Change, Dorset, Ontario, Canada
Pelto, Mauri S., Nichols College, Dudley, Massachusetts
Perkins-Kirkpatrick, S., University of New South Wales, Sydney, Australia
Pétron, G., Cooperative Institute for Research in Environmental Sciences, University of Colorado, and NOAA/OAR Global Monitoring Laboratory, Boulder, Colorado
Phillips, C., Department of Atmospheric and Oceanic Sciences, University of Wisconsin-Madison, Madison, Wisconsin
Pinty, Bernard, European Commission, Joint Research Centre, Ispra, Italy
Po-Chedley, S., Lawrence Livermore National Laboratory, Livermore, California
Polvani, L., Columbia University, New York, New York
Preimesberger, W., Department of Geodesy and Geoinformation, TU Wien - Vienna University of Technology, Vienna, Austria
Pulkkanen, M., Finnish Environment Institute SYKE, Freshwater Centre, Helsinki, Finland.
Randel, W. J., National Center for Atmospheric Research, Boulder, Colorado
Rémy, Samuel, Institut Pierre-Simon Laplace, CNRS / UPMC, Paris, France
Ricciardulli, L., Remote Sensing Systems, Santa Rosa, California
Richardson, A. D., School of Informatics, Computing, and Cyber Systems and Center for Ecosystem Science and Society, Northern Arizona University, Flagstaff, Arizona
Rieger, L., University of Saskatchewan, Saskatoon, Canada
Robinson, David A., Department of Geography, Rutgers University, Piscataway, New Jersey
Rodell, Matthew, Hydrological Sciences Laboratory, NASA Goddard Space Flight Center, Greenbelt, Maryland
Rosenlof, Karen H., NOAA/OAR Earth System Research Laboratories, Boulder, Colorado
Roth, Chris, University of Saskatchewan, Saskatoon, Saskatchewan, Canada
Rozanov, A., University of Bremen, Bremen, Germany
Rusak, James A., Dorset Environmental Science Centre, Ontario Ministry of the Environment and Climate Change, Dorset, Ontario, Canada
Rusanovskaya, O., Institute of Biology, Irkutsk State University, Russia
Rutishäuser, T., Institute of Geography and Oeschger Center, University of Berne, Berne, Switzerland
Sánchez-Lugo, Ahira, NOAA/NESDIS National Centers for Environmental Information, Asheville, North Carolina
Sawaengphokhai, P., Science Systems and Applications, Inc., Hampton, Virginia
Scanlon, T., Department of Geodesy and Geoinformation, TU Wien - Vienna University of Technology, Vienna, Austria
Schenzinger, Verena, Department of Meteorology and Geophysics, University of Vienna, Austria

Editor and Author Affiliations (alphabetical by name)

Schladow, S. Geoffey, Tahoe Environmental Research Center, University of California at Davis, Davis, California
Schlegel, R. W., Physical Oceanography Department, Woods Hole Oceanographic Institution, Woods Hole, Massachusetts
Schmid, Martin, Eawag, Swiss Federal Institute of Aquatic Science and Technology, Kastanienbaum, Switzerland
Selkirk, H. B., Universities Space Research Association, NASA Goddard Space Flight Center, Greenbelt, Maryland
Sharma, S., York University, Toronto, Ontario, Canada
Shi, Lei, NOAA/NESDIS, National Centers for Environmental Information, Asheville, North Carolina
Shimaraeva, S. V., Institute of Biology, Irkutsk State University, Russia
Silow, E. A., Institute of Biology, Irkutsk State University, Russia
Simmons, Adrian J., European Centre for Medium-Range Weather Forecasts, Reading, United Kingdom
Smith, C. A., Cooperative Institute for Research in Environmental Sciences, University of Colorado Boulder, and Physical Sciences Laboratory, NOAA/Earth System Research Laboratories, Boulder, Colorado
Smith, Sharon L., Geological Survey of Canada, Natural Resources Canada, Ottawa, Ontario, Canada
Soden, B. J., Rosenstiel School of Marine and Atmospheric Science, University of Miami, Key Biscayne, Florida
Sofieva, Viktoria, Finnish Meteorological Institute (FMI), Helsinki, Finland
Sparks, T. H., Poznań University of Life Sciences, Poznań, Poland
Stackhouse, Jr., Paul W., NASA Langley Research Center, Hampton, Virginia
Stanitski, Diane M., NOAA/OAR Earth System Research Laboratories, Boulder, Colorado
Steinbrecht, Wolfgang, German Weather Service (DWD), Hohenpeissenberg, Germany
Streletskiy, Dimitri A., Department of Geography George Washington University, Washington D.C.
Taha, G., GESTAR, Columbia, Maryland
Telg, Hagen, NOAA/OAR Earth System Research Laboratories and Cooperative Institute for Research in the Environmental Sciences, University of Colorado, Boulder, Colorado
Thackeray, S. J., Centre for Ecology and Hydrology, Lancaster, United Kingdom
Timofeyev, M. A., Institute of Biology, Irkutsk State University, Russia
Tourpali, Kleareti, Aristotle University, Thessaloniki, Greece
Tye, Mari R., Capacity Center for Climate and Weather Extremes (C3WE), National Center for Atmospheric Research, Boulder, Colorado
van der A, Ronald J., Royal Netherlands Meteorological Institute (KNMI), De Bilt, Netherlands
van der Schalie, Robin, VanderSat B.V., Haarlem, Netherlands
van der Schrier, Gerard, Royal Netherlands Meteorological Institute (KNMI), De Bilt, Netherlands
van der Werf, Guido R., Vrije Universiteit Amsterdam, Amsterdam, Netherlands
Verburg, Piet, National Institute of Water and Atmospheric Research, Hamilton, New Zealand
Vernier, Jean-Paul, NASA Langley Research Center, Hampton, Virginia
Vömel, Holger, Earth Observing Laboratory, National Center for Atmospheric Research, Boulder, Colorado
Vose, Russell S., NOAA/NESDIS National Centers for Environmental Information, Asheville, North Carolina
Wang, Ray, Georgia Institute of Technology, Atlanta, Georgia
Watanabe, Shohei G., Tahoe Environmental Research Center, University of California at Davis, Davis, California
Weber, Mark, University of Bremen, Bremen, Germany
Weyhenmeyer, Gesa A., Department of Ecology and Genetics/Limnology, Uppsala University, Uppsala, Sweden
Wiese, David, Jet Propulsion Laboratory, California Institute of Technology, Pasadena, California
Wilber, Anne C., Science Systems and Applications, Inc., Hampton, Virginia
Wild, Jeanette D., NOAA Climate Prediction Center, College Park, Maryland; ESSIC/University of Maryland, College Park, Maryland
Willett, Kate M., Met Office Hadley Centre, Exeter, United Kingdom
Wong, Takmeng, NASA Langley Research Center, Hampton, Virginia
Woolway, R. Iestyn, Dundalk Institute of Technology, Dundalk, Ireland
Yin, Xungang, ERT Inc., NOAA/NESDIS National Centers for Environmental Information, Asheville, North Carolina
Zhao, Lin, School of Geographical Sciences, Nanjing University of Information Science & Technology, Nanjing, China
Zhao, Guanguo, University of Illinois at Urbana-Champaign, Champaign, Illinois
Zhou, Xinjia, Center for Satellite Applications and Research, NOAA, College Park, Maryland
Ziemke, Jerry R., Goddard Earth Sciences Technology and Research, Morgan State University, Baltimore, Maryland, and NASA Goddard Space Flight Center, Greenbelt, Maryland
Ziese, Markus, Global Precipitation Climatology Center, Deutscher Wetterdienst, Offenbach am Main, Germany

Editorial and Production Team

Andersen, Andrea, Technical Editor, Innovative Consulting Management Services, LLC, NOAA/NESDIS National Centers for Environmental Information, Asheville, North Carolina
Griffin, Jessicca, Graphics Support, Cooperative Institute for Satellite Earth System Studies, North Carolina State University, Asheville, North Carolina
Hammer, Gregory, Content Team Lead, Communications and Outreach, NOAA/NESDIS National Centers for Environmental Information, Asheville, North Carolina
Love-Brotak, S. Elizabeth, Lead Graphics Production, NOAA/NESDIS National Centers for Environmental Information, Asheville, North Carolina
Misch, Deborah J., Graphics Support, Innovative Consulting Management Services, LLC, NOAA/NESDIS National Centers for Environmental Information, Asheville, North Carolina
Riddle, Deborah B., Graphics Support, NOAA/NESDIS National Centers for Environmental Information, Asheville, North Carolina
Veasey, Sara W., Visual Communications Team Lead, Communications and Outreach, NOAA/NESDIS National Centers for Environmental Information, Asheville, North Carolina

2. Table of Contents

2. Table of Contents

***Please refer to Chapter 8 (Relevant datasets and sources) for a list of all climate variables and datasets used in this chapter for analyses, along with their websites for more information and access to the data.**

2. GLOBAL CLIMATE

R. J. H. Dunn, D. M. Stanitski, N. Gobron, and K. M. Willett, Eds.

a. Overview—R. J. H. Dunn, D. M. Stanitski, N. Gobron, and K. M. Willett

The assessments and analyses presented in this chapter focus predominantly on the measured differences of climate and weather observables from previous conditions, years, and decades to place 2019 in context. Many of these differences have direct impacts on people, for example, their health and environment, as well as the wider biosphere, but are beyond the scope of these analyses.

For the last few *State of the Climate* reports, an update on the number of warmer-than-average years has held no surprises, and this year is again no different. The year 2019 was among the three warmest years since records began in the mid-to-late 1800s. Only 2016, and for some datasets 2015, were warmer than 2019; all years after 2013 have been warmer than all others back to the mid-1800s. Each decade since 1980 has been successively warmer than the preceding decade, with the most recent (2010–19) being around 0.2°C warmer than the previous (2000–09).

This warming of the land and ocean surface is reflected across the globe. For example, lake and permafrost temperatures have increased; glaciers have continued to lose mass, becoming thinner for the 32nd consecutive year, with the majority also becoming shorter during 2019. The period during which Northern Hemisphere (NH) lakes were covered in ice was seven days shorter than the 1981–2010 long-term average, based on in situ phenological records. There were fewer cool extremes and more warm extremes on land; regions including Europe, Japan, Pakistan, and India all experienced heat waves. More strong than moderate marine heat waves were recorded for the sixth consecutive year. And in Australia (discussed in more detail in section 7h4), moisture deficits and prolonged high temperatures led to severe impacts during late austral spring and summer, including devastating wildfires. Smoke from these wildfires was detected across large parts of the Southern Hemisphere (SH).

The year 2019 was also one of the three warmest above Earth's surface and within the troposphere, while middle and upper stratospheric temperatures were at their lowest recorded values since 1979, as is expected because of the increasing concentration of greenhouse gases in the atmosphere.

The continuing warm conditions also influenced water around the globe, with atmospheric water vapor (specific humidity) being high over the ocean surface (one of the moistest years on record) and also aloft, and well above average near the land surface. However, in terms of saturation (relative humidity), the atmosphere was very dry near the land surface, setting a new record low for the global average, and about average over the ocean surface and aloft. There were strong hemispheric differences in soil moisture anomalies with, on average, negative anomalies in the south and positive anomalies in the north. Globally, the second half of 2019 saw an increase in the land area experiencing drought to higher, but not record, levels by the end of the year, but annual precipitation amounts were around average, with regional peaks in intense rainfall from, for example, Cyclones Idai and Kenneth in southeastern Africa.

Many climate events in Africa, Asia, and Australia were influenced by the strong positive Indian Ocean dipole (IOD), while the weak-to-neutral prolonged El Niño–Southern Oscillation (ENSO) conditions during 2019 appeared to have only limited impacts.

As a primary driver for our changing climate, the abundance of many long-lived greenhouse gases continues to increase. Globally averaged CO_2 at Earth's surface reached 409.8 ± 0.1 ppm, a 2.5 ± 0.1 ppm increase from 2018; and CH_4 reached 1866.6 ± 0.9 ppb in 2019, a 9.2 ± 0.9 ppb increase from 2018, which is among the three largest annual increases (with 2014 and 2015) since 2007, when a rapid rise in methane concentration began. The mean global atmospheric N_2O abundance in 2019 was 331.9 ± 0.1 ppb, an increase of 1.0 ± 0.2 ppb from 2018. However, the atmospheric abundances of most ozone-depleting substances (ODS) are declining or leveling off, decreasing the stratospheric halogen loading and radiative forcing associated with ODS.

Stratospheric water vapor variability is strongly affected by the absolute humidity of air entering the stratosphere in the tropics, which is in turn largely determined by the temperature of the tropical cold point tropopause. Following 2018, a year in which lower stratospheric water vapor in the tropics dropped to a very low value (~20% below the 2004–19 average in December), water vapor abundance in the tropical lower stratosphere increased during 2019 to about 10% above average in the latter half of the year.

Both hemispheric average and global average tropospheric ozone in 2019 indicate a continuing increase from previous years based on satellite measurements (starting year 2004) and surface measurements (starting in the mid-1970s). The largest trends in tropospheric ozone over the last 15 years occurred above India and East/Southeast Asia at a rate of ~ +3.3 DU decade^{-1} (~ +1% yr^{-1}); these increases are consistent with expected increases of ozone precursor emissions across this region.

The year saw exceptional fire events over Australia, Indonesia, and parts of Siberia, but was also marked by lower amounts of dust over most of the Sahara. In the latter part of 2019, the Raikoke (Russia) and Ulawun (Papua New Guinea) volcanic eruptions and the large Australian wildfires loaded the stratosphere with aerosol levels unprecedented since the post-Mt. Pinatubo era 25 years ago. Despite this, 2019 was near-record warm at the surface.

The responses of the terrestrial biosphere to climatic conditions were also visible. Phenological land indicators show an average excess of eight days for the duration of the growing season in the NH in 2019 relative to the 2000–10 baseline. A deficit of plant productivity in the SH resulted in a lighter surface and hence higher albedo, whereas northern latitudes presented a darker surface and lower albedo, largely due to below-average snow cover. However, the rate of photosynthesis increased in eastern China with vegetation growth due to major human changes in land use.

New additions to this chapter in 2019 include lake water levels (last included in 2011) and sidebars on lake ice cover and stratospheric aerosols. Marine temperature extremes are also included this year alongside the land–surface indices, and we see the return of an update on the Mauna Loa solar transmission record.

Time series and anomaly maps for many of the variables described in this chapter are shown in Plates 1.1 and 2.1, respectively. A number of sections refer to supplemental figures that can be found in Appendix 2.

(a) Surface Temperature

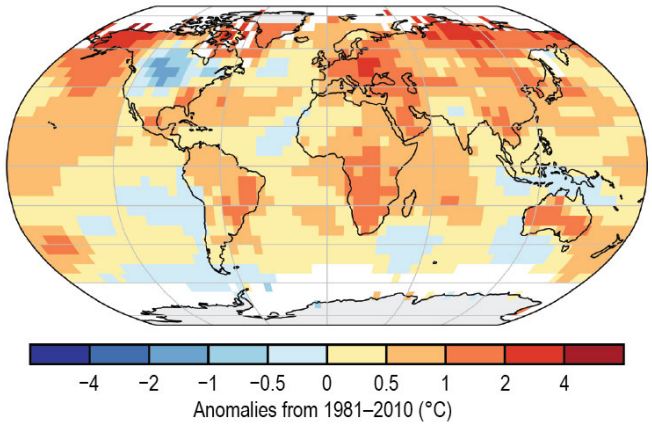

(b) Lake Temperatures

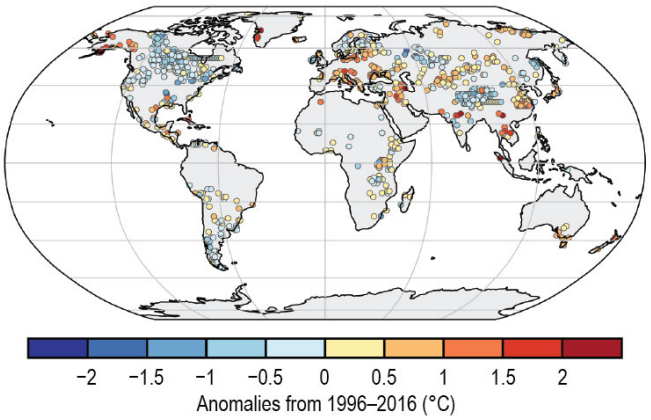

(c) Warm Days

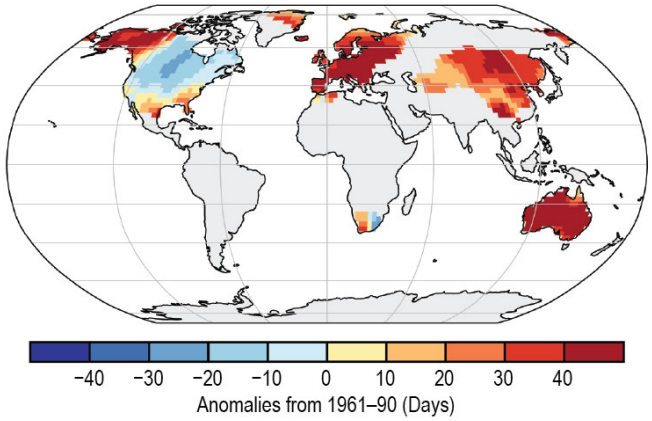

(d) Cool Nights

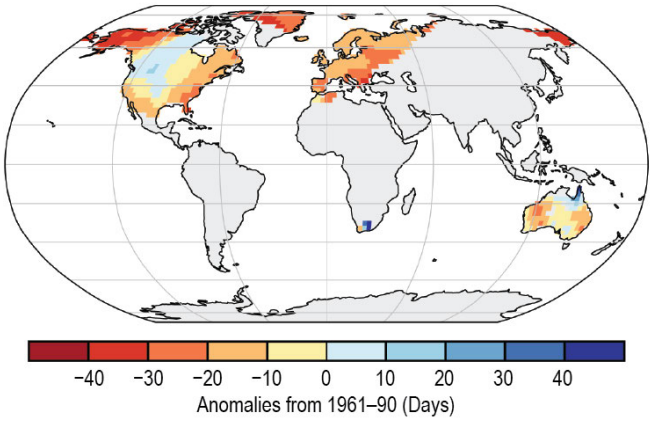

(e) Lower Tropospheric Temperature

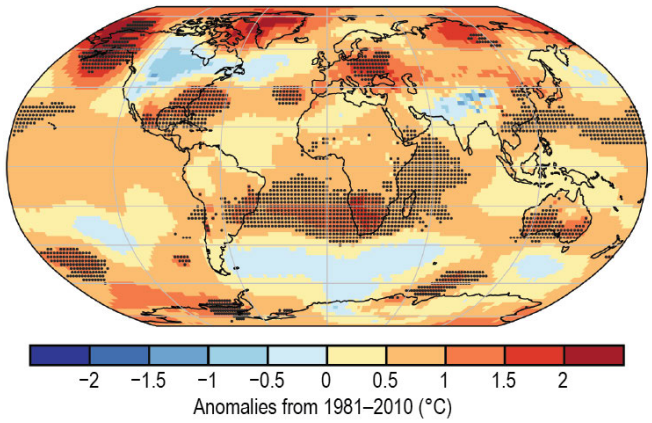

(f) Lower Stratospheric Temperature

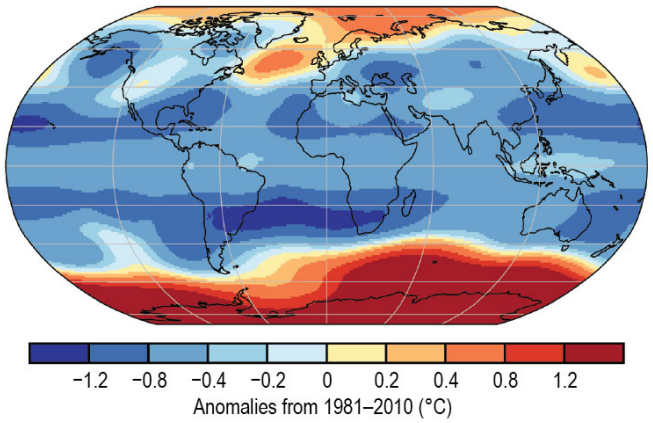

(g) Surface Specific Humidity

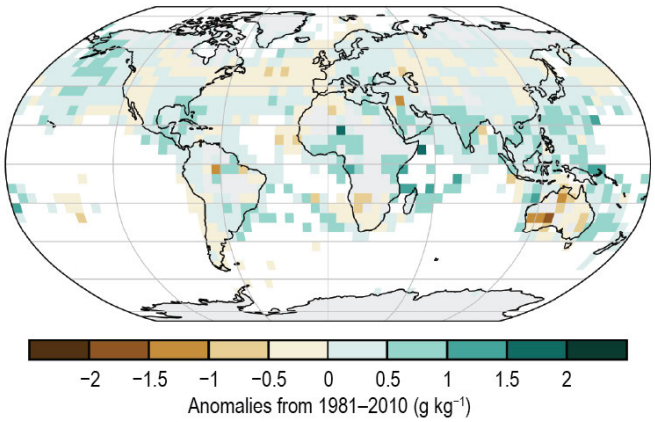

Plate 2.1. (a) NOAA NCEI Global land and ocean surface annual temperature anomalies (°C); (b) Satellite-derived lake surface water temperature anomalies (°C) in 2019. The anomalies are calculated for the meteorological warm season (JJA in NH; DJF in SH, and over Dec–Aug 2018/19 within 23.5° of the equator). The longitude of some of the lakes has been shifted slightly to enable them to be displayed clearly. The latitude has been maintained; (c) GHCNDEX warm day threshold exceedance (TX90p); (d) GHCNDEX cool night threshold exceedance (TN10p); (e) ERA5 annual temperature anomalies of LTT (°C). Stippling indicates grid points in which the 2019 value was the highest of the 41-year record; (f) ERA5 annual temperature anomalies of LST (°C); (g) HadISDH surface specific humidity anomalies (g kg^{-1});

(h) Surface Relative Humidity

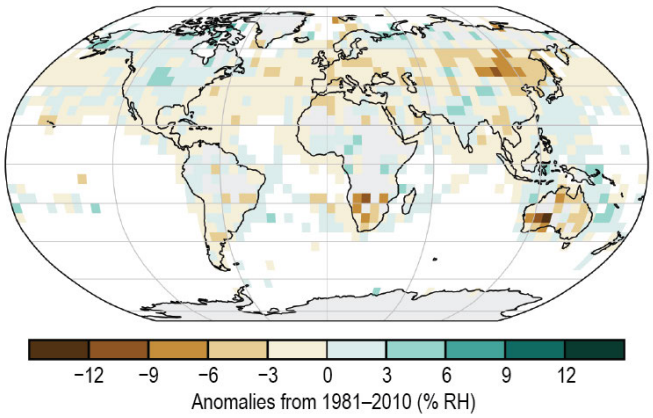

(i) Total Column Water Vapor

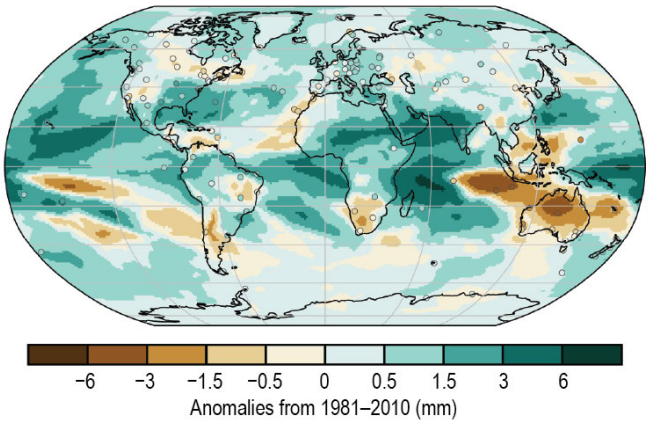

(j) Upper Tropospheric Humidity

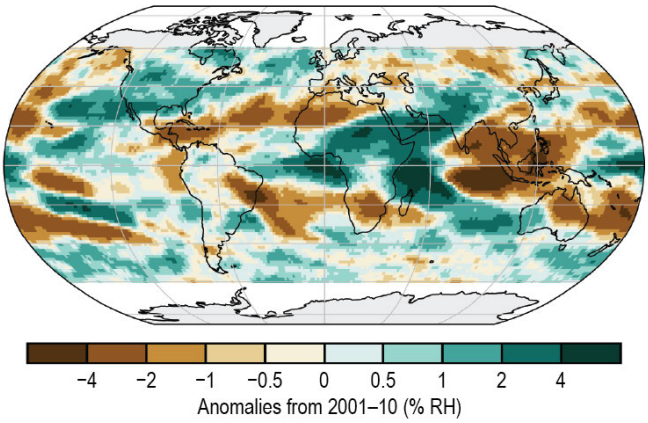

(k) Precipitation

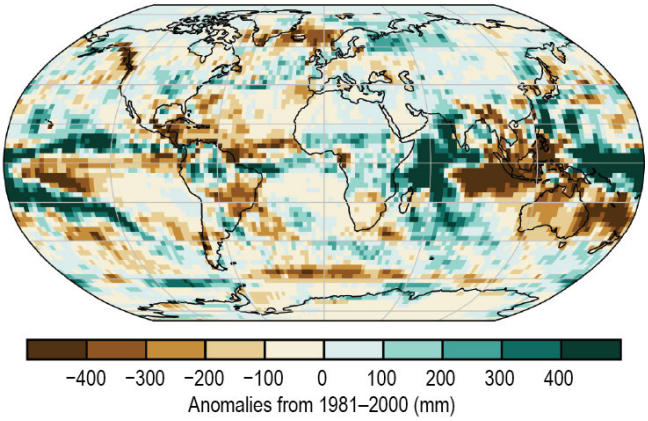

(l) R10mm

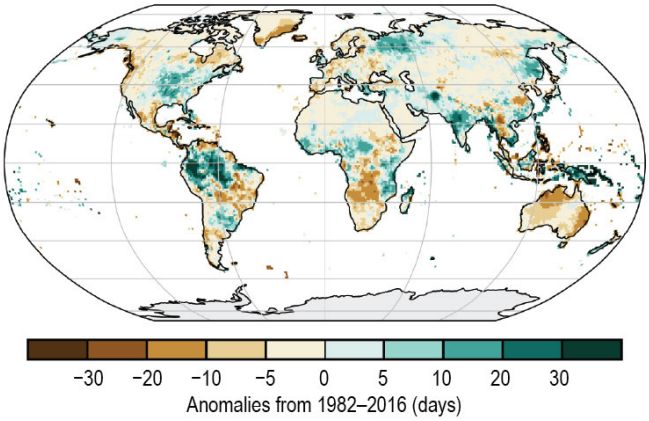

(m) Lake Water Level

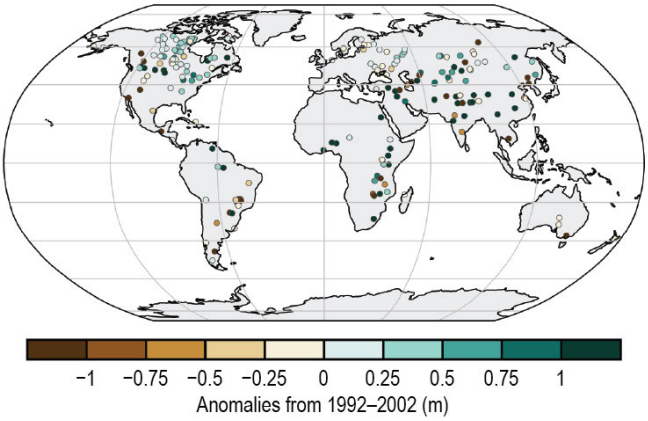

(n) Cloudiness

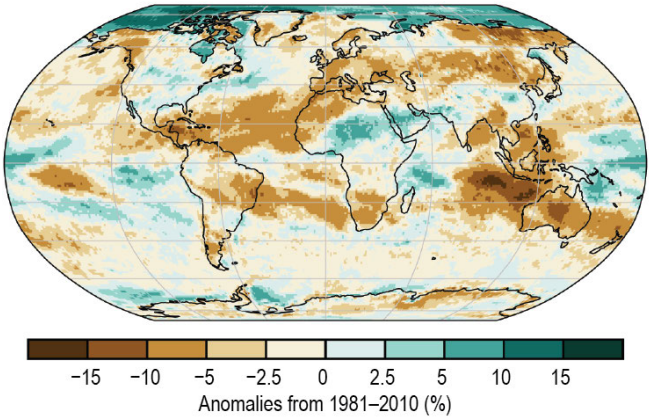

Plate 2.1. (cont.) (h) HadISDH surface relative humidity anomalies (% RH); (i) ERA5 reanalysis of TCWV anomalies (mm). Data from GNSS stations are plotted as filled circles; (j) "All sky" microwave-based UTH dataset annual average UTH anomalies (% RH); (k) GPCP v2.3 annual mean precipitation anomalies for 2019 (mm yr^{-1}); (l) Anomalies for the 2019 GPCC-First Guess Daily R10mm index (days); (m) Lake water level anomalies (meters) based on satellite altimeters for 198 large lakes; (n) Global cloudiness anomalies (%) generated from the 30-year PATMOS-x/AVHRR cloud climatology;

(o) River Discharge

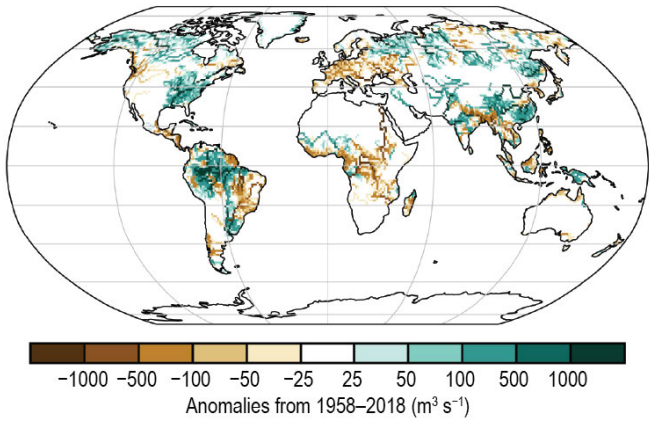

(p) Runoff

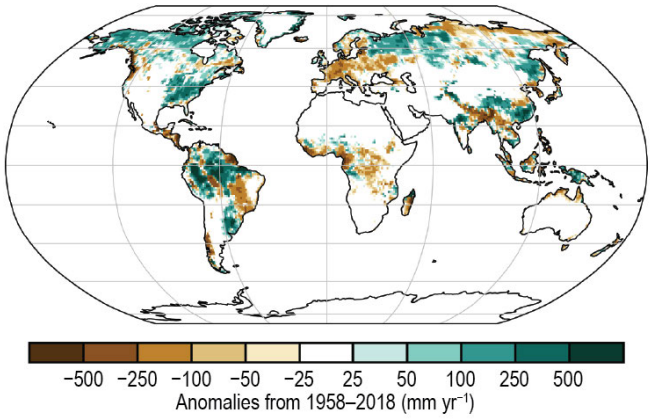

(q) Terrestrial Water Storage

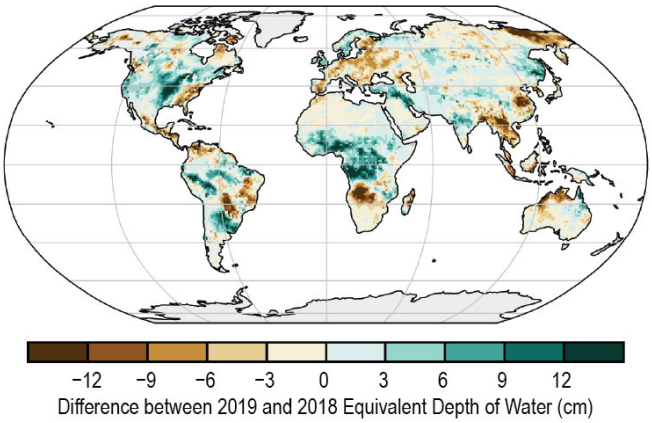

(r) Soil Moisture

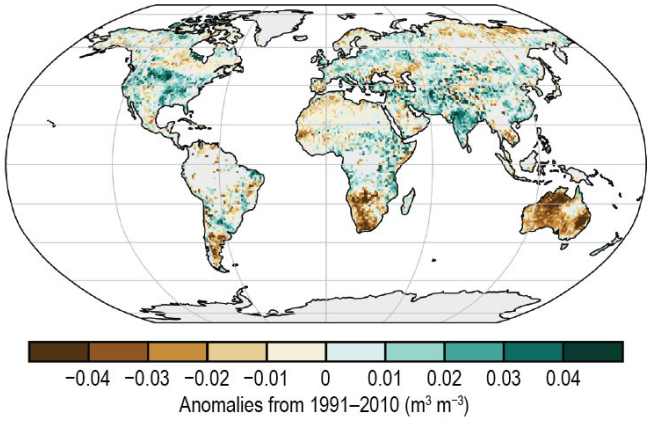

(s) Land Evaporation

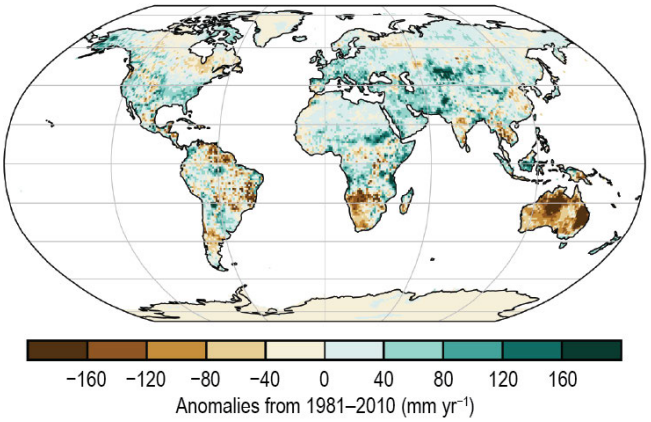

(t) Drought

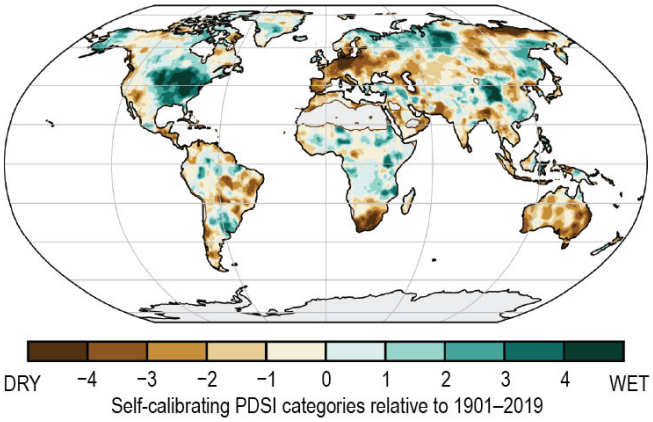

Plate 2.1. (cont.) (o) Global distribution of river discharge anomalies ($m^3 s^{-1}$) from JRA-55; (p) Global distribution of runoff anomalies (mm yr^{-1}) from JRA-55; (q) Changes in annual-mean terrestrial water storage (the sum of groundwater, soil water, surface water, snow, and ice, as an equivalent height of water in cm) between 2018 and 2019, based on output from a GRACE and GRACE-FO data-assimilating land surface model. No data are shown over Greenland, Antarctica, the gulf coast of Alaska, parts of Patagonia, and most polar islands; (r) ESA CCI Soil Moisture average surface soil moisture anomalies ($m^3 m^{-3}$). Data were masked as missing where retrievals are either not possible or of very low quality (dense forests, frozen soil, snow, ice, etc.); (s) GLEAM land evaporation anomalies (mm yr^{-1}); (t) Mean scPDSI for 2019. Droughts are indicated by negative values (brown), wet episodes by positive values (green). No calculation is made where a drought index is meaningless (gray areas: ice sheets or deserts with approximately zero mean precipitation);

(u) Sea Level Pressure

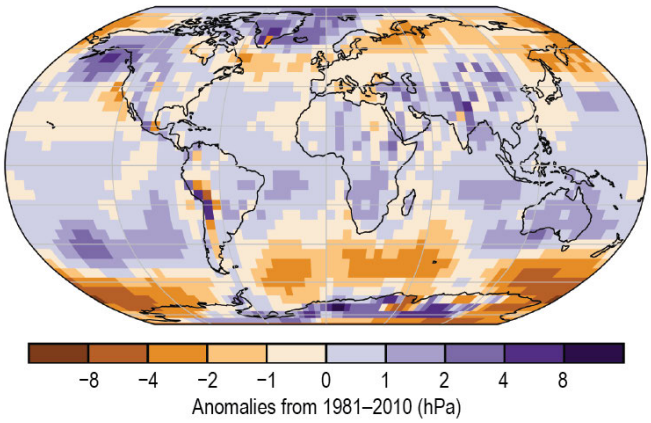

(v) Surface Winds

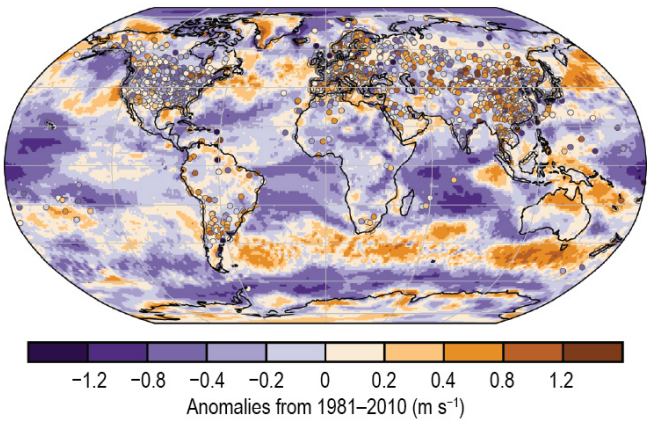

(w) Upper Air (850-hPa) Winds

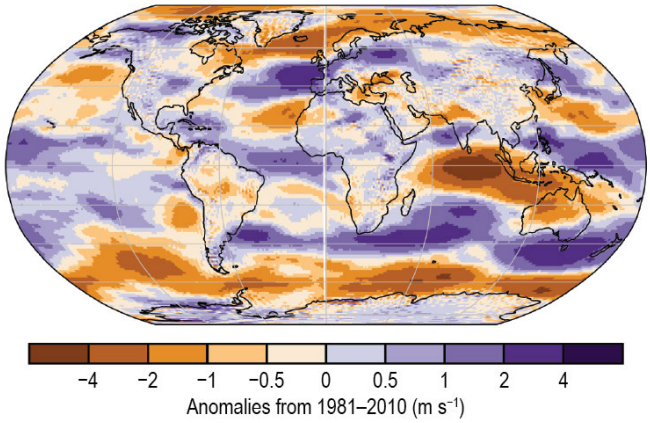

(x) Total Aerosol

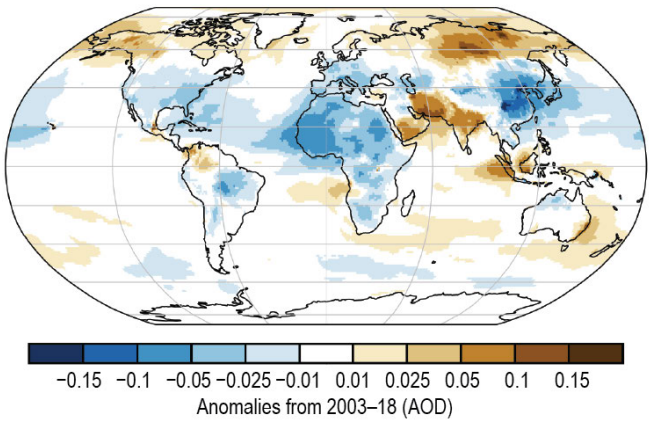

(y) Extreme Aerosol Days

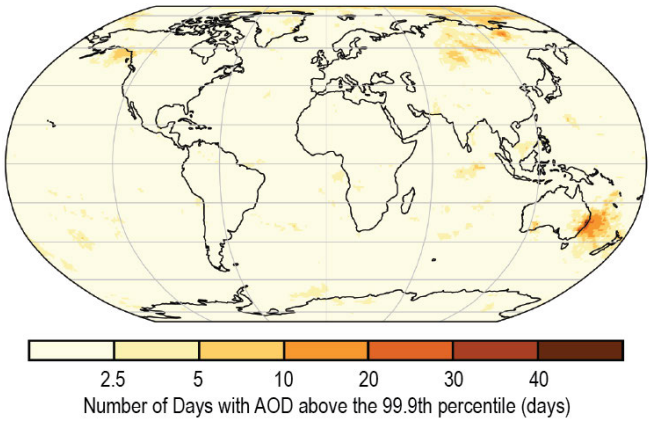

(z) Stratospheric (Total Column) Ozone

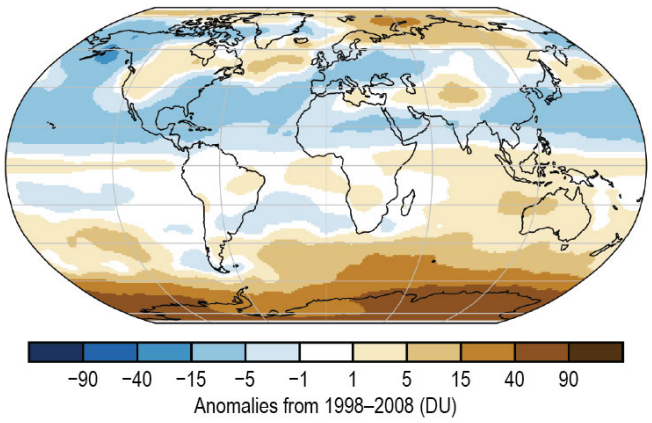

Plate 2.1. (cont.) (u) HadSLP2r surface pressure anomalies (hPa); (v) Surface wind speed anomalies (m s^{-1}) from the observational HadISD3 dataset (land, circles), the MERRA-2 reanalysis output (land, shaded areas), and RSS satellite observations (ocean, shaded areas); (w) ERA5 Aug–Dec average 850-hPa eastward wind speed anomalies (m s^{-1}); (x) Total aerosol optical depth (AOD) anomalies at 550 nm; (y) Number of days with extremely high AOD (extreme being defined as above the local 99.9th percentile of the 2003–18 average; (z) Total column ozone anomalies (DU) in 2019 from Global Ozone Monitoring Experiment-2 (GOME-2A) measurements with respect to the 1998–2008 mean determined from the merged multi-sensor data combining GOME, SCIAMACHY, and GOME-2 (GSG, Weber et al. 2018);

(aa) OMI/MLS Tropospheric Column Ozone

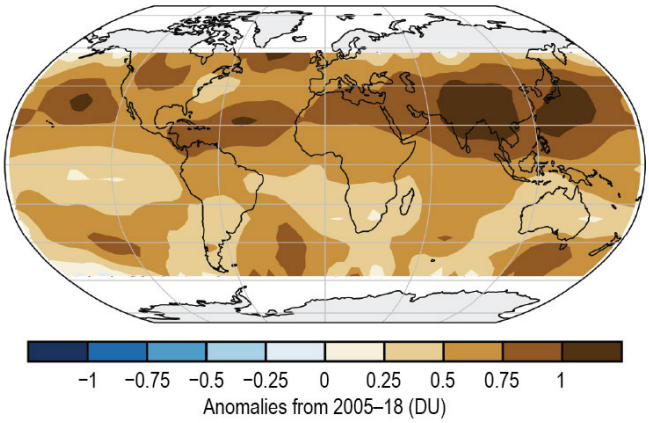

(ab) Carbon Monoxide

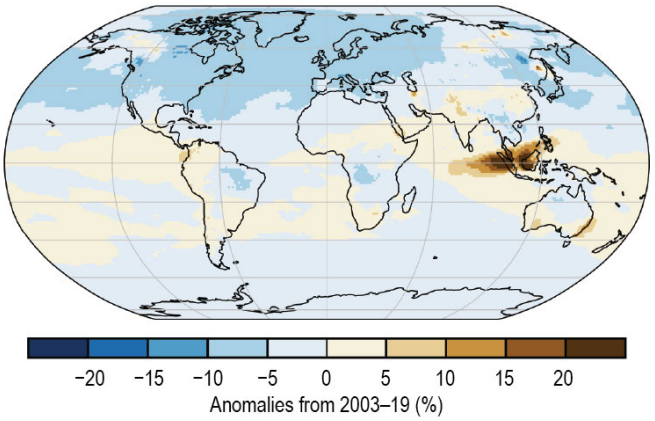

(ac) Land Surface Albedo in the Visible

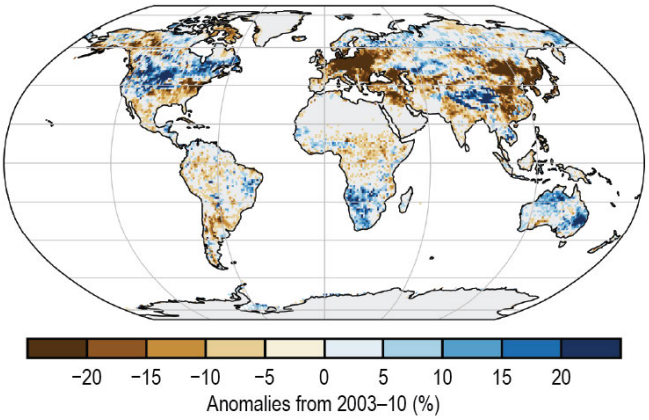

(ad) Land Surface Albedo in the Near-Infrared

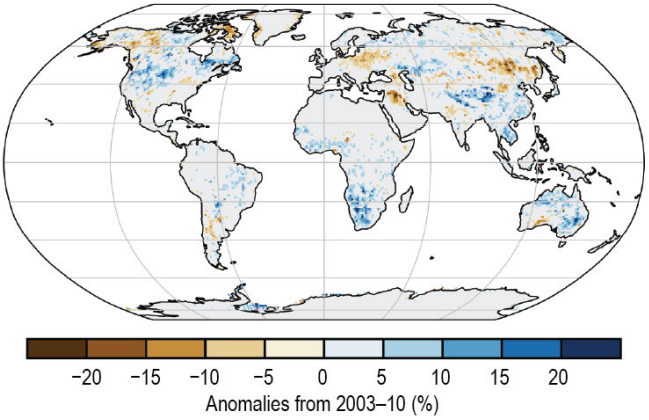

(ae) Fraction of Absorbed Photosynthetically Active Radiation

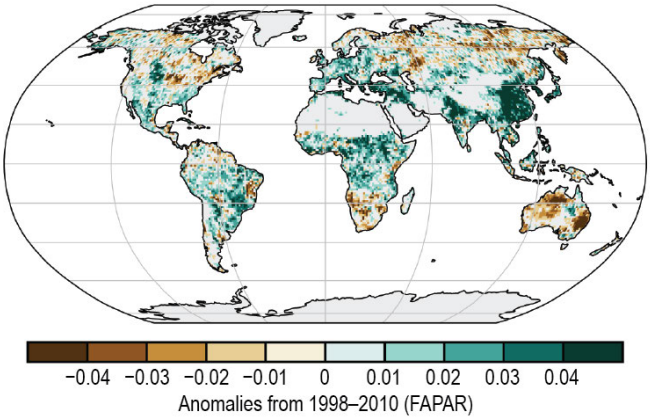

(af) Carbon Emissions from Biomass Burning

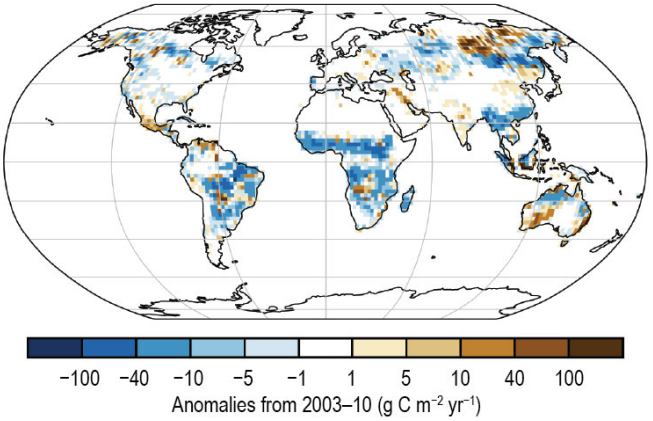

Plate 2.1. (cont.) (aa) Tropospheric ozone anomalies (DU) for 2019, relative to 2005–18 average, as detected by the OMI/MLS satellite instruments; (ab) CAMS reanalysis total column CO anomalies (%); (ac) Land surface visible albedo anomalies (%); (ad) Land surface near-infrared albedo anomalies (%); (ae) FAPAR anomalies; (af) GFAS1.4 carbonaceous emission anomalies (g C m^{-2} yr^{-1}) from biomass burning.

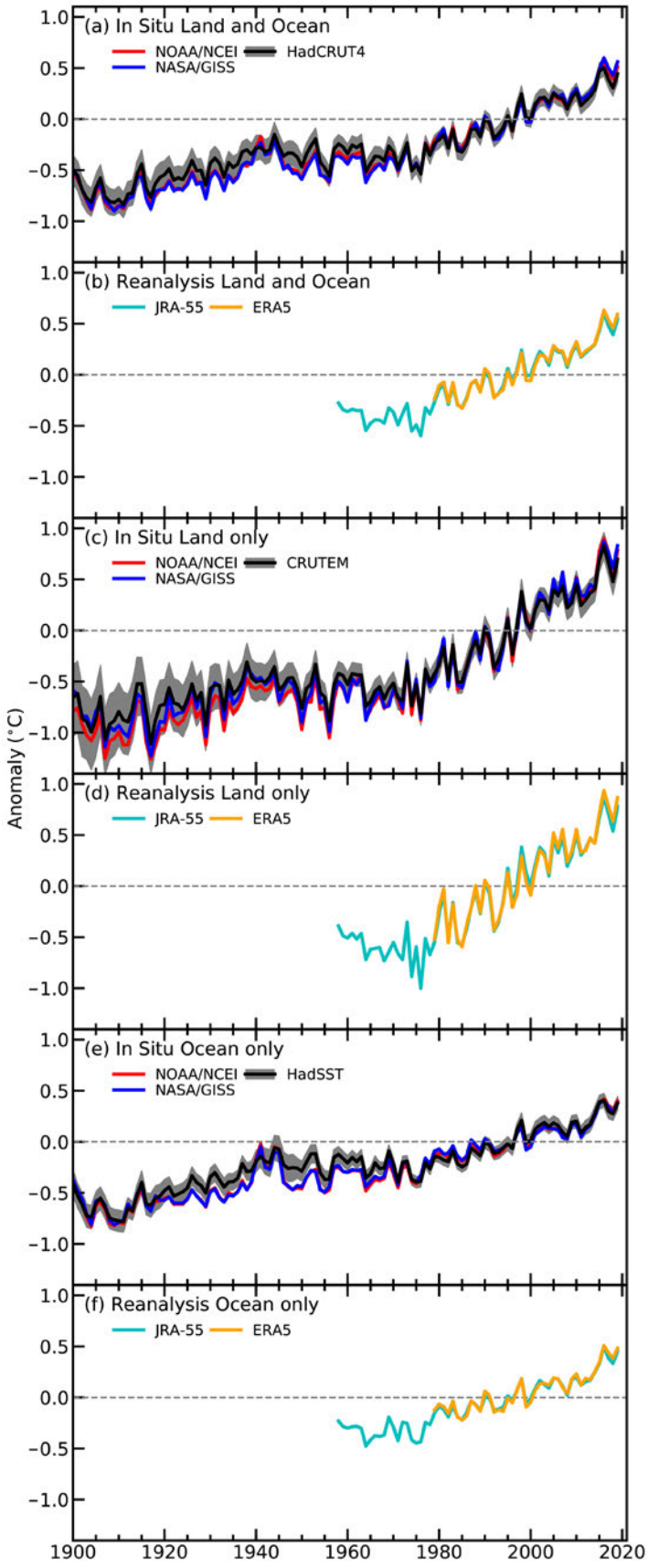

Fig. 2.1. Global average surface air temperature anomalies (°C; 1981–2010 base period). In situ estimates are shown from NOAA/NCEI (H.-M. Zhang et al. 2019), NASA-GISS (Lenssen et al. 2019), HadCRUT4 (Morice et al. 2012), CRUTEM4 (Jones et al. 2012), HadSST3 (Kennedy et al. 2011a,b). Reanalyses estimates are shown from ERA5 (Hersbach et al. 2020), and JRA-55 (Kobayashi et al. 2015).

b. Temperature

1) Global surface temperature—

A. Sánchez-Lugo, C. Morice, J. P. Nicolas, and A. Argüez

The 2019 global land and ocean surface temperature was 0.44°–0.56°C above the 1981–2010 average (Table 2.1) and was among the three highest yearly temperatures since global records began in the mid-to-late 1800s (Fig. 2.1), according to three independent in situ analyses (NASA-GISS, Lenssen et al. 2019; HadCRUT4, Morice et al. 2012; NOAAGlobalTemp, H.-M. Zhang et al. 2019). The NOAAGlobalTemp and NASA-GISS datasets ranked 2019 as the second-warmest year on record, just 0.04°C behind 2016. The HadCRUT4 dataset ranked 2019 as the third-warmest year, behind 2016 (+0.50°C) and 2015 (+0.47°C). A weak El Niño was present across the tropical Pacific Ocean at the start of the year (see section 4b). The presence of an El Niño (La Niña) typically has a warming (cooling) influence on global temperatures (e.g., Foster and Rahmstorf 2011). The El Niño transitioned to El Niño–Southern Oscillation (ENSO) neutral by mid-2019.

The three in situ global surface temperature analyses assessed here are derived from air temperatures observed at weather stations over land and sea surface temperatures (SSTs) observed from ships and buoys. Differences between analyses are mainly due to how each methodology treats areas with little to no data and how each analysis accounts for changes in measurement methods (for more details see Kennedy et al. [2010]; Hansen et al. [2010]; and Sánchez-Lugo et al. [2017]). Although each analysis differs in methodology, leading to minor differences in temperature anomalies and ranks, the three in situ datasets are overall in close agreement (Fig. 2.1), with an average rate of increase of 0.07°C per decade since 1880 and a little over double that rate at 0.18°–0.19°C per decade since 1971. The

last six years (2014–19) were the six warmest years since global records began in the mid-to-late 1800s, contributing to the warmest decade on record with a decadal temperature of 0.32°–0.39°C above the 1981–2010 mean. Each decade since 1980 has been successively warmer than the preceding decade, with the 2010–19 decadal temperature departure from average surpassing the previous record warm decade of 2000–09 by 0.15°–0.22°C.

While annual temperature rankings provide a simple measure of the state of global temperatures, a recently introduced global annual temperature score (Argüez et al. 2020) complements the annual temperature ranking by providing a basic characterization of the impacts of natural variability on global temperature relative to the sustained upward trend since the mid-1970s. Scores range from 1 to 10, with a score of 1 (10) indicating the coldest (warmest) 10% of anomalies relative to the trend line. In an era of seemingly perpetual near-record warm rankings, the annual temperature scores can help characterize whether the annual temperature ranking attained in a given year was due primarily to continuation of the trend, natural variability, or both. For example, 2016 was not only the warmest year on record, but it also exhibited a temperature score of 10, whereas 2014 previously attained a ranking of warmest yet exhibits a temperature score of 4 (on the colder half of the scale). This indicates that, on top of the long-term upward trend, natural variability had a prominent contribution to the record temperature in 2016, whereas natural variability did not have a prominent contribution to 2014's previous record temperature. Using global annual time series from 1975 through 2019, the year 2019 registers a global annual temperature score of 9 (corresponding to the 80th to 90th percentile) in the NASA-GISS and NOAAGlobalTemp datasets and a score of 7 (60th to 70th percentile) in the HadCRUT4 dataset. This indicates that 2019 was moderately-to-considerably warmer than we would expect due to continuation of the upward trend alone, suggesting that its ranking as second or third warmest was attributable to the combined effects of natural variability and progression of the upward temperature trend.

The 2019 annual surface temperatures were above average across much of the world's land and ocean surfaces (Plate 2.1a; Figs. A2.1, A2.2). The most notable positive anomalies (+1.0°C or higher) were observed across Alaska, the Gulf of Alaska, northeastern Canada, Baffin Bay, Greenland, Europe, the Middle East, Russia, eastern Asia, Australia, southern Africa, and parts of Brazil. In contrast, near- to below-average conditions were present across a large swath of North America and across parts of the southeastern and southwestern Pacific Ocean, the Atlantic Ocean, and Indian Ocean.

The global temperature over land surfaces was 0.70°–0.83°C above average—the second highest on record, behind 2016. The global ocean temperature was 0.38°–0.40°C above average and the second or third highest on record, depending on the dataset.

Globally averaged surface air temperatures are also estimated using full-input reanalyses. A full-input reanalysis uses an objective algorithm and a weather prediction model to combine information from a range of satellite, aircraft, and in situ observational data sources to reconstruct historical weather and climate across the whole globe. A surface-input reanalysis is similar but combines information from only surface-based observations. Both can suffer from regional model biases and the effects of changes in the observation network during the analysis period. However, surface temperatures from reanalyses should be consistent with in situ analyses in regions of good observational coverage. Here, two full-input reanalyses are considered: ERA5 (Hersbach et al. 2020) and JRA-55 (Kobayashi et al. 2015). Currently, these reanalyses provide data from 1979 onward for ERA5 and from 1958 onward for JRA-55.

For both reanalyses, the globally averaged annual mean 2-m air temperature over land and ocean for 2019 was the second highest since the start of their respective records, being 0.59°C above average in ERA5 and 0.51°C above average in JRA-55 (Table 2.1). These estimates fall within the range of those derived from the three observational datasets mentioned above. Comparatively, the two reanalysis temperatures for 2016 (the warmest year on record) were 0.63°C and 0.56°C above average, respectively.

Table 2.1. Temperature anomalies (°C) and uncertainties (where available) for 2019 w.r.t. the 1981–2010 base period. Where uncertainty ranges are provided, the temperature anomalies correspond to the central values of a range of possible estimates. Uncertainty ranges represent a 95% confidence interval. Note that for the HadCRUT4 column, land values were computed using the CRUTEM.4.6.0.0 dataset (Jones et al. 2012), ocean values were computed using the HadSST.3.1.1.0 dataset (Kennedy et al. 2011a,b), and global land and ocean values used the HadCRUT4.6.0.0 dataset (Morice et al. 2012).

Global	NASA-GISS (°C)	HadCRUT4 (°C)	NOAA GlobalTemp (°C)	ERA5 (°C)	JRA-55 (°C)
Land	+0.83	+0.70 ± 0.13	+0.78 ± 0.14	+0.87	+0.78
Ocean	+0.38	+0.38 ± 0.07	+0.40 ± 0.16	+0.48	+0.39
Land and Ocean	+0.56 ±0.05	+0.44 ± 0.08	+0.51± 0.15	+0.59	+0.51

For 2019, the reanalyses also show warmer-than-average conditions over many regions of the world (Figs. A2.3, A2.4), particularly over high northern latitudes. Over both global ocean and global land, the two reanalyses agree that the 2019 2-m air temperature was the second highest on record and that the last five years (2015–19) were the five warmest years on record over both global ocean and global land (as well as globally).

2) Lake surface temperature—L. Carrea, R. I. Woolway, C. J. Merchant, M. T. Dokulil, C. L. DeGasperi, E. de Eyto, S. Kelly, R.S. La Fuente, W. Marszelewski, L. May, A. M. Paterson, M. Pulkkanen, J. A. Rusak, O. Rusanovskaya, S. G. Schladow, M. Schmid, S. V. Shimaraeva, E. A. Silow, M. A. Timofeyev, P. Verburg, S. Watanabe, and G. A. Weyhenmeyer

In 2019, the worldwide averaged satellite-derived lake surface water temperature (LSWT) warm-season (June–August in the Northern Hemisphere [NH]; December–February 2018/19 in the Southern Hemisphere [SH]; and December–August 2018/19 for the tropical region of 23.5°N–23.5°S) anomaly was +0.025 ± 0.022°C compared with the 1996–2016 base period. The mean warming trend from 1995 to 2019 was 0.21 ± 0.02°C decade^{-1}, broadly consistent with previous analyses (Woolway et al. 2017, 2018; Carrea et al. 2019). On average, anomalies (with respect to the 1996–2016 baseline) in 2019 were less positive than in 2018 and in 2017, 0.23°C and 0.19°C less, respectively. The warm-season anomalies for each lake are shown in Plate 2.1b. Per lake, the LSWT anomaly was positive for 47% of lakes, and negative for 53%. Some similarities between the 2019 warm-season lake temperature anomalies and the ice cover anomalies, in terms of spatial distribution in the NH (Sidebar 2.1; Fig. SB2.1), can be observed in regions where longer ice duration is related to negative lake water temperature anomalies.

In the NH, distinctive warmer and cooler regions can be identified: Alaska, Greenland, Europe (except the northeast) show clearly positive anomalies, while Tibet and parts of North America show clear

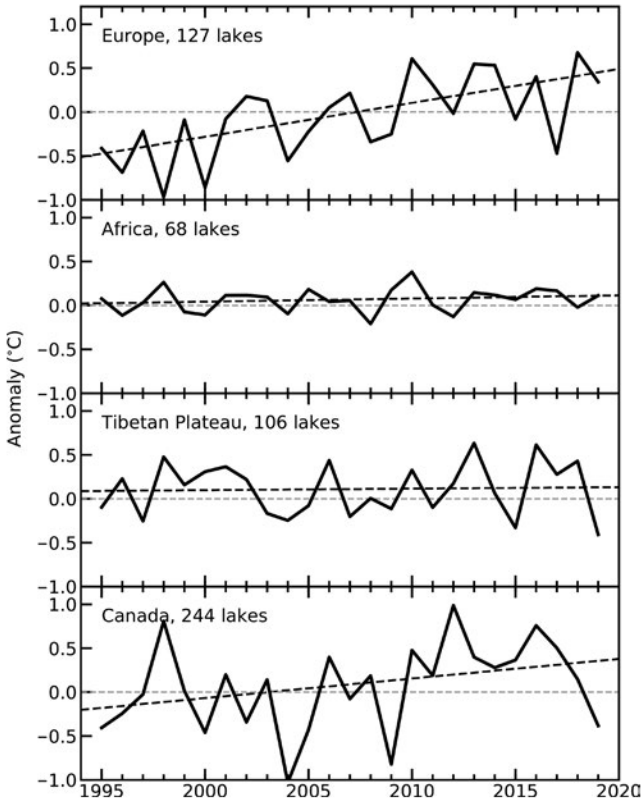

Fig. 2.2. Satellite-derived annual LSWT anomalies (°C; relative to 1996–2015) from 1995 to 2019 for Europe, Africa, Tibet, and Canada. These values were calculated for the meteorological warm season (Jun–Aug in the NH; Dec–Feb in the SH; and over the whole year in the tropics).

negative anomalies. Four regions are shown in more detail: Europe (n = 127), Tibet (n = 106), Africa (n = 68), and Canada (n = 244). The warm-season LSWT calculated from the satellite data shows a warming tendency of +0.39 ± 0.03°C decade^{-1} in Europe and +0.22 ± 0.04°C decade^{-1} in Canada. In Africa and Tibet the tendency is more neutral (Fig. 2.2.). The year 2018 was the warmest since records began in 1995 for European lakes over the June–August (JJA) period (similar to the finding for July–September [JAS] in Carrea et al. 2019). The anomaly in Europe in 2019 was more moderately positive than in 2018, due to the contribution of cooler lakes in northern Europe and Ireland (see section 7f for details). In particular, the border between Scandinavia and Finland delimits regions with contrasting behaviors, i.e., positive anomalies for Scandinavia and a few negative anomalies for Finland and the Karelia region of Russia, respectively. Modeled lake temperature anomalies in the ECMWF ERA5 reanalysis (Hersbach et al. 2020) are available that include lakes smaller than are observable in the satellite data (≥ ~1 km^2), modeled as the fraction of each land surface grid cell covered by inland water (so-called "lake tiles"). The reanalysis lake tile temperatures are shown in Fig. 2.3. For the lakes in Ireland, the observed LSWT anomalies are moderately negative in contrast to the moderately positive ERA5 modeled data, while LSWT anomalies from satellite data are generally consistent with the ERA5 data in Canada, Tibet, and Africa (Fig. 2.3). ERA5 data are driven by the reanalysis surface meteorological conditions (Balsamo et al. 2012) and in general, the lake temperature anomalies broadly track observed air temperature, although factors such as wind speed, humidity, insolation, and the thermal time constants of lakes influence variations within this broad pattern.

LSWT time series were derived from satellite observations from the series of Along Track Scanning Radiometers (ATSR) and the Advanced Very High Resolution Radiometers (AVHRR) on MetOp A and B platforms. The retrieval method of MacCallum and Merchant (2012) was applied on image pixels filled with water according to both the inland water dataset of Carrea et al. (2015) and a reflectance-based water detection scheme. The satellite-derived LSWT data are spatial averages for each of a total of 927 lakes, for which high-quality temperature records were available through August 2019. Lake-wide average surface temperatures have been shown to give a more representative picture of LSWT responses to climate change than single-point measurements (Woolway and Merchant 2018). In addition, in situ LSWT observations have been analyzed (n = 32) for which long time-series are available.

Eighty-one percent (n = 26) of lakes with in situ LSWT measurements were found to have positive anomalies in

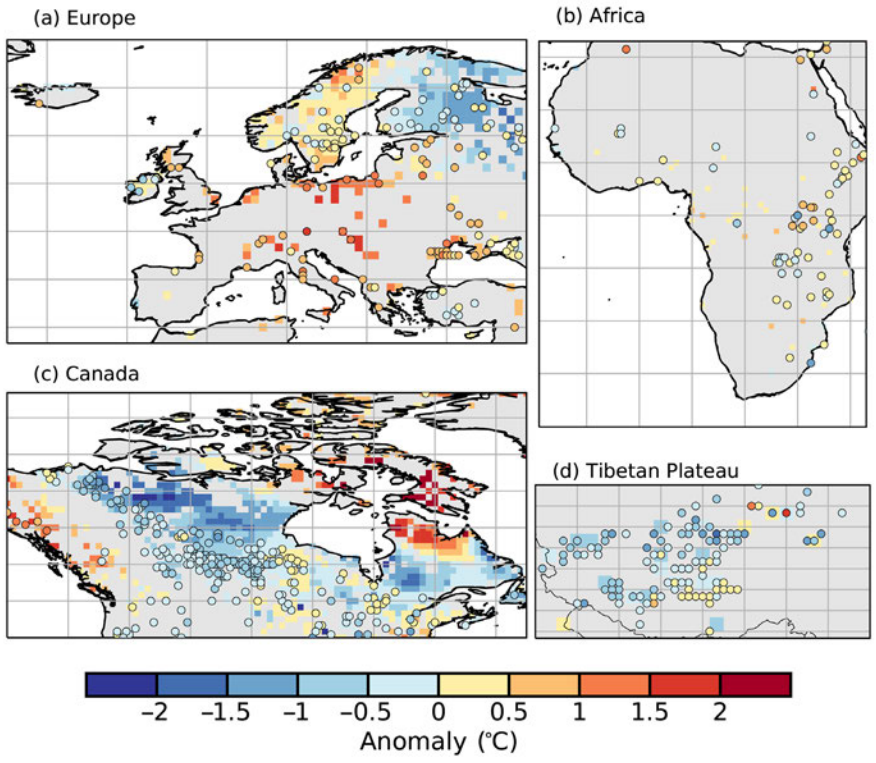

Fig. 2.3. Satellite-derived LSWT anomalies in 2019 (colored points) together with surface lake water temperature from the ECMWF ERA5 modeled data in Europe, Africa, Canada, and Tibet. The two sets of LSWT anomalies (°C; relative to 1996–2015) are calculated for the meteorological warm season (Jun–Aug in NH; Dec–Feb in SH; and over the whole year in the tropics).

2019. Similar to the satellite data, positive anomalies were found for Europe in 2019. For example, the second-largest lake in Sweden by surface area, Vättern, experienced an LSWT anomaly of +0.98°C in 2019, while that of Mondsee, Austria, was +2.1°C. The average LSWT anomaly in lakes with in situ data was +0.6 ± 0.15 °C in 2019, which is substantially higher than the global average anomaly calculated from the satellite-derived observations (+0.025°C). This difference can be due to various factors, including the restricted global coverage of lakes with in situ data (these lakes are primarily situated in Europe and North America), the difference in lake size among the datasets (more lakes with in situ data tend to be small) and, unlike the in situ observations, which are restricted to a single point within a lake, the satellite data capture the intra-lake heterogeneity of LSWT anomalies, thus capturing within-lake regions that are either warming rapidly or experiencing relatively minimal change (Woolway and Merchant 2018).

3) Land and marine temperature extremes—R. J. H. Dunn, S. Perkins-Kirkpatrick, R. W. Schlegel, and M. G. Donat

Over land, 2019 recorded the most number of warm days (TX90p, see Table 2.2 for definition) in the record dating to 1950, with over 60 days compared to the average of 36.5 (Fig. 2.4). The number of cool nights (TN10p) was low compared the last 70 years, but above average for the most recent decade. As the spatial coverage of the in situ GHCNDEX (Donat et al. 2013) dataset is not complete due to delayed or lacking report of up-to-date station data in many regions, the time series from the ERA5 reanalysis (Hersbach et al. 2020; Fig. 2.5; Fig. A2.5) is also shown. A similar picture emerges, but the number of warm days does not exceed the record maximum set in 2016. Similarly, the number of cool nights is also close behind the record minimum of 2016. Differences with GHCNDEX may be the result of the more complete coverage of ERA5.

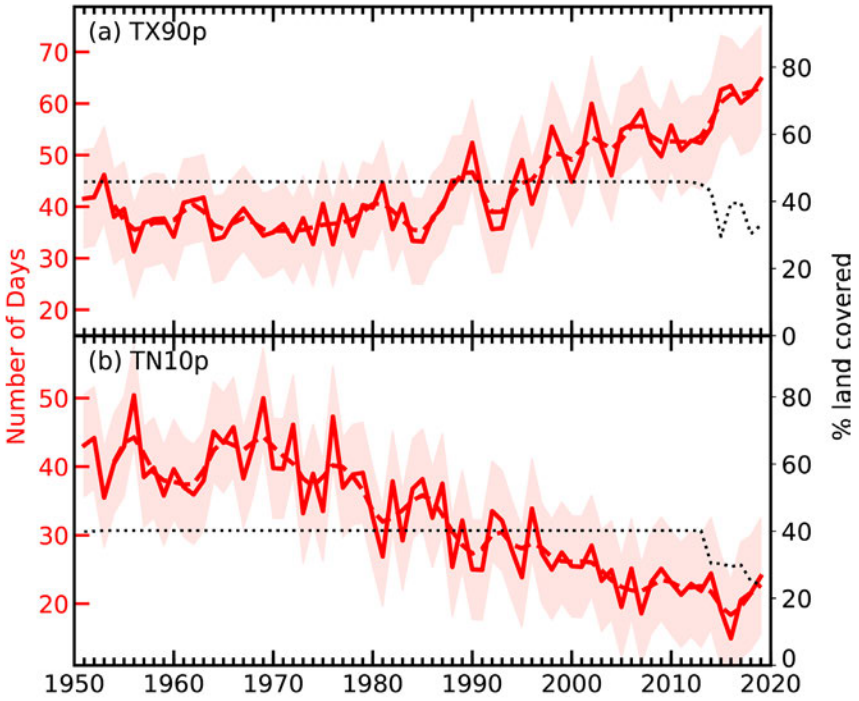

Fig. 2.4. Time series of (a) TX90p (warm days) and (b) TN10p (cool nights). The red dashed line shows a binomial smoothed variation, and the shaded band the uncertainties arising because of incomplete spatio-temporal coverage estimated using ERA5 following Brohan et al. (2006). The dotted black line shows the percentage of land grid boxes with valid data in each year. (Source: GHCNDEX.)

The number of warm days is high over Europe and Australia from GHCNDEX (Plate 2.1c),

Table 2.2. WMO Expert Team on Climate Change Detection and Indices (ETCCDI; Zhang et al. 2011) temperature indices used in this section and their definitions.

Index	Name	Definition
TX90p	Warm days	Count of days where the maximum temperature was above the climatological 90th percentile (defined over 1961–90, days)
TN10p	Cool nights	Count of days where the minimum temperature was below the climatological 10th percentile (defined over 1961–90, days)
TNx	Maximum "night-time" temperature	Warmest minimum temperature (TN, °C)

corresponding with the strong heat wave events in both these regions during 2019. In June large parts of Europe experienced daily maximum temperatures over 35°C, and France broke its national record with 46.0°C at Vérargues on the 28th. In July, France also sweltered under its record warmest night (TNx), with a national average of 21.4°C on 24–25 July, and a new maximum temperature record of 42.6°C was set for Paris on the 25th. Many other nations also experienced temperatures over 40°C during this period, with national station records broken in the United Kingdom (38.7°C), Germany (42.6°C), the Netherlands (40.7°C), Belgium (41.8°C), and Luxembourg (40.8°C). The World Meteorological Organization (WMO) declared the month of July 2019 tied as the hottest on record for the globe (WMO 2019), based on ERA5 (Hersbach et al. 2020).

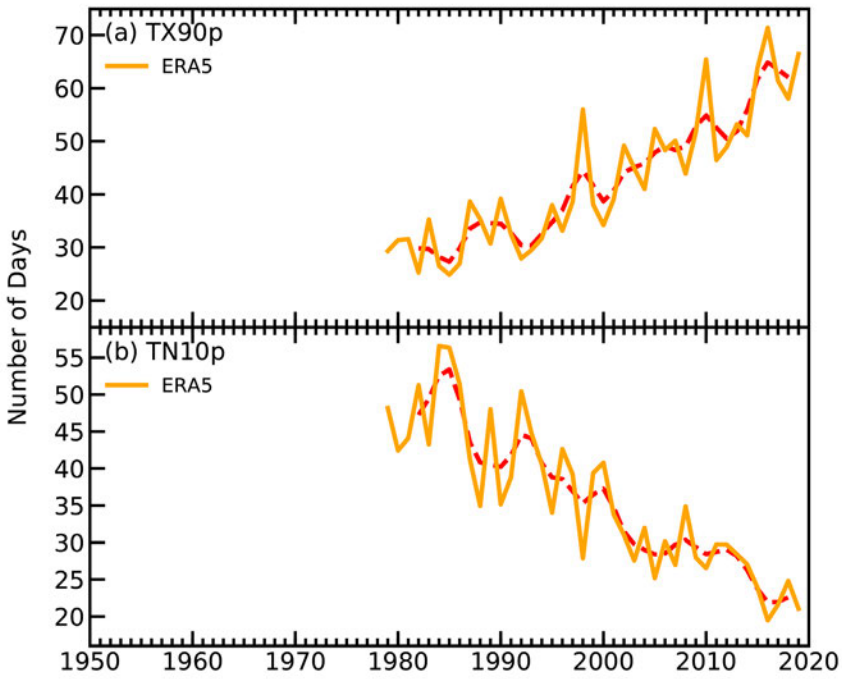

Fig. 2.5. Time series of (a) TX90p (warm days) and (b) TN10p (cool nights). The red dashed line shows a binomial smoothed variation. (Source: ERA5.)

Australia experienced heat waves both early and late in the year. A prolonged and extensive heat wave affected much of the country from late December 2018 through January 2019. Records set include Adelaide's hottest day on record at 46.6°C on 24 January (with new records also set at neighboring stations) and Canberra's longest run of days above 40°C on four consecutive days (14–17 January 2019). The all-time national average maximum temperature record was set on 17 December 2019 at 41.9°C, 1.59°C above the 2013 record, and 2.09°C above average (1961–90). January, March, and December 2019 were nationally the warmest on record for the respective months, with February, April, July, October, and November each among their respective 10 warmest. The most recent Australian heat wave in summer 2019/20 is presented in detail in Sidebar 7.6.

Heat waves also occurred in May and June in Japan, with a maximum temperature of 39.5°C (Saroma, Hokkaido) on 26 May (monthly record for this site), and also Pakistan (51.1°C Jacobabad on 1 June) and India with (50.8°C Churu, 2 June). In February, the United Kingdom experienced above-average temperatures with maxima of 21.2°C recorded in London on the 26th (monthly record), around 14°C above average. Extreme temperatures also occurred over South America in 2019. Overall, the continent observed its second-warmest year on record, with heat waves during January in Chile and southeastern Brazil contributing to the warmth. Santiago, Chile, set a new maximum temperature record of 38.3°C on 27 January. In North America, the state of Alaska experienced its warmest year on record. Please refer to the relevant sections in Chapter 7 for more regional temperature details.

GHCNDEX (Donat et al. 2013), a gridded dataset of ETCCDI (Expert Team on Climate Change Detection and Indices) extremes indices, was used to characterize the extreme temperatures over land. Indices are calculated from daily temperature values from the GHCND (Menne et al. 2012) and have been interpolated onto a 2.5° × 2.5° grid. As can be seen in Plates 2.1c,d, the spatial coverage is sparse, with available data for 2019 restricted to North America and parts of Eurasia and Australia. This lack of coverage arises both from gaps in the historical coverage (e.g., sub-Saharan

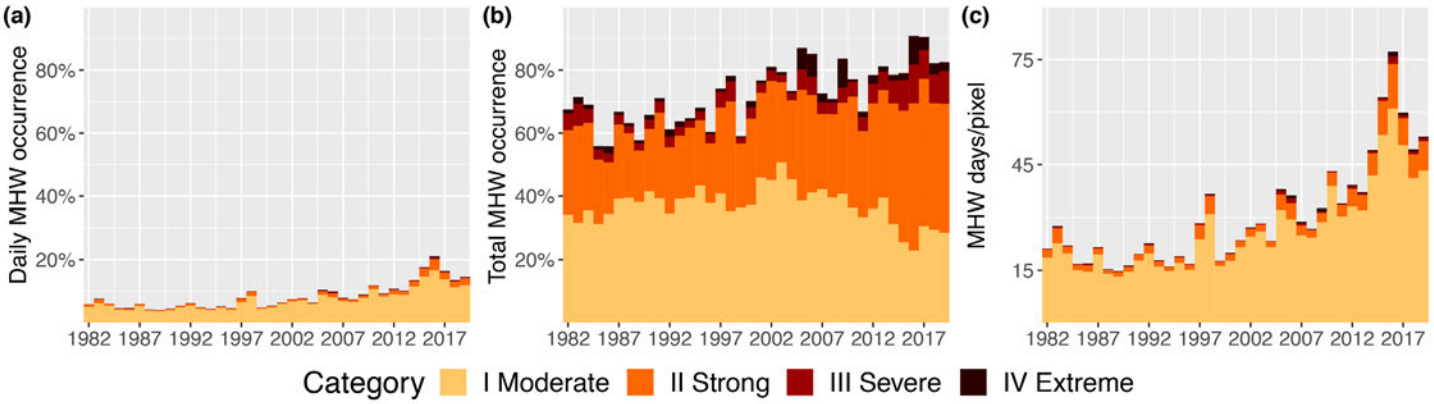

Fig. 2.6. Annual MHW occurrence using a climatology base period of 1982–2011. (a) Daily average percent of the ocean that experienced a MHW. (b) Total percent of the ocean that experienced a MHW at some point during the year. The values shown are for the highest category of MHW experienced. (c) Total average of daily MHW occurrence throughout the entire ocean. (Source: NOAA OISST.)

Africa) and also from delays in data transmission. ERA5 reanalysis (Hersbach et al. 2020) can be used to fill in some of these gaps, but because this dataset has a shorter temporal coverage, the reference period is necessarily different (1981–2010 compared to 1961–90 in GHCNDEX), which can lead to apparently different temporal behavior (Dunn et al. 2020).

Extreme heat, known as marine heat waves (MHWs), may enter the oceans through surface heat flux or advection. Satellite observations of SST can be used to monitor and categorize MHWs, as defined in Hobday et al. (2016, 2018). A category "I Moderate" MHW is defined as a period of time in which SST is above the 90th-percentile threshold of temperatures at a given location and day-of-year for five days or longer (Hobday et al. 2018). The MHW is categorized as "II Strong" if the largest temperature anomaly during the event is more than twice as large as the difference between the seasonally varying climatology and the 90th-percentile threshold. The MHW is "III Severe" if the largest anomaly is more than triple the difference, and "IV Extreme" if four times the difference or greater. Using NOAA OISST v2.1 (Banzon et al. 2020), the MHW category recorded most often in the ocean for 2019 was "II Strong" (41% of ocean surface), exceeding the lower category "I Moderate" (30%) for the sixth consecutive year (Fig. 2.6). Category "III Strong" MHWs (2%) were exceeded by "IV Extreme" MHWs (3%) for the fourth consecutive year. In total, 84% of the surface of the ocean experienced an MHW in 2019. There was an average of 74 MHW days per ocean pixel, an increase from 61 in 2018, but below the 2016 record of 83. The average daily MHW occurrence throughout the ocean was 20%, an increase over the 2018 average of 17%, and less than the 2016 record of 23%.

4) Tropospheric temperature—J.R. Christy, C. A. Mears, S. Po-Chedley, and L. Haimberger

The 2019 global lower tropospheric temperature (LTT), which encompasses the atmosphere from the surface to ~10 km, ranked second warmest in seven datasets and first or third in the remaining two (Fig. 2.7). These records extend back to 1958 using radiosonde (balloon-borne instrumentation) data and one reanalysis dataset (JRA55), which demonstrate reasonable agreement with the 40+ year satellite record (since late 1978) and two other reanalysis datasets (since 1979 and 1980, ERA5 and MERRA2, respectively). A weak El Niño contributed to increased global temperatures as 2019 values were +0.44° to +0.68°C higher than the 1981–2010 average (depending on the dataset), being just slightly cooler (~0.07°C on average) than the record warm year of 2016. At least four of the five globally complete datasets (ERA5, MERRA2, JRA55, RSS, UAH) recorded each of the four months—June, September, November, and December—as experiencing their warmest monthly global LTT.

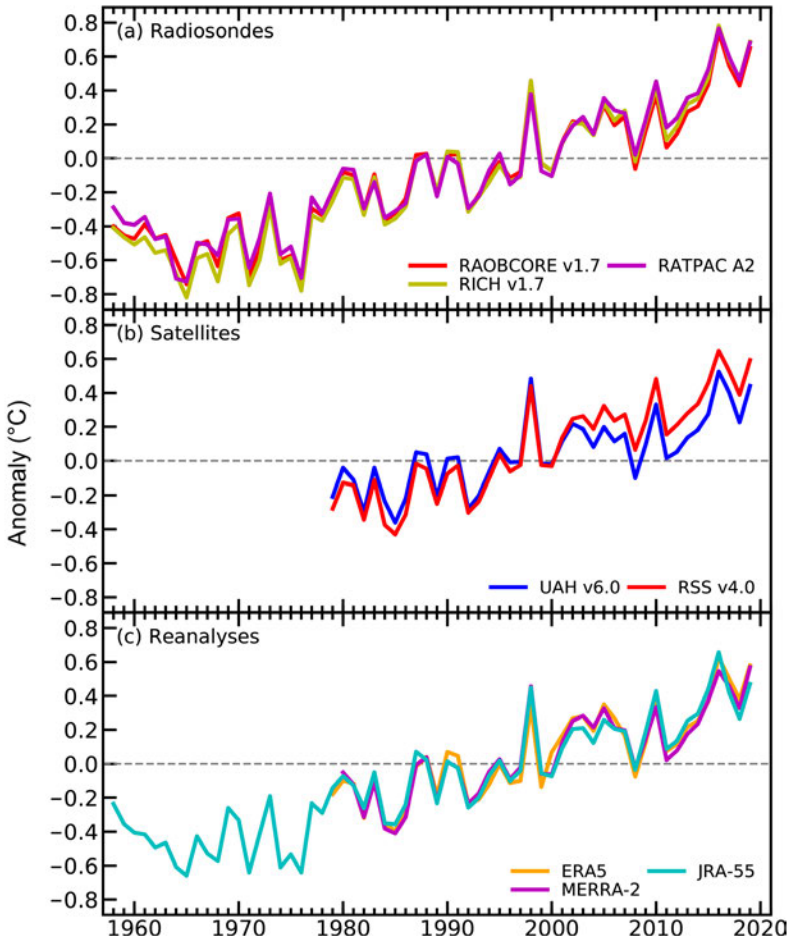

Fig. 2.7. Time series of global annual temperature anomalies (°C) for the lower troposphere from (a) radiosondes, (b) satellite microwave emissions, and (c) reanalyses.

Table 2.3. Estimates of lower tropospheric temperature (LTT) and tropical tropospheric temperature (TTT) decadal trends (°C decade^{-1}) beginning in 1958 and 1979 from the available datasets.

Area		Global	Global	Tropical	Tropical
Layer		LTT	LTT	TTT	TTT
Start Year		1958	1979	1958	1979
Radiosonde	NOAA/RATPACvA2	+0.18	+0.21	+0.16	+0.16
	RAOBCOREv1.7	+0.18	+0.19	+0.15	+0.15
	RICHv1.7	+0.20	+0.21	+0.19	+0.22
Satellite	RSSv4.0	—	+0.21	—	+0.18
	UAHv6.0	—	+0.13[1]	—	+0.13
	NOAA/STARv4.1	—	—	—	+0.23
	UWv1.0	—	—	—	+0.17
Reanalyses	ERA5	—	+0.17	—	+0.16
	JRA-55	+0.16	+0.16	+0.16	+0.15
	NASA/MERRA-2[2]	—	+0.17	—	+0.16
Median		**+0.18**	**+0.18**	**+0.16**	**+0.16**

[1]The UAH LTT weighting function is slightly different in order to reduce the impact of surface emissions and enhance the tropospheric signal, resulting in a global trend value typically cooler by 0.01°C decade^{-1} relative to the standard LTT weighting function.

[2]NASA/MERRA-2 begins in 1980.

The warming rate of the global troposphere since 1958, as the median of available datasets, is +0.18 (range +0.16 to +0.20) °C decade^{-1}. The median warming rate since 1979 is also +0.18 (range +0.13 to +0.21) °C decade^{-1}, which includes records derived from microwave satellite measurements (Table 2.3). Taking into consideration the temporary cooling due to volcanic aerosols caused by eruptions in 1982 and 1991, as well as the El Niño/La Niña cycle, there remains a global warming trend since 1979 of +0.12 ± 0.04°C decade^{-1} unexplained by these ephemeral, natural phenomena (Christy and McNider 2017, updated and calculated using ERA5, RSS, and UAH datasets).

The spatial details of the departures of LTT from the 1981–2010 mean are depicted in Plate 2.1e as provided by the European Centre for Medium-Range Forecasts Reanalysis version 5 (ERA5). Above-average anomalies dominate the 2019 ERA5 map with negative regions occupying only 8.1% of the global surface area, including much of North America, a portion of South Asia, and midlatitude regions of the southern oceans. These below-average LTTs comprise the third-smallest such area after 2016 and 2017.

Much higher-than-average temperatures included several regions that experienced record high temperatures relative to this 41-year period of observations. Alaska, Greenland, central Europe, and southern Africa were especially warm. The broad warmth of the tropical belt is a typical signature of an El Niño year.

The warming trend may be depicted in a geographical context by determining

the year in which the extreme high (and low) annual values at each grid point occurred, then summing those areally-weighted grids by year. If all regions of Earth experienced a monotonically increasing temperature, then each new year would see 100% of the global area achieving a record high temperature; however, if the global trend were zero over the 41-year period of record but characterized by random inter-annual variability, each year would experience, on average, an area of 2.4% of record high (or low) temperatures. With our climate system characterized by both an increasing trend and inter-annual variations since 1979, the area in 2019 of record high temperatures was 15.6% (calculated as the average of ERA5, RSS, and UAH). The stippling in Plate 2.1e identifies these grids (see also Fig. A2.6). Two years with major El Niño events, 1998 and 2016, recorded areal extents for the highest temperatures of 16.9% and 20.1%, respectively (no repeated records). Since 1979, the year with the largest coverage of record low annual-average temperatures was 1985 with 19.8% due in part to a concurrent La Niña event.

Global and tropical trends are listed in Table 2.3. When examining the time series of these three methods (radiosondes, satellites, reanalyses), the radiosondes display an increasing trend over the past 10 years relative to the other methods (see trend values in column Global LTT 1979 and Fig. A2.7) This may be related to a change in software installed after 2009 in many stations to improve the tropospheric humidity and temperature values (Christy et al. 2018).

The tropical (20°N–20°S) tropospheric temperature (TTT, surface to ~15 km) variations and trends are similar to those of the global values. The median TTT trends from the available datasets since 1958 and 1979 are both +0.16°C decade^{-1} with ranges of +0.15 to +0.19 and +0.13 to +0.23°C decade^{-1}, respectively (Table A2.1). This layer in the tropics is a key area of interest due to its expected significant response to forcing, including that of increasing greenhouse gas concentrations (McKitrick and Christy 2018; see Fig. A2.8).

Radiosondes provide coverage wherever the stations exist. Considerable areas of the globe are thus not sampled, and this can lead to a misrepresentation of the global average. Satellites essentially observe the entire Earth each day, providing excellent geographic coverage, but whose radiances provide bulk-layer atmospheric measurements only. There are some key adjustments that are required too, and the methods adopted by different teams lead to the range in the results (Haimberger et al. 2012; Po-Chedley et al. 2015; Mears and Wentz 2016; see also Figs. A2.7 and A2.9). Full input reanalyses use essentially all available data, including radiosonde and satellite, ingested into a continuously updated global circulation model, thus providing full geographic and vertical coverage. Given the many differences in how the reanalyses are constructed from center to center, the consistency among their 41-year trends is encouraging.

5) Stratospheric temperature—W. J. Randel, C. Covey, and L. Polvani

Temperatures in the middle and upper stratosphere continued to decline to their lowest recorded values since 1979, i.e., the beginning of the satellite era. Lower stratosphere temperatures have been relatively constant since ~1998, with small interannual changes. The polar stratospheric regions were influenced by sudden stratospheric warming (SSW; Charlton and Polvani 2007) events in both hemispheres, in the Arctic in January 2019 and in the Antarctic in September 2019. The Antarctic event was highly unusual, being only the second SSW observed in the SH since 1979 (see Sidebar 6.1 for more details).

Time series of annual anomalies of middle and upper stratosphere temperatures from satellite observations are shown in Figs. 2.8a–c. These data represent ~20-km thick layer measurements from the Stratospheric Sounding Unit (SSU) merged with more recent satellite measurements (Randel et al. 2016; Zou and Qian 2016). Middle and upper stratospheric temperatures show distinctive cooling since 1979, with stronger negative trends at higher altitudes, which is a characteristic response to increases in atmospheric CO_2 (Manabe and Wetherald 1967). The cooling is modulated by upper stratospheric ozone changes, with somewhat weaker stratospheric cooling after 1998 tied to observed increases in ozone. The ozone is evolving as a response to changes

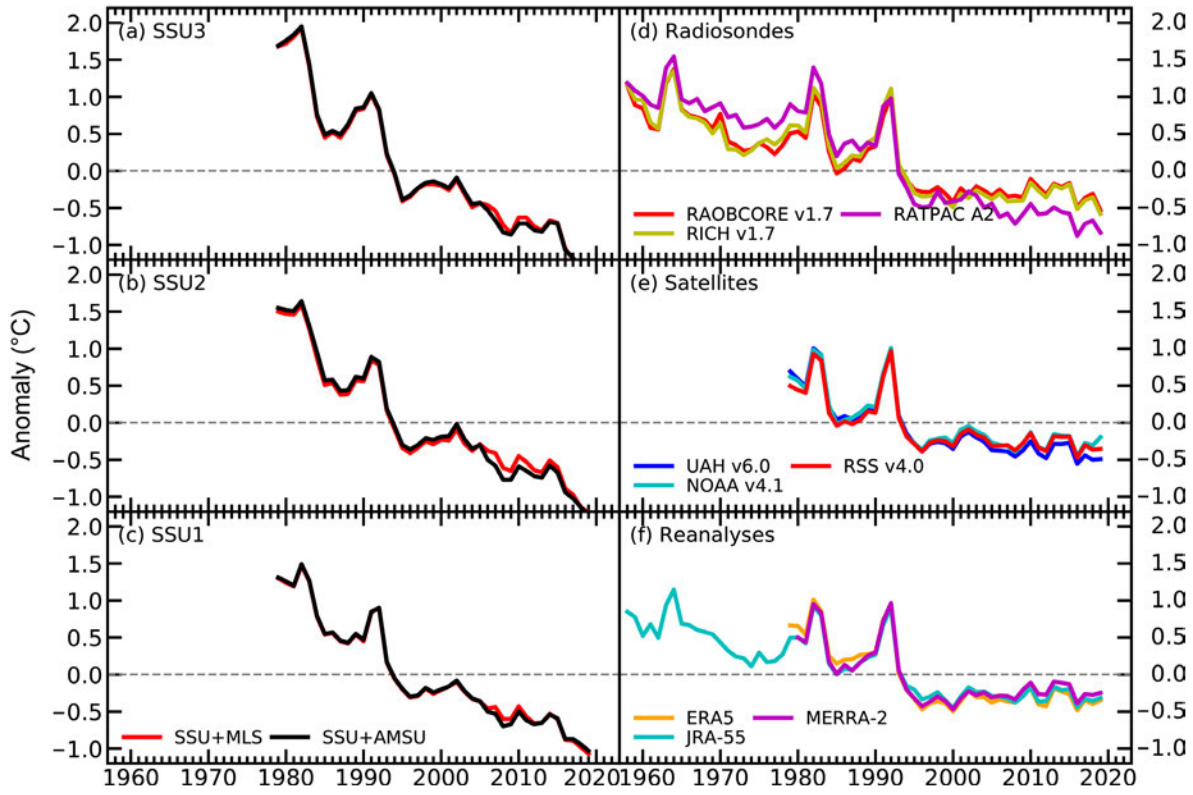

Fig. 2.8. (a)–(c) Annual anomalies of global middle to upper stratospheric temperatures from Stratospheric Sounding Unit channels 1–3, representing thick-layer averages centered near 30, 38, and 45 km (SSU1, SSU2, and SSU3, respectively). Results from two different merged datasets are shown (Randel et al. 2016; Zou and Qian 2016). (d)–(f) Annual anomalies of global lower stratosphere temperature (LST; ~13–22-km layer average) from (a),(d) radiosondes; (b),(e) satellites; and (c),(f) reanalyses. For direct comparison, the radiosondes and reanalyses have been convolved with the satellite LST weighting function.

in ozone depleting substances (ODS) linked to the Montreal Protocol (see section 2g4; Maycock et al. 2018; WMO 2018). In addition to long-term cooling, the time series highlight modulation by the 11-year solar cycle in the upper stratosphere and transient warming from volcanic eruptions in 1982 and 1991.

Time series of global lower stratospheric temperature (LST; layer mean over ~13–22 km) from satellites, radiosondes, and reanalyses in Figs. 2.8d–f all show long-term cooling trends, in addition to transient warming events tied to large volcanic eruptions in 1963, 1982, and 1991. The time series also show very small changes since 1998. Over most of the globe the LST layer more or less spans the cross-over between tropospheric warming and stratospheric cooling associated with CO_2 increases; long-term LST cooling prior to ~1998 is tied to observed ozone decreases in the lower stratosphere, while small ozone changes thereafter are linked to nearly constant temperatures (Maycock et al. 2018).

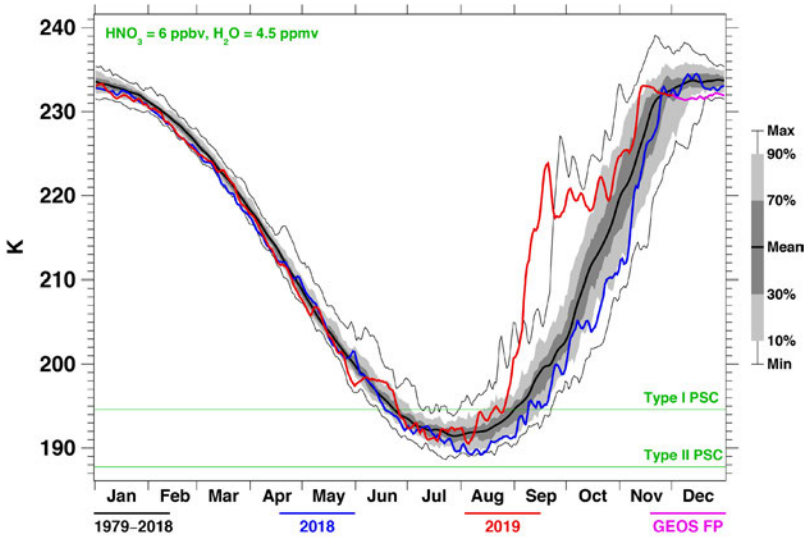

Fig. 2.9. Daily time series of 50-hPa temperatures for 60°–90°S for 2018 (blue) and 2019 (red), against the background of percentile variability (gray lines and shades) since 1980.

Transient but common features of stratospheric temperature variability are polar SSWs that occur episodically during winter, mainly in the NH. At least one SSW occurred in 34 of the past 62 winters in the NH, while only one was observed in the SH (in 2002) prior to 2019. Time series of 50-hPa temperature over the Antarctic during the last several years are shown in Fig. 2.9, in the context of the historical average and range of observations. The September 2019 SSW resulted in a 50-hPa temperature increase over the polar cap of ~30°C over two weeks, with temperatures well outside the range of previous variability. While these SSW events have strong effects on polar temperatures, they have minimal influence on global mean stratospheric temperatures. However, Australian hot and dry extremes are statistically associated with weakening and warming of the Antarctic stratospheric polar vortex (Lim et al. 2019). The September 2019 SSW is one of many possible factors contributing to this year's eastern Australian bushfires (see section 7h4 for more details; Phillips and Bogrady 2020).

c. Cryosphere

1) Permafrost thermal state—J. Noetzli, H. H. Christiansen, K. Isaksen, S. Smith, L. Zhao, and D. A. Streletskiy

The global picture of permafrost state and changes continued in 2019: permafrost is warming in both mountain and polar regions, and the highest increase is observed where permafrost temperatures and ice contents are lowest. At warmer and ice-rich locations the temperature change is smaller due to the energy uptake during ice melt processes. The thickness of the active layer (ALT)—the uppermost ground layer above the permafrost subject to positive temperatures during summer—is globally increasing.

In the Arctic regions, permafrost temperatures measured at 20-m depth at many of the monitoring sites during 2019 were the highest observed during the observation period, continuing the trend reported by Meredith et al. (2019). Observations now cover up to four decades at several sites. At some locations, temperatures were 2°–3°C higher than 30 years ago. More details on the Arctic region are given in Chapter 5. For Antarctica, increasing permafrost temperatures were reported for the past decade (cf. Noetzli et al. 2019). However, for 2019 no data update is available yet.

Mountain permafrost accounts for nearly 30% of the global permafrost area (Hock et al. 2019), but datasets for many mountain regions are obtained at only a limited number of sites. Data are primarily available from boreholes and networks in the European Alps, the Nordic countries, and central Asia (Qinghai-Tibetan Plateau, QTP). A general warming trend during recent decades until 2016 is also reported for mountain ranges in Canada, Mongolia, and Tien Shan in central Asia (Hock et al. 2019). Due to the high spatial variability in characteristics and permafrost temperatures, warming rates are highly heterogeneous, depending on topography, snow regime, and ground ice content.

Permafrost temperatures observed in the European Alps in 2019 were influenced by an early and long-lasting snow cover—trapping the heat from summer 2018—followed by another extremely warm summer in 2019. Permafrost temperatures continued the increasing trend since 2010 after a temporary interruption of the warming trend due to snow-poor winters reported in 2017 (Fig. 2.10; Noetzli et al. 2018; PERMOS 2019). At most sites, the temperatures at 10-m depth in 2019 were slightly below the record temperatures measured in 2015 (updated from PERMOS 2019). Likewise, permafrost temperatures at 20-m depth increased since 2018, but not above the previous high from 2015. Repeated electrical resistivity tomography at several borehole sites indicate a decrease in ice content, particularly for sites close to 0°C (Mollaret et al. 2019; PERMOS 2019). Permafrost temperatures measured at steep bedrock sites at high elevation are typically not influenced by annual snow conditions and have continuously increased, with 2019 values higher than those previously recorded down to 10-m depth (updated from PERMOS 2019; Magnin et al. 2015). Further, rock glacier creep velocities generally follow permafrost temperatures and have increased considerably in the past decade (PERMOS 2019).

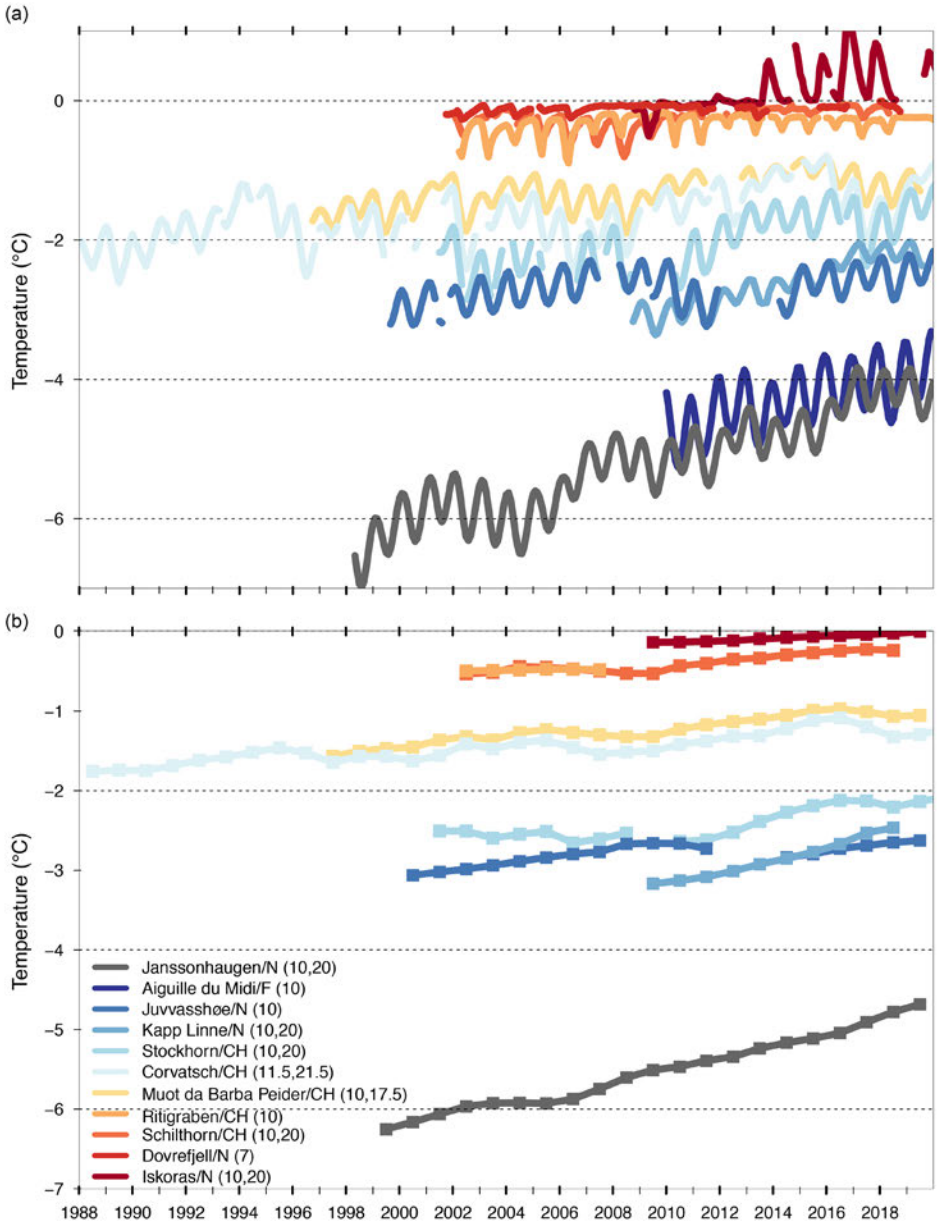

Fig. 2.10. Permafrost temperature (°C) measured in boreholes in the European Alps and the Nordic countries at a depth of approximately 10 m (monthly means) and 20 m (annual means). (Sources: Swiss Permafrost Monitoring Network PERMOS; Norwegian Meteorological Institute and the Norwegian Permafrost Database NORPERM, updated from Magnin et al. 2015.)

In Nordic countries, permafrost temperatures increased to their highest levels in both cold and warm permafrost (updated from Isaksen et al. 2007; Christiansen et al. 2010). In southern Norway, permafrost at 20-m depth warmed between 2015 and 2019 (for Juvvasshøe + 0.04°C yr^{-1}), following a period of cooling between 2010 and 2014 (Fig. 2.10). In northern Norway (Iškoras since 2008), latent heat exchanges appeared to dominate the annual temperature amplitude at 10-m depth in the beginning of the series. Since 2013/14, an increase in annual temperature amplitude has been observed with present temperatures well above 0°C (Fig. 2.10). At 20-m depth, ground temperatures have risen to 0°C. Borehole temperatures measured in the hinterland of the QTP showed remarkable warming tendencies with variable rates that are highest in lower-temperature permafrost (Cheng et al. 2019; Sun et al. 2019).

The ALT continued to increase in 2019 for the majority of the observational sites. Out of 92 sites that reported data in 2018/19 in the Northern Hemisphere (NH), only a few had below-average ALT relative to the 2003–12 period. About 66% of the sites had larger 2019 ALT than in 2018. At North American sites, ALT continues to increase since the beginning of the observations in the mid-1990s, with the highest increase in the Alaskan Interior and smaller increases in the Mackenzie Valley of northwestern Canada and the Alaska North Slope. In 2019, ALT was close to maximum values at the group of sites located in the Pacific Arctic sector (Alaska, Chukotka). At many interior Alaska sites, the active layer did not freeze completely down to the underlying permafrost due to a combination of long-term warming and the relatively mild and snowy past two winters (2017/18 and 2018/19). During all previous years of observations, complete active layer freeze-up was observed. North Atlantic Arctic sites had the largest or close-to-largest ALT in 2019; sites in Svalbard and Greenland show at least 0.05 m larger ALT than average. The Russian Arctic, with the exception of northeast Siberia, experienced a

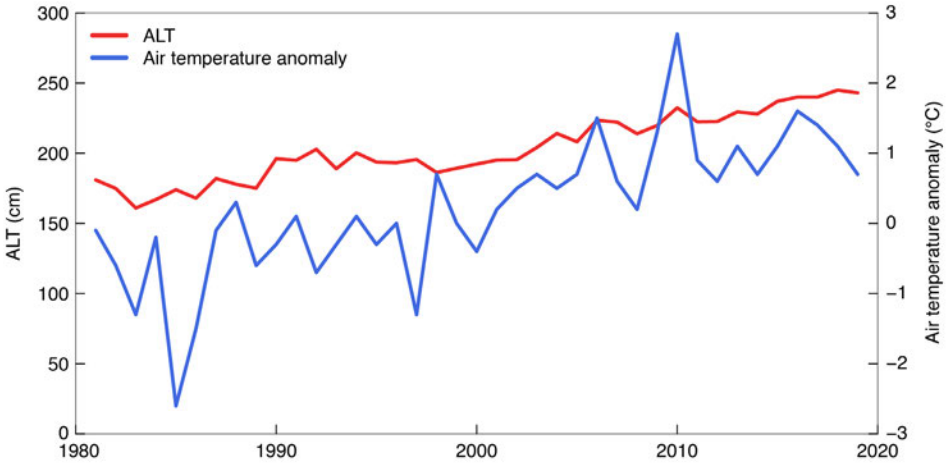

Fig. 2.11. Annual ALT (cm) and air temperature anomaly (°C) across the Qinghai Tibet Highway.

larger-than-average ALT, with deviations from the mean of 0.05 m in northern European Russia to 0.02 m in West Siberia (see section 5h for more details). In Scandinavia and the European Alps, values up to about 0.05 m above or near-record maximum values were observed at many of the sites. ALT also continued to increase at sites located in permafrost regions of the hinterland of the QTP by about 0.2 m decade^{-1} since the 1980s (Fig. 2.11; Cheng et al. 2019; Zhao et al. 2019). In 2019, ALT was, on average, slightly smaller in the QTP than in 2018 (0.02 m).

Long-term observation of permafrost change relies on ground temperatures measured in boreholes, which are collected in the framework of the Global Terrestrial Network for Permafrost (GTN-P) as part of the Global Climate Observing System of the World Meteorological Organization. Borehole temperatures are logged manually or continuously using multi-sensor cables down to at least the depth of the zero annual amplitude (ZAA), the depth where seasonal variations become negligible. An assessment of the measurement accuracy of borehole temperatures in permafrost worldwide varied from 0.01° to 0.25°C and a mean overall accuracy of about 0.1°C can be assumed (Biskaborn et al. 2019; Romanovsky et al. 2010). The current global coverage of permafrost temperature monitoring in boreholes is sparse and very limited in regions such as Siberia, central Canada, Antarctica, and the Himalayan and Andes Mountains. The distribution of observation sites is typically biased to accessible locations (highways or cable cars).

2) Northern Hemisphere snow cover extent—D.A. Robinson

Annual snow cover extent (SCE) over NH lands averaged 24.8 million km^2 in 2019. This is 0.8 million km^2 smaller than the 2018 mean extent and 0.3 million km^2 smaller than the 50-year average (mapping extends back to late 1966; however, several early years in the record are incomplete) and ranks 2019 as having the 17th-least extensive cover on record (Table 2.4). SCE over Eurasia and North America, including the Greenland ice sheet (GrIS), is considered in this analysis. Monthly SCE in 2019 ranged from 47.2 million km^2 in January to 2.5 million km^2 in August.

January 2019 NH SCE was near average, ranking as the 27th-most extensive over the past 53 years. Both Eurasia and North America ranked similarly. The NH as a whole had near-average SCE in February; however, North America and Eurasia ranked fourth and 42nd largest, respectively. The continental disparity continued into March with the combined rank falling into the lowest third. This decline became greater through the spring and early summer, with both continents ranking in the lower tercile throughout this interval. June had the largest negative monthly NH anomaly of the year (3.6 million km^2 or 38% below normal). NH SCE has been below average for 14 of the past 15 years in May and all of the past 15 years in June (Fig. 2.12).

Autumn SCE emerged at an average pace in September but increased rapidly in October, having the largest positive monthly anomaly of 2019 at 3.8 million km^2. October and November SCE each ranked fifth largest of the satellite era for their respective months. NH SCE has now been above average in 10 of the past 11 years in October and all of the past 11 years in November. December SCE was also above average over North America, but Eurasian cover increased slowly during

Table 2.4. Monthly and annual NH and continental snow extent (million km²) between Nov 1966 and Dec 2019. Included are the numbers of years with data used in the calculations, means, standard deviations, 2019 values, and rankings. The years 1968, 1969, and 1971 have 1, 5, and 3 missing months respectively, thus are not included in the annual (Ann) calculations. Ranks are from most extensive (1) to least (ranges from 50 to 54 depending on the month).

	Years of data	Mean SCE	Std. dev.	2019	2019 NH rank	2019 Eurasia rank	2019 N Am. rank
Jan	53	47.2	1.5	47.2	26	25	27
Feb	53	46.0	1.8	46.0	23	42	4
Mar	53	40.5	1.8	39.5	37	47	9
Apr	53	30.5	1.7	29.1	42	41	35
May	53	19.2	1.9	17.1	44	46	46
Jun	52	9.5	2.4	5.9	49	46	50
Jul	50	3.9	1.2	2.6	44	38	47
Aug	51	3.0	0.7	2.5	41	40	34
Sep	51	5.4	0.9	5.1	32	27	36
Oct	52	18.5	2.7	22.3	5	7	3
Nov	54	34.2	2.1	37.1	5	14	3
Dec	54	43.7	1.8	43.5	36	42	18
Ann	**50**	**25.1**	**0.8**	**24.8**	**34**	**40**	**20**

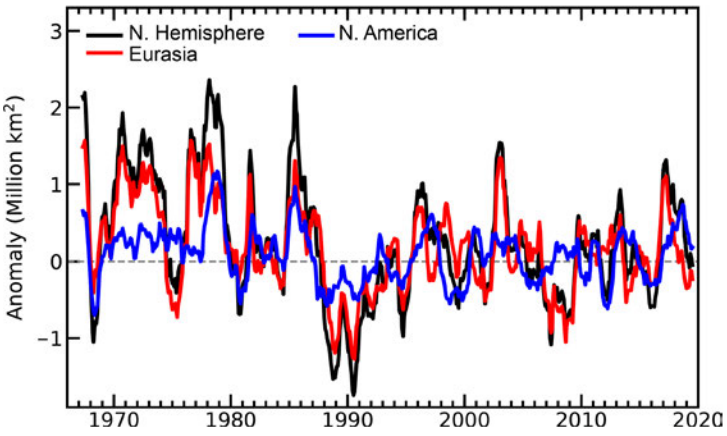

Fig. 2.12. Twelve-month running anomalies of monthly snow cover extent (million km²) over NH lands as a whole and Eurasia and North America separately plotted on the seventh month using values from Nov 1966 to Dec 2019. Anomalies are calculated from NOAA snow maps. Mean hemispheric snow extent is 25.1 million km² for the full period of record. Monthly means for the period of record are used for nine missing months between 1968 and 1971 in order to create a continuous series of running means. Missing months fall between Jun and Oct; no winter months are missing.

the month, resulting in the 13th-smallest December extent (Table 2.4).

The 2019 SCE over the contiguous United States was near average in January. February and March had their fourth- and sixth-most extensive SCE, respectively. April SCE returned to near average, while May SCE was quite low. While not much in terms of coverage, September SCE was record large for the month, followed by the third-largest October extent, and 11th-largest November extent, which was similar to Canada. SCE was near-average in December.

SCE is calculated at the Rutgers Global Snow Lab from daily SCE maps produced by meteorologists at the National Ice Center (a U.S. joint NOAA, Navy, and Coast Guard facility), who rely primarily on visible satellite imagery to construct the maps (https://snowcover.org).

3) Glaciers—M. S.Pelto and World Glacier Monitoring Service

The World Glacier Monitoring Service (WGMS) record of mass balance and terminus behavior (WGMS 2017) provides a global index for alpine glacier behavior. Glacier mass balance is the difference between accumulation and ablation, reported here in millimeter of water equivalence (mm). In 2019, a negative annual mass balance was reported from all 45 glaciers where annual mass balance was measured and reported to the WGMS, including 26 glaciers of the reference glacier network. The mean mass balance of the reference glaciers reporting for the 2018/19 hydrological year is –1241 mm; this includes data from 12 nations on four continents. This makes 2019 the 32nd consecutive year with a global alpine reference glacier mass balance loss and the 10th consecutive year with a mean global mass balance loss greater than 700 mm.

Figure 2.13 illustrates glacier mass balance for a set of global reference glaciers with more than 30 continuous observation years for the time period 1950–2019. Global values are calculated using

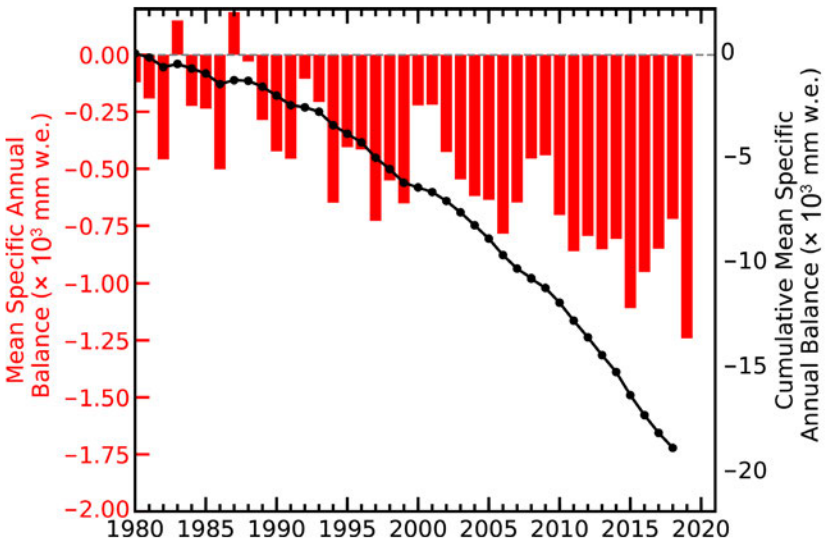

Fig. 2.13. Global alpine glacier annual mean mass balance record (× 10^3 mm w.e.) of reference glaciers submitted to the WGMS 1980–2018, based on average annual value determined for 19 different alpine regions. The 2019 value is the mean of all reporting reference glaciers.

a single value (averaged) for each of 19 mountain regions in order to avoid a bias to well-observed regions. In the hydrological year 2016/17, all observed glaciers experienced an ice loss of –550 mm, and 2017/18 of –720 mm. For the 2018/19 hydrological year, a regionally averaged value will become available in late 2020; however, the overall mean of all reference glaciers was –1241 mm, compared to –1183 mm in 2017/18. Zemp et al. (2019) calculated that the collective loss of alpine glaciers from 2006 to 2016 contributed to a global sea level rise of 0.92 ± 0.39 mm yr^{-1}.

The decadal-averaged annual mass balance for the reference glaciers was –172 mm in the 1980s, –460 mm in the 1990s, –500 mm for the 2000s, and –889 mm for the 2010s. The increasing rate of glacier mass loss, with 8 out of the 10 most negative mass balance years recorded after 2010, during a period of retreat, indicates that alpine glaciers are not approaching equilibrium and retreat will continue to be the dominant terminus response (WGMS 2017). The lack of retained snow cover on two WGMS reference glaciers is a visual illustration of the mass balance loss (Fig. 2.14).

All 14 glaciers in the Alps with mass balance observations had negative measurements, averaging –1100 mm in 2019. In Austria in 2018, of the 93 glaciers with annual terminus observations, 89 (95.7%) withdrew and four remained stationary (Lieb and Kellerer-Pirklbauer 2019). This retreat trend has continued in 2019 based on preliminary observations. The 2018/19 winter in the Alps featured above-average snowpack. During several heat waves in the summer of 2019, glacier melt peaked, leading to another year with large losses in ice mass balance loss.

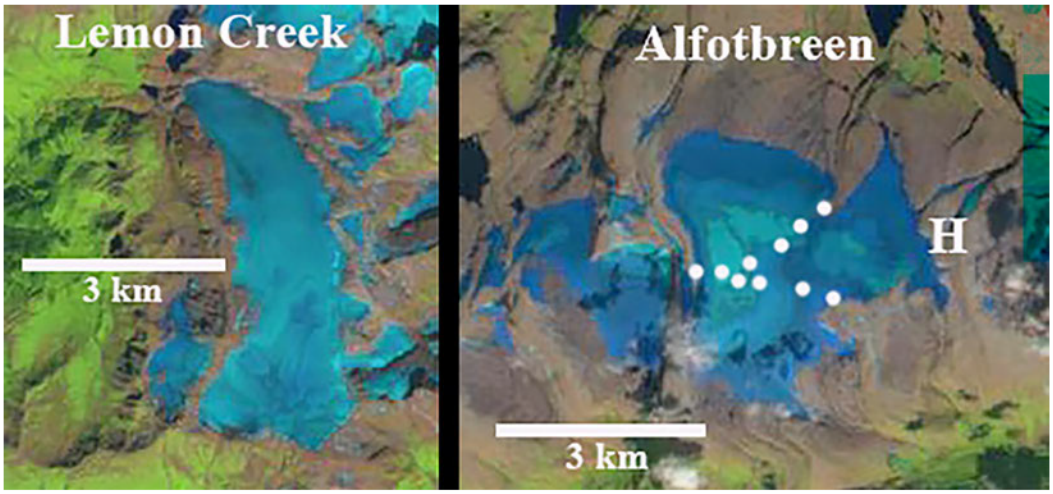

Fig. 2.14. Lemon Creek Glacier, United States, and Alfotbreen, Norway, had significant negative annual mass balance in 2019 at –2400 mm and –3400 mm. Alfotbreen's boundary is marked by white dots. On Alfotbreen, less than 20% of the glacier has retained snow cover in this 26 Aug Landsat image. On Lemon Creek Glacier, there is no significant snow accumulation retained in this 8 Aug Landsat image. The darkest blue color is bare glacier ice, with firn that is more than year old a medium blue and snow from the 2019 winter a light blue.

In Norway, the seven glaciers reporting mass balance had an average loss of –1354 mm in 2019. This loss leads to continued retreat; in 2018, of 32 glaciers measured, 28 retreated more than 10 m, and four were approximately stationary, retreating, or advancing less than 6 m (Kjøllmoen et al. 2019).

In Alaska and Washington, all 15 glaciers observed in 2019 had a negative mass balance, averaging –1372 mm. This is significantly larger than the long-term average of four USGS benchmark glaciers, which have a cumulative mass loss since the mid-twentieth century that average from –580 to –300 mm yr^{-1} (O'Neel et al. 2019). During the 74-year annual mass balance record for Taku Glacier, Alaska, the end of summer snowline, which is the equilibrium line altitude, had never exceeded 1225 m until 2018, when it reached 1425 m, and then reached a new maximum of 1450 m in 2019 (Pelto 2019).

In South America, 2019 mass balance data were reported from one glacier in Chile and three in Argentina, and indicate a mean of –1559 mm. This is greater than the 2000–18 average loss observed in the Andes of –720 ± 220 mm, with the Patagonia Andes having the highest rate of loss at –780 ± 250 mm (Dussaillant et al. 2019).

In High Mountain Asia, all five reporting glaciers had negative mass balances. King et al. (2019) found no substantial difference in the mass loss of debris-covered and clean-ice glaciers but more negative mass balances for lake-terminating glaciers for the 1974–2015 period. The continued expansion of established proglacial lakes and the formation of new proglacial lakes will enhance ice mass loss from the region in coming decades (King et al. 2019).

Sidebar 2.1: **Lake Ice**—S. SHARMA AND R.I. WOOLWAY

Lake ice is a sensitive indicator of climate as it integrates antecedent air temperatures in the range of weeks to months prior to ice breakup and closely tracks the 0°C isotherm (Brown and Duguay 2010). Lake ice has long fascinated people because of its importance to transportation, refrigeration, and recreation, thus comprising some of the earliest records of climate before the advent of meteorological stations (Magnuson et al. 2000; Sharma et al. 2016). Records of lake ice phenology (defined as the timing of ice-on and ice-off) benefit from in situ records with high temporal resolution, satellite records, and reanalyses (i.e., ERA5) with high spatial resolution. This section covers the 2018/19 Northern Hemisphere (NH) winter, with ice-on data from autumn 2018 and ice-off from spring 2019. The winter season spans two years and is defined as the time lakes experience seasonal ice cover, typically between November and April. For example, the 1981 winter would typically begin in November 1980 and end in April 1981.

In 2019, lake ice phenology anomalies across the NH, derived from ice cover data from ERA5 reanalysis (Hersbach et al. 2020), showed that on average, ice-on was one day later and ice-off was two days earlier than the 1981–2010 base period over the winter season (Figs. SB2.1 and SB2.2). Lake ice froze later, melted earlier, and had shorter seasonal ice duration over western North America, northern Europe, and northern Asia. In contrast, lake ice-on was earlier, ice-off was later, and ice duration was longer across Canada (except the west), the northern United States, and southern Eurasia (Fig. SB2.1).

Ice-on was four days later and ice-off was three days earlier on average for lakes distributed across the NH in 2019 based on long-term in situ phenological records (Fig. SB2.2). For monitored lakes in Europe, ice duration was 18 days shorter than the 1981–2010 base period. In contrast, for North American lakes, ice duration was nine days longer. Generally, across the NH, lake ice cover followed the long-term warming trend such that since 1981, lake ice duration is seven days shorter per decade on average for the 18 lakes with in situ measurements. Lake ice-on is five days later $decade^{-1}$, with the most negative trend at 0.2 days earlier $decade^{-1}$ (95% confidence interval: –3.6, 3.3 days $decade^{-1}$) and the most positive trend at 11 days later $decade^{-1}$ (95% confidence interval: 5, 17 days $decade^{-1}$). Lake ice-off is on average two days earlier $decade^{-1}$, but varies from 4.1 days earlier $decade^{-1}$ (95% confidence interval: –5.9, –2.3 days $decade^{-1}$) to 1.2 days later $decade^{-1}$ (95% confidence interval: –2.1, 4.5 days $decade^{-1}$).

This year, the Great Lakes of North America had greater maximum ice cover, suggesting a cooler winter. On average, the Great Lakes had 30.1% additional ice coverage than the 1981–2010 normal. The larger and most northern of the Great Lakes had the highest positive anomaly, such that Lake Superior (82 103 km^2) had 34.2% more ice cover, whereas the smaller southern lakes, such as Lakes Erie (25 744 km^2) and Ontario (18 960 km^2), had 13% additional maximum ice coverage (Fig. SB2.3). During the 2019 winter, Lakes Superior, Huron, and Erie had ice coverage across more than 90% of their respective surfaces.

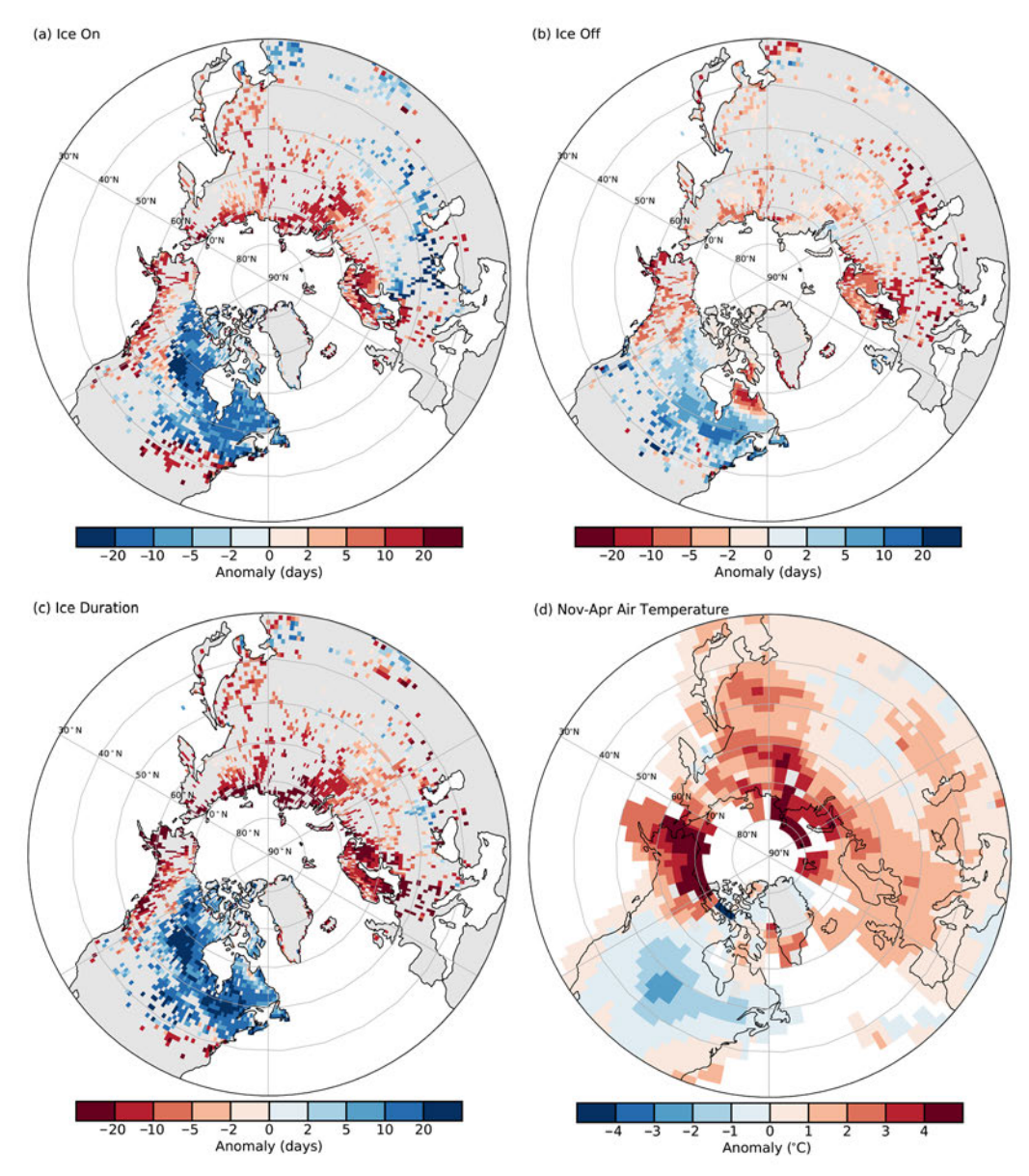

Fig. SB2.1. Lake ice 2019 anomalies for (a) ice-on, (b) ice-off, and (c) ice duration for lakes across the NH (base period: 1981–2010). (Source: ERA5.) (d) Nov–Apr 2018/19 air temperatures. (Source: GISTEMP.)

The changes in ice cover in 2019 relate to air temperature anomalies across the NH. Specifically, the spatial pattern in ice-on, ice-off, and ice duration are consistent with NH cold season (November–April) averaged surface air temperature anomalies (Fig. SB2.1). Regions with shorter ice duration, later ice-on, and earlier ice-off, such as northern Eurasia and western North America, are those with positive air temperature anomalies during the cold season in 2019 (Fig. SB2.1d). Conversely, regions with longer ice cover duration, such as the Great Lakes region, are those with negative air temperature anomalies during the cold season in 2019. Thus, lake ice cover anomalies in 2019 broadly track surface air temperatures (section 2b1), although factors such as wind speed, humidity, snow cover, hydrology, and lake morphometry contribute to variations in ice cover (Brown and Duguay 2010). The relationship between air temperature and lake ice cover, published in previous studies (Palecki and Barry 1986; Weyhenmeyer et al. 2004; Brown and Duguay 2010), suggest that antecedent air temperatures are the most important drivers of ice cover and phenology in 2019. For example, in past years, winter air temperatures alone explain 93% of variation in ice duration in Lake Muggelsee, Germany (Adrian and Hintze 2000), and in 55 Alaskan lakes, air temperature, along with lake area, explain over 80% of the variation in ice-off dates (Arp et al. 2013).

Ice-on, ice-off, and ice duration were derived from ECMWF's ERA5 reanalysis product for land pixels filled with water (>1% coverage) on a 0.25° × 0.25° latitude-longitude grid

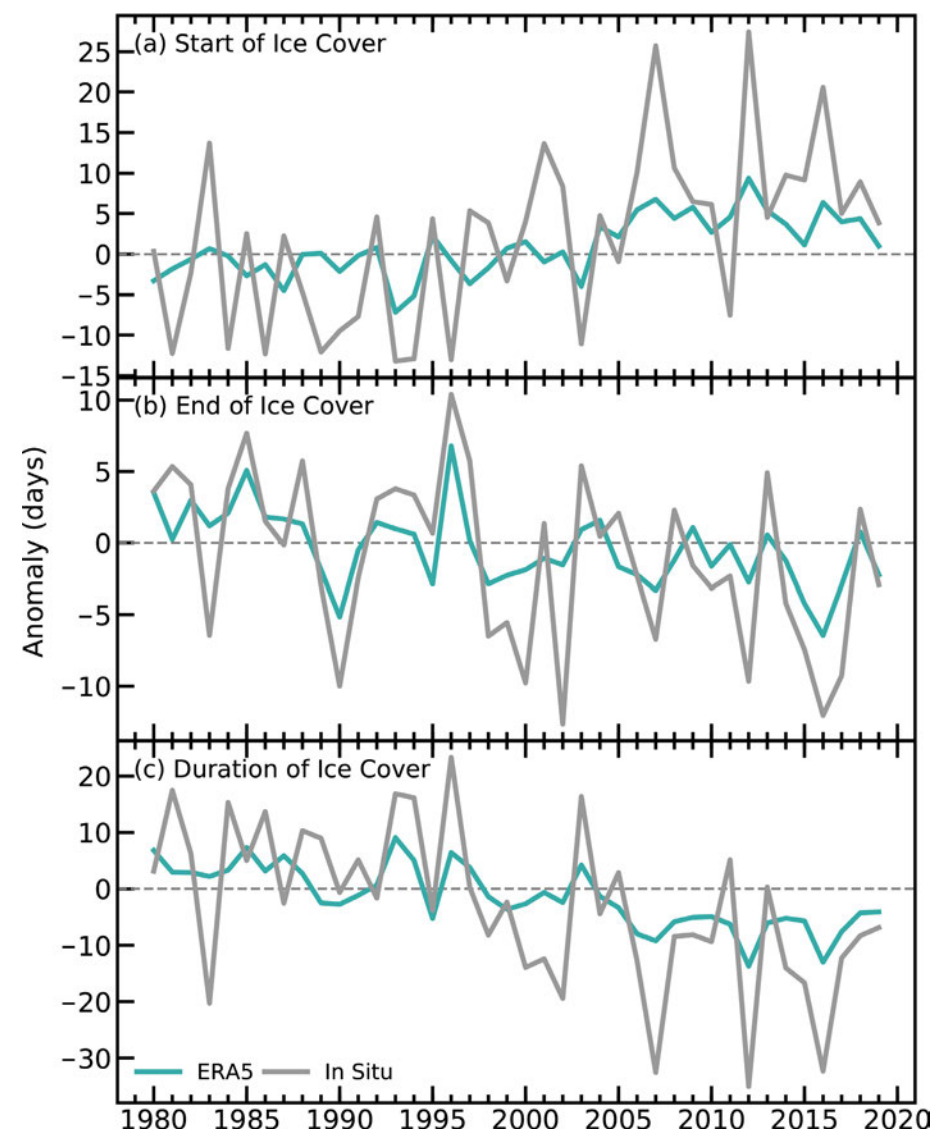

Fig. SB2.2. ERA5 (teal line) and in situ-derived (gray line) anomalies (days) based on an arithmetic mean for (a) ice-on, (b) ice-off, and (c) ice duration from 1980 to 2019.

(Hersbach et al. 2020). Ice cover within ERA5 is simulated via the Freshwater Lake model (FLake; Mironov 2008; Mironov et al. 2010), which is implemented within the Hydrology Tiled ECMWF Scheme for Surface Exchanges over Land (HTESSEL; Dutra et al. 2010; Balsamo et al. 2012) of the European Centre for Medium-Range Weather Forecasts (ECMWF) Integrated Forecasting System (IFS). A detailed description of the model and its implementation in ECMWF's IFS is provided by ECMWF (2018).

In situ ice phenology data were acquired for 18 lakes across the NH where ice-on, ice-off, and ice duration have been collected for at least 130 years (Benson et al. 2000). We updated ice phenology data to 2019 for 10 lakes in Sweden and Finland, one lake in Russia, and seven lakes in the United States. We calculated trends using linear regression models and calculated 95% confidence intervals for the slope of the line. Lastly, we acquired annual maximum ice cover for the Great Lakes encompassing 1973–2019 from the Great Lakes Environmental Research Laboratory. The maximum amount of ice coverage observed over the winter season is calculated across the entire area of each of the Great Lakes by using a combination of composite ice charts and observations from satellites, ships, and air craft (https://www.glerl.noaa.gov/data/ice/).

Surface air temperature data for November–April were downloaded from the NASA Goddard Institute for Space Studies (GISS) surface temperature analysis (Lenssen et al. 2019). Temperature anomalies were calculated relative to the 1981–2010 average.

d. Hydrological cycle

1) Surface humidity—K. M. Willett, A. J. Simmons, M. Bosilovich, and D. I. Berry

Surface specific humidity remained high in 2019 (Fig. 2.15). Over land, the global average anomaly relative to the 1981–2010 average was between 0.14 and 0.25 g kg^{-1} across all estimates, slightly higher than in 2018. Over ocean, 2019 had higher anomalies than 2018 and was one of the moistest years on record, between 0.21 and 0.35 g kg^{-1}.

Simultaneously, 2019 was the driest year on record in terms of relative humidity over land for all products, ranging between −0.86 and −1.27 %RH below average, albeit not significantly so given the 2 std. dev. uncertainty spread for HadISDH at least (Fig. 2.15). Over ocean, relative humidity anomalies were close to or below average, between −0.29 and 0.03 %RH. This moister, yet less saturated, land surface atmosphere occurred along with near-record temperatures over land and ocean (section 2b).

Collectively, 2019 humidity continued the long-term trends of increasing moisture over land and ocean while decreasing levels of saturation over land. From HadISDH, the corresponding 1973–2019 trends (90th percentile confidence intervals) are 0.09 (0.07 to 0.11) g kg^{-1} decade^{-1},

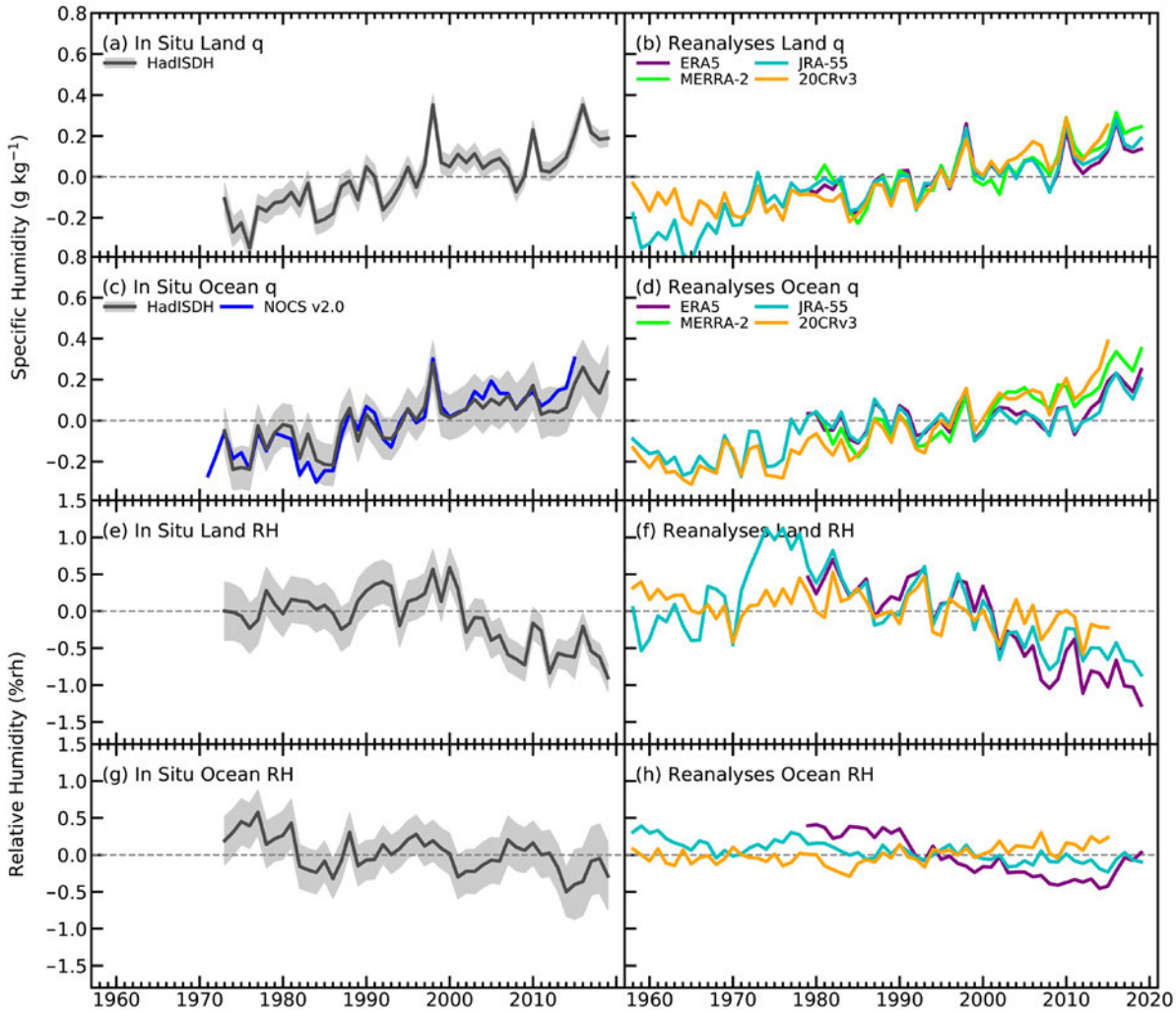

Fig. 2.15. Global average surface humidity annual anomalies (1981–2010 base period). For the in situ datasets, 2-m surface humidity is used over land and ~10-m over the oceans. A 2 std. dev. uncertainty range is shown for HadISDH, capturing the observation, gridbox sampling, and spatial coverage uncertainty. For the reanalysis, 2-m humidity is used over the whole globe. For ERA5 ocean series, only points over open sea are selected, and background forecast values are used as opposed to analysis values because of unreliable use of ship data in producing the analysis. (Sources: HadISDH [Willett et al. 2013, 2014, in review]; NOCSv2.0 [Berry and Kent 2009, 2011]; ERA5 [C3S 2017; Hersbach et al. 2020]; JRA-55 [Ebita et al. 2011]; MERRA-2 [Gelaro et al. 2017]; and 20CRV3 [Slivinski et al. 2019].)

0.08 (0.06 to 0.09) g kg^{-1} decade^{-1}, and −0.16 (−0.29 to −0.03) %RH decade^{-1}, respectively. Water vapor increased relative to 2018 far more over ocean compared to land. The 2019 record low land relative humidity is consistent with the small land specific humidity increase. Global specific humidity values over both land and ocean have remained above the 1981–2010 average for a decade now, and land relative humidity values have remained below average since the early 2000s, although HadISDH uncertainty spread crosses the zero-line periodically, particularly for ocean specific humidity. Both ERA5 and HadISDH suggest that ocean relative humidity has been lower in recent years, but the wide uncertainty spread suggests low confidence in this. Overall, the 2010s were the moistest yet least saturated decade since records began (Fig. 2.15).

Spatially (Plates 2.1g,h; Figs. A2.10–A2.13), 2019 specific humidity was moister than average over the tropical Pacific Ocean and drier than average over Australia. Although such features are often seen during El Niño years, generally, spatial patterns were not ENSO-like.

The high specific humidity signal came largely from the Indian Ocean and is consistent with other variables (see section 2d) and the strong Indian Ocean dipole (IOD). There were also very strong moist anomalies over southern Asia, the central and northeastern Pacific Ocean, the Gulf of Mexico, and the southern tropical Atlantic to some extent. These ocean regions were also anomalously warm during 2019. Aside from southern Asia and especially India, much of the land had weaker moister-than-average anomalies with widespread drier-than-average anomalies that were particularly strong over southern Africa and Australia. The very high specific humidity anomalies over India were associated with much higher-than-average relative humidity anomalies. Conversely, most of the land and oceans had lower-than-average relative humidity anomalies. HadISDH has uncertainty estimates from observation quality, gridbox sampling, and spatio-temporal coverage (Willett et al. 2014, 2020 - in review; Fig. 2.15). These uncertainties are larger for relative humidity than specific humidity and larger over ocean than land, particularly for recent years when digital ocean metadata are unavailable. They do not bring the long-term trend into question nor the fact that 2019 was much moister and yet less saturated than average.

The degree to which the products agree or disagree also provides uncertainty information. Although there is reasonable agreement in the year-to-year variability and long-term trends, there are differences between the in situ and reanalysis products and between the reanalyses themselves. Relative humidity is particularly problematic, with MERRA-2 showing moistening over Asia, unlike ERA5, and HadISDH land and ocean relative humidity showing quite different features. It is not clear which is most reliable. Recently, Freychet et al. (2020) found and adjusted inhomogeneities in Chinese stations. Resulting long-term relative humidity trends were near constant and were larger in wet-bulb temperature compared to ERA5. These trends also differ from those in HadISDH where homogenization was necessarily automated and, therefore, unlikely to be as powerful as regionally applied methods that utilize known changes.

This year version 3 of the 20th Century Reanalysis (20CRv3) is included. Although ending in 2015, it is a useful monitoring tool to compare with other products. ERA-Interim (Dee et al. 2011) is no longer being updated and has been replaced by ERA5. These are similar for the global land surface but differ over ocean, especially for relative humidity (Willett et al. 2019). Greater temporal stability is expected in ERA5 compared to ERA-Interim, and ERA5 assimilates more data, generally. However, uncertainties remain, especially for hydrological cycle variables. These uncertainties arise from errors remaining in the assimilated data, changing data streams over time, and the fact that ERA5 does not impose balance on its water or energy budget (Gelaro et al. 2017; Hersbach et al. 2020).

2) Total column water vapor—C. Mears, S. P. Ho, Olivier Bock, Xinjia Zhou, and Julien P. Nicolas

In 2019, total column water vapor (TCWV) anomalies were below the record levels observed in 2016, but remained above the 1981–2010 climatological average in most locations (Plate 2.1i; Fig. A2.14). TCWV estimates are available from satellite-borne microwave radiometers over ocean (Mears et al. 2018); from COSMIC; Metop-A,-B, and -C; and COSMIC2 GPS-RO (Global Positioning System–Radio Occultation) over land and ocean (Ho et al. 2010a,b, 2020; Teng et al. 2013; Huang et al. 2013; Ho et al. 2020, submitted to *Remote Sens.*); and from ground-based Global Navigation Satellite System (GNSS) stations (Bock and Parracho 2019; Bock 2019). In addition, TCWV data from three global atmospheric reanalysis products are also used here: ERA5 (Hersbach et al. 2020), MERRA-2 (Gelaro et al. 2017), and JRA-55 (Kobayashi et al. 2015). Note that all three reanalyses assimilate satellite microwave radiometer and GPS-RO data and are therefore not independent from these two datasets.

The most prominent feature in Plate 2.1i for 2019 was the strong east–west dipole in the equatorial Indian Ocean, associated with the positive phase of the IOD mode observed in late 2019 (see section 4h). A similar dipole feature was also observed in precipitation (section 2d4). A positive IOD phase has been linked to reduced precipitation over Australia (Ashok et al. 2003), as depicted in Plate 2.1i. There were also moderate wet anomalies in the western tropical Pacific and in sub-Saharan Africa. Other regions showed a mix of smaller wet and dry anomalies, with more regions slightly wetter than the 1981–2010 normal. The patterns in TCWV from ERA5 (Plate 2.1i) over the ocean are confirmed by microwave radiometers (Fig. A2.14), COSMIC ocean measurements, and by output from the three additional reanalyses. Over land, the patterns from COSMIC and other RO missions (satellite RO) are generally similar to the reanalysis output except over northern Africa, where RO shows a pronounced dry anomaly not present in reanalysis. The ground-based GNSS results are also in good agreement with reanalysis.

Over the ocean, the TCWV anomaly time series (Figs. 2.16a,b) from reanalyses and microwave radiometers show maxima in 1983/84, 1987/88, 1997/98, 2009/10, and 2015/16 associated with El Niño events, with 2019 approaching the 2015/16 record levels. The radiometer data show an increasing trend of 0.43 mm decade^{-1} over their period of record (1988–2019). The different reanalysis products, on the other hand, show a wide range of long-term trends over the entire period, but agree well with the radiometer data after the mid-1990s. The satellite RO data are in relative agreement with both the radiometer and reanalysis data after COSMIC began in 2006. Note that the uncertainty in these large-scale averages is larger at the beginning and end of the time

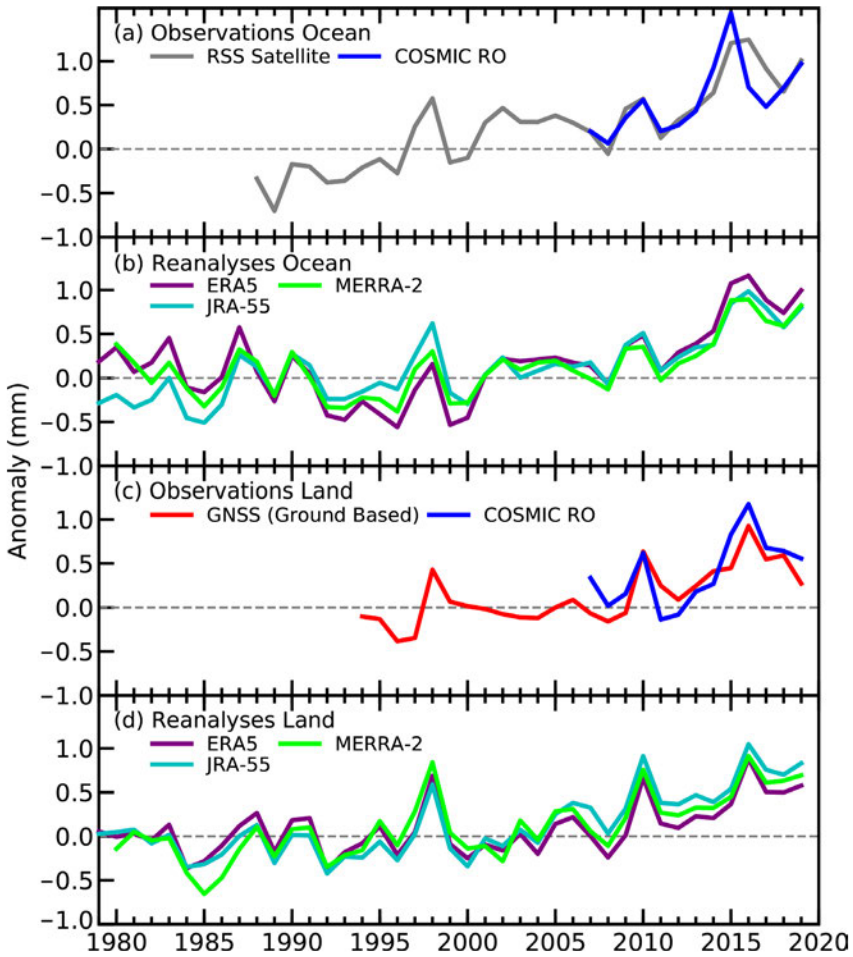

Fig. 2.16. Global mean TCWV annual anomalies (mm) for (a) ocean observations, (b) ocean reanalysis, (c) land observations, and (d) land reanalysis averaged over 60°N–60°S. The shorter time observational series have been adjusted so that there is zero mean difference relative to the ERA5 results during their respective periods of record.

series due to reduced sampling. TCWV is strongly driven by ENSO conditions and to a lesser extent by stratospheric aerosols from volcanic eruptions. After the 2015/16 El Niño peak, all datasets show a return to drier conditions due to generally neutral/weak La Niña conditions in 2017/18, followed by wetter conditions linked to the weak El Niño in winter–spring 2018/19.

Over land, the three reanalyses, satellite RO missions, and GNSS are in good agreement (Figs. 2.16c,d). The small differences in GNSS anomalies are due to asymmetry in the spatial sampling (more stations are located in the Northern Hemisphere [NH]), but the general trend and inter-annual variability are well observed. A latitude–time Hövmuller plot of TCWV anomalies over land and ocean derived from ERA5 (Fig. 2.17) indicates that the long-term increase in TCWV is occurring at all latitudes, with less variability outside the tropics. Following the most recent El Niño in 2015/16, elevated moisture has persisted in the tropics, particularly north of the equator.

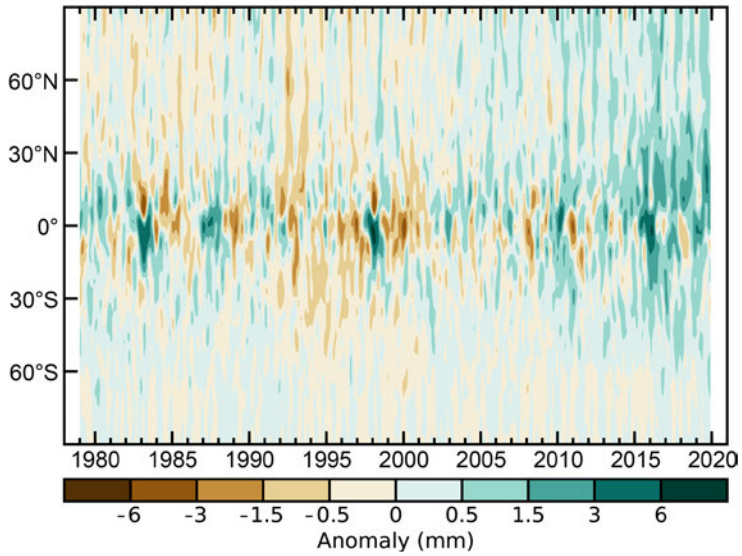

Fig. 2.17. Hövmuller plot of TCWV anomalies (mm; base period 1981–2010) including both land and ocean anomalies derived from the ERA5 reanalysis.

3) Upper tropospheric humidity—V. O. John, L. Shi, E.-S. Chung, R. P. Allan, S. A. Buehler, and B. J. Soden

The 2019 global-average upper tropospheric (relative) humidity (UTH) continued to stay close to the 2001–10 average (+0.016 %RH for the microwave dataset; Fig. 2.18). This implies a continued moistening of the upper troposphere with warming. A near-zero decadal trend in the UTH indicates an increase in absolute (specific) humidity in line with the warming mid- and upper troposphere (about 0.2 K decade^{-1} as shown for example in Santer et al. [2017]; section 2b4), and hence is consistent with a positive (amplifying) water vapor feedback (Chung et al. 2016). The water vapor feedback is determined mainly by the mid- to upper-troposphere (Allan et al. 1999; Held and Soden 2000), because the radiative effect of water vapor is proportional to relative changes in water vapor (John and Soden 2007) and not to the absolute amount.

During the first half of 2019, the anomalies were slightly below average (–0.071 %RH compared to 0.103 %RH in the second half for the microwave dataset), indicating weak El Niño-like conditions, in which an intensified Hadley circulation leads to enhanced subsidence in dry zones (e.g., Tivig et al. 2020). During the second half of the year, the anomalies were generally above average, associated with ENSO-neutral conditions.

There is broad agreement among the three available datasets (HIRS infrared satellite [Shi and Bates, 2011]; microwave satellite data [Chung et al. 2013]; ERA5

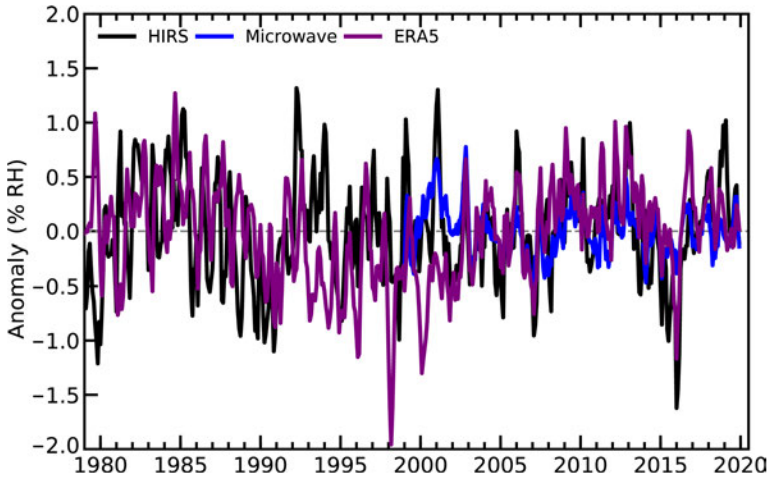

Fig. 2.18. Global (60°N–60°S) average time series of UTH anomalies (%RH) using HIRS (black), microwave (blue), and ERA5 (purple) datasets. Anomalies are computed with respect to the 2001–10 average, and the time series are smoothed to remove variability on time scales shorter than three months.

reanalysis [Hersbach et al. 2020]) in the interannual variability despite their structural differences. During their common period, there is a correlation of 0.6 between the two satellite datasets and 0.5 between ERA5 and either of the satellite datasets. The inter-satellite calibrated and bias-corrected infrared and microwave satellite measurements sample a broad upper tropospheric region (roughly between 500 and 200 hPa, but this layer varies slightly depending upon the atmospheric humidity profile) two times per day, and infrared observations only sample clear-sky scenes (John et al. 2011). The ERA5 reanalysis is based on model runs constrained with in situ and satellite data including the HIRS and microwave radiances. ERA5 samples all regions every hour, but here only displayed at 400 hPa. During the common period (1999–2019), the mean and standard deviation of the anomaly time series are −0.39 ± 0.48, 0.08 ± 0.61, and 0.00 ± 0.34 %RH for the ERA5, HIRS, and microwave datasets, respectively. Compared to its previous version (ERA-Interim), the ERA5 time series shows improved consistency with the satellite datasets but displays anomalies more negative than HIRS or the microwave data.

Annual anomalies of UTH for 2019 are shown in Plate 2.1j and Fig. A2.15 for the microwave and HIRS datasets, respectively. Positive anomalies in central and eastern Africa reflect above-average precipitation and flooding events in those areas. Negative anomalies over southern Africa indicate the drought conditions there (see section 2d12). The strong positive phase of IOD can also clearly be seen in the anomalies. During the positive phase of IOD, sea surface temperatures (SSTs) in the Indian Ocean near Africa's east coast are higher than usual, while SSTs in the waters northwest of Australia are comparatively lower. These conditions led to below-average precipitation across Australia, which is also reflected in the negative UTH anomalies over most of Australia. The close connection of UTH to convection makes it suitable for monitoring large-scale dynamics of the troposphere.

4) Precipitation—R. S. Vose, R. Adler, A. Becker, and X. Yin

Precipitation over global land areas in 2019, as estimated from three different monitoring products, was below the 1981–2000 long-term average (Fig. 2.19a). The observational datasets with the most complete global coverage, that is, the gauge-based product from the Global Precipitation Climatology Centre (GPCC; Becker et al. 2013) and the blended gauge–satellite product from the Global Precipitation Climatology Project (GPCP; Adler et al. 2018), had almost identical anomalies for 2019 (–16.57 mm and –18.32 mm, respectively). The gauge-based Global Historical Climatology Network (GHCN; Peterson and Vose 1996) dataset was closer to the long-term average, with an anomaly of –4.80 mm. All three products indicate that 2019 was marginally drier than 2018.

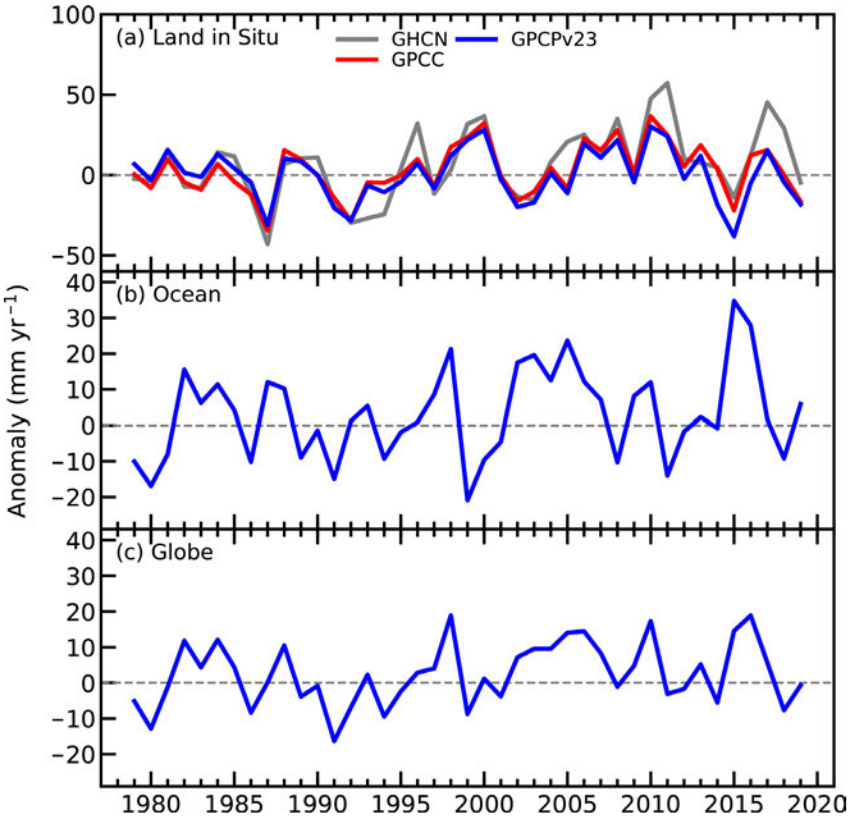

Fig. 2.19. Globally averaged precipitation anomalies (mm yr^{-1}) relative to the 1981–2000 base period over (a) land, (b) ocean, and (c) globe. Land and ocean time series were created using a proportional land/sea mask at the 1° × 1° scale.

According to the GPCP dataset, the precipitation anomaly over the global ocean (Fig. 2.19b) was +5.9 mm and the global combined land and ocean anomaly (Fig. 2.19c) was −0.68 mm, both of which were slight increases from the previous year.

As is always the case, there was substantial variability across the planet in 2019. Much of Africa, Eurasia, North America, and the Amazon basin were wetter than normal, as were the equatorial western Pacific Ocean and the western Indian Ocean (Plate 2.1k). The wet anomaly in the Indian Ocean extended into east Africa, where floods were prevalent during 2019, including floods in March 2019 associated with Cyclone Idai, which killed over 1200 people in Mozambique, Zimbabwe, Malawi, and Madagascar (see Sidebar 7.3 for details). The eastern Indian Ocean, the Maritime Continent, and Australia all experienced much-below-normal precipitation; likewise, Australia had its driest year on record and a very active wildfire season. Parts of the western Atlantic and central Pacific Oceans were also much drier than normal. Large-scale anomaly patterns for 2019 were generally comparable to those of 2018, with notable exceptions; for instance, departures from normal in 2018 were less extreme in the Indian Ocean, the Maritime Continent, and Australia, and the region of drier-than-normal conditions in the equatorial Pacific was deeper and extended farther to the west.

The most striking feature in 2019 was the large rainfall deficit from the eastern Indian Ocean to the South Pacific Ocean east of Australia. With weak El Niño or neutral ENSO conditions during the year, the strong features in this area were driven by conditions in the Indian Ocean; notably, the IOD was strongly positive during the last few months of the year, indicating higher-than-normal SSTs in the western Indian Ocean and lower-than-normal SSTs closer to Australia. The IOD index decreased to near neutral by the end of December, but the rainfall patterns persisted (see section 4h for details).

5) Land surface precipitation extremes—S. Blenkinsop, M. R. Tye, M. G. Bosilovich, M. G. Donat, I. Durre, A. J. Simmons, and M. Ziese

Precipitation extremes in 2019 were typically mixed, with strong regional signals of both above- and below-average anomalies of frequency (R10mm, R20mm) and intensity (Rx1day, Rx5day; Table 2.5). In many regions, above-average anomalies of either, or both, components led to flooding events. Overall, these extremes' anomalies contributed to a global mean precipitation anomaly below the climatological mean (see section 2d4).

The data used include gauge (GHCNd; Menne et al. 2012) and gridded (GPCC-First Guess Daily; Schamm et al. 2013) observations, GHCNd-derived gridded extremes (GHCNDEX; Donat et al. 2013), and reanalysis products (ERA5; Hersbach et al. 2020; MERRA-2; Gelaro et al. 2017).

Observational and reanalysis estimates of 2019 R10mm (Plate 2.1l; Fig. 2.20a) and R20mm (not shown) frequency anomalies revealed fewer-than-average heavy (and very heavy) precipitation days over Australia, Japan, most of Europe, and interior Russia, with above-average frequencies over much of the United States and northeast Russia. There is broad agreement between the global datasets and the more limited coverage of GHCNDEX (not shown) over these areas, but disagreement on the sign of anomalies over Scandinavia and southeast Asia. The above-average heavy precipitation days in the United States were consistent with extensive flooding in the Midwest

Table 2.5. WMO Expert Team on Climate Change Detection and Indices (ETCCDI; Zhang et al. 2011) precipitation indices used in this section and their definitions.

Index	Name	Definition
Rx1day	Max 1-day precipitation amount	Highest 1-day precipitation amount (mm)
Rx5day	Max 5-day precipitation amount	Highest 5-day precipitation amount (mm)
R10mm	Heavy precipitation days	Heavy precipitation days > 10 mm (days)
R20mm	Very heavy precipitation days	Very heavy precipitation days > 20 mm (days)

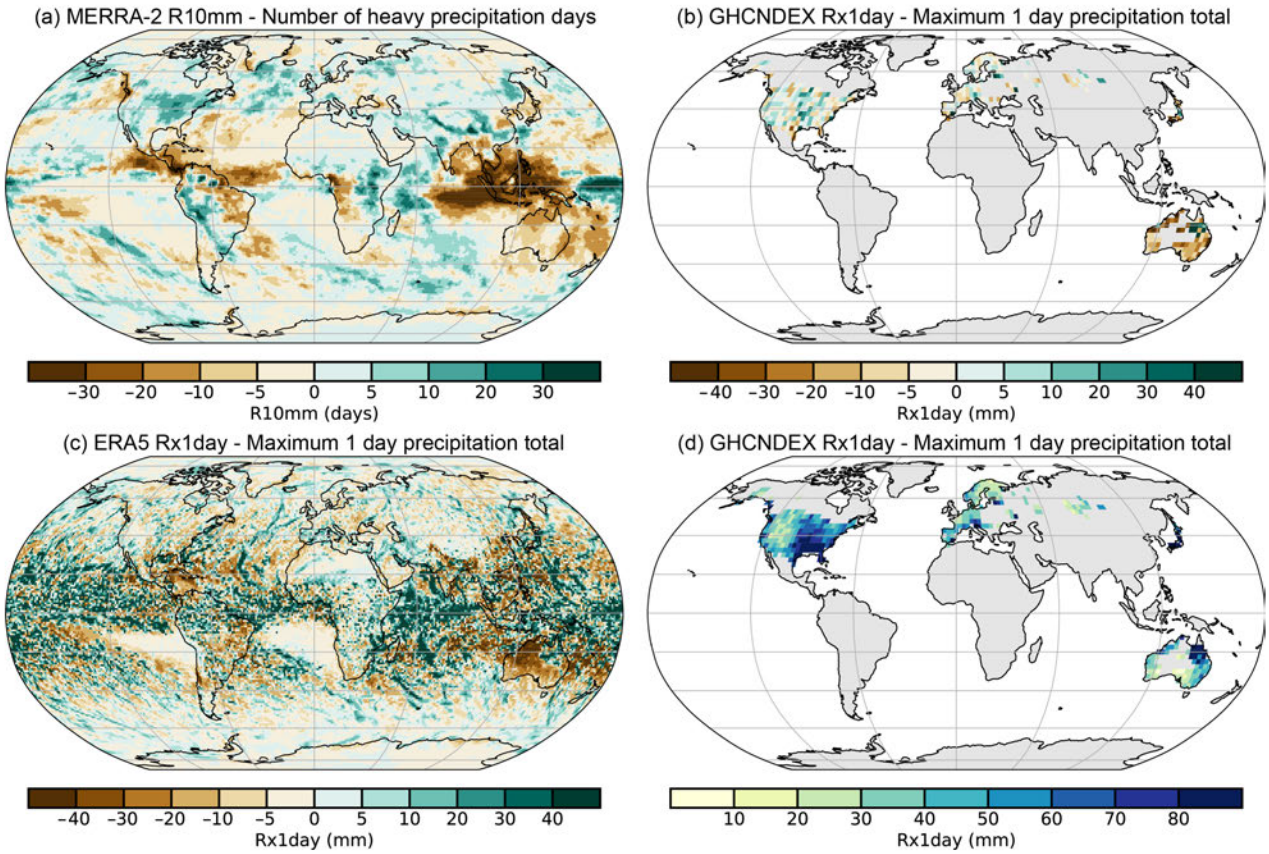

Fig. 2.20. Anomalies of 2019 indices for (a) R10mm derived from MERRA-2 relative to a 1981–2010 baseline and Rx1day derived from (b) GHCNDEX relative to 1961–90 and (c) ERA5 relative to 1981–2010. (d) 2019 absolute Rx1day values from GHCNDEX.

throughout spring and summer, notably the Mississippi and Missouri basins. The globally complete datasets indicated above-average frequencies over Peru, western Brazil, and eastern Africa, all areas affected by flooding in 2019. High frequencies over northern India were associated with late monsoon rainfall and resulted in extensive flooding. There were additional localized areas of high frequency over Afghanistan and Iran, also resulting in flash floods throughout the spring (Floodlist 2019).

Maximum intensity anomalies of Rx1day (Figs. 2.20b,c) and Rx5day (not shown) were noisier than the frequency indices, but largely consistent. GHCNDEX (Fig. 2.20b) shows below-average intensities for most of Australia and western Europe and areas of above-average intensity across the United States. The values of Rx1day for 2019 shown in Fig. 2.20d provide a reference point for these anomalies in absolute terms to enable an estimation of proportional anomalies. The GPCC dataset and the ERA5 (Fig. 2.20c) and MERRA-2 reanalysis products broadly agree and, in particular, confirm a consistent signal over Australia. This reflects the record dry conditions there described in section 7h4 and suggests that severe drought conditions were at least partly related to an absence of heavy precipitation events (see also R10mm). Only over northern Queensland is there a positive anomaly of Rx1day across all data products due to a notable extreme event (e.g., 562 mm at Mossman at the end of January, see section 7h4), contrasting with a closer-to-average signal for R10mm over this part of the state. The more extensive coverage provided by the reanalyses also suggests maxima of below-average intensity over India (contrasting with higher frequency extreme precipitation), parts of China, and central and southern Brazil (see section 2d4); GPCC-First Guess Daily (not shown) also indicates more extensive areas of below-average intensity in tropical and equatorial regions compared with other datasets, which may reflect its coarser resolution and highlighting some of the uncertainty in estimates of precipitation extremes, particularly where gauge data are sparse. Above-average Rx1day intensities were also

clearly identifiable in the reanalysis and GPCC products over Mozambique, producing a stronger signal there than R10mm. This was associated with the destructive tropical cyclones Idai and Kenneth, in March and April, respectively (see section 4f6 and Sidebar 7.3 for more details).

The spatial and temporal variability of precipitation extremes and relatively short records makes detection of long-term change difficult; historical context for 2019 is only provided for available long series of indices (≥50 years) over Europe, Australia, and the United States. Ranking 2019 extreme precipitation indices over Europe from the European Climate Assessment and Dataset blended time series (Klein Tank et al. 2002) revealed 76 (1.3% of gauges) new Rx1day and 16 (0.3%) new Rx5day records, although some were likely from the same event (for example, the Rx1day total includes new records at five gauges in Murcia, Spain, in September; see section 7f4 for details). In total, 10.6% (5.1%) of Rx1day (Rx5day) values ranked in the top decile for an individual gauge in 2019 compared with 15.4% (16.8%) in 2017; 2018 was anomalously dry (Vose et al. 2019) and saw only 7.9% (4.4%) of gauges in the top decile. The R10mm and R20mm frequency indices also confirmed fewer heavy precipitation days in 2019, with only 3.9% of gauges recording frequencies in the top decile compared with 14.7% in 2017. This is consistent with Plate 2.1l in suggesting that 2019 saw relatively few heavy precipitation days across much of Europe but with localized high annual maxima.

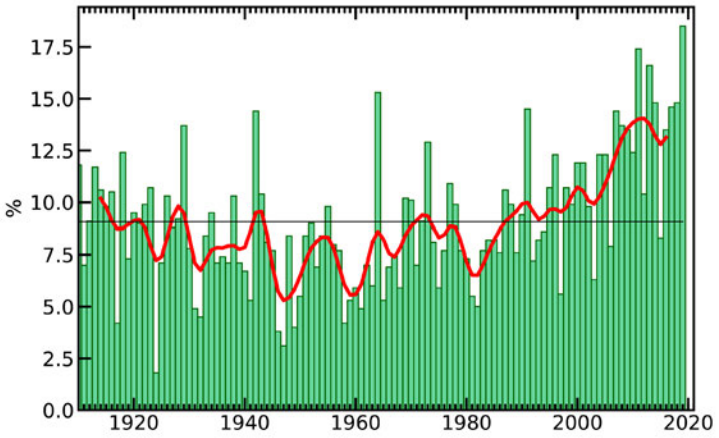

Fig. 2.21. Percentage (%) of the contiguous United States with a much-greater-than-normal proportion of precipitation derived from extreme (highest 10th percentile) 1-day precipitation events in MAM for the period 1910–2019. Red line denotes smoothed Gaussian filter and the black horizontal line denotes the series mean.

Australian GHCNd observations also included few new records for Rx1day (3 from 1359 gauges) and Rx5day (10), as ENSO moved from a weak El Niño to a neutral state and due to the influence of a strong positive IOD in late 2019. Only 3% (2.5%) of locations experienced Rx1day (Rx5day) in their top decile compared with 13.7% (11.2%) in 2017. The new records were set in northern Australia where, for example, in early February, Yabulu, Queensland, received 948 mm over a 5-day period.

An updated assessment of the U.S. NOAA Climate Extremes Index (Gleason et al. 2008) indicated that annually, component 4 of the index (area of the United States that experienced 1-day precipitation totals exceeding the 90th percentile) ranked 20th in the 110-year record (CEI4 = 13.6%) compared to the 2018 ranking of eighth (17.7%). However, the spring CEI4 of 18.5% was the highest spring value on record for the contiguous United States, with 6 of the 10 highest spring totals occurring in the 2010s (Fig. 2.21). The season also saw record highs in the South (30.6%) and Southwest (38.0%) climate regions.

6) Lake water levels—B. M. Kraemer

Near real-time variation in lake water levels can serve as an integrative indicator of current global hydrological change. Based on nearly three decades of water level variation analysis for 198 of Earth's largest lakes with publicly available satellite altimetry data (U.S. Department of Agriculture G-REALM project), the annual average water level across these lakes for 2019, giving equal weight to each lake, was 1.70 m higher than the mean water level for each lake from 1992 to 2002 (minimum level: −23.55 m; first quartile: −0.13 m; median: +0.26 m; third quartile: +1.05 m; maximum: +114.04 m). Water levels were above average in 68% of the lakes analyzed here (134 out of the 198). However, the average volumetric anomaly across lakes (calculated as an approximate

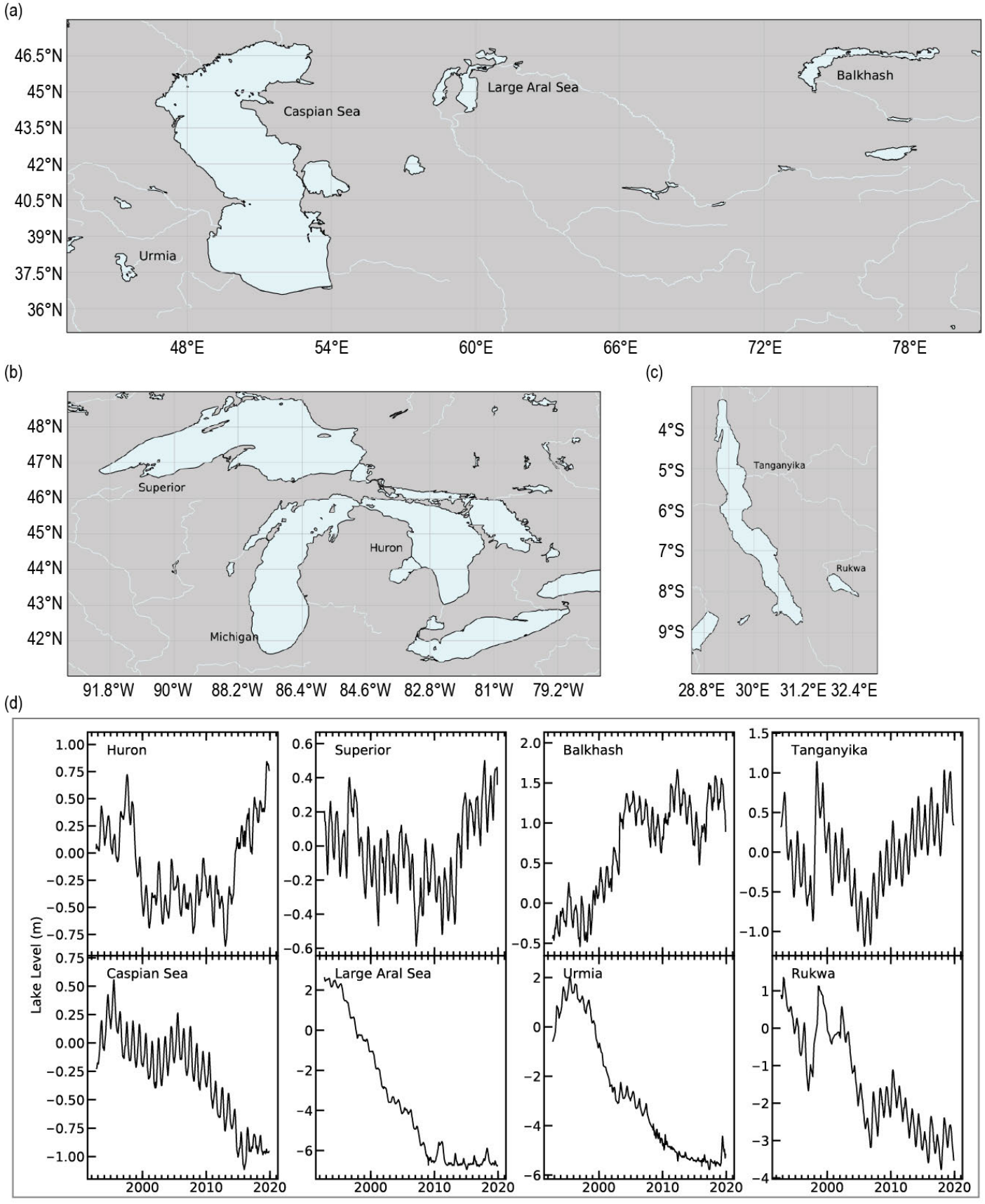

Fig. 2.22. Time series of lake water level (m) for the lakes with the largest volumetric anomalies (2019 water level anomaly × average lake surface area). The top four panels in (d) show lakes with the four largest positive anomalies The bottom four panels in (d) show the lakes with the largest negative anomalies. "Large" Aral Sea is meant to distinguish the lake water level data shown here from water level data for the two other basins formed as the Aral Sea desiccated. Lake Michigan is excluded from the time series because it is hydrologically connected to Lake Huron and its water level variation is nearly equivalent.

estimate by multiplying the water level anomalies for each lake by their average surface area) was −0.46 km^3, and the cumulative volumetric change was −91.2 km^3. The contrast between the 2019 positive mean water level anomaly and negative mean volumetric anomaly arises from the large volumetric decrease in the Caspian Sea, which offsets the numerically more increases in less voluminous lakes.

The water level anomaly estimates presented here differ widely across lakes and across regions, reflecting the heterogeneity of underlying changes in regional hydrological fluxes. As shown in Fig. 2.22, the lakes with the largest positive volumetric anomalies occurred in Huron-Michigan (North America), Superior (North America), Balkash (central Asia), and Tanganyika (eastern Africa) while the largest negative volumetric anomalies occurred in the Caspian Sea (central Asia), Large Aral Sea (central Asia), Urmia (western Asia), and Rukwa (eastern Africa). Some regions showed coherent changes across lakes in their water level anomalies. Lakes in central Brazil, the southwestern United States, Ukraine, and eastern China had consistent negative water level anomalies while equatorial Africa, eastern Kazakhstan, the northeastern United States, and central Canada had consistent positive water level anomalies (Plate 2.1m). Conversely, lake water level anomalies varied substantially within other regions. For example, Tanganyika and Rukwa, the lakes with the fourth-largest positive volumetric anomaly and the fourth-largest negative volumetric anomaly, respectively, are within only 85 km of each other. The Tibetan plateau, the Middle East, and southern Africa all included lakes with both strong positive water level anomalies and strong negative anomalies often in close proximity, highlighting the strong lake-to-lake variation within regions. Variation in water level anomalies across lakes is also partially attributable to upstream land use and land cover change as well as anthropogenic water extractions and diversions.

Water level data were acquired from the NASA/CNES Topex/Poseidon and Jason-1 satellite missions via the Global Reservoir and Lake Monitoring (G-REALM) project version 2.3 (Crétaux et al. 2016). Although these altimeters were developed to map ocean surface height, they have also been used to detect water level changes in lakes (Crétaux et al. 2016). Only a small subset of the world's lakes is monitored in this way because the space-borne sensors must pass directly over the lake with sufficient regularity to produce accurate and complete time series. The lakes in this study comprise the 198 lakes with the longest (>28 years) and highest temporal resolution time series. Comparing satellite altimeter measurements derived from the NASA/CNES Topex/Poseidon and Jason-1 satellite missions to in situ measurements, the root mean-squared error of elevation variations is ~5 cm for large lakes. Water levels are typically measured every 10 days, but the exact dates on which water levels are measured vary from lake to lake. To make water level data temporally consistent, each lake's time series was linearly interpolated to the daily scale so that all lakes had time series of the same interval. Seventy-two of the 198 water level time series had substantial data gaps from 2003 through the middle of 2008, so a period prior to these gaps (1992–2002) was used as the baseline for calculating 2019 water level anomalies.

7) Global cloudiness—M. J. Foster, L. Di Girolamo, R. A. Frey, A. K. Heidinger, C. Phillips, W. P. Menzel, and G. Zhao

Global cloudiness in 2019 decreased relative to 2018 (−0.3 ± 0.3%), based on several satellite cloud records including PATMOS-x/AVHRR (Pathfinder Atmospheres Extended/Advanced Very High Resolution Radiometer), *Aqua* MODIS C6 (Moderate Resolution Imaging Spectroradiometer Collection 6), MISR (Multi-angle Imaging SpectroRadiometer), HIRS High Cloud (High Resolution Infrared Sounder), and PATMOS-x/*Aqua* MODIS (this last record applies the PATMOS-x algorithms to Aqua MODIS measurements and was created for this report). Figure 2.23 shows global cloudiness from 1979 to 2019, with additional long-term records that do not currently extend through 2019: CALIPSO (Cloud-Aerosol Lidar and Infrared Pathfinder Satellite Observation), CERES (Clouds and the Earth's Radiant Energy System), CLOUD_CCI (Cloud Climate Change Initiative AVHRR-PM v3.0), CLARA-A2 (cloud, albedo and radiation dataset), and SatCORPS (satellite cloud and radiative property retrieval system).

A decrease in global annual cloudiness from 2018 to 2019 of 0.3% seems like a small change; however, mean annual cloudiness tends to be very stable. Several of the cloud records shown in Fig. 2.23 are derived from sensors on satellites flown as part of NASA's Earth Observing System (EOS) project. The EOS satellites represented here include *Terra*, *Aqua*, and CALIPSO and the records begin as early as 2000. The standard deviations of mean annual cloudiness for these records range from 0.2% to 0.3%. These records show that 2019 was the least cloudy year in over a decade. Cloud records that rely on the NOAA Polar Operational Environmental Satellites (POES) begin as far back as 1979, and these standard deviations range from 0.7% to 1.5%. These records have more variability due to less stability in the 1980s and 1990s. Large-scale events, such as the volcanic eruptions of El Chichón and Pinatubo, and strong El Niños, may contribute to some of this variability. Instrumental factors such as fewer measurements (from fewer available satellites), increased orbital drift (satellites drift from their original orbit resulting in an aliasing effect), fewer available spectral channels (e.g., 5-channel AVHRR versus the 36-channel MODIS), and the lack of on-board visible calibration systems may also contribute to increased variability (Stubenrauch et al. 2012). It should be noted that the convergence of the records seen in Fig. 2.23 beginning after 2000 is partly due to the use of a common period (2003–15) when creating the cloudiness anomalies.

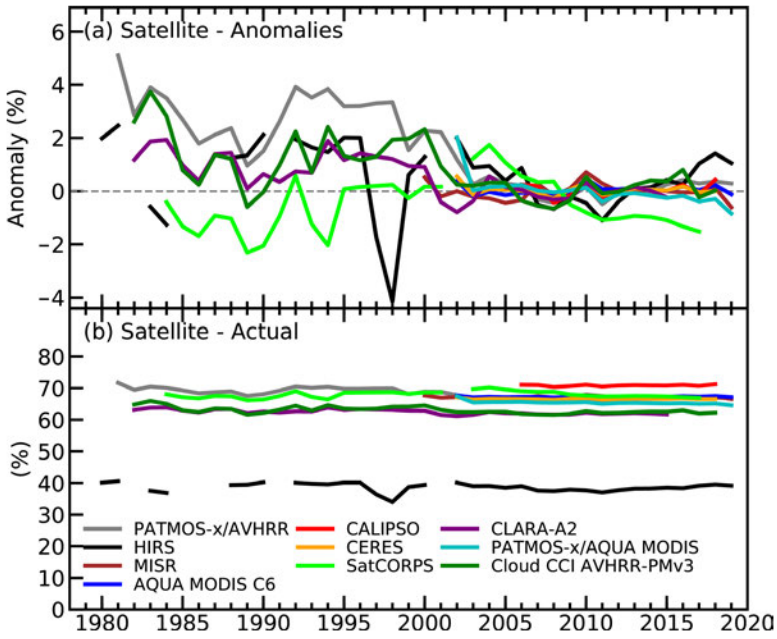

Fig. 2.23. Annual global cloudiness anomalies (%) for 1980–2019, defined as the annual value minus the mean, derived between 2003 and 2015, a period common to the satellite records excluding CALIPSO, where the entire record was used instead. (b) Annual actual global cloudiness (%).

Although globally-averaged cloudiness does not tend to change much year-to-year, the global distribution of clouds can vary significantly. The distribution of clouds over the Pacific Ocean is affected by the phase of ENSO. The gradients of SST and low-level wind between the central equatorial Pacific and Indonesia serve to enhance or suppress convection, which drives the formation of clouds. During years where there is a strongly positive or negative phase of ENSO, this can result in statistically significant cloudiness anomalies over the Pacific. This can be seen in Fig. 2.24, where positive and negative cloudiness anomalies are consistent with phases of ENSO in the PATMOS-x/AVHRR record. In 2019, the ENSO index was weakly positive or neutral throughout the year

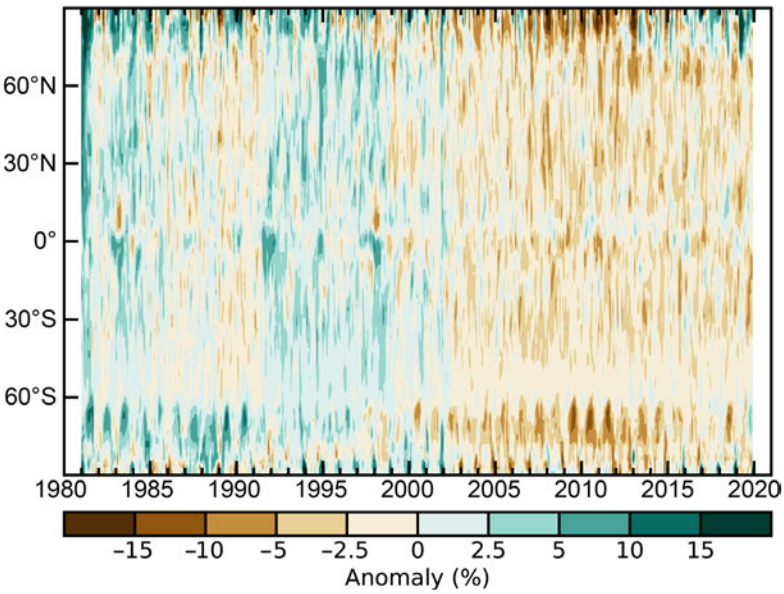

Fig. 2.24. Annual global cloudiness anomalies (%, relative to the 1981–2010 base period) from the PATMOS-x/AVHRR record calculated using the same method as Plate 2.1n but zonally for each degree latitude.

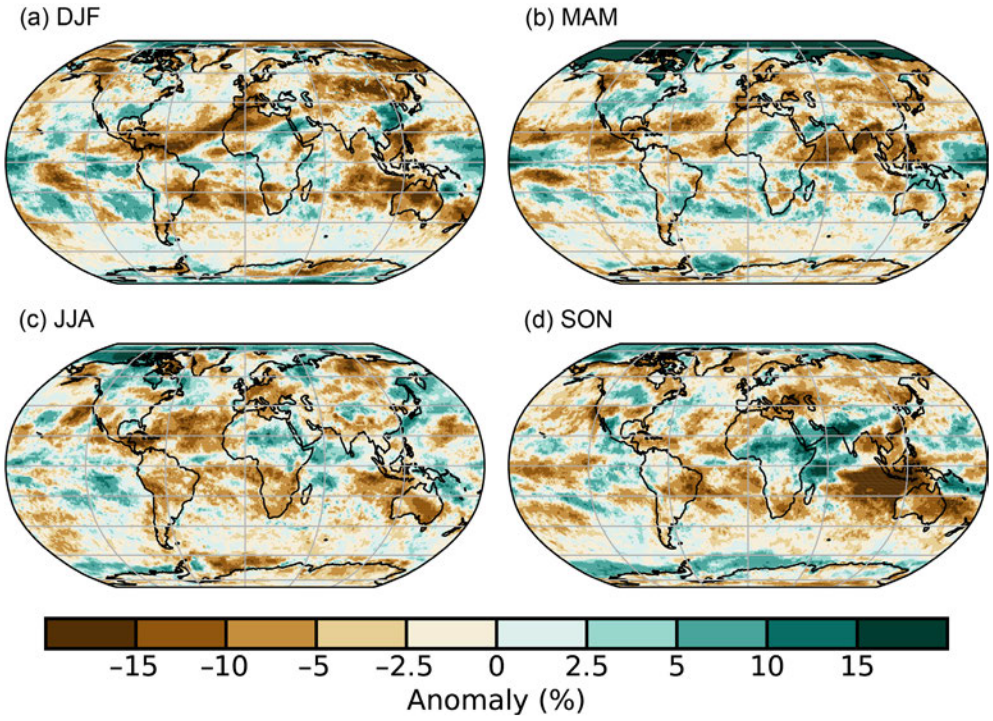

Fig. 2.25. Global seasonal cloudiness anomalies (% relative to 1981–2010) for 2019 from the 30-year PATMOS-x/AVHRR cloud climatology.

(MEI.v2; T. Zhang et al. 2019), and no cloudiness anomalies greater than two standard deviations from the mean were detected over the Pacific. However, other areas of the world experienced similar large-scale weather patterns that had more significant impacts on the global distribution of cloudiness. The IOD is similar to ENSO in that it involves the SST temperature gradient between opposite ends of the Indian Ocean. When the eastern part of the Indian Ocean experiences below-average temperatures relative to the western part, the IOD is considered to be in a positive phase. In this event, eastern Africa frequently experiences positive cloudiness anomalies while southeast Asia and Australia experiences negative cloudiness anomalies. In 2019, the IOD index became positive in the boreal summer and continued to increase, peaking in October in a strong positive phase (BoM 2020; see section 4h). In terms of cloudiness, the positive phase IOD coincided with a significant negative cloudiness anomaly in the eastern Indian Ocean that had the largest spatial extent of any anomaly observed in 2019 (Fig. 2.25). Cloudiness in this area was reduced by 10% to 20% for the year. This extended into Australia, which experienced dry conditions and severe wildfires (see section 7h4 and Sidebar 7.6). There were also significant negative anomalies in the Atlantic Ocean, ranging from 5% to 10%, the largest being located in the tropics north of the equator and extending into the northern subtropics. Minimum cloudiness in this region occurred in the boreal winter, but much of the year saw reduced cloudiness. Combined, these anomalies and the lack of positive anomalies, contributed to the overall decrease in global cloudiness.

8) River discharge and runoff—H. Kim

Runoff is a key component in the water cycle: it balances precipitation with evapotranspiration and storage changes through the energy and water balance at Earth's surface. In numerical models, it is defined as water draining out from a soil column when infiltration capacity is exceeded. A river is an integrated transport of runoff to the ocean. It has important roles, not only the lateral distribution of water (Kim et al. 2009) but also energy (Tokuda et al. 2019) and biogeochemical constituents (Beusen et al. 2016). In this section, we focus on mass transportation (i.e., freshwater discharge) which is more directly related with both climate variability and society (e.g., Hirabayashi et al. 2013; Dankers et al. 2014; Schewe et al. 2014; Madakumbura et al. 2019).

Global distributions of discharge (Plate 2.1o) and run off (Plate 2.1p) anomalies for 2019 (compared to the 1961–90 reference period) indicate many regions where anomalies are opposite to those in 2018. In 2019, large areas of eastern North America and southern China became anomalously wetter (under strong dry conditions in 2018; Kim 2019), while areas including the Indochina peninsula, the western Maritime Continent, northern India, and eastern Siberia became anomalously drier.

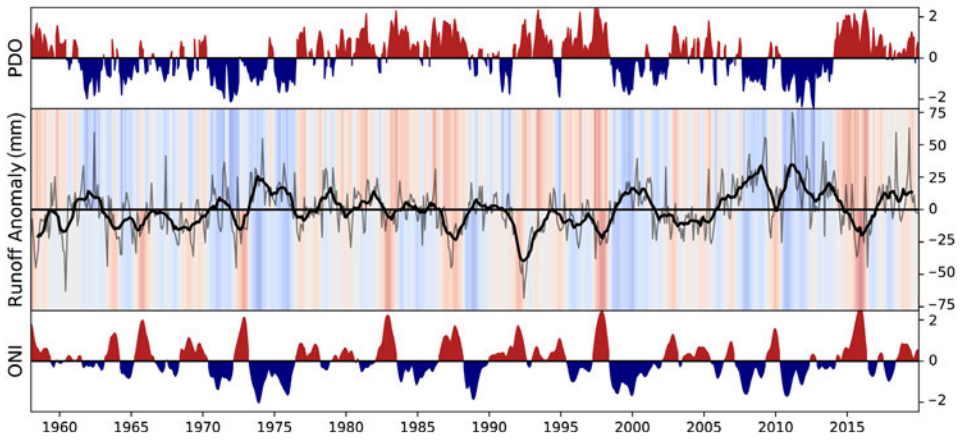

Fig. 2.26. Interannual variability of ONI (lower), PDO (upper), and global runoff (middle; mm; thick line is 12-month moving average). ONI and PDO are shaded red (positive phase) or blue (negative phase). Shading above and below the zero-line of global runoff is proportional to PDO and ONI, respectively.

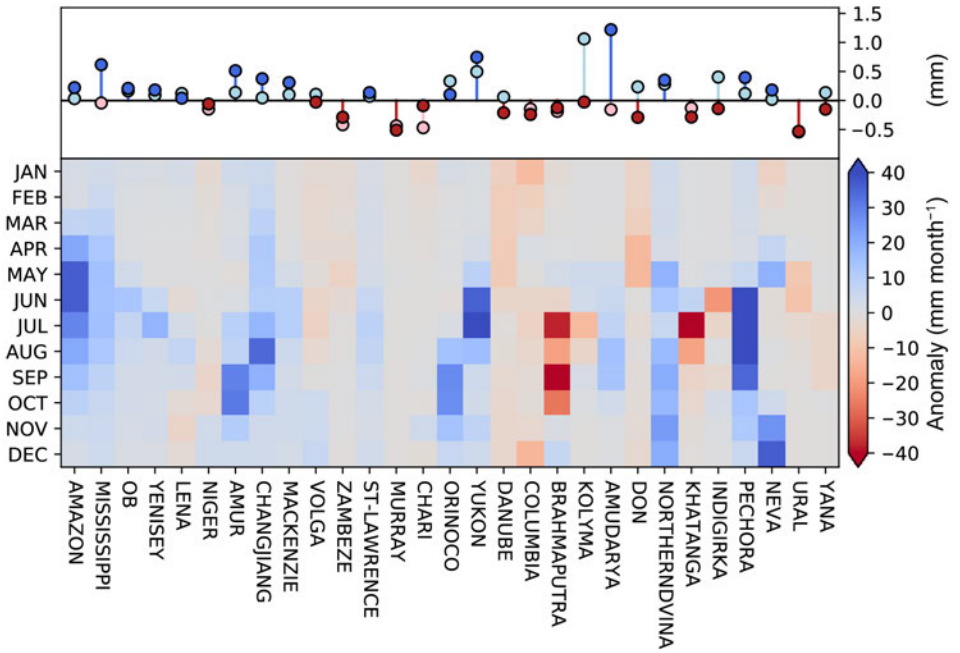

Fig. 2.27. Monthly anomaly for the long-term seasonality (lower, mm month^{-1}) and relative annual anomaly (upper, %; open [uncolored] and closed [colored] circles indicate 2018 and 2019, respectively) of 30 major global rivers' discharge. The basin mask used in the analysis is referred to here: http://hydro.iis.u-tokyo.ac.jp/~hjkim/soc/30basins.png.

Northern North America, western Siberia, and northern South America (wet), and eastern South America, central Africa, Europe, eastern Siberia, and the Korean Peninsula (dry) saw greater intensification of their hydrologic states compared to 2018.

Global total freshwater discharge is strongly correlated with ENSO and the Pacific Decadal Oscillation (PDO; Zhang et al. 1997; e.g., Kim 2017, 2018, 2019). Figure 2.26 shows the long-term variability of the total runoff, with the ONI and PDO indices indicating that in the global average, dry and wet states tend to be in accord with positive and negative phases of ENSO and PDO, respectively. According to multivariate regression analysis, the variance contribution of the Oceanic Niño Index (ONI) and PDO together comprises ~49% of the total variance of global runoff. In 2019, the average global runoff remained at a level similar to the previous year after a bounce-back from the anomalous dry state in 2016 that was associated with the strong El Niño. The ONI and PDO indices also remained in a slightly warm phase, similar to 2018, and the global runoff anomaly increased from 1032 km^3 yr^{-1} to 1758 km^3 yr^{-1}.

The state of wetness in 2019 was analyzed for 30 major global basins with consideration of geographical distributions and quality of the estimations, as suggested by Kim et al. (2009; Fig. 2.27). In general, the wet deviations were stronger, but the discharge increases were typically less than 50% when compared to their climatological means for the given reference period. In 2019, the wet state of the rivers in South America (i.e., Amazon and Orinoco) was due to the wetter-than-average wet season. In contrast, the African rivers (i.e., Niger, Zambezi, and Chari) were relatively dry, and seasonal discharge was persistently below average throughout the year, except during the wet seasons (September–December) for the Niger and Chari. In the United States, the Mississippi River was irregularly wet throughout the year (see section 7b2), while the Columbia River was dry due to the Pacific Northwest drought in 2018–19 and 2019–20. The Mackenzie and

Yukon Rivers in northern North America had above-average discharge, with an anomalous wet season contributing to the Yukon's high discharge. The major Arctic basins, including the Ob, Yenisei, and Lena, were in slightly wet states during 2018 and 2019, and the rivers in eastern Siberia (Kolyma, Indigirka, and Yana) shifted to weak dry states in 2019. Rivers affected by the Asian summer monsoon system (i.e., Amur, Brahmaputra, and Changjiang) experienced opposing states during the boreal summer of 2019. The Amur and Changjiang during the East Asian Monsoon were wetter than their mean states, while the Brahmaputra was in a drier state during the South Asian Monsoon. The Mekong was in a dry but near-normal state in 2019; it is speculated that the severe drought in 2019 in this region was heavily affected by human impacts (e.g., dam operation).

The 62-year (1958–2019) record is based on off-line land surface simulations of the Ensemble Land State Estimator (ELSE; Kim et al. 2009) over 1° grids globally. To produce the atmospheric boundary conditions, the Japanese global atmospheric reanalysis (JRA-55; Kobayashi et al. 2015) and the GPCC Monitoring Product version 6 (Schneider et al. 2018) were combined. The configurations of the modeling system remain the same as previously (e.g., Kim 2018), and human interventions are not considered.

9) Groundwater and terrestrial water storage—M. Rodell, B. Li, and D. Wiese

Groundwater, soil moisture, surface water, snow, and ice are the components of terrestrial water storage (TWS). On multi-annual timescales, groundwater typically controls TWS variability, except in permanently frozen regions (Li et al. 2015). Even on an annual basis, TWS changes are a reasonable proxy for groundwater storage changes, the latter being insufficiently observed in most of the world. From 2002 to 2017, the Gravity Recovery and Climate Experiment (GRACE; Tapley et al. 2004) and since 2018 the GRACE Follow On (GRACE-FO) satellite missions have enabled estimation of TWS anomalies (departures from the long-term mean) based on precise observations of variations in Earth's gravity field. To bridge the 11-month gap between GRACE and GRACE-FO, we make use of output from a land surface model that assimilates data from both missions (Li et al. 2019).

Plate 2.1q maps the changes in annual mean TWS between 2018 and 2019, as equivalent heights of water in centimeters, based on the data assimilation results. TWS changes reflect integrated hydrometeorological variations, including precipitation, solar radiation, air temperature, and other model forcings.

Australia had its warmest and driest year on record (dating to 1910 and 1900, respectively), with TWS losses almost everywhere save for the northeast of the country, contributing to notorious wildfire damage (see Sidebar 7.6). Central Africa saw TWS gains following two dry years, while Angola and Zambia in southern Africa dried considerably. Conditions were mixed in South America, with drought accompanying heat across southeastern Brazil, leading to TWS losses in that region, and TWS gains in many other parts of the continent. The effects of heavy precipitation and subsequent record spring and summer flooding in the midwestern United States can be seen in Plate 2.1q, as well as a return

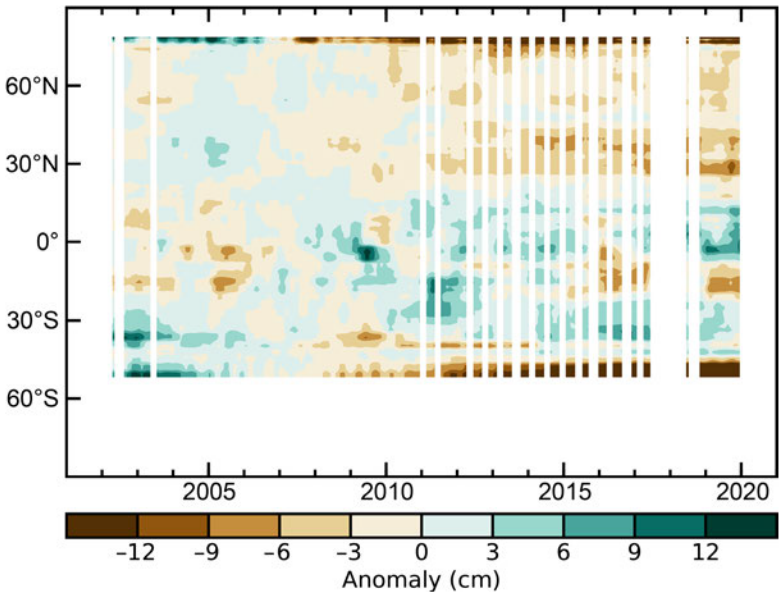

Fig. 2.28. Zonal mean terrestrial water storage anomalies (cm equivalent height of water), based on observations from GRACE (through Jun 2017) and GRACE-FO (beginning Jun 2018), excluding the previously identified ice-covered regions. Anomalies are relative to a 2005–10 base period.

to normal conditions after a particularly wet 2018 in the East. Near-record heat drove TWS losses across most of Europe despite near-normal precipitation. In Siberia and parts of southeastern Asia, drought caused water storage declines. TWS in Iraq and western Iran, on the other hand, was replenished by increased rainfall.

TWS changes in ice-covered regions have been dominated by ice sheet and glacier losses during the past two decades, to the point that annual hydroclimates there must be interpreted from the GRACE and GRACE-FO observations with caution. Hence, TWS changes in Greenland, Antarctica, the Gulf Coast of Alaska, parts of Patagonia, and most polar islands are omitted here. Despite those omissions, ice losses continue to contribute to the high latitude trends (Fig. 2.28) and to the global mean, deseasonalized, monthly TWS anomaly time series (Fig. 2.29). Drying across three continents centered near 15°S, as seen in Plate 2.1q, is evident in Fig. 2.28, as is wetting just north of that. Most of the NH resumed a long-term drying trend, and, overall, 2019 was near the lower end of the range of global mean TWS since 2002, with monthly anomalies that ranged from −2.10 to −0.77 cm equivalent height of water.

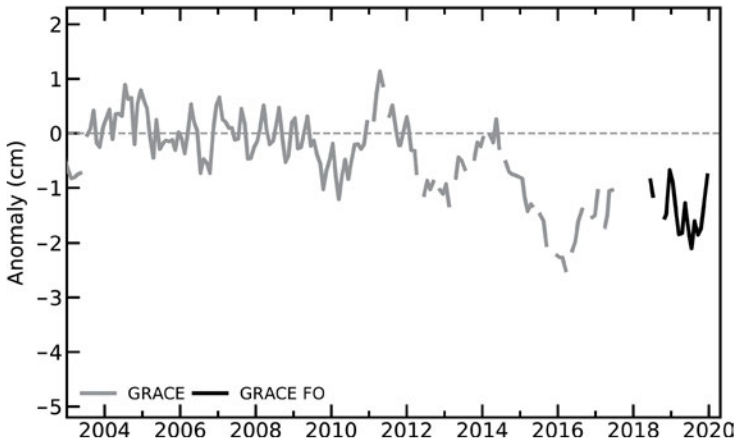

Fig. 2.29. Global average terrestrial water storage anomalies from GRACE (gray lines) and GRACE-FO (black lines), excluding the previously identified ice-covered regions, in cm equivalent height of water relative to a 2005–10 mean base period.

10) Soil moisture—W. Preimesberger, A. Pasik, R. van der Schalie, T. Scanlon, R. Kidd, R. A. M. de Jeu, and W. A. Dorigo

Global soil moisture in 2019 was characterized by significant differences between the two hemispheres: this discrepancy was the largest yet recorded. The strongest negative anomalies were recorded throughout Australia, southern Africa, and Argentinian Patagonia in the Southern Hemisphere (SH), while parts of North America, East Africa, and Asia in the Northern Hemisphere (NH) experienced above-average soil moisture conditions due to an increase in precipitation (section 2d4; Plate 2.1k). A continuation of drier-than-usual conditions observed in 2018 across the SH (Scanlon et al. 2019) is evident, with anomalies in 2019 being even stronger and more widespread. Meanwhile, the 2019 global average soil moisture conditions were close to the 1991–2010 mean despite the evident difference between the hemispheres (Fig. 2.30).

Australia experienced both its driest and warmest year since records began (section 7h4), resulting in strong negative soil moisture anomalies throughout the continent and priming the land for

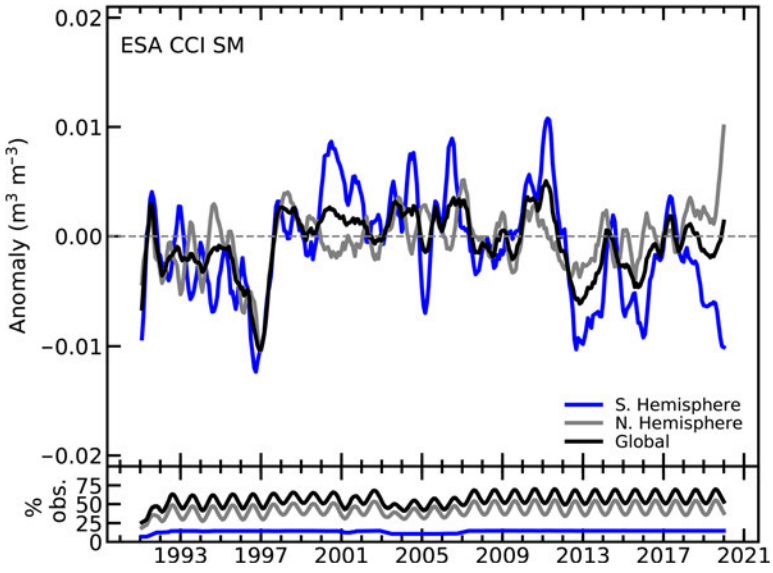

Fig. 2.30. Time series of average NH, SH, and global surface soil moisture anomalies for 1991–2019 (upper, $m^3\ m^{-3}$; 1991–2010 base period) and the percentage of land points with valid observations (lower, %). Data were masked as missing where retrievals were either not possible or of low quality due to dense forests, frozen soil, snow, ice, etc. (Source: ESA CCI Soil Moisture.)

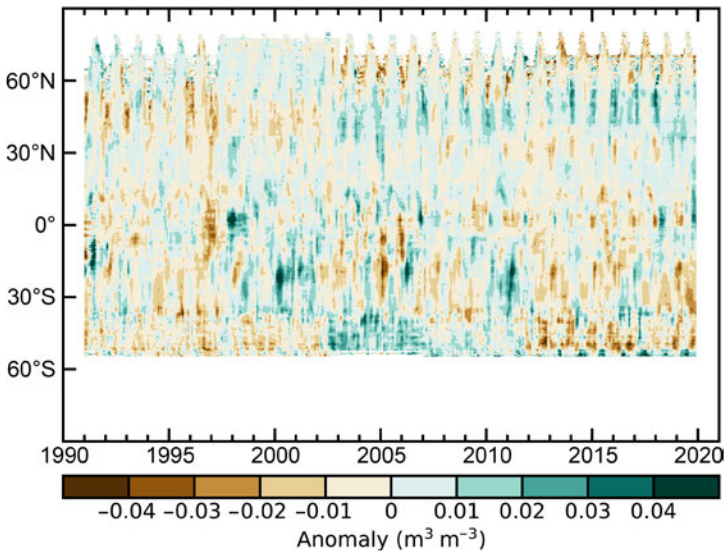

Fig. 2.31. Time–latitude diagram of surface soil moisture anomalies ($m^3\ m^{-3}$; 1991–2010 base period). Data were masked as missing where retrievals are either not possible or of low quality due to dense forests, frozen soil, snow, ice, etc. (Source: ESA CCI Soil Moisture.)

catastrophic wildfires in the latter part of the year. One of the climatic drivers responsible for this situation was a strong positive phase of the IOD, an index of SST difference between the eastern and western Indian Ocean influencing rainfall patterns in Australia and the Indian Ocean basin.

While contributing to a reduction in precipitation over Australia, the positive IOD also contributed to excess rainfall to the Greater Horn of Africa from August through December. This resulted in widespread flooding across East Africa (see section 7e4 for details and impacts). The influence of IOD on soil moisture in India and East Africa is manifested as a strong positive anomaly in the latitudes between the equator and 30°N visible in Fig. 2.31.

Heavy rains led to severe floods in parts of India, especially during August and September (Figs. A2.16h,i). Soil moisture measurements show extremely wet conditions from September through December (Figs. A2.16i–l), largely due to rainfall driven by the positive IOD. Soil moisture conditions for the year as a whole were also above average (Plate 2.1r).

Very dry soil moisture conditions continued in southern Africa for the fifth consecutive year (Dorigo et al. 2017b, 2018). The resulting prolonged and increasingly severe drought was especially apparent in Namibia. Zambia was also among the most affected countries in the region after the 2018/19 rainfall season was among the driest since 1981; the consequent soil moisture deficit is visible in the annual anomalies (Plate 2.1r).

In 2019, the United States received above-average rainfall, with many precipitation records set, especially in the north and the Midwest (see section 7b2). This excess precipitation resulted in above-average soil moisture conditions across large parts of the country throughout the year.

In March, large parts of Iran recorded above-average precipitation, leading to nationwide floods following this period (Fig. A2.16c). Soil moisture conditions were exceptionally high between February and May, declining to around average in November (Figs. A2.16b,e,k, respectively).

Soil moisture observations for this analysis were obtained from the COMBINED product of ESA's Climate Change Initiative for Soil Moisture (ESA CCI SM) v04.7. The product merges measurements from passive and active microwave remote sensing instruments into a single long-term data product based on the quality of available observations (Dorigo et al. 2017a; Gruber et al. 2019). ESA CCI SM therefore achieves higher spatial and temporal (more than 40 years) data coverage than the single-satellite sensor products and is validated against in situ soil moisture measurements and multiple reanalysis products (Dorigo et al. 2017a). Satellite soil moisture observations are representative of the surface layer only (~5 cm) and are masked in cases of snow coverage or frozen soil conditions and for areas covered by dense vegetation or with high topographic complexity (mountains).

11) Land evaporation—D. G. Miralles, B. Martens, H. E. Beck, and M. F. McCabe

At the planetary scale, terrestrial evaporation comprises about two-thirds of terrestrial precipitation. This "loss of water" from the land surface to the atmosphere plays a key role in water management (Teuling et al. 2013) and agricultural planning (Liu et al. 2015), and it is also central in modulating the strength and behavior of the water cycle (Huntington 2006) and associated

extreme events (Miralles et al. 2019). Currently, in the same way that evaporation is invisible to our eyes, it remains invisible to our satellite sensors, making it one of the most uncertain components of Earth's energy and water balance (Dolman et al. 2014). However, models that combine satellite-observed landscape attributes with meteorological drivers of terrestrial evaporation (e.g., vegetation cover, solar radiation, temperature) are often applied to yield global climatological records of the flux (McCabe et al. 2016; Miralles et al. 2016). Based on simulations from one of the few regularly updated and long-term global records, namely the Global Land Evaporation Amsterdam Model (GLEAM; Miralles et al. 2011), Plate 2.1s illustrates the geographical patterns of land evaporation anomalies for 2019.

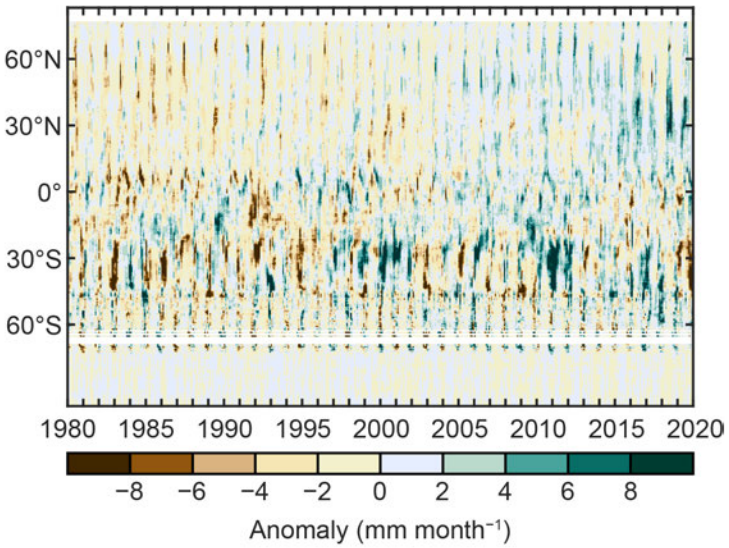

Fig. 2.32. Zonal mean terrestrial evaporation anomalies (mm month^{-1}; relative to 1981–2010 base period). (Source: GLEAM.)

During the year, several regions in the tropics and the SH subtropics experienced anomalously low values of evaporation (Plate 2.1s), in particular, southern Africa (mainly Namibia and Botswana), Australia, and parts of South America (including northern Amazonia). All of these regions suffered from intense drought conditions during 2019. In Australia, the extraordinary drought (see sections 2d12 and 7h4) led to a decline in terrestrial evaporation, which itself was mostly attributed to anomalies in plant transpiration (Fig. A2.17). In accordance with these global patterns (Plate 2.1s), the latitudinal distribution in Fig. 2.32 highlights unusually low values around 30°S, which were exacerbated at the beginning of the austral summer due to water stress. At the other end of the distribution, unusually high values of land evaporation can be observed in Plate 2.1s, concentrated over the Horn of Africa, the east Sudanian Savanna, and central Asia, among other less extensive regions. The spatially extensive positive anomaly in central Asia was one of the most pronounced in 2019. Initiated during the first half of the year, as shown in Fig. 2.32 (see anomaly around 30°N), it was associated with a combination of positive temperature and precipitation anomalies. In Europe and North America, mild positive anomalies were widespread, except for a few regions such as Canada and the Iberian Peninsula (see Plate 2.1s), which were drier.

The 40-year (1980–2019) evolution of evaporation shown in Fig. 2.33 illustrates the statistically significant long-term tendency toward higher annual values that has been reported extensively in the literature (Y. Zhang et al. 2016; Miralles et al. 2014; Brutsaert 2017; Anabalón and Sharma 2017). The average terrestrial evaporation in 2019 was 77×10^3 km^3, slightly below this long-term global trend, yet still higher than the long-term mean (Fig. 2.33). The positive trend is more pronounced in the NH and mostly related to increasing temperatures and global greening (Cheng et al. 2017; Zhang

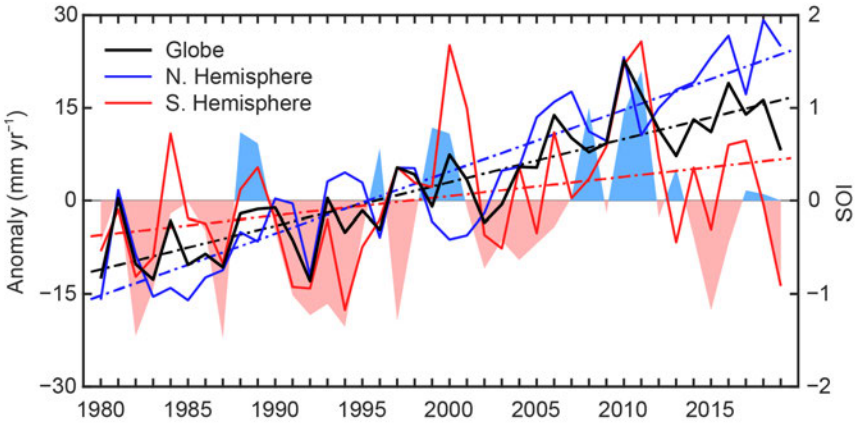

Fig. 2.33. Land evaporation anomaly (mm yr^{-1}; 1981–2010 base period) for the NH, SH, and the entire globe (blue, red, and black solid lines, respectively). Linear trends in evaporation (dashed lines) and the SOI from CRU (right axis, shaded area) are also shown. (Source: GLEAM.)

et al. 2016; Miralles et al. 2014). Indeed, for the NH, 2019 represented the third-largest positive anomaly on record after 2018 and 2016. On the other hand, the year-to-year variability in the SH has previously been reported to be dictated largely by ENSO, due to the drought conditions it triggers in regions such as South Africa and Australia (Martens et al. 2018; Miralles et al. 2014). In agreement with that thesis, prevailing marginal El Niño conditions in 2019 appear once again to be influencing the below-average mean values in the SH. In fact, the geographical patterns of evaporation anomalies shown in Plate 2.1s closely mimic those characteristic of El Niño years (Miralles et al. 2014), and thus may relate to the weak El Niño that developed in 2019 (see SOI [Southern Oscillation Index] in Fig. 2.33).

The results shown here are based on recent simulations of GLEAM v3.4a (Martens et al. 2017). Its accuracy has been reported to be on the order of 0.7 mm day^{-1} (unbiased root mean square error), with correlations against in situ eddy covariance measurements of around 0.8 on average (Martens et al. 2017). Notwithstanding the steady progress in remote-sensing and modeling communities to improve the product accuracy and spatial resolution of land evaporation estimates (McCabe et al. 2019; Fisher et al. 2017; McCabe et al. 2017), trends and patterns in satellite-based evaporation should be interpreted with care, and a weighting based on multiple retrieval approaches is usually recommended (Jiménez et al. 2018). Still, as of today, the algorithms dedicated to estimating evaporation using satellite observations at global scales are mostly intended for research applications and are not regularly updated (Fisher et al. 2017), which constrains the undertaking of a comprehensive analysis that would ensure a more thorough uncertainty appraisal.

12) Monitoring global drought using the self-calibrating Palmer Drought Severity Index—

J. Barichivich, T. J. Osborn, I. Harris, G. van der Schrier, and P. D. Jones

Hydrological drought results from a period of abnormally low precipitation, sometimes exacerbated by additional evapotranspiration (ET), and its occurrence can be apparent in reduced river discharge, soil moisture, and/or groundwater storage, depending on the season and duration of the event. Here, an estimate of drought called the self-calibrating Palmer Drought Severity Index (scPDSI; Wells et al. 2004; van der Schrier et al. 2013) is presented, using precipitation and Penman-Monteith Potential ET from an early update of the CRU TS 4.04 dataset (Harris et al. 2020). Moisture categories are calibrated over the complete 1901–2019 period to ensure that "extreme" droughts and pluvials (wet periods) relate to events that do not occur more frequently than in approximately 2% of the months. This affects direct comparison with other hydrological cycle variables in Plate 2.1 that use a different baseline period.

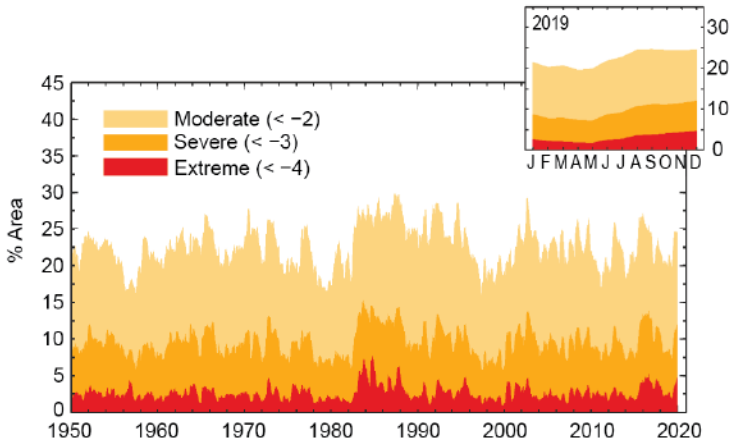

Fig. 2.34. Percentage of global land area (excluding ice sheets and deserts) with scPDSI indicating moderate (< −2), severe (< −3), and extreme (< −4) drought for each month of 1950–2019. Inset: Each month of 2019.

Drought area according to the scPDSI decreased slightly across the globe in 2018 (Barichivich et al. 2019) and continued decreasing through early 2019, but then rose sharply after May (Fig. 2.34). The global land area undergoing extreme drought conditions increased from a minimum of 1.7% in May to 4.7% in December, surpassing the most recent previous peak of 4.3% in October 2017, but not as extensive as some earlier periods of extreme drought. Also from May to December 2019, the area including severe and extreme drought conditions increased from 7.2% to 12% of the global land area, while moderate or worse drought conditions increased from a minimum of 19.2% to 24.6% of the global land area.

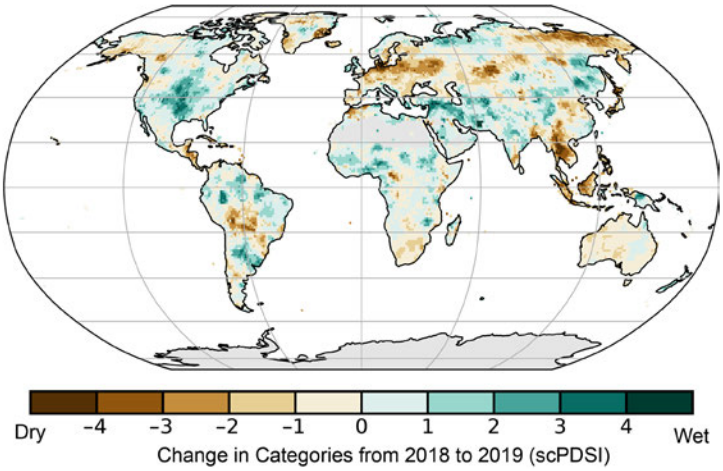

Fig. 2.35. Change in drought from 2018 to 2019 (mean scPDSI for 2019 minus mean scPDSI for 2018). Increases in drought severity are indicated by negative values (brown), decreases by positive values (green). No calculation is made where a drought index is meaningless (gray areas: ice sheets or deserts with approximately zero mean precipitation).

Similar to 2018, moderate to severe drought conditions during 2019 were extensive in South America, the western United States, and the Middle East. Previous moderate to severe drought conditions over Europe, southern Africa, and Australia intensified to extreme drought (Plate 2.1t). The east–west moisture contrast observed across the United States since 2017 further strengthened in 2019, with extensive wetter conditions extending over the whole eastern half and drier in the west. Protracted drought over most of the semiarid northeastern region of Brazil (Jimenez-Muñoz et al. 2016) and central Chile (Garreaud et al. 2017) intensified again in 2019 (Fig. 2.35).

A large part of South Africa experienced extreme drought during 2019 (Plate 2.1t), continuing or intensifying (Fig. 2.35) dry conditions from previous years. In the Cape region, this is consistent with a long-term drying associated with human-caused climate change (Seager et al. 2019), which increases the risk of such rare events (Otto et al. 2018). Previous moderate to severe drought along parts of the west coast of Africa appear to have eased, while wetter conditions in most of central and eastern Africa persisted in 2019 (Fig. 2.35). However, these changes should be interpreted with caution as station data are sparse in these regions. See section 7e for more detailed precipitation analyses for Africa.

Extreme drought conditions that affected Afghanistan in 2018 eased through 2019, and the area under drought was reduced and concentrated mostly over the south of the country. Drought severity also decreased in parts of the Arabian Peninsula that have seen dry conditions since 2017 (Fig. 2.35). Most of Australia saw an increase in drought intensity to severe and extreme conditions due to the continuation of the rainfall deficit combined with record high temperatures. These extreme conditions contributed to the most devastating fire season on record. Fire spread through the southeastern states causing unprecedented devastation. Extreme drought in the Murray–Darling Basin has been characterized as the worst on record. See section 7h4 and Sidebar 7.6 for details.

Antecedent dry conditions, below-average spring precipitation, and extreme summer heat waves pushed most of Europe into drought during 2019 (Plate 2.1t). The most intense drought in the annual average occurred across northern Germany and Poland, where there was already a strong soil moisture deficit in 2018 (Fig. 2.35). The sustained low precipitation in spring and summer in combination with exceptionally high temperatures in late winter-early spring—especially February—and the record-breaking temperatures in June and July further intensified the drought conditions in much of midlatitude Europe.

e. Atmospheric circulation

1) Mean sea level pressure and related modes of variability—R. Allan

Mean sea level pressure (MSLP) data can be used to derive indices of many regional modes of variability that drive significant weather and climate events (Kaplan 2011) such as El Niño–Southern Oscillation (ENSO), the Arctic Oscillation (AO), the North Atlantic Oscillation (NAO), and the Antarctic Oscillation (AAO; Fig. 2.36). ENSO, which is measured in the atmosphere by the sea level pressure derived Southern Oscillation Index (SOI; Allan et al. 1996; Kaplan 2011), arguably has the most global impact.

ENSO describes a variety of events and episodes that, individually, can exhibit wide-ranging characteristics across the Indo-Pacific region and have teleconnections to higher latitudes in both hemispheres (Capotondi et al. 2015; L'Heureux et al. 2017; Wang et al. 2017; Timmermann et al. 2018; Santoso et al. 2019). These different "flavors" of ENSO include protracted El Niño and La Niña episodes (Allan and D'Arrigo 1999; Allan et al. 2019), which are manifest by persistent sea surface temperature (SST) anomalies in the Niño 4 region in the western equatorial Pacific.

Some international ENSO forecasts and outlooks have deemed 2019 conditions as starting with a weak El Niño and changing to ENSO-neutral in July. However, since March–April 2018, monthly Niño 4 SST anomalies have remained positive and, if they continue to be so for 24 months or more (March–April 2020), they will pass one criterion for this period being indicative of a protracted El Niño episode (Allan et al. 2019). The second criterion, for the SOI to have acted similarly by being consistently negative (allowing for only any two months to have gone positive), has held since June 2018 (https://iridl.ldeo.columbia.edu/maproom/ENSO/Time_Series/SOI.html), and this is reflected in Plate 2.1u. This period of continuously warm Niño 4 SST anomalies has led to enhanced atmospheric convection over that region and the generation of a teleconnection that caused large-scale subsidence and suppressed rainfall across eastern Australia in the early-2018 to early-2020 period (see section 7h4 and Sidebar 7.6 for more details). The Niño 4 SST response during the 2018–20 "protracted" El Niño episode may also have been possibly enhanced by anthropogenic forcing, as suggested by Newman et al. (2018).

In the Northern Hemisphere (NH), the last several boreal winters have displayed a variety of AAO and NAO conditions (Figs. 2.36, 2.37). Over the 2017/18 boreal winter (Figs. 2.37a,d), the NAO was mainly positive except in late February (Fig. 2.37d), with temperatures in Europe mostly mild to warm, and the region experienced its fifth-warmest year on record. In particular,

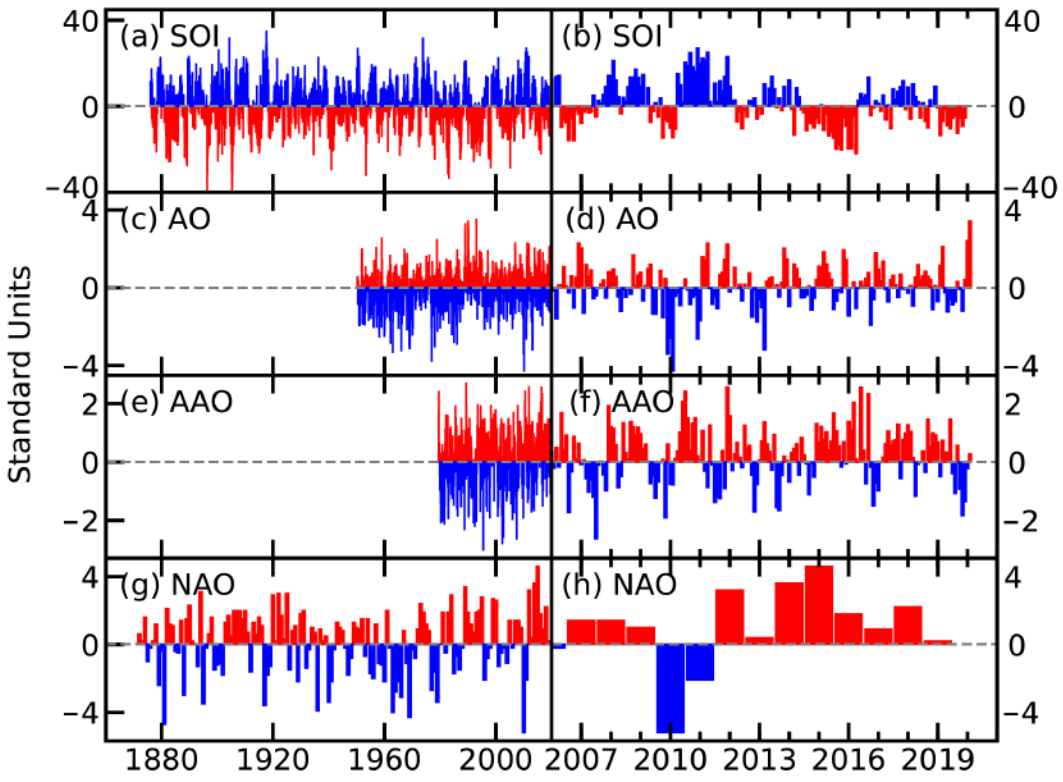

Fig. 2.36. Time series for modes of variability described using sea level pressure for the (left) complete period of record and (right) 2006–19. (a),(b) SOI (provided by the Australian Bureau of Meteorology); (c),(d) AO (NOAA NCEP Climate Prediction Center); (e),(f) AAO (NOAA NCEP Climate Prediction Center); (g),(h) winter (Dec–Feb) NAO average (NCAR; presented for winter at the beginning of each year so winter 2019/20 is not shown).

France, Germany, Switzerland, the Netherlands, and Denmark experienced record or near-record warm conditions in 2018.

During the 2018/19 boreal winter (Figs. 2.37b,e), the NAO swung from moderate positive values in early-to-mid-December to moderate negative values from late December to mid-January 2019, fluctuating between positive and negative values thereafter (Fig. 2.37e). The anticyclonic circulation was dominated by southerly flow over Europe, which led to exceptionally high temperatures in February 2019.

The 2019/20 boreal winter (Figs. 2.37c,f) was characterized by a persistent, mainly positive NAO, which led to warm and mild conditions across the entire European region, with heavy rainfall leading to flooding, and a series of deep Atlantic cyclones. The winter was dominated by a strong stratospheric polar vortex extending down through the troposphere, associated with one of the coldest Arctic winters in the last 10 years.

In the Southern Hemisphere (SH) during the latter half of 2019, the AAO transitioned from being predominantly in its positive phase since 2015/16 (Figs. 2.36f) to negative. This favored a

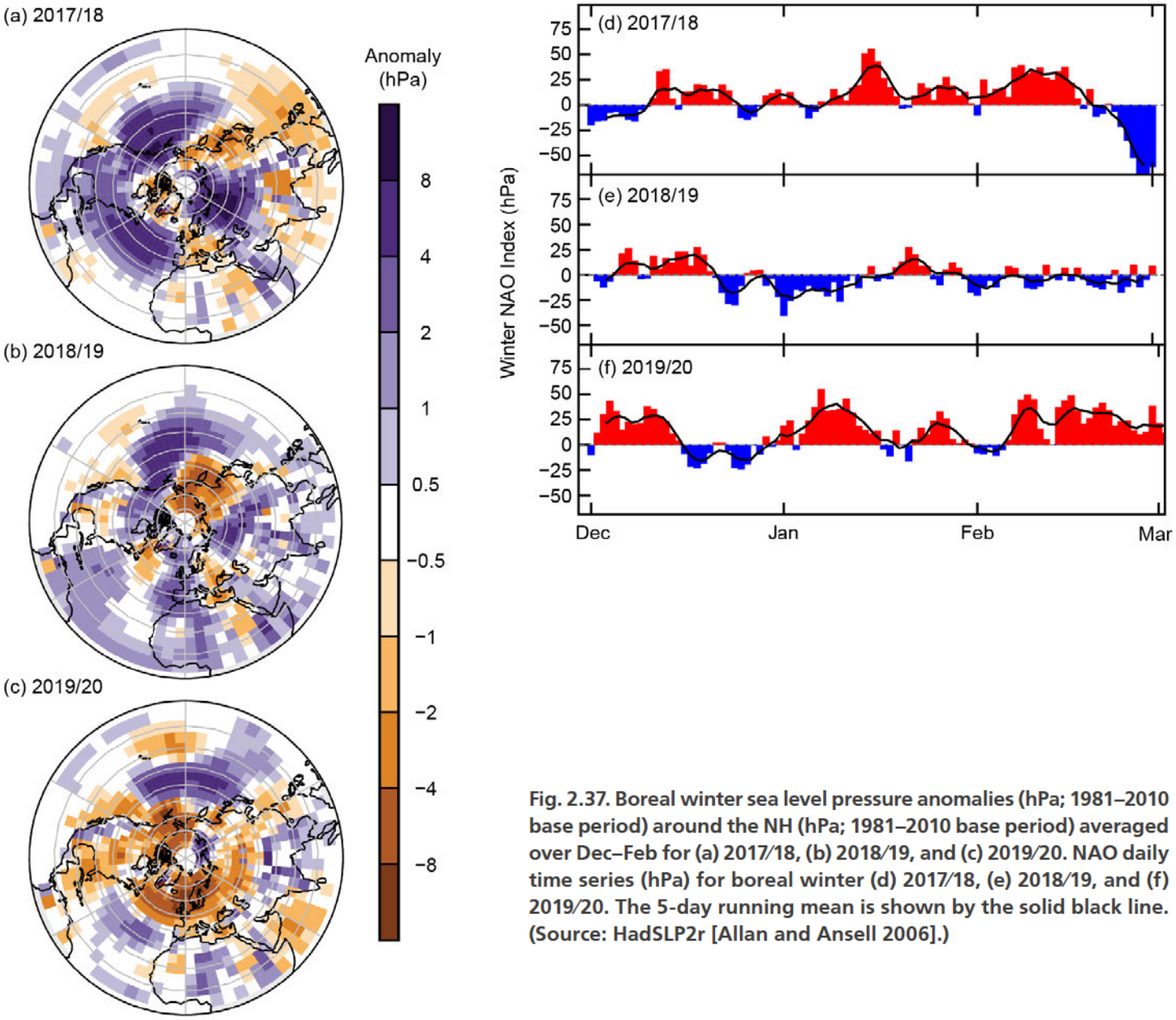

Fig. 2.37. Boreal winter sea level pressure anomalies (hPa; 1981–2010 base period) around the NH (hPa; 1981–2010 base period) averaged over Dec–Feb for (a) 2017/18, (b) 2018/19, and (c) 2019/20. NAO daily time series (hPa) for boreal winter (d) 2017/18, (e) 2018/19, and (f) 2019/20. The 5-day running mean is shown by the solid black line. (Source: HadSLP2r [Allan and Ansell 2006].)

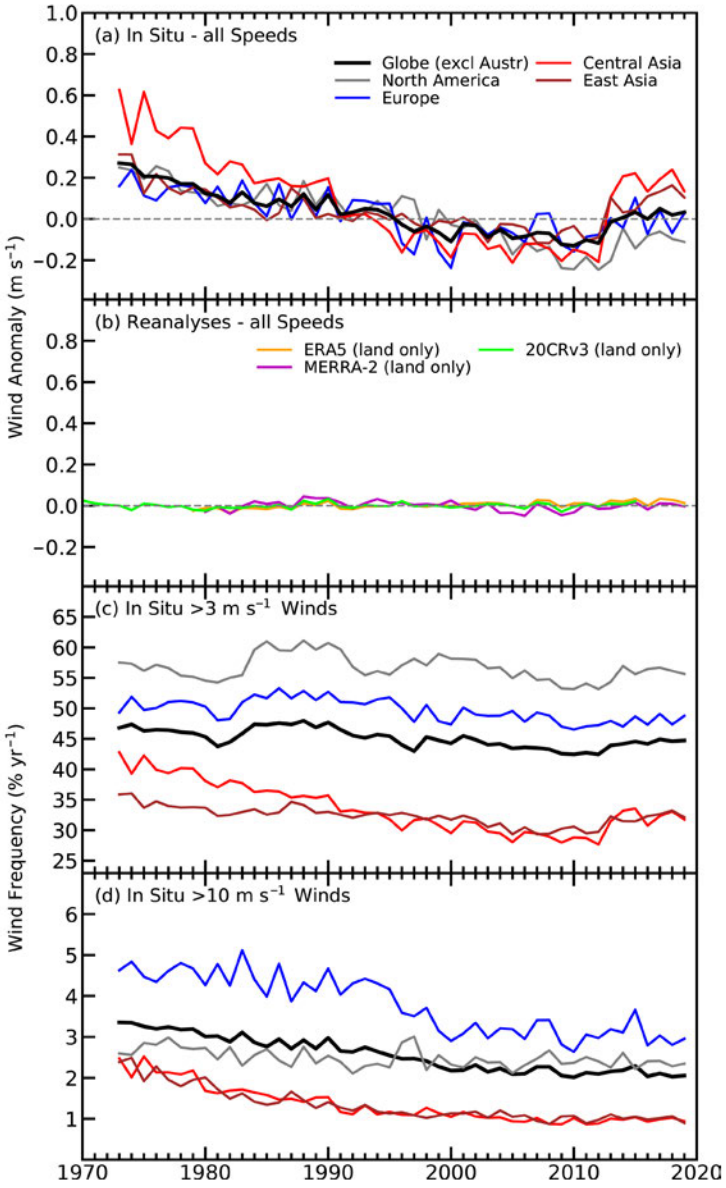

lack of rainfall-bearing systems across eastern Australia and a reinforcement of the drought conditions prevailing in 2019 (see also Sudden Stratospheric Warming discussion in section 2b5).

2) Land and ocean surface winds—

C. Azorin-Molina, R. J. H. Dunn, L. Ricciardulli, C . A. Mears, T. R. McVicar, J. P. Nicolas, G. P. Compo, and C. A. Smith

Global average near-surface wind speed over land (i.e., ~10 m above the ground) has continued the reversal described in previous reports (e.g., Azorin-Molina et al. 2019), which started around 2010 (Zeng et al. 2019; Fig. 2.38a). The 30–50 years leading up to 2010 were dominated by a gradual reduction in surface winds over land, termed *global terrestrial stilling* (Roderick et al. 2007). In 2019, the global (excluding Australia) average wind speed anomaly was +0.033 m s^{-1} with respect to the 1981–2010 climatology (Table 2.6), the third-largest positive wind speed anomaly since 2010. Regionally, Europe showed the largest rebound as the negative anomaly in 2018 became positive in 2019. In contrast, the positive anomalies in central Asia and east Asia were smaller than in 2018. Lastly, North America still showed a negative anomaly yet smaller than the lowest one recorded in 2012 (Iacono and Azorin-Molina

Fig. 2.38. Global (excluding Australia in panels [a], [c], and [d]) and regional annual time series of land surface wind speed anomaly (m s^{-1}; relative to 1981–2010) using (a) HadISD3 (1973–2019), and (b) ERA5 (1979–2019), MERRA-2 (1980–2019), and 20CRv3 (1836–2015, only 1970–2015 shown here). HadISD3 occurrence frequencies (in %) for wind speeds (c) >3 m s^{-1} and (d) >10 m s^{-1}.

Table 2.6. Global and regional statistics for land surface wind speed (m s^{-1}) using the observational HadISD3 dataset for the period 1979–2019.

Region	Mean 1981–2010 (m s^{-1})	Anomaly 2019 (m s^{-1})	Trend 1979–2019 (m s^{-1} $decade^{-1}$) and 5th–95th percentile confidence range	Number of stations
Globe (excluding Australia)	3.326	+0.033	−0.058 (−0.067 → −0.046)	2536
North America	3.705	−0.112	−0.081 (−0.091 → −0.072)	569
Europe	3.689	+0.028	−0.046 (−0.058 → −0.036)	759
Central Asia	2.897	+0.134	−0.100 (−0.127 → −0.076)	257
East Asia	2.719	+0.104	−0.031 (−0.040 → −0.019)	458

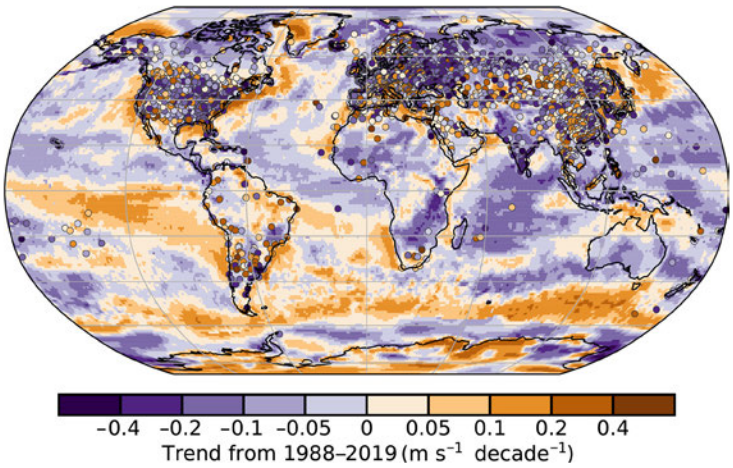

Fig. 2.39. Wind speed trends (m s^{-1} decade^{-1}) for the observational HadISD3 dataset (circles) over land, and MERRA-2 reanalysis output over land/ice and Remote Sensing Systems (RSS) satellite radiometers (SSM/I, SSMIS, TMI, GMI, AMSR2, ASMR-E, and WindSat) over ocean for 1988–2019 (shaded areas).

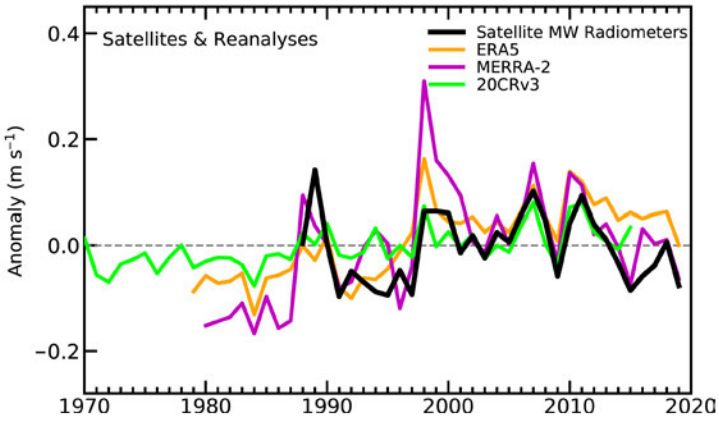

Fig. 2.40. Annual anomalies of global mean wind speed (m s^{-1}; 1981–2010 base period) over the ocean from satellite radiometers and reanalysis outputs.

2014). The recovery observed since 2010 was discussed in regional (e.g., Kim and Paik 2015; Azorin-Molina et al. 2018a; R. Zhang et al. 2019) and global (Zeng et al. 2019) studies. As in previous years, this recovery comes from an increase in the frequency of moderate winds around 2013 (>3 m s^{-1}; e.g., see central and east Asia in Fig. 2.38c), whereas strong winds (>10 m s^{-1}; Fig. 2.38d) are still declining (Azorin-Molina et al. 2016).

The multi-decadal variability and trends of surface winds over land during the 1979–2019 period have been assessed here using station-based observations and gridded reanalysis products. The observations consist of global quality-controlled anemometer observations from 2536 stations from the HadISD3 dataset (1973–2019, Dunn et al. 2016; Dunn 2019). The reanalysis data are based on three products: the full-input ERA5 (1979–2019, Hersbach et al. 2020), MERRA-2 (1980–2019, Gelaro et al. 2017), and the surface-input 20CRv3 (1836–2015, Slivinski et al. 2019, the latter of which is included to reinforce the other products in common years). The reanalyses provide complete spatial and temporal coverage; however, their inability to reproduce the observed long-term changes in wind anomalies (Fig. 2.38b) is a limitation (Torralba et al. 2017; Ramon et al. 2019; Wohland et al. 2019).

One of the key effects of the recent reversal and stabilization of land surface wind speeds is a lower magnitude of the negative trends. Globally, terrestrial surface winds declined at a rate of −0.058 m s^{-1} decade^{-1} during 1979–2019 (Table 2.6), which is close to half of the lowest trend recorded for 1981–2012 (−0.111 m s^{-1} decade^{-1}; see Table 2.4 in McVicar et al. 2013). Regionally, the magnitude of negative trends is slightly weaker than in previous years, being most negative in central Asia, followed by North America and Europe, and least negative in East Asia. The 5th to 95th percentile confidence ranges also shifted toward less negative trend values. In order to compare with Remote Sensing Systems (RSS), Fig. 2.39 shows HadISD and MERRA-2 trends over the 1988–2019 period. Negative trends (59.0% of stations) dominated northern midlatitude regions, with MERRA-2 also showing declining values for regions with scarce observations, e.g., South America, Africa, and Australia.

Over ocean, the three above-mentioned reanalyses and satellite-based products were used to assess surface winds for the period 1987–2019: the Special Sensor Microwave/Imager (SSM/I), the Special Sensor Microwave Imager/Sounder (SSMIS), the Advanced Microwave Scanning Radiometer (AMSRE and AMSR2), Tropical Rainfall Measuring Mission Microwave Imager (TMI), and WindSat (Wentz 1997, 2015; Wentz et al. 2007). The 2019 mean global mean wind speed anomaly over the ocean (Fig. 2.40) shows negative values for satellite radiometers and MERRA-2, but only

a weak negative anomaly for ERA5. According to the satellite measurements, 2019 marked the second-lowest wind speed anomaly over ocean in the twenty-first century. The global spatial anomalies (Plate 2.1v) show a dominance of negative anomalies, in particular over the western Pacific and over the Indian Ocean (< –1 m s^{-1}), due to an intense positive phase of the Indian Ocean dipole (IOD), and in the central Pacific and South Atlantic Ocean; in contrast, positive anomalies (> +1 m s^{-1}) occurred over the Southern Ocean, North Atlantic Ocean, and the Bering, Mediterranean, and Coral Seas. As in 2018, ocean wind speed trends for 1988–2019 (Fig. 2.39) were mostly dominated by weak negative values along with a clear tendency toward a strengthening of winds in the Southern Ocean, the trade winds in the Pacific and Atlantic Oceans, and some isolated regions (Young and Ribal 2019).

The potential causes underlying global terrestrial stilling and its reversal over the last decade are varied (Azorin-Molina et al. 2018b) and likely not all presently known. Recently, Zeng et al. (2018) rejected the attribution of the slowdown of winds to the increase of terrestrial surface roughness due to vegetation/urbanization growth (Vautard et al. 2010), and Zeng et al. (2019) proposed that the major driving force of wind speed changes (i.e., both the stilling and the recent rebound of winds) is associated with decadal ocean–atmosphere oscillations and changes in large-scale atmospheric circulation patterns. Moreover, Zeng et al. (2019) concluded that the relationship of ocean–atmosphere oscillations to anthropogenic warming and the impact on surface wind speed variability remains unclear, representing a large scientific challenge.

3) Upper air winds—L. Haimberger, M. Mayer, and V. Schenzinger

As in past years, we examine the 200-hPa velocity potential to evaluate the imprint of tropical climate anomalies on upper air divergent winds. A strong positive IOD event developed in the course of 2019, peaking in boreal autumn (see section 4h). Figure 2.41 displays anomalous 200-hPa velocity potential and divergent winds for August–December 2019 and shows a clear imprint of the IOD event. The positive IOD event occurred in the absence of classical El Niño conditions, which is relatively rare but linked to the protracted El Niño (section 2e1). Consequently, the strongest velocity potential anomalies were found over the Indian Ocean. There is a prominent dipole in the velocity potential, with positive anomalies over the Indo-Pacific Warm Pool and negative anomalies over the western Indian Ocean, which leads to a westerly divergent wind anomaly over the Indian Ocean. The positive anomalies and associated wind convergence over the Warm Pool are indicative of reduced

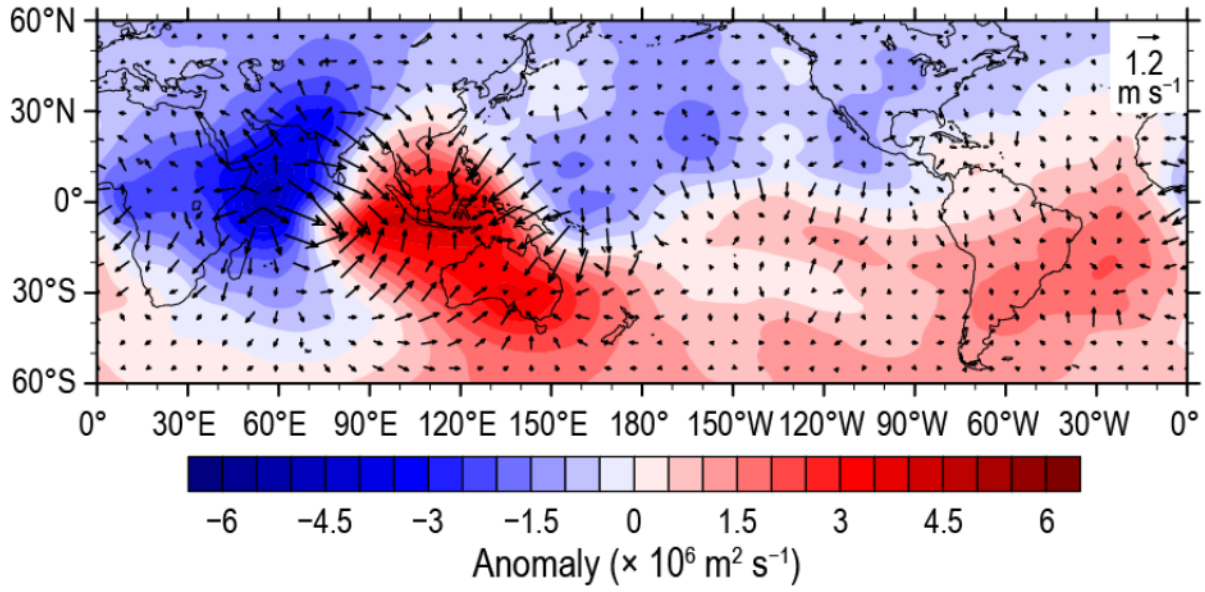

Fig. 2.41. Anomalous 200-hPa velocity potential (× 10^6 m^2 s^{-1}) and divergent winds (m s^{-1}) averaged over Aug–Dec 2019 (1981–2010 base period) based on ERA5 data.

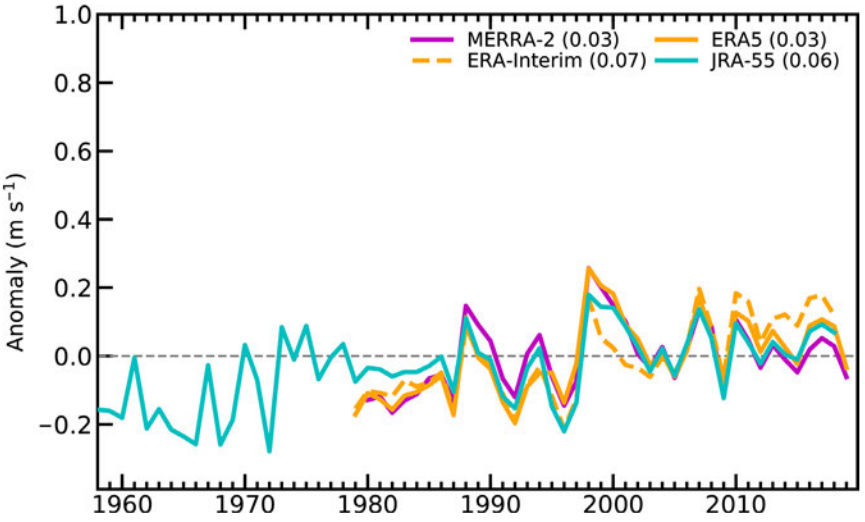

Fig. 2.42. Annual anomalies of global mean wind speed (m s^{-1}; 1981–2010 base period) at 850 hPa from four reanalyses (ERA5, ERA-Interim, MERRA-2, JRA-55). The numbers in parentheses are linear trends in m s^{-1} decade^{-1} for the period 1980–2019.

convection in this region, consistent with negative SST anomalies in the eastern Indian Ocean.

The positive velocity potential anomalies extend well over Australia, with a secondary maximum over the south of the continent. The associated upper air wind convergence and sinking motion is consistent with the persistent dry conditions over the Australian continent (see section 7h4 for more details).

Plate 2.1w shows the 850-hPa eastward wind patterns in autumn 2019. The most obvious feature is the anticyclonic structure over Australia and the Indian Ocean, with strong easterly anomalies over the equator south of India and over northern Australia together with strong westerly anomalies over the southern Indian Ocean and south of Australia, which is perhaps enhanced by the negative Antarctic Oscillation in 2019. This indicates a strong anomalous anticyclonic circulation over the Australian continent, which is consistent with the drought conditions observed there (Ummenhofer et al. 2009). Together with the patterns shown in Fig. 2.41, the easterly 850-hPa wind anomaly over the equatorial Indian Ocean completes the picture of the perturbed Walker circulation in this region, with anomalous upward motion in the western Indian Ocean and anomalous sinking motion over the Maritime Continent.

The 2019 global mean wind speed at 850 hPa was lower than in 2018 and slightly below the 1981–2010 average (Fig. 2.42). The positive trend over the past 40 years still remains in all four reanalyses presented here.

The 2019 behavior of the Quasi-Biennial Oscillation (QBO) can be described as being fairly regular (see Fig. A2.18). The westerly phase had a maximum amplitude of 17 m s^{-1}, which is comparably high (mean 14.8 ± 1.8 m s^{-1}), but not at record levels. It descended with about 1 km yr^{-1} on average, well within the long-term range of descent rates (1.2 ± 0.6 km yr^{-1}) and lasted for 25.8 months in total, which is about 2.5 months shorter than on average. At 10 hPa, the easterly phase started in April, which is a common month for a phase transition at this height. Its descent progressed with 0.8 km yr^{-1} so that it reached the 30 hPa level by the end of the year. However, one noteworthy behavior was the onset of the easterly phase at 45 hPa at the end of October, which means that it developed within a zone of westerly winds, similar to the anomaly in the 2015/16 boreal winter.

f. Earth radiation budget

1) Earth radiation budget at top of atmosphere—T. Wong, P. W. Stackhouse, Jr., D. P. Kratz, P. Sawaengphokhai, A. C. Wilber, S. K. Gupta, and N. G. Loeb

The energetic state of the Earth–atmosphere system is defined by the balance of the incoming total solar irradiance (TSI) and the reflected shortwave (RSW) and outgoing longwave radiation (OLR) from Earth. This balance defines Earth's radiation budget (ERB) at the top of the atmosphere (TOA), and its regional distribution drives atmosphere and ocean circulations.

An analysis of all CERES ERB measurements (Table 2.7) shows that 2019 global annual mean OLR increased by ~0.60 W m^{-2} and RSW decreased by ~0.55 W m^{-2} relative to their corresponding values in 2018 (rounded to nearest 0.05 W m^{-2}). Over the same timeframe, the global annual mean TSI remained nearly unchanged. The sum of these components amounts to a near zero

Table 2.7. Global annual mean top of the atmosphere (TOA) radiative flux changes between 2018 and 2019, the 2019 global annual mean radiative flux anomalies relative to their corresponding 2001–18 mean climatological values, and the 2-sigma interannual variabilities of the 2001–18 global annual mean fluxes (all units in W m^{-2}) for the outgoing longwave radiation (OLR), total solar irradiance (TSI), reflected shortwave (RSW), and total net fluxes. All flux values are rounded to the nearest 0.05 W m^{-2} and only balance to that level of significance.

	One-year change (2019 minus 2018) (W m^{-2})	2019 Anomaly (relative to climatology) (W m^{-2})	Interannual variability (2001–18) (W m^{-2})
OLR	0.60	+0.55	±0.60
TSI	0.00	–0.10	±0.15
RSW	–0.55	–1.20	±0.95
Net	–0.05	+0.55	±0.80

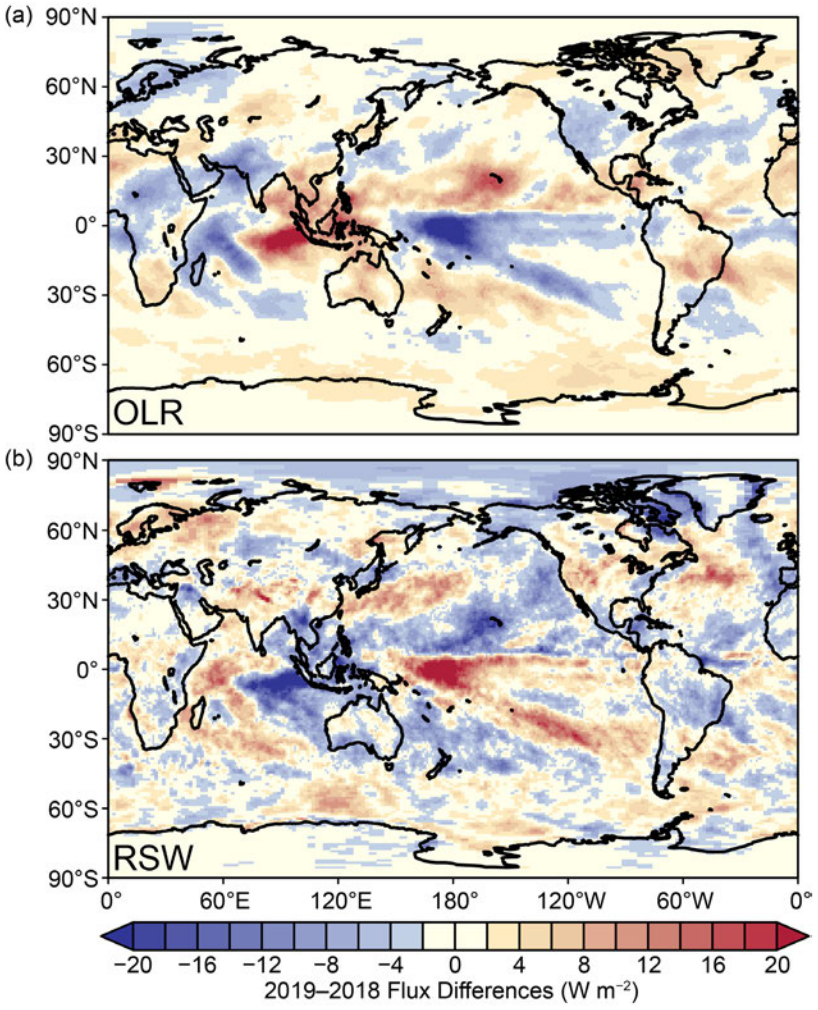

Fig. 2.43. Annual average TOA flux differences between 2019 and 2018 for the (a) OLR (top panel) and (b) TOA RSW (bottom panel). The pattern of differences shows several significant features including changes over the tropical Pacific, Indian, and North Atlantic Oceans. The tropical Pacific pattern is dominated by an atmospheric shift from La Niña conditions during the first half of 2018, to weak El Niño in the first half of 2019, to near-neutral condition by the end of 2019.

change (decrease of ~0.05 W m^{-2}) in the global annual mean total net radiation into Earth's climate system for 2019 compared with 2018. Figure 2.43 shows the annual mean regional difference maps in the OLR and RSW between 2019 and 2018. Peak OLR flux changes are largely compensated by RSW changes, but OLR increases are spread over broader areas including the Indian Ocean, continental Asia, Australia, and South America. Large reductions in OLR and increases in RSW are observed over large areas of the Pacific that stretch from east of New Guinea to the eastern equatorial Pacific and from east of New Guinea to the southern Pacific. These regional changes are associated with the tropical climate oscillation between minor La Niña conditions in early 2018, weak El Niño conditions during the first half of 2019, and near-neutral conditions by the end of 2019. Relative to the multiyear data average from 2001 to 2018, the 2019 global annual mean flux anomalies (Table 2.7) are +0.55, –0.1, –1.20, and +0.55 W m^{-2} for OLR, TSI, RSW, and total net flux, respectively. With the exception of RSW, these global annual averaged anomalies are within the corresponding 2-sigma interannual variability (Table 2.7) for this period. The 2-sigma anomaly in the RSW relative to climatology indicates significant variability that could

be indicative of cloud and/or snow/ice changes. More analysis is needed to attribute the source of the variability.

The global monthly mean anomaly time series of TOA fluxes (Fig. 2.44) reveal that the global monthly mean OLR anomaly remained mostly positive throughout 2019. The OLR anomalies in 2019 began with a value of +0.10 W m^{-2}, reached +0.77 W m^{-2} in March, dropped to −0.10 W m^{-2} in June, then mostly increased each month for the rest of the year. It ended the year with a very large positive OLR anomaly (~ +1.62 W m^{-2}). This large December OLR anomaly is consistent with the values obtained from the NOAA HIRS OLR (Lee and NOAA CDR Program 2011) and NASA AIRS OLR (Susskind et al. 2012) dataset. The global monthly mean absorbed shortwave (TSI − RSW) anomaly remained entirely positive during 2019, and the magnitudes of this anomaly were larger than the corresponding OLR anomaly. The absorbed shortwave anomaly began with a value of +0.58 W m^{-2}, oscillated around the value of +1.0 W m^{-2} throughout the year, reached its maximum value of +1.71 W m^{-2} in October, ending the year with a value of +1.40 W m^{-2}. For the year as a whole, the 2019 global annual mean absorbed shortwave anomaly was +1.1 W m^{-2}. The global monthly mean total net anomaly, which is calculated from the absorbed shortwave anomaly minus the OLR anomaly, began 2019 with a value of +0.48 W m^{-2}, remained positive throughout the year, reached a maximum value of +1.51 W m^{-2} in October, and ended the year with a value of −0.22 W m^{-2}. The positive absorbed shortwave anomalies in 2019 dominated the negative effect of the OLR anomaly and resulted in the positive 2019 global annual mean total net anomaly of +0.55 W m^{-2}. This was the sixth consecutive year that the TOA global annual mean total net anomaly was positive relative to climatology. Long-term trend analyses that include the last two months of the merged dataset are discouraged because of the natural fluctuation in ERB components, uncertainty from the data merging process, and potential for drift in the FLASHFlux product.

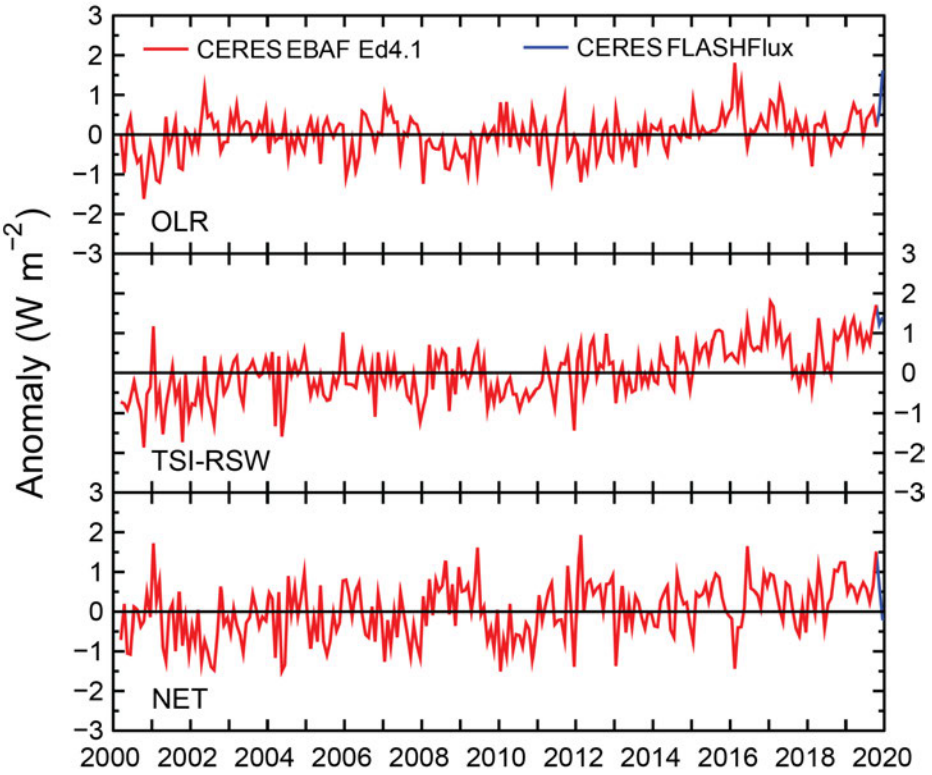

Fig. 2.44. Time series of global monthly mean deseasonalized anomalies (W m^{-2}) of TOA Earth radiation budget for OLR (upper), absorbed shortwave (TSI–RSW; middle), and total net (TSI–RSW–OLR; lower) from Mar 2000 to Dec 2019. Anomalies are relative to their calendar month climatology (2001–18). Time series shows the CERES EBAF Ed4.1 1° data (Mar 2000–Oct 2019) in red and the CERES FLASHFlux version 3C data (Nov–Dec 2019) in blue; see text for merging procedure. (Sources: https://ceres-tool.larc.nasa.gov/ord-tool/jsp/EBAF41Selection.jsp and https://ceres-tool.larc.nasa.gov/ord-tool/jsp/FLASH_TISASelection.jsp.)

The TSI data used in this study are provided by the Total Irradiance Monitor aboard the Solar Radiation and Climate Experiment (SORCE) mission (Kopp and Lean 2011) and the Royal Meteorological Institute of Belgium composite dataset (Dewitte et al. 2004), both renormalized to the SORCE Version 15. The RSW and OLR data were obtained from the CERES mission (Wielicki et al. 1996, 1998) aboard *Terra* and *Aqua* spacecraft.

The time series (Fig. 2.44) were constructed from the CERES EBAF (Energy Balanced And Filled) Ed4.1 product (Loeb et al. 2009, 2012, 2018) for March

2000–October 2019 and from the CERES Fast Longwave and Shortwave Radiative Fluxes (FLASH-Flux) version 3C product (Kratz et al. 2014) for November–December 2019. The normalization of the FLASHFlux data (Stackhouse et al. 2016) results in 2-sigma monthly uncertainties of ±0.42, ±0.08, ±0.22, and ±0.52 W m^{-2} for the OLR, TSI, RSW, and total net radiation, respectively. Global annual averaged maps were normalized on a region-by-region basis for November and December 2019.

2) Mauna Loa clear-sky "apparent" solar transmission—J. A. Augustine, K. O. Lantz, J.-P. Vernier, and H. Telg

Apparent solar transmission has been measured at the Mauna Loa Observatory in Hawaii by NOAA's Global Monitoring Division and its predecessors since the International Geophysical Year in 1958. It is the longest record of its kind. Because the observatory is in a pristine environment, elevated far above the marine boundary layer, the Mauna Loa apparent transmission is an effective proxy for stratospheric aerosol loading, although it is affected each spring by perennial tropospheric Asian dust events (Bodhaine et al. 1981). It has been used primarily to track background stratospheric aerosols and the decay of volcanic plumes that had been injected into the stratosphere. Other studies have examined the influence of water vapor, ozone, and the Quasi-Biennial Oscillation (QBO) on the transmission at Mauna Loa (Dutton et al. 1985; Dutton and Bodhaine 2001; Dutton 1992).

Figure 2.45 presents monthly averages of the apparent transmission through December 2019 in time series along with a locally weighted scatterplot smoothing (LOWESS) fit smoothed with six-month filter. The high frequency variability of the fit reveals the springtime minimum each year as dust from Asia passes over. The cleanest extended period of the record is its first five years prior to the Agung eruption (Indonesia, 1963–64). After the recovery from Agung, that level of "background" stratospheric cleanliness, delineated by the horizontal dotted line in Fig. 2.45, has only been achieved for brief periods. The largest anomalies are from the eruptions of El Chichón (Mexico, 1982) and Mt. Pinatubo (Philippines, 1991), for which minimum transmissions of 0.80 and 0.82, respectively, were realized. Recoveries from those events lasted five to six years. About five years after the stratosphere recovered from the effects of Pinatubo, a series of medium-scale volcanic events, some of which were at high latitudes (Vernier et al. 2011; Andersson et al. 2015), impacted the stratosphere over Mauna Loa. Their combined effect was a small downward trend in transmission of –0.001 $decade^{-1}$ from 2002 through 2012 (large shaded area in Fig. 2.45) that is consistent with a reported increase in stratospheric aerosols of 4%–7% per year during the first half of the period (Hofmann et al. 2009). The anchor of that small trend is the effect from the plume of the Nabro eruption (Eritrea, June 2011) that lasted through 2012. The largest anomaly after Pinatubo was when transmission values of 0.90 and 0.91 in March and April of 2009 matched the maximum effect from Agung. Mt. Redoubt

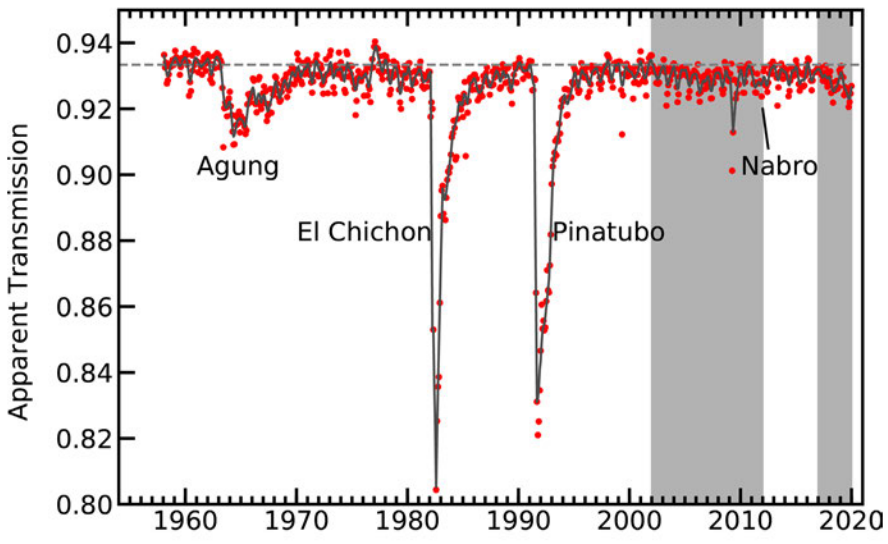

Fig. 2.45. Time series of the clear-sky apparent transmission at MLO, Hawaii, for 1958–2019. Red circles represent monthly means. The gray curve is a six-month smoothed LOWESS fit to the time series. The horizontal dotted line represents the mean pre-Agung "background" transmission from 1958 to 1962 (0.934). Major events that impacted the transmission record are labeled, and shaded areas are relevant to the discussion.

(Alaska) erupted in March 2009 and did reach the stratosphere, but trajectories show that its plume did not escape the high latitudes. Because this short-term anomaly was not seen by the Mauna Loa stratospheric lidar, tropospheric events may be responsible for the observed reduction in transmission. Kilauea (~32 km east of Mauna Loa) was highly active during that period, and effluent from its lava flowing into the sea ~40 km southeast of Mauna Loa and strong Asian dust events are both evident in satellite imagery (https://worldview.earthdata.nasa.gov) during those two months.

After the effect from Nabro subsided in 2012, the transmission over Mauna Loa was relatively high through 2016. However, since 2017 the transmission has been generally decreasing (small shaded area in Fig. 2.45). The initial decrease in 2017 may be from Asian dust, but the decrease in the latter half of that year is likely due an active wildfire season and associated pyro-thunderstorm activity in British Columbia and the northwestern United States. Those events lofted smoke into the stratosphere that was observed by CALIPSO, SAGE III, and surface-based lidars in France into 2018 (Khaykin et al. 2018). The minimum transmission in September 2019 is very likely associated with the Raikoke eruption on the Kuril Islands on 22 June 2019, which was larger than Sarychev (Kuril Islands, 2009) and Nabro. Balloon measurements in Virginia on 4 October 2019, three months after the eruption, show the Raikoke plume residing in the lower stratosphere between 15 and 25 km above ground level. A combination of the CALIPSO space-borne lidar and a trajectory model (Vernier et al. 2013) shows the plume over Hawaii on that day, and as of January 2020 it was still significantly impacting the composition of the stratosphere (see Fig. SB2.5).

The observatory is located near the top of the Mauna Loa volcano on the island of Hawaii at 3400 m above mean sea level. "Apparent transmission" is calculated from the ratio of solar beam measurements at two fixed solar elevations (Ellis and Pueschel 1971), which is mathematically equivalent to a traditional vertical column transmission calculation. For this application, representative daily transmissions are computed as the mean of three such ratios from pyrheliometer measurements at solar pathlengths of 2, 3, 4, and 5 atmospheres. To avoid contamination from afternoon upslope winds, only morning measurements are used. This method minimizes error because neither the calibration of the pyrheliometer nor the solar intensity at TOA are needed, resulting in a precise time series back to 1958. The monthly product reported is the average of all acceptable clear-sky morning transmissions of a particular month.

g. Atmospheric composition

1) Long-lived greenhouse gases—X. Lan, B. D. Hall, G. Dutton, J. Mühle, and J. W. Elkins

Increases in atmospheric greenhouse gas burdens, especially the long-lived greenhouse gases (LLGHGs) carbon dioxide (CO_2), methane (CH_4), and nitrous oxide (N_2O), are mainly the result of human activity since the industrial revolution and largely responsible for increasing global temperature (IPCC 2013).

The atmospheric pre-industrial abundance of CO_2 is estimated to be ~278 ppm (parts per million by moles in dry air), based on air extracted from ice in Greenland and Antarctica (Etheridge et al. 1996). Systematic measurements of atmospheric CO_2 began at Mauna Loa, Hawaii (MLO), in 1958, when the atmospheric CO_2 abundance was about 315 ppm. In 2019, annually averaged CO_2 at MLO reached 411.4 ± 0.1 ppm (all uncertainties are 68% confidence intervals), while globally averaged CO_2 at Earth's surface was 409.8 ± 0.1 ppm (Fig. 2.46a).

Annual growth in global mean CO_2 has risen steadily from 0.6 ± 0.1 ppm yr^{-1} in the early 1960s to an average of 2.3 ppm yr^{-1} during 2009–18, with large interannual variability (Fig. 2.46a). The increase in global mean CO_2 from 2018 to 2019 was 2.5 ± 0.1 ppm (Table 2.8).

Variations in the atmospheric CO_2 show the changing imbalance between its emissions and sinks. From 1850 to 2018, 440 ± 20 Pg C (1 Pg C = 10^{15} g C) were emitted as CO_2 from fossil fuel burning (Friedlingstein et al. 2019). For 2018 alone, global fossil fuel emissions reached 10 ± 0.5 Pg C yr^{-1} for the first time in history (Friedlingstein et al. 2019). About half of the CO_2 emitted

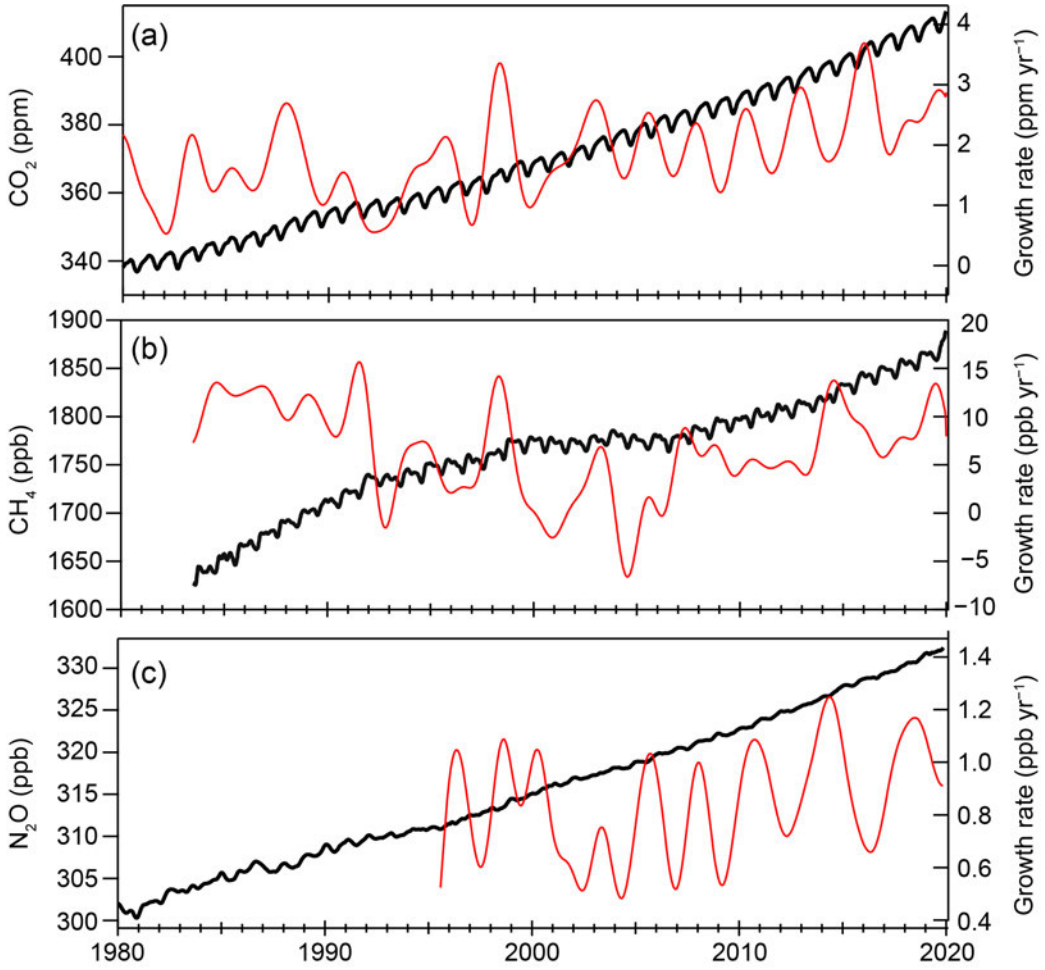

Fig. 2.46. Global monthly mean dry-air surface mole fractions (black) of (a) CO_2, (b) CH_4, and (c) N_2O derived from the NOAA air-sampling network. Instantaneous growth rates (red), calculated as time-derivatives of deseasonalized trend curves (see Dlugokencky et al. 1994b for methods), are shown on the right axis (insufficient and noisy N_2O data prior to 1995 hinder calculation of a growth rate).

Table 2.8. Summary table of long-lived greenhouse gases for 2019 (CO_2 mixing ratios are in ppm, N_2O and CH_4 in ppb, and all others in ppt).

Industrial designation or common name	Chemical formula	Radiative efficiency (W m^{-2} ppb^{-1})[a]	Radiative forcing (W m^{-2})	Mean surface mole fraction, 2019 (change from prior year)[b]	Lifetime (years)
Carbon Dioxide	CO_2	1.37×10^{-5}	2.08	409.8 (2.5)	—
Methane	CH_4	3.63×10^{-4}	0.52	1866.6 (9.2)	9.1
Nitrous Oxide	N_2O	3.00×10^{-3}	0.20	331.9 (1.0)[c]	123
Chlorofluorocarbons					
CFC-11	CCl_3F	0.26	0.059	226.5 (–1.6)[c]	52
CFC-12	CCl_2F_2	0.32	0.161	501.5 (–4.2)[c]	102
CFC-113	CCl_2FCClF_2	0.30	0.021	69.7 (–0.6)[c]	93
Hydrochlorofluorocarbons					
HCFC-22	$CHClF_2$	0.21	0.052	246.8 (2.7)	11.9
HCFC-141b	CH_3CCl_2F	0.16	0.004	24.4 (0.0)	9.4
HCFC-142b	CH_3CClF_2	0.19	0.004	22.0 (0.0)	18

(cont.) Table 2.8. Summary table of long-lived greenhouse gases for 2019 (CO_2 mixing ratios are in ppm, N_2O and CH_4 in ppb, and all others in ppt).

Industrial designation or common name	Chemical formula	Radiative efficiency (W m^{-2} ppb^{-1})[a]	Radiative forcing (W m^{-2})	Mean surface mole fraction, 2019 (change from prior year)[b]	Lifetime (years)
Hydrofluorocarbons					
HFC-134a	CH_2FCF_3	0.16	0.017	107.8 (5.8)	14
HFC-152a	CH_3CHF_2	0.10	<0.001	6.9 (0.0)	1.6
HFC-143a	CH_3CF_3	0.16	0.004	23.8 (1.6)	51
HFC-125	CHF_2CF_3	0.23	0.007	29.1 (3.1)	30
HFC-32	CH_2F_2	0.11	0.002	19.2 (2.8)	5.4
HFC-23	CHF_3	0.18	0.006	32.5 (1.3)	228
HFC-365mfc	$CH_3CF_2CH_2CF_3$	0.22	< 0.001	1.01 (0.04)	8.9
HFC-227ea	CF_3CHFCF_3	0.26	< 0.001	1.56 (0.14)	36
Chlorocarbons					
Methyl Chloroform	CH_3CCl_3	0.07	< 0.001	1.6 (–0.3)	5.0
Carbon Tetrachloride	CCl_4	0.17	0.013	78.4 (–0.8)[c]	32
Methyl Chloride	CH_3Cl	0.01	< 0.001	546.5 (1.4)	0.9
Bromocarbons					
Methyl Bromide	CH_3Br	0.004	< 0.001	6.56 (–0.06)	0.8
Halon 1211	$CBrClF_2$	0.29	0.001	3.25 (–0.10)	16
Halon 1301	$CBrF_3$	0.30	0.001	3.28 (0.01)	72
Halon 2402	$CBrF_2CBrF_2$	0.31	< 0.001	0.40 (–0.01)	28
Fully fluorinated species					
Sulfur Hexafluoride	SF_6	0.57	0.006	9.96 (0.35)	> 600
PFC-14	CF_4	0.09	0.005	85.5 (0.9)	~ 50000
PFC-116	C_2F_6	0.25	0.001	4.85 (0.09)	~ 10000
PFC-218	C_3F_8	0.28	< 0.001	0.69 (0.03)	~ 2600
PFC-318	c-C_4F_8	0.32	< 0.001	1.76 (0.07)	~ 3200

[a]Radiative efficiencies and lifetimes were taken from Appendix A in WMO (2018), except for SF_6 lifetime from Ray et al. (2017), CH_4 lifetime from Prather et al. (2012). For CO_2, numerous removal processes complicate the derivation of a global lifetime. AGGI = Annual Greenhouse Gas Index. For radiative forcing, see https://www.esrl.noaa.gov/gmd/aggi/aggi.html

[b]Mole fractions are global, annual surface means for the indicated calendar year determined from the NOAA cooperative global air sampling network (Hofmann et al. 2006), except for PFC-14, PFC-116, PFC-218, PFC-318, and HFC-23, which were measured by AGAGE (Mühle et al., 2010; Miller et al., 2010). Changes indicated in brackets are the differences between the 2019 and 2018 means. All values are preliminary and subject to minor updates.

[c]Global mean estimates derived from multiple NOAA measurement programs ("Combined Dataset").

since 1850 remains in the atmosphere. The rest of it has partially dissolved in the world's oceans where it has made seawater ~30% more acidic (as indicated by [H^+], Tans 2009), with potential impacts on marine life. While the terrestrial biosphere is currently also a sink for fossil fuel CO_2, the cumulative emissions of CO_2 from land use changes such as deforestation cancel terrestrial uptake over the 1850–2018 period (Friedlingstein et al. 2019). While emissions of CO_2 from fossil fuel combustion drive its increasing atmospheric burden, the large interannual variability in CO_2 growth rate is mostly driven by terrestrial exchange of CO_2 influenced by changing meteorology; for example, the strong El Niño that peaked in late 2015 contributed to a strong global CO_2 increase of 3.0 ppm yr^{-1} (Betts et al. 2016). The connection between meteorology and terrestrial CO_2 exchange is under investigation, as an important step to understand climate feedbacks. For example, regionally, enhanced carbon uptake by North American ecosystems during the 2015 El Niño was suggested to be due to increased water availability and favorable temperature conditions (Hu et al. 2019).

The global mean CH_4 abundance at Earth's surface increased from 722 ± 15 ppb (parts per billion) in 1750 to 1866.6 ± 0.9 ppb in 2019 (Fig. 2.46b). The growth rate of CH_4 varies decadally and interannually. A stabilization in CH_4 burden was observed during 1999–2006 after a large rise in the 1980s and 1990s, followed by a period of rapid increase since 2007. The increase in global mean CH_4 from 2018 to 2019 was 9.2 ± 0.9 ppb, which is among the three largest annual increases (with 2014 and 2015) since 2007. The drivers behind the changing CH_4 growth rates are still being debated, mainly due to the complexity and uncertainty in the atmospheric CH_4 budget. Although total global emissions of CH_4 are well-constrained by the current network of atmospheric measurements and an estimate of its lifetime (Dlugokencky et al. 2011), the magnitude and trend in emissions from individual sources and trends in CH_4 atmospheric lifetime are still uncertain. The sources of atmospheric CH_4 are from anthropogenic (50%–65%) and natural origins (Saunois et al. 2016). The CH_4 loss process is atmospheric oxidation, mainly through reaction with the short-lived (~1 second lifetime) hydroxyl radical (OH), which is poorly constrained by observations. Other processes are destruction by bacteria in soils and reaction with chlorine radicals in the atmosphere, both of which are highly uncertain. The large variability in the CH_4 growth rate results predominantly from changes in emissions from wetlands and biomass burning driven by meteorology, but it has also been affected by volcanic eruptions (Banda et al. 2013; Dlugokencky et al. 1994) and fossil fuel emissions (Dlugokencky et al. 1998). Measurements of CH_4 abundance and its isotopic composition suggest the drivers behind the post-2006 rise are mainly increased emissions from biogenic sources and from natural and/or anthropogenic origins (Nisbet et al. 2019; Schaefer et al. 2016; Schwietzke et al. 2016), while a decrease in biomass burning and a small increase in fossil fuel emissions (Worden et al. 2017) can also play a minor role. Some studies have proposed a significant role of increased shale gas emissions from the United States (Franco et al. 2016; Hausmann et al. 2016; Helmig et al. 2016) in the past decade, but Lan et al. (2019) argue that this assertion is inconsistent with CH_4 measurements from aircraft and tall towers from NOAA's North American Network.

Nitrous oxide (N_2O) is an ozone-depleting LLGHG (Ravishankara et al. 2009) mainly produced from natural and agriculture soils, animal manure (Davidson 2009), and from the oceans. The observed increase in atmospheric N_2O over its preindustrial level (at 270 ppb) is mostly caused by nitrogen-containing fertilizers and manure used for agriculture (Davidson 2009). Atmospheric N_2O has been increasing steadily throughout the industrial era except for a brief period in the

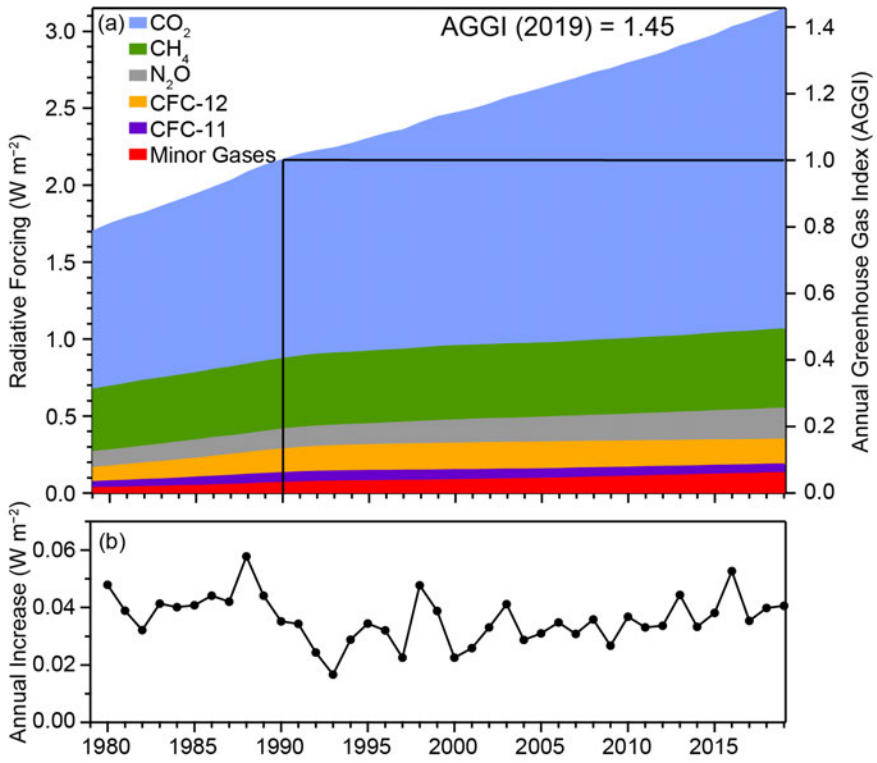

2.47. (a) Direct radiative forcing (W m^{-2}) due to five major LLGHG and 15 minor gases (left axis) and the associated values of the NOAA AGGI (right axis). The five major LLGHG include CO_2, CH_4, N_2O, CFC-11, and CFC-12. The 15 minor gases consist of halogenated gases (CFC-113, CCl_4, CH_3CCl_3, HCFCs 22, 141b and 142b, HFCs 134a, 152a, 23, 143a, and 125, SF_6, and halons 1211, 1301 and 2402). (b) Annual increase in direct radiative forcing referenced to 1990 (solid black line).

1940s (MacFarling Meure et al. 2006; Thompson et al. 2019). The mean global atmospheric N_2O abundance in 2019 was 331.9 ± 0.1 ppb, an increase of 1.0 ± 0.2 ppb from 2018 (Fig. 2.46c). This 1.0 ppb increase in the annual mean is similar to the average annual increase over 2009–18 (1.0 ± 0.2 ppb) but larger than the average annual increase over 1995–2008 (0.8 ± 0.2 ppb).

The impacts of these LLGHGs on global climate is estimated by their abilities to change the global radiative energy. Compared with preindustrial times, increasing atmospheric CO_2 has increased radiative forcing by > 2.0 W m^{-2}. The increase in CH_4 has contributed to a 0.51 W m^{-2} increase in direct radiative forcing while the CH_4-related production of tropospheric ozone (O_3) and stratospheric water (H_2O) also contributes to ~ 0.30 W m^{-2} indirect radiative forcing (Myhre et al. 2014). NOAA's Annual Greenhouse Gas Index (AGGI; Fig. 2.47) summarizes trends in the combined direct radiative forcing by CO_2, CH_4, N_2O, CFC-11, CFC-12, and 15 minor gases (Table 2.8; Hofman et al. 2006). This index represents the annual cumulative radiative forcing of these gases relative to the Kyoto Protocol baseline year of 1990. The 2019 AGGI was 1.45, suggesting a 45% increase in radiative forcing since 1990 (combined radiative forcing in 2019 was 3.14 W m^{-2}). While the atmospheric burdens of some greenhouse gases such as chlorofluorocarbons have declined in recent decades (Fig. 2.48), the combined radiative forcing of LLGHGs has increased each year (Fig. 2.47). Year-to-year variations in the AGGI increment correspond roughly with variability in CO_2, since CO_2 is responsible for about 65% of radiative forcing by LLGHGs and its rate of increase during 2014–19 accounts for 82% of total increase in radiative forcing (Fig. 2.46).

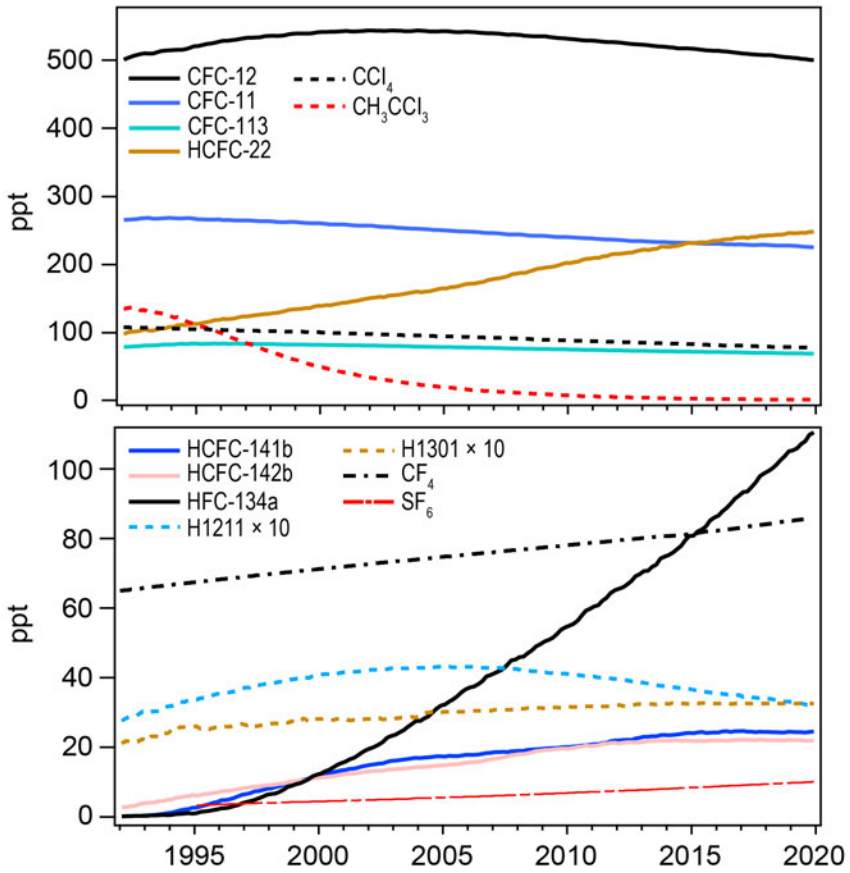

Fig. 2.48. Global mean mole fractions at Earth's surface (ppt; dry air) for several LLGHG, many of which also deplete stratospheric ozone. See Table 2.8 for the 2019 global mean mole fractions of these and other gases.

2) Ozone-depleting substances—B. D. Hall, S. A. Montzka, G. Dutton, B. R. Miller, and J. W. Elkins

Halogenated gases, such as CFCs and HCFCs, influence climate directly through radiative forcing and indirectly by contributing to stratospheric ozone depletion (Karpechko et al. 2018). The emissions and atmospheric abundances of most ozone depleting substances (ODS) are declining as expected due to controls implemented in the Montreal Protocol (Engel et al. 2018). By mid-2019, tropospheric CFC-11 and CFC-12 declined 15% and 7.5% from their maximum abundances in the mid-1990s and early 2000s, respectively (see Fig. 2.48). However, CFC-11 has not been declining as fast after 2012, likely indicating a resumption of production, in violation of the Montreal Protocol (Montzka et al. 2018a; Rigby et al. 2019), which banned production for emissive use starting in 2010. Global CFC-11 emissions, derived from atmospheric data, were 13%–25% higher during 2014–16 compared to 2008–12 (Montzka et al. 2018a). The globally averaged decline in CFC-11 from 2018 to 2019 (1.6 ppt; Table 2.8) is slightly larger than in previous years (Hall et al. 2019), although the significance of this difference and the influence of potential emission changes and atmospheric processes (Ray et al. 2020) on these recent observations have not yet been determined.

Atmospheric abundances of HCFCs, which are replacements for CFCs, increased as CFC production was phased out. In recent years the rates of increase of HCFC-22, HCFC-141b, and HCFC-142b have slowed (Fig. 2.48). In fact, globally averaged abundances of HCFC-141b and HCFC-142b did not change between 2018 and 2019 (Table 2.8). Substitutes for HCFCs, known as HFCs, do not deplete ozone, but do contribute to radiative forcing. Abundances of many HFCs are increasing at rates of several percent per year, although as a group their contribution to current forcing is still small relative to that from ozone-depleting gases (~11%; Montzka et al. 2018b). Of the HFCs, HFC-134a contributes most to radiative forcing (17 mW m^{-2} in 2019). Its abundance increased by 5.8 ppt from 2018 to 2019, which is similar to the average increase (5.6 ppt yr^{-1}) since 2010.

Equivalent effective stratospheric chlorine (EESC) is a measure of the ozone-depleting potential of the stratospheric halogen loading at a given time and place. EESC is calculated from global average surface mole fractions of long-lived ozone-depleting gases and weighting factors that include surface-to-stratosphere transport times, mixing during transit, photolytic reactivity, and ozone-destruction efficiency (Montzka et al. 1996; Newman et al. 2007). EESC is typically calculated for two regions that differ in total available reactive halogen: the Antarctic and the midlatitude stratosphere (Fig. 2.49). EESC is larger in the Antarctic compared to the midlatitudes because a larger fraction of ODSs are converted into reactive halogen as they are transported to the Antarctic. Even though the abundances of CFCs are decreasing, their contribution to EESC is still substantial because of their long atmospheric lifetimes (Table 2.8). In contrast, the contribution

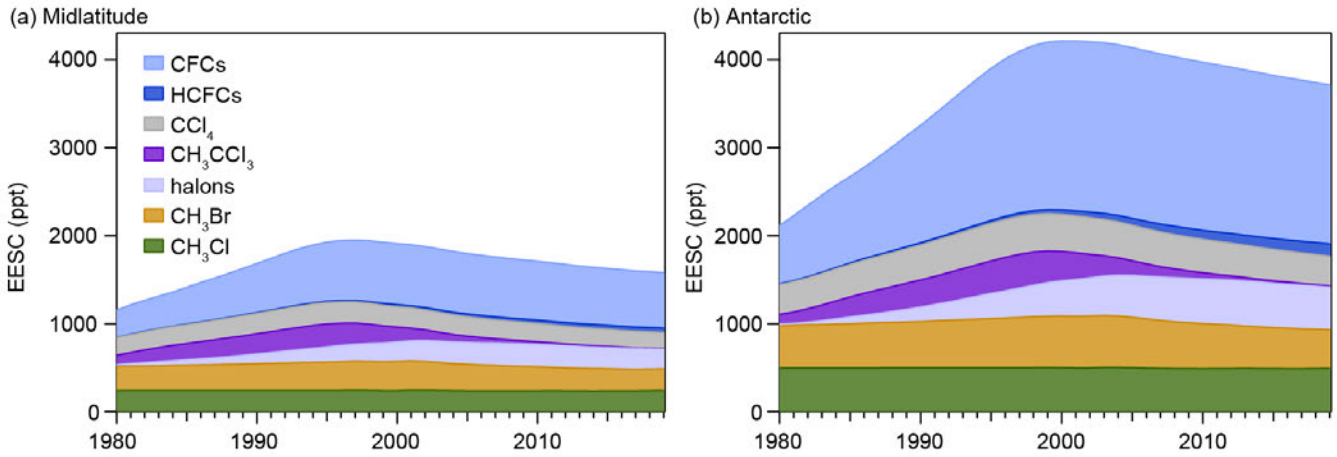

Fig. 2.49. EESC for the midlatitude and Antarctic stratosphere derived from NOAA surface measurements of long-lived ODSs, supplemented with data from the WMO A1 scenario (Carpenter et al. 2018). EESC values correspond to Jan of each year. In this context, Antarctic and midlatitude represent regions of the stratosphere having a mean age-of-air equal to 5.5 and 3 years, respectively.

of methyl chloroform (CH_3CCl_3) to EESC is now very small because emissions have decreased to near zero and its lifetime is relatively short (five years).

By the beginning of 2019, EESC decreased to 3710 ppt and 1575 ppt in Antarctic and midlatitude regions, respectively. These represent 22% and 47% reductions from the peak values in EESC over Antarctica and the midlatitudes, respectively, toward the 1980 benchmark values (see also www.esrl.noaa.gov/gmd/odgi/). EESC is expected to return to 1980 benchmark levels around 2050 in the midlatitudes and around 2075 in the Antarctic (Carpenter et al. 2018).

3) Aerosols—S. Rémy, N. Bellouin, Z. Kipling, M. Ades, A. Benedetti, and O. Boucher

Atmospheric aerosols play an important role in the climate system by scattering and absorbing radiation, and by affecting the life cycle, optical properties, and precipitation activity of clouds. Aerosols also represent a serious public health issue in many countries, and hence are subject to monitoring and forecasting as part of air quality policies.

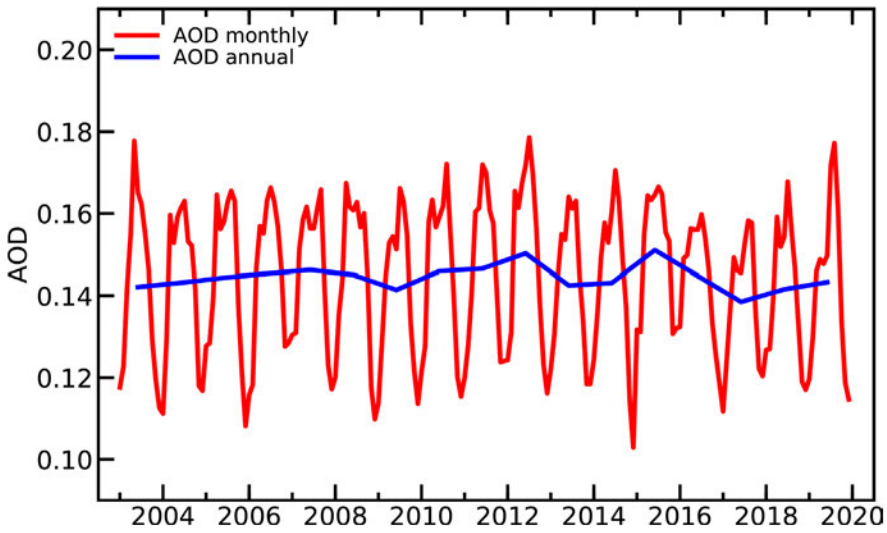

Fig. 2.50. Globally averaged total AOD at 550 nm over monthly (red) and annual (blue) periods for 2003–19.

The Copernicus Atmosphere Monitoring Service (CAMS) runs a near-real time global analysis of aerosols and trace gases. The CAMS project also produced a reanalysis of global aerosols and trace gases that covers the years 2003–19, named the CAMS reanalysis (CAMSRA; Inness et al. 2019) by combining state-of-the-art numerical modeling and aerosol remote-sensing retrievals from MODIS (Levy et al. 2013) and the Advanced Along Track Scanning Radiometer (AATSR; Popp et al. 2016). Other reanalysis products, such as MERRAero (Buchard et al. 2016), are also available. Verification of aerosol optical depth (AOD) at 550 nm against independent AERONET observations shows that the CAMS reanalysis has a smaller bias and error than its predecessors, the CAMS interim reanalysis (Flemming et al. 2017) and the Monitoring Atmospheric Composition and Climate (MACC) reanalysis (Inness et al. 2013). This section uses data exclusively from the CAMS reanalysis.

The time series of monthly and yearly globally averaged total AOD during 2003–19 (Fig. 2.50) shows strong seasonality, driven mainly by dust episodes between March and July in the Sahara, Middle East, and Taklimakan/Gobi and seasonal biomass burning in Africa, South America, Indonesia, and other regions. There is no significant trend over the period, but extreme events such as the September–October 2015 fires over Indonesia associated with El Niño are prominent. The summer maximum was very pronounced in 2019 mainly because of the large fires in July and August, particularly over Alaska, Siberia, and in the Amazon basin.

The AOD climatology between 2003 and 2019 (Fig. 2.51a) is marked by high values over the highly populated regions of India and China, mainly caused by anthropogenic emissions. High AOD over the Sahara and Middle East is primarily from dust, while the maxima over central Africa, Indonesia, the Amazon basin, and parts of Siberia are caused by fire emissions. The high values over Hawaii and close to Mexico City are a known artefact of the CAMS reanalysis related to volcanic outgassing.

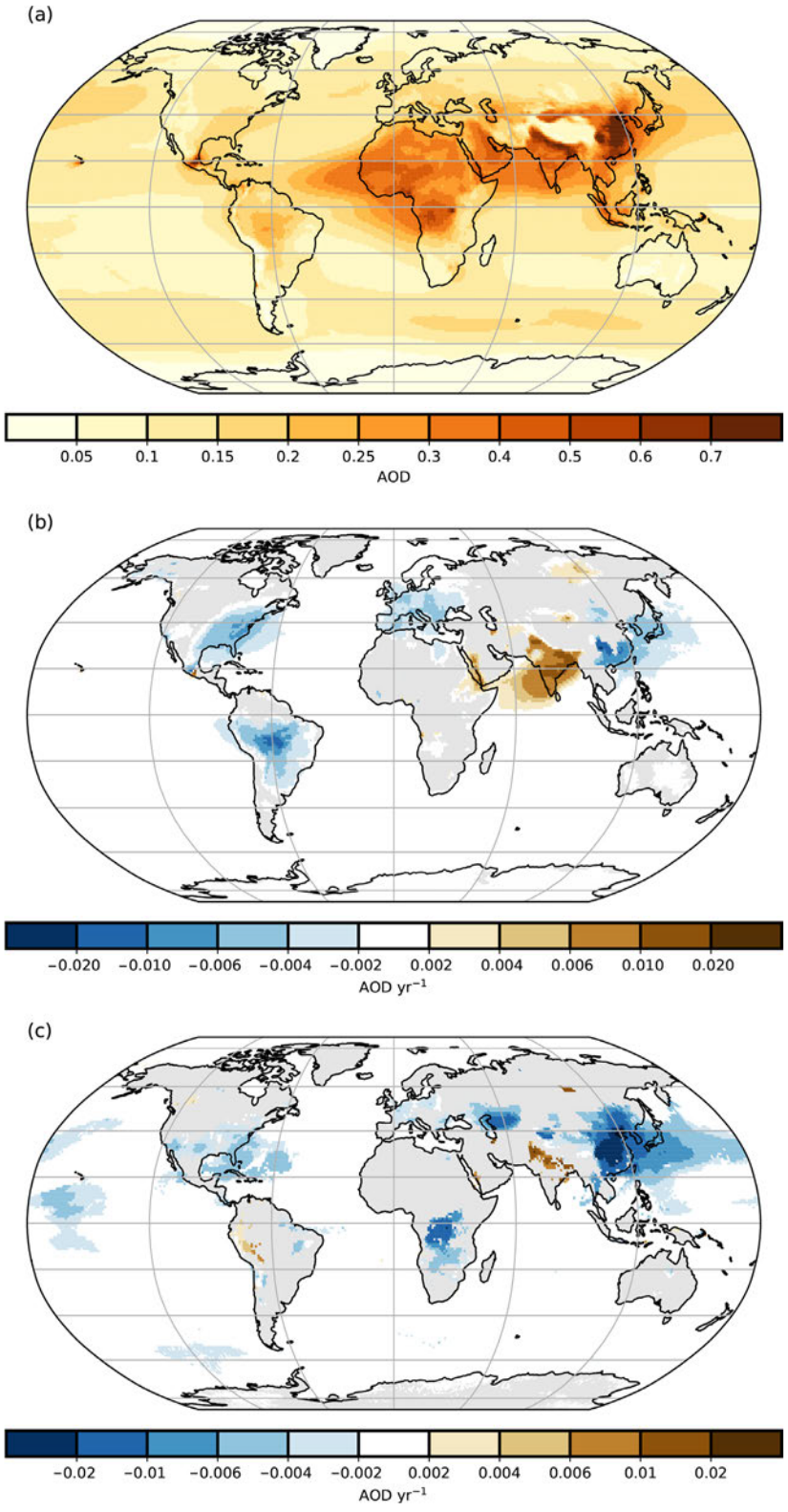

Fig. 2.51. (a) Total AOD at 550 nm averaged over the period 2003–19. Note the regional differences, with much greater total AOD values over parts of northern Africa, the Arabian Peninsula, southern Asia, and eastern China. Linear trends of total AOD (AOD yr^{-1}) for (b) 2003–19 and (c) 2012–19. Only trends that are statistically significant (95% confidence) are shown. Color scales have been constructed to highlight trends.

As compared to the 2003–18 average from the CAMS reanalysis, 2019 saw negative anomalies of total AOD over most of the United States, Europe, and Africa, as well as China, Korea, Japan, and parts of the Amazon basin (Plate 2.1x), although AOD in the last was significantly higher than in 2018. The negative anomalies over Brazil, the United States, Europe, and China are part of a longer trend over these regions, as shown in Fig. 2.51b. Figure 2.51c indicates that the trend is much more negative over China for 2012–19 than for 2003–19, which is consistent with the observed decrease in industrial sulfur dioxide (SO_2) emissions driven by tighter emission standards (Karplus et al. 2018). The 2012–19 trends are not significant over much of the Amazon basin, showing that most of the decrease in AOD occurred before 2012. The negative anomaly over the Sahel and Sahara (Plate 2.1x) was caused by reduced dust production in 2019, while the negative anomaly over most of west Africa is explained by a less active biomass burning season than usual there.

Positive anomalies of total AOD in 2019 (Plate 2.1x) are found in the southern part of the Arabian Peninsula, Iran, Pakistan, northern India, and parts of Iran, caused by more active dust production over these regions. The positive anomaly over the Indian subcontinent corresponds to a long-term trend of increasing anthropogenic emissions (Satheesh et al. 2017), as shown in Figs. 2.51b,c. Positive anomalies (Plate 2.1x) were also caused by extreme fires, such as over Alaska, northern Canada, and large parts of Siberia during boreal summer, and over Australia and Indonesia from October to December. Some of these events even led to the injection of aerosol in the stratosphere (see Sidebar 2.2). The drought that provoked the increased occurrence of fires over southeastern Australia and Indonesia was caused in part

by a strong anomaly of the Indian Ocean dipole (IOD), the main cause of extreme droughts over Australia (Ummenhofer et al. 2009). The exceptional severity of the Australian fires is highlighted in Plate 2.1y, which shows the number of days with daily AOD at 550 nm above 99.9% of the daily record between 2003 and 2018. Sidebar 7.6 discusses these fires in more detail.

Radiative forcing resulting from aerosol–radiation (RFari) and aerosol–cloud interactions (RFaci) for the period 2003–19 is shown in Fig. 2.52, as estimated using the methods described in Bellouin et al. (2020). The year 2019 was close to the long-term average in terms of both RFari and RFaci. Time series indicate no statistically significant trends in aerosol radiative forcing because the radiative impact of decreasing trends over Europe, North America, and China is offset by increasing trends over India. Evaluating trends remains statistically challenging because of large uncertainties in the estimates, which are mostly due to lack of knowledge of the anthropogenic fraction of the aerosol and its radiative forcing efficiency.

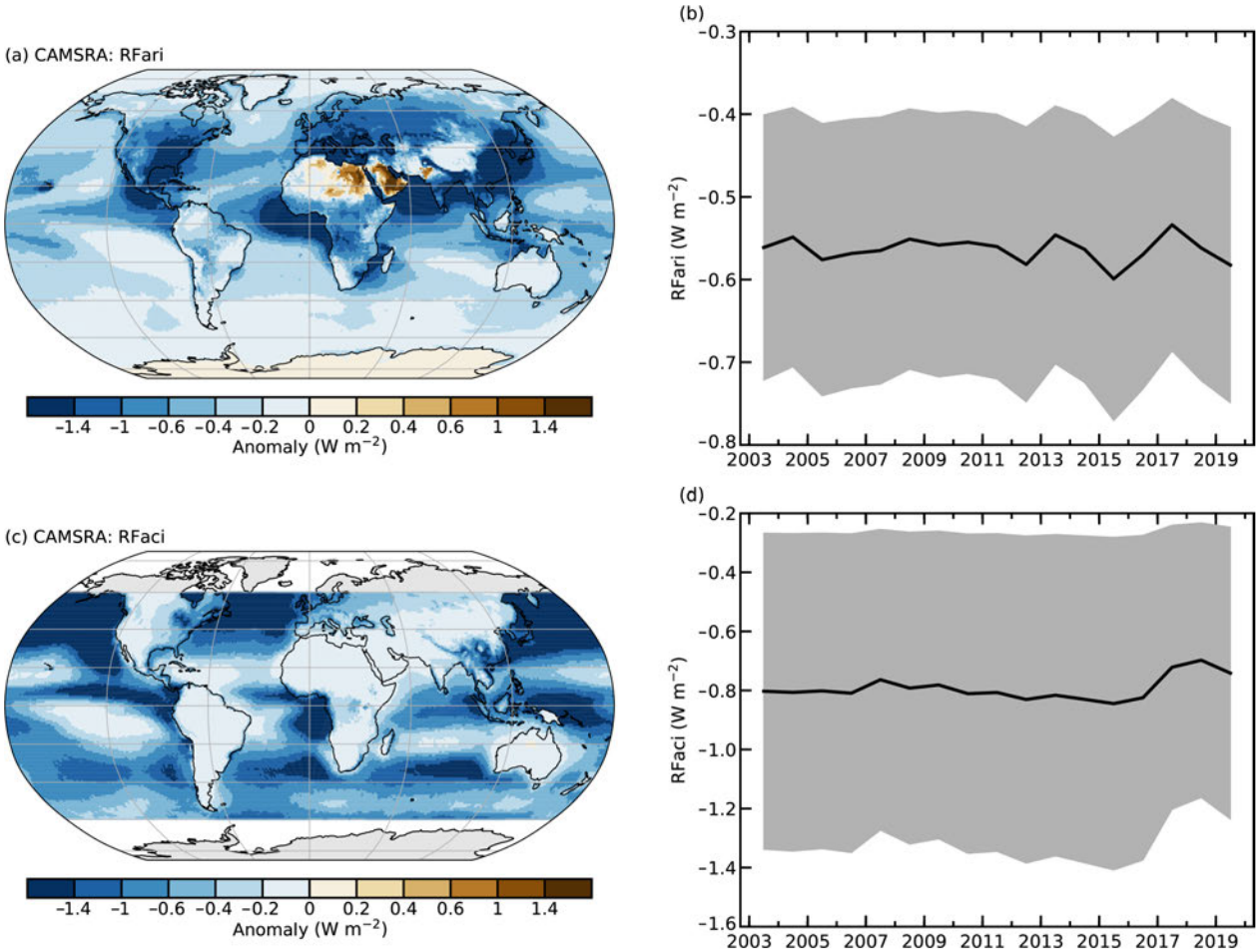

Fig. 2.52. Radiative forcing in the shortwave spectrum of (a), (b) aerosol-radiation (RFari) and (c), (d) aerosol-cloud interactions (RFaci) for 2003–19. The left column shows the average distribution. The right column shows time series of global averages, with the uncertainties of these estimates shown in gray.

4) Stratospheric ozone—M. Weber, W. Steinbrecht, C. Arosio, R. van der A, S. M. Frith, J. Anderson, M. Coldewey-Egbers, S. Davis, D. Degenstein, V. E. Fioletov, L. Froidevaux, D. Hubert, C. S. Long, D. Loyola, A. Rozanov, C. Roth, V. Sofieva, K. Tourpali, R. Wang, and J. D. Wild

The ozone layer that protects the biosphere from the harmful effects of ultraviolet radiation (UV) resides in the stratosphere. The total ozone column, with its main contributions from lower stratospheric ozone, determines how much UV reaches the surface. Over recent decades, changes in the upper stratospheric ozone have shown the clearest signs of ozone recovery due to the phasing out of ODSs since the late 1980s, following the Montreal Protocol (section 2g2). The total ozone

column annual mean anomaly distribution for 2019 in Plate 2.1z shows opposite behavior in the two hemispheres. While the Southern Hemisphere (SH) shows positive anomalies with respect to the long-term mean, steadily increasing towards the South Pole and over Australia, negative anomalies cover most of the Northern Hemisphere (NH) with some positive values, mostly at high

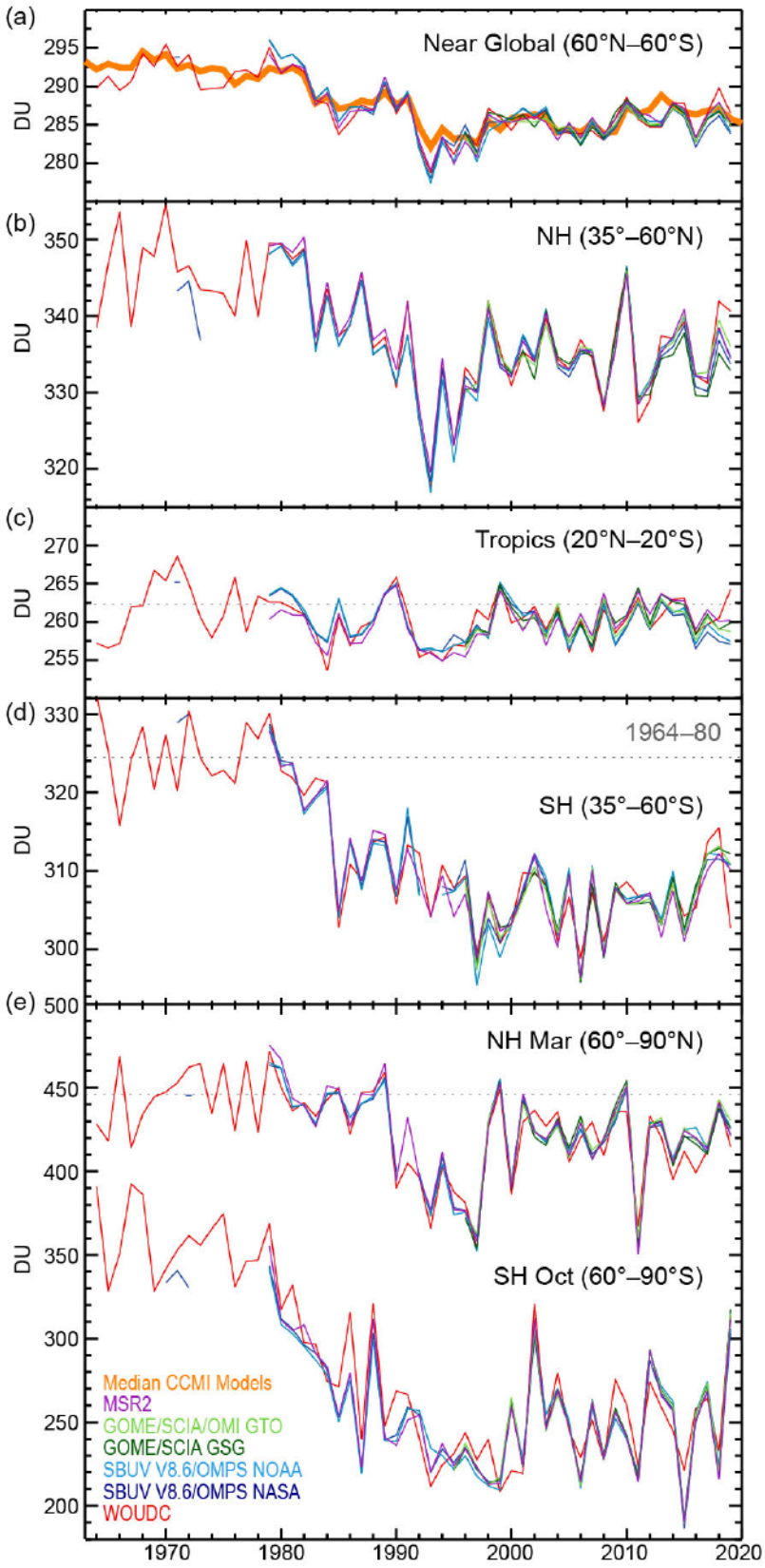

Fig. 2.53. Time series of annual mean total ozone (DU) in (a)–(d) four zonal bands, and (e) polar (60°–90°) total ozone in Mar (NH) and Oct (SH), the months when polar ozone losses usually are largest. Data are taken from WOUDC (World Ozone and Ultraviolet Radiation Data Centre) ground-based measurements combining Brewer, Dobson, SAOZ (Système D'Analyse par Observations Zénithales), and filter spectrometer data (red; Fioletov et al. 2002; 2008); the BUV/SBUV/SBUV2 V8.6/OMPS merged products from NASA (MOD V8.6, dark blue; Frith et al. 2014, 2017) and NOAA (light blue; Wild and Long, pers. comm., 2019); the GOME/SCIAMACHY/GOME-2 products GSG from University of Bremen (dark green; Weber et al. 2018) and GTO from ESA/DLR (light green, Coldewey-Egbers et al. 2015; Garane et al. 2018). MSR-2 (purple) assimilates nearly all ozone datasets after corrections with respect to the ground data (van der A et al. 2015). All six datasets have been bias corrected by subtracting averages for the reference period 1998–2008 and adding back the mean of these averages. The dotted gray lines in each panel show the average ozone level for 1964–80 calculated from the WOUDC data. The thick orange lines shows the average from chemistry-climate (CCMI) model runs (Eyring et al. 2013; Morgenstern et al. 2017; WMO 2018; SPARC/IO3C/GAW 2019). All observational data for 2019 are preliminary.

northern latitudes. Total ozone levels vary from year to year, depending on the dynamical state of the global atmosphere mainly determined by El Niño–Southern Oscillation (ENSO) and the Quasi-Biennial Oscillation (QBO). Both ENSO and the QBO are tropical phenomena that have a strong influence on the Brewer-Dobson circulation (BDC) determining the global stratospheric ozone distribution (e.g., Diallo et al. 2018; Olsen et al. 2019). Throughout 2019, the QBO was in its west phase, which generally leads to higher total ozone in the inner tropics and lower ozone in the subtropics and beyond (Plate 2.1z). The extended regions of below-average total ozone at low to middle NH latitudes are possibly linked to the weak ENSO condition in 2019 (Olsen et al. 2019). A major feature of 2019 is the very weak stratospheric SH winter polar vortex, a very small ozone hole (see Sidebar 6.1), and above-average total ozone at high southern latitudes during austral winter/spring as well as in the annual mean (Plate 2.1z). During the 2019 Antarctic winter/spring season, a stratospheric warming event, which is rare in the SH but frequent in the NH, strongly perturbed the polar vortex. A persistent weak polar vortex in winter/spring, as in 2019, is associated with a stronger hemispheric BDC, occurring usually during west QBO phases, that leads to more ozone being transported into middle to high latitudes throughout much of the SH. In addition, higher polar winter stratospheric temperatures also reduce polar chemical ozone loss (e.g., Weber et al. 2011). As a consequence, annual mean total ozone in 2019 was fairly high, by up to 65 DU above the long-term average, at high southern latitudes (Plate 2.1z).

Figure 2.53 displays the annual mean total column ozone time series from various merged datasets for the near-global (60°N–60°S) average, tropics, extratropics, and selected months in the polar regions. In October 2019, the SH polar cap total ozone (Fig. 2.53e) was as high as in 2002 and 1988, both years characterized by high dynamical activity and perturbed winter vortices (Schoeberl et al. 1989; Sinnhuber et al. 2003) and about 100 DU above the value in October 2015, a year with substantial polar ozone loss (Solomon et al. 2016). On the global scale (Fig. 2.53a), total ozone mean values in 2019 were lower than the previous year but within the variability observed during the last two decades. The same is true for the NH midlatitudes and the tropics (Figs. 2.53b,c) while midlatitude SH values were above the post-1990 average (Fig. 2.53d). In Fig. 2.53a, the median of 17 climate-chemistry model CCMI runs are also shown (Eyring et al. 2013; Morgenstern et al. 2017; WMO 2018; SPARC/IO3C/GAW 2019). The agreement of the observations with models that account for changes in ODS and greenhouse gases gives strong evidence that total ozone is on its slow path of recovery. However, in 2019 and previous years, the global ozone means from observations, as well from the CMI models, are still about 3% below the average from the period 1964–1980, when ODS levels were low.

Figure 2.54 shows ozone changes at two different altitudes, in the upper stratosphere (panels a–c, 42 km altitude) and in the lower stratosphere (panels d–f, 22 km). Ozone in the upper stratosphere shows the larger decline due to ODS increases until the late 1990s (WMO 2018). This large decline was stopped as a result of measures mandated in the international Montreal Protocol to phase-out ODS. Since about 2000, we have been in a phase of slow ozone recovery. In 2019, ozone values in the upper stratosphere were above the 1998–2008 average. In the lower stratosphere, long-term ozone variations are dominated by meteorological variations and transport (e.g., Chipperfield et al. 2018). Figures 2.54d–f show no clear sign of ozone increases in the lower stratosphere over the last 20 or so years. In 2019, the lower stratospheric values were at the lower end of expectations (gray shaded area of model predictions) in the NH and tropical bands (Figs. 2.54d,e). The continuing tropical decline (20°N–20°S) has been linked to climate change-related acceleration of the meridional BDC (Ball et al. 2018; Chipperfield et al. 2018; WMO 2018). Large interannual variations, as well as uncertainties in the observational data records (spread between different datasets), make reliable detection of the expected small underlying trends rather difficult, especially in the lower stratosphere.

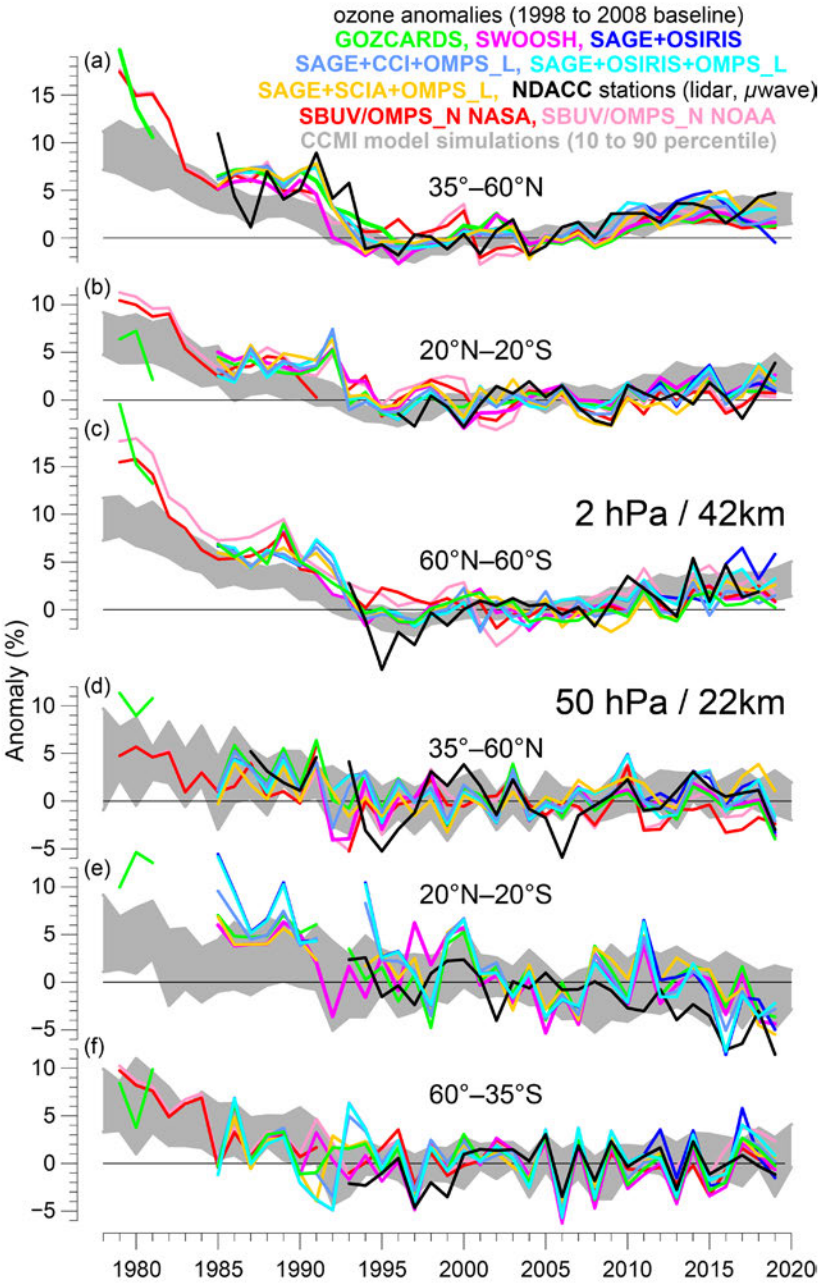

Fig. 2.54. Annual mean anomalies of ozone in the upper stratosphere (a)–(c) near 42 km altitude or 2 hPa pressure and in the lower stratosphere (d)–(f) near 22 km or 50 hPa, for three zonal bands: 35°–60°N, 20°N–20°S (tropics), 35°–60°S, respectively. Anomalies are referenced to the 1998–2008 baseline. Colored lines are for long-term records obtained by merging different limb (GOZCARDS, SWOOSH, SAGE+OSIRIS, SAGE+CCI+OMPS-L, SAGE+SCIAMACHY+OMPS-L) or nadir viewing (SBUV, OMPS-N) satellite instruments. Black line is from merging ground-based ozone records at seven NDACC stations employing differential absorption lidars and microwave radiometers. See Steinbrecht et al. (2017), WMO (2018), and Arosio et al. (2018) for details on the various datasets. Gray-shaded area shows the range of chemistry-climate model from CCMI (WMO 2018; SPARC/IO3C/GAW 2019; Dhomse et al. 2018). Ozone data for 2019 are not yet complete for all instruments and are still preliminary.

5) Stratospheric water vapor—S. M. Davis, K. H. Rosenlof, D. F. Hurst, H. Vömel, and H. B. Selkirk

Stratospheric water vapor (SWV) is a radiatively and chemically important trace gas with its variability strongly affected by the absolute humidity of air entering the stratosphere in the tropics, which is in turn largely determined by the temperature of the tropical cold point tropopause. Following 2018, a year in which lower stratospheric water vapor in the tropics dropped to a near-record low for the *Aura* Microwave Limb Sounder (MLS) satellite record (2004–19), water vapor abundance in the tropical lower stratosphere increased slightly during 2019 (Fig. 2.55). In January 2019, the *Aura* MLS monthly mean tropical (15°N–15°S) lowermost SWV anomaly (at 82 hPa, or ~17 km) was −0.6 ppm (parts per million, equivalent to a mole fraction of μmol mol^{-1}), about 20% below the 2004–19 January average. The tropical lower SWV anomaly transitioned to positive in April and remained between +0.3 and +0.4 ppm (within 10% of the average value for each month) for the remainder of the year (Fig. 2.55).

In general, the qualitative behavior of lowermost SWV observed by *Aura* MLS is consistent with balloon-borne frost-point hygrometer soundings at five locations (Fig. 2.56), although a small drift in MLS relative to the balloon measurements noted in earlier work persists (Hurst et al. 2016). The

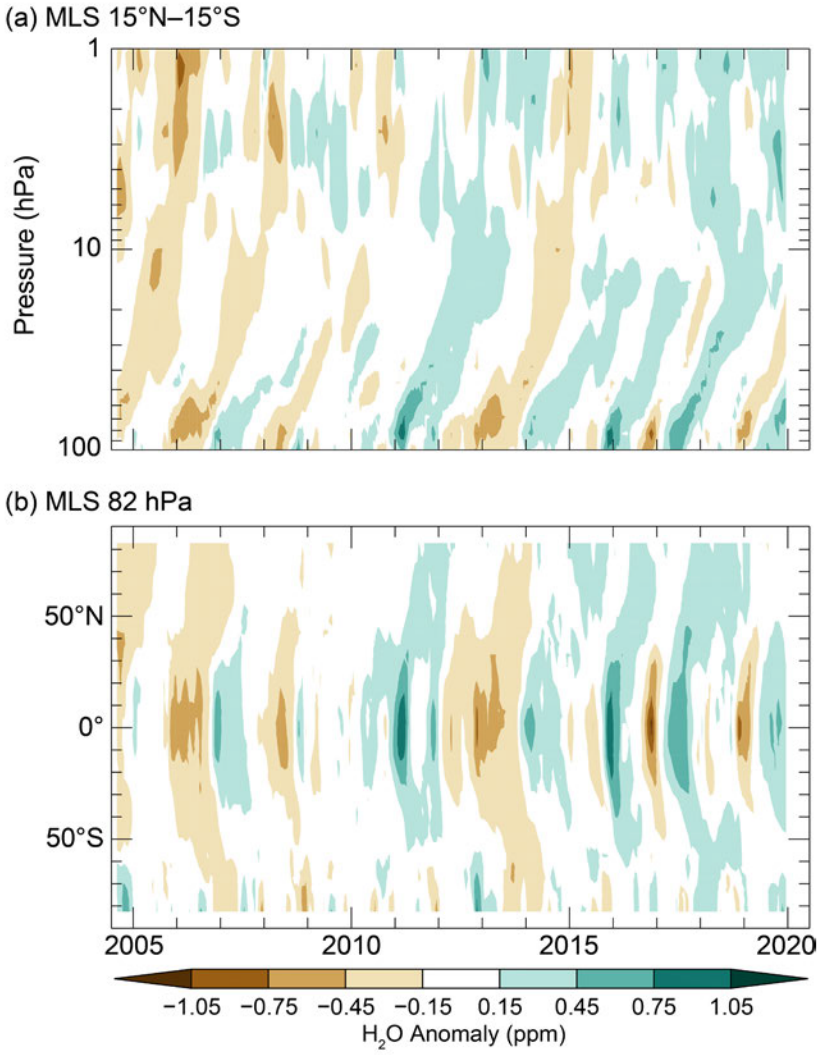

Fig. 2.55. (a) Time series of vertical profiles of tropical (15°N–15°S) SWV anomalies and (b) latitudinal distributions of SWV anomalies at 82 hPa. Both are based on *Aura* MLS data. Anomalies are differences from the mean 2004–19 water vapor mixing ratios (ppm) for each month. Panel (b) shows the propagation of tropical lower SWV anomalies to higher latitudes in both hemispheres as well as the influences of dehydrated air masses from the Antarctic polar vortex as they are transported toward the SH midlatitudes at the end of each year.

dry anomaly at San José, Costa Rica (10°N), at the start of 2019 propagates northward to progressively reach Hilo, Hawaii (20°N), Boulder, Colorado (40°N), and then Lindenberg, Germany (52°N), by mid-2019 (Figs. 2.55b, 2.56). In contrast, the dry anomaly was barely observed in the southern midlatitude records from MLS (Fig. 2.55b, Fig. 2.56e) and frost point hygrometers launched at Lauder, New Zealand (45°S, Fig. 2.56e). Similarly, the subsequent wet anomaly at San José starting in April 2019 propagates poleward and can be seen at Boulder by the end of the year.

At the tropical sites Hilo and San José, the seasonal and interannual variability of SWV is well correlated with variations in the cold-point temperature (CPT), as expected (Fig. 2.56d). Monthly mean tropical CPT anomalies increased from very cold at the beginning of 2019 (–1 K) to moderately warm at the end of the year (+0.5 K), congruent with the dry-to-wet transition in tropical lower SWV.

In general, interannual variations in CPTs are correlated with those observed in several modes of large-scale climate variability such as tropical lower stratospheric upwelling rates, an important part of the BDC, ENSO, and QBO in tropical stratospheric winds (Dessler et al. 2014). After January 2019, the QBO was in its westerly (warm) phase at 50 hPa. ENSO was in a weak El Niño phase for the first half of the year, followed by six months in its neutral phase. Reduced tropical upwelling due to the QBO westerly phase may have produced warming tropical tropopause temperatures and, therefore, the positive tropical lower SWV anomalies during the latter half of the year. Additionally, it is worth noting that the IOD was in its positive phase from May 2019 through the end of the year, including record-setting positive indices in October and November (see section 4h for details). It is unknown whether the IOD impacts SWV, but there is some indication of correlation between SWV and Indian Ocean sea surface temperatures (SSTs; Garfinkel et al. 2018).

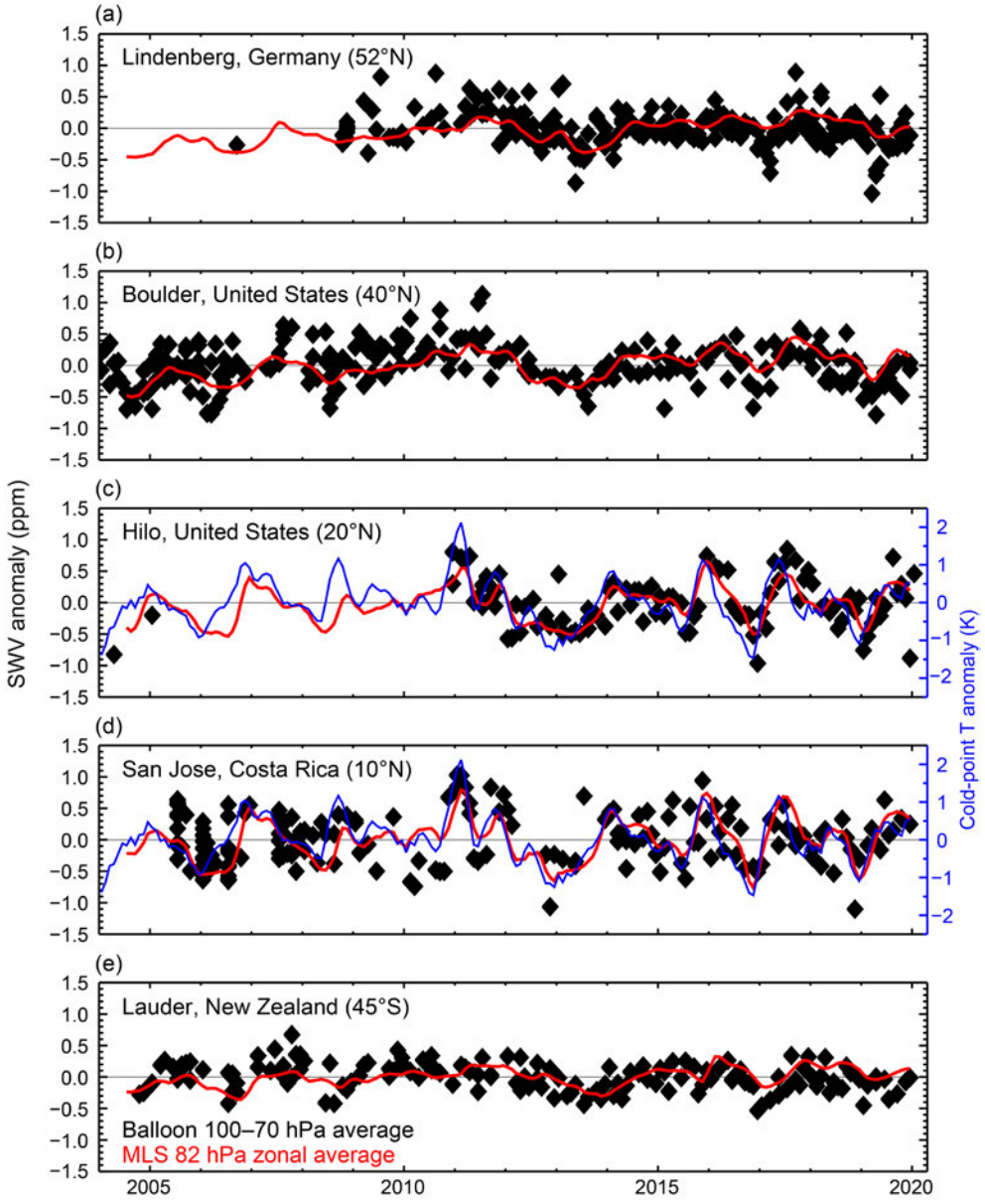

Fig. 2.56. Lower SWV anomalies over five balloon-borne frost-point (FP) hygrometer stations. Each panel shows the lower stratospheric anomalies of individual FP soundings (black) and of monthly zonal averages of MLS retrievals at 82 hPa in the 5° latitude band containing the FP station (red). High-resolution FP vertical profile data were averaged between 70 and 100 hPa to emulate the MLS-averaging kernel for 82 hPa. Each MLS monthly zonal mean was determined from 2000–3000 profiles. Anomalies for MLS and FP data are calculated relative to the 2004–19 period for sites except for Lindenberg (2009–19) and Hilo (2011–19). Tropical CPT anomalies based on the MERRA-2 reanalysis (d; blue curve), which are generally well correlated with the tropical lower SWV anomalies, are the driving force behind the variations in tropical SWV during 2019.

6) Tropospheric ozone—J. R. Ziemke and O. R. Cooper

The Intergovernmental Panel on Climate Change identifies tropospheric ozone as the third most influential greenhouse gas, following carbon dioxide and methane (IPCC 2013). Tropospheric ozone contributes to net warming of the atmosphere, with average global radiative forcing of 0.4 ± 0.2 W m^{-2}. While tropospheric ozone is a surface pollutant detrimental to human health and vegetation (Fleming et al. 2018; Mills et al. 2018), it is also the dominant producer of the hydroxyl radical (OH), the primary oxidant of pollutants in the troposphere. Sources for tropospheric ozone include ozone from the stratosphere and photochemical production from precursors in the troposphere including methane, volatile organic compounds, biogenic hydrocarbons, lightning NOx, and emissions generated from combustion of fossil fuels and biomass burning (Neu et al. 2014;

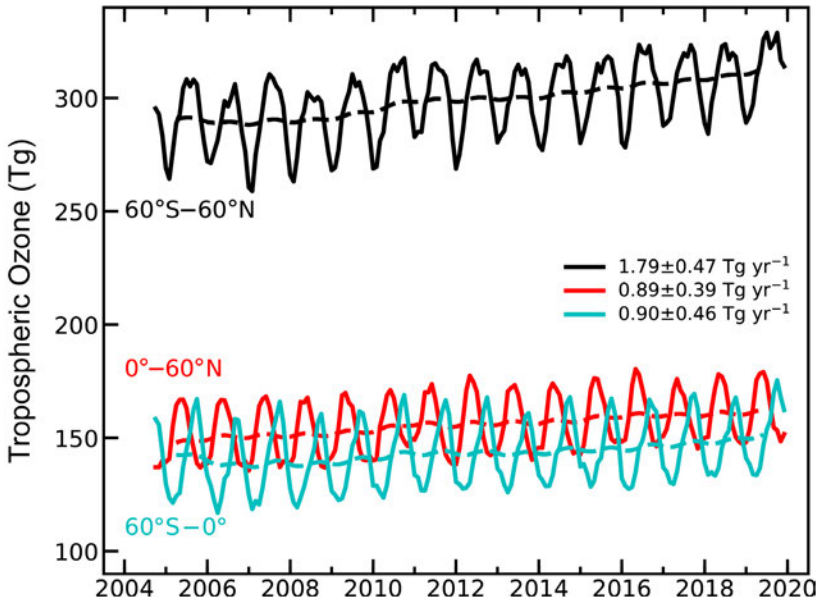

Fig. 2.57. Monthly averages of OMI/MLS tropospheric ozone burdens (Tg) from Oct 2004 through Dec 2019. The top curve (black) shows 60°N–60°S monthly averages (solid line) with 12-month running mean (dashed line). The bottom two curves show monthly averages (solid lines) and running means (dashed lines) for the NH (red) and SH (blue). Slopes of linear fits to the data are presented with their 95% confidence-level uncertainties. All three trends are deemed statistically significant at the 95% confidence level.

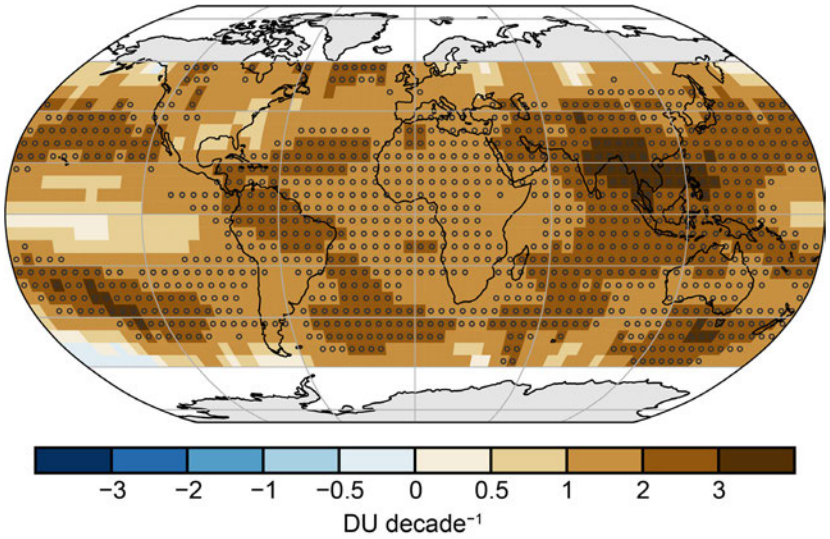

Fig. 2.58. Linear trends in OMI/MLS tropospheric column ozone (DU decade^{-1}) on a 5° × 5° grid from Oct 2004 through Dec 2019. Circles denote trends with *p*-values less than 0.05. Trends were calculated using a multivariate linear regression model (e.g., Randel and Cobb 1994, and references therein) that includes a seasonal cycle fit and the Niño 3.4 index as an ENSO proxy; trend uncertainties include autoregressive adjustment via Weatherhead et al. (1998).

Young et al. 2013, 2018; Monks et al. 2015). The main drivers of planetary-scale variability of tropospheric ozone include dynamical forcing from ENSO and the Walker circulation in the tropics, and baroclinic waves in midlatitudes (Chandra et al. 1998, 2009; Sun et al. 2014; Ziemke et al. 2015). Main drivers of small-scale patterns are largely dependent on local emissions of ozone precursors, both anthropogenic and natural, such as fossil fuel combustion and biomass burning. The high temporal and spatial variability of tropospheric ozone makes it difficult to determine decadal trends on regional or global scales based solely on in situ observations (Cooper et al. 2014; Lin et al. 2014; Barnes et al. 2016; Strode et al. 2019; Gaudel et al. 2018; Tarasick et al. 2019).

All *State of the Climate* reports since 2012 have provided updates on global tropospheric ozone based on independent measurements from ground- and satellite-based instruments (Ziemke and Cooper 2018). Due to limited spatial coverage and annual updates of ground-based observations, these reports have relied primarily on combined *Aura* Ozone Monitoring Instrument (OMI) and MLS satellite ozone measurements (Ziemke et al. 2019). OMI/MLS data show broad regions of positive 2019 tropospheric ozone column anomalies (relative to the 2005–18 average) of ~1.3 DU (4%) in the NH midlatitudes, with smaller anomalies of ~1 DU or less elsewhere (Plate 2.1aa). Hemispheric and global average tropospheric ozone burdens and their 95% confidence levels for 2019 were 162 ± 7 Tg (0°–60°N), 151 ± 8 Tg (0°–60°S), and 313 ± 8 Tg (60°N–60°S) (Fig. 2.57). Trends in hemispheric and global burdens from October 2004 through December 2019 indicate clear increases of ~0.6% yr^{-1}. Spatially, trends are overwhelmingly positive, the strongest of which are ~ +3.3 DU decade^{-1} (~ +1% yr^{-1}) above India and east/southeast Asia, extending eastward over

the North Pacific Ocean (Fig. 2.58). These trends are consistent with model estimates based on strengthening emissions of ozone precursors from southeast, east, and south Asia, primarily due to fossil fuel combustion (Zhang et al. 2016; Lin et al. 2017). The models indicate that ozone produced in these areas is transported eastward in the free troposphere over the North Pacific Ocean, supported by the trends in Fig. 2.58. Positive trends in the SH extra-tropics have been linked to a broadening of the Hadley circulation (Lu et al. 2018a).

Three long-term baseline monitoring sites, with quality-assured data, are available for updating surface ozone trends through 2019: 1) Mauna Loa Observatory (MLO), Hawaii (19.5°N, 155.6°W, 3397 m a.s.l.); 2) South Pole Observatory (SPO), Antarctica (90°S, 59°E, 2840 m a.s.l.); and 3) Barrow Atmospheric Baseline Observatory, Utqiaġvik, Alaska (71.3°N, 156.6°W, 11 m a.s.l.). Continuous measurements began at MLO in September 1973, at SPO in January 1975, and at Barrow in March 1973, with additional observations available at SPO for the years 1961–63 and at MLO for the years 1957–59 (Tarasick et al. 2019).

The limited data at MLO and SPO from the 1950s/1960s indicate that ozone at these remote high-elevation sites was similar in the mid-twentieth century despite being located in different hemispheres. Ozone at SPO has changed little since the exploratory measurements of the early 1960s, with only a slight increase of ~2 ppbv during the period of continuous measurements (1975–2019; Fig. 2.59). In contrast, ozone at MLO increased at the rate of 0.14 ± 0.05 ppbv yr^{-1}, resulting in a 17% (6.4 ppbv) increase since 1973. MLO experiences high inter-annual ozone variability due to its location in the transition region between tropical and extratropical air masses. The ozone trend in the extratropical air masses can be isolated by focusing on the dry air masses, which tend to originate at higher altitudes and latitudes to the west and northwest of MLO (Gaudel et al. 2018). The trend in the dry air masses (23%, or 9.9 ppbv, total increase since 1974) is 50% greater compared to the trend using all air masses, which implies that the site is influenced by ozone increases in upwind regions to the west and northwest, most likely Asia where surface and free tropospheric ozone has generally increased over the past two decades (Cohen et al. 2018; Lu et al. 2018b; Gaudel et al. 2018).

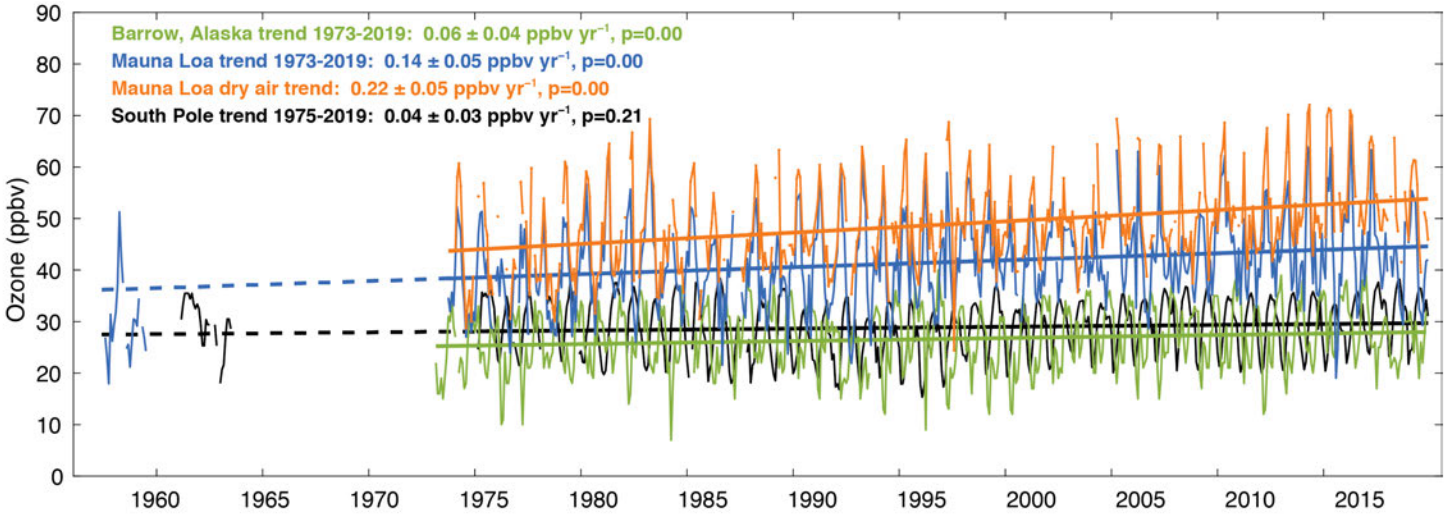

Fig. 2.59. Monthly median ozone at Utqiaġvik (Barrow), Alaska (Mar 1973–Dec 2019, green) and South Pole (Jan 1975–Dec 2019, black) using data from all hours of the day. Additional data from South Pole are shown for the early 1960s. Also shown are nighttime monthly median ozone values at MLO calculated with all available data for months with at least 50% data availability, Oct 1973–Dec 2019 (blue), with early observations from the late 1950s. MLO data are limited to nighttime observations to focus on free tropospheric air masses. In addition, the monthly median values associated with dry air masses (orange) at MLO are included (dewpoint < the climatological monthly 40th percentile, and a sample size of at least 24 individual hourly nighttime observations). Trends (solid straight lines) are based on least-squares linear regression fit through the monthly values (1970s–2019), and reported with 95% confidence intervals and *p*-values. The MLO and South Pole trend lines are extrapolated back in time to the late 1950s (dashed lines).

7) Carbon monoxide—J. Flemming, A. Inness, A. Crotwell, and G. Pétron

Carbon monoxide (CO) is a short-lived air pollutant with indirect impacts on climate forcing. CO is emitted by incomplete combustion sources and produced during the oxidation of methane and nonmethane hydrocarbons (Hartmann et al. 2013). In the troposphere CO has a lifetime of one to three months. It is destroyed mostly by hydroxyl radicals, OH, which are also the main sink for CH_4. Due to its short lifetime, atmospheric levels of CO reflect the distribution and seasonality of its sources and the OH sink.

Unusually strong wildfire activity in 2019, especially over Indonesia, eastern Siberia, Alaska, Amazonia, and Australia led to regional CO anomalies at the seasonal time scale, as shown in Plate 2.1ab, which is based on CAMS reanalysis. On the other hand, tropical and southern Africa, an area that generally has one of the largest contributions from fires to the global CO burden, did not have increased emission in 2019.

The most pronounced CO anomaly in 2019 appeared over Maritime Southeast Asia in autumn because of intense wildfires in the region, which were the third strongest since 2003. The fire-driven CO anomalies occurred against a background of a continually decreasing CO burden in the NH.

Figure 2.60a shows a time series of the monthly mean global burden of CO from the CAMS reanalysis for the period 2003–19 (Inness et al. 2019). Approximated with a linear trend over the whole period, the total global CO burden has declined by –1.7 Tg yr^{-1}, and as piecewise trends following Flemming and Inness (2018) for the periods 2003–07, 2008, and 2009–19 by –3.1, –14.0, and +0.1Tg yr^{-1}, respectively. The global CO burden in 2019 was similar to most years in the last decade, with the exception of 2015 when wildfires in Indonesia led to exceptionally large burdens. Clean marine boundary layer observations of CO are shown in Fig. 2.61. Background CO declined at an average rate of –1 ppb yr^{-1} in the NH temperate latitudes and –1.5 ppb yr^{-1} for latitudes north of 53°N (Novelli et al. 2003; Pétron et al. 2019). Based on measurements of Greenland firn air (old air trapped in perennial snowpack), this negative trend in the NH started in the 1970s or 1980s and is likely explained by decreasing anthropogenic CO emissions (Petrenko et al. 2013).

The spatial distribution of the 2019 CO anomalies with respect to the period 2003–19 is shown in Plate 2.1ab. Small negative anomalies of up to –5% were seen for most of the NH. 2019 was a year of increased fire activity in areas experiencing positive temperature anomalies and dry conditions. Intensive fire activity in Indonesia during September–November increased the CO burden in this region by up to 20 Tg, which was the third highest since 2003 after the two El Niño years 2006 and 2015 (Fig. 2.60b). Furthermore, unusually strong fires in Alaska, Siberia, and

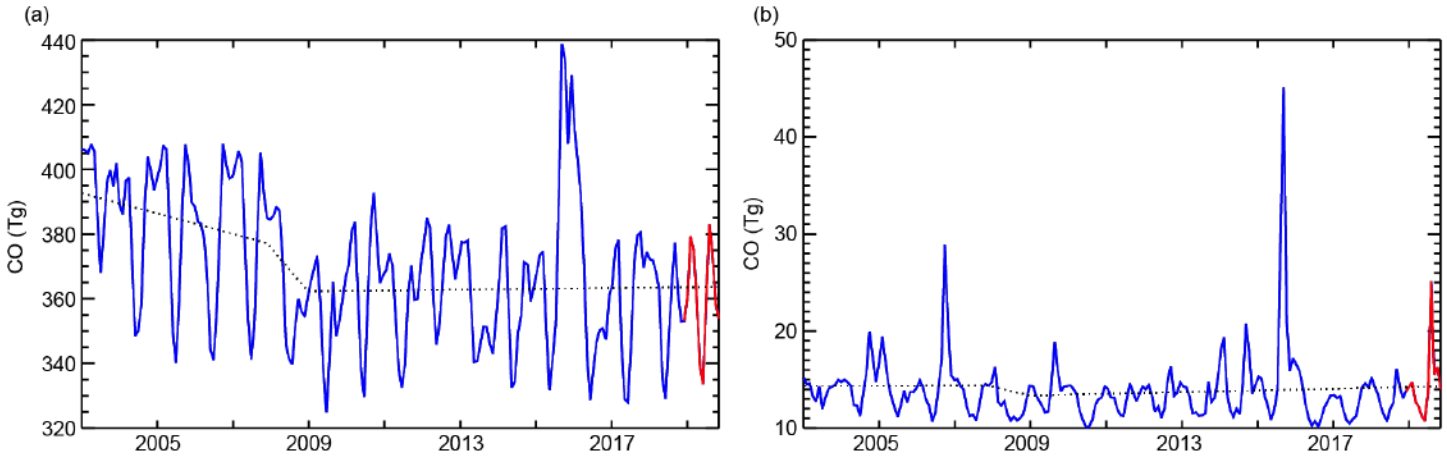

Fig. 2.60. Time series of monthly CO burdens (Tg) for (a) the whole globe and (b) over Maritime Southeast Asia from the CAMS reanalysis for 2003–19 (2019 is shown in red) and a piecewise linear trend (dotted line) for the periods 2003–07, 2008, and 2009–19.

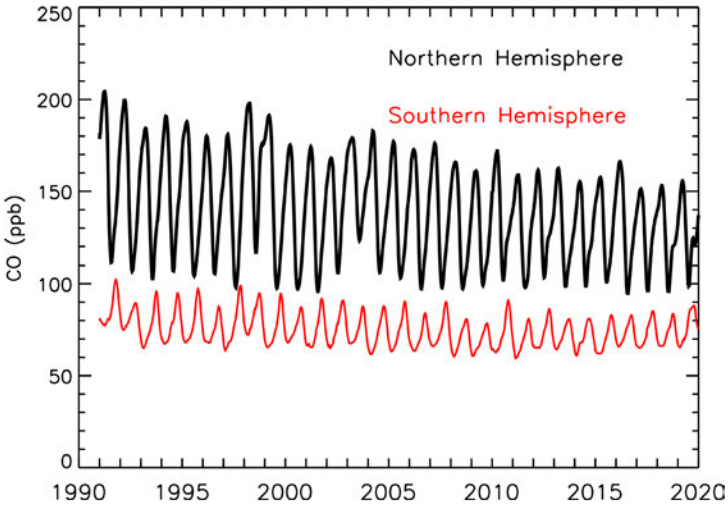

Fig. 2.61. Time series of surface CO (ppb) measured at 31 NOAA in situ flask observations sites and averaged over the clean marine boundary layer for the NH (0°–90°N, black) and SH (0°–90°S, red) for the period 1991–2019.

western South America in northern summer and in southwest (January 2019) and southeast (December 2019) Australia led to localized positive anomalies of up to 10% on the annual time scale and of more than 30% on the seasonal time scale, but which had insignificant impact on the global or hemispheric CO burdens.

The global CO burden since the early 2000s has been recorded by reanalyses of atmospheric composition, which assimilate CO satellite retrievals in chemistry transport modeling systems (Miyazaki et al. 2015; Flemming at al. 2017; Gaubert et al. 2017; Inness et al. 2019). The CAMS reanalysis assimilated TIR version 6 total column CO retrievals of the Measurement of Pollution in the Troposphere (MOPITT) instrument (Deeter et al. 2014) globally, only excluding observations poleward of 65°N/S using the ECWMF 4D-VAR data assimilation system. The CAMS reanalysis can be compared with independent CO column retrievals, xCO, at the ground-based Total Carbon Column Observing Network (TCCON) site, Park Falls, Wisconsin, for the 2003–19 period. At Parks Falls retrieved xCO decreased with a rate of −0.56 ppb yr^{-1}, and the CAMS reanalysis at a rate of −0.48 ppb yr^{-1} (Fig. 2.62). Park Falls was chosen to illustrate the quality of the CAMS reanalysis because it has the longest record, dating to 2004. More comprehensive validation of the CAMS reanalysis against TCCON data can be found in Inness et al. (2019).

Surface CO dry air mole fractions are measured using in situ sensors and discrete air analysis using flask samples. NOAA and its cooperative air-sampling partners have been monitoring CO levels since 1991 through a global network of remote surface sites (Novelli et al. 2003; Pétron et al. 2019). The long-term calibrated CO measurements are available through the WMO Global Atmospheric Watch Programme World Data Center for Greenhouse Gases (https://gaw.kishou.go.jp/).

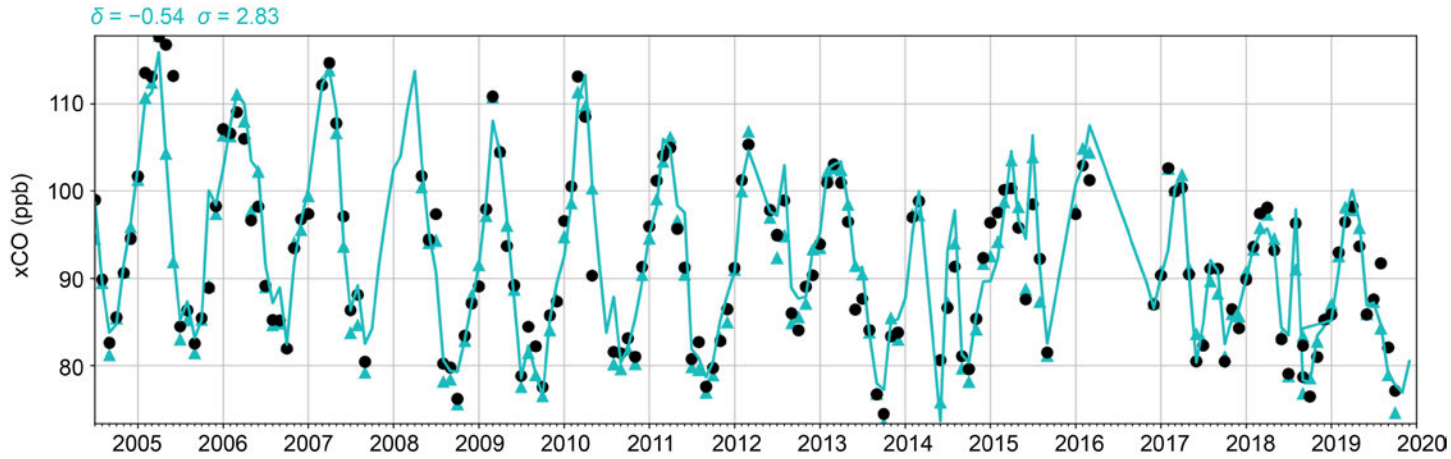

Fig. 2.62. Column-averaged CO (xCO, in ppb) at the Park Falls TCCON station. Monthly mean observations are shown by the black dots, and corresponding monthly mean xCO columns calculated using the TCCON-averaging kernels are shown by the blue triangles. The continuous blue line is the monthly xCO from the CAMS reanalysis.

Sidebar 2.2. **2019: A 25-year high in global stratospheric aerosol loading**—T. LEBLANC, F. CHOUZA, G. TAHA, S. KHAYKIN, J. BARNES, J.-P. VERNIER, AND L. RIEGER

The role of stratospheric aerosols in Earth's radiative budget and chemistry has long been recognized (Mitchell 1971; Robock 2000; Hofmann and Solomon 1989; Aquila et al. 2013). Their presence in the stratosphere is mainly driven by the injection from below of tropospheric aerosols and sulphur-containing compounds (e.g., sulfur dioxide [SO_2] and carbonyl sulfide [OCS]) that act as precursors for the formation of sulfuric acid droplets in the stratosphere. Explosive volcanic eruptions are the major source of stratospheric sulfur, but in volcanic quiescent periods, OCS and other non-sulfate compounds such as ash, black carbon, organic aerosols, and smoke particles from biomass burning contribute to the background stratospheric aerosol burden. The last major volcanic eruption that critically affected stratospheric aerosol loading was Mt. Pinatubo in 1991, which resulted in an estimated total mass injection of nearly 20 Tg, i.e., 30–60 times the estimated background content (Guo et al. 2004). As a result of the Pinatubo eruption, the global surface temperature was estimated to have decreased by 0.4°C after two years (Thompson et al. 2009). Stratospheric aerosol loading did not return to background levels until 1997, when nearly a decade of volcanic quiescence started. After this period, several eruptions moderately impacted the midlatitudes of both hemispheres between 2005 and 2012, and the Southern Hemisphere (SH) between 2012 and 2017. The past 2–3 years, however, have shown a break from the previous years, with several volcanic and biomass burning events that loaded the stratosphere with aerosol levels unprecedented since the Mt. Pinatubo era. Results from ground-based lidar and satellite measurements provide a fresh, near-real-time view of these recent events.

Ground-based data come from two lidars located at Mauna Loa (MLO; 19.5°N, 155.6°W), namely the Jet Propulsion Laboratory's (JPL) Mauna Loa Stratospheric Ozone Lidar (MLSOL; McDermid et al. 1995), and the NOAA Aerosol Lidar (Barnes and Hofmann 1997), which have monitored stratospheric aerosols for several decades for the global Network for the Detection of Atmospheric Composition Change (NDACC). The satellite data come from 1) GloSSAC v1.1, a merged dataset combining the measurements of SAGE and SAGE-II between 1979 and mid-2005, and OSIRIS and CALIPSO since 2005 (Thomasson et al. 2018), and 2) OMPS/LP (2012–present; Chen et al. 2018).

Figure SB2.4a shows a time–altitude cross-section of monthly-mean aerosol extinction at MLO derived from MLSOL. MLO is located in a region of stratospheric aerosol minimum, on the edge of the tropical reservoir and away from the main entry pathways (Tropical Tropopause Layer [TTL], Asian Summer Monsoon Anticyclone [ASMA], volcanoes, and wildfires), thus facilitating detection of background levels. The injection of aerosols from below is clearly characterized by transient plumes

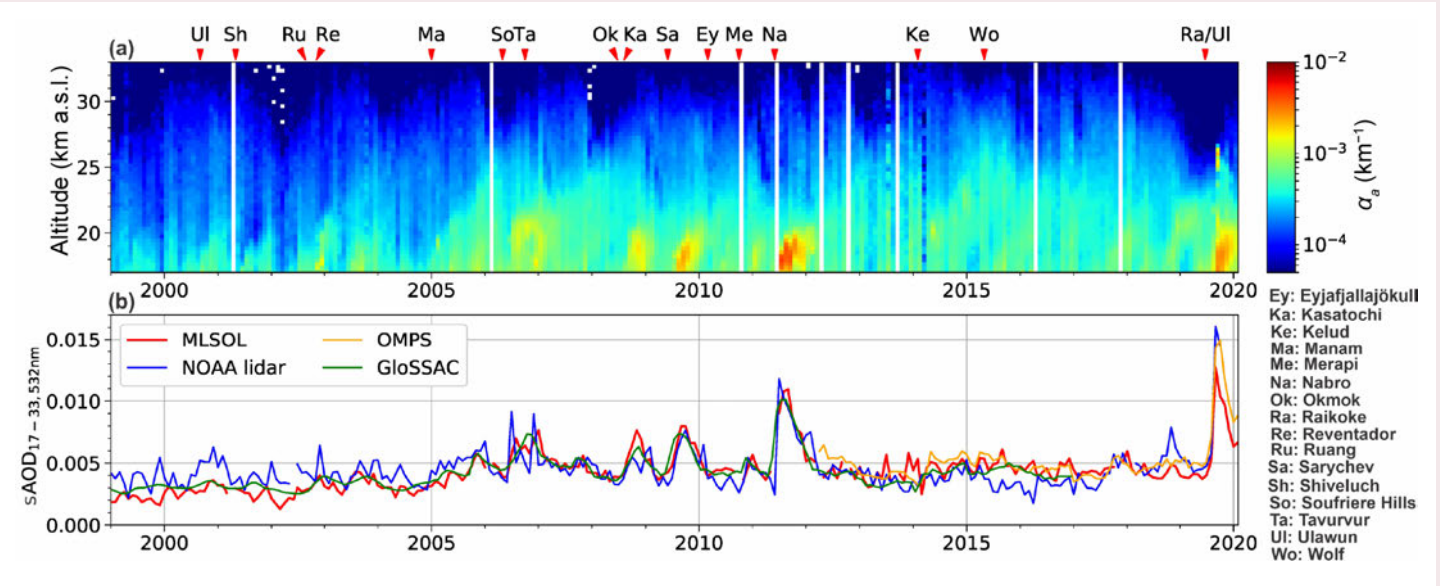

Fig. SB2.4. (a) Time–altitude cross-section of the monthly mean aerosol extinction profiles at MLO derived from the MLSOL lidar. (b) Time series of stratospheric aerosol optical depth (sAOD; 17–33 km) from the MLSOL lidar, NOAA lidar, GloSSAC at 17.5°N, and OMPS/LP near MLO (see text for coincidence criterion). Significant volcanic eruptions are denoted by red arrows and letters in (a). White lines represent gaps in the data.

spreading upwards with time, mostly visible below 23 km. The upward propagation speed depends on the timing of the injection (Vernier et al. 2011b; Trepte and Hitchman 1992) and roughly ranges between 3 and 6 km per year, consistent with Quasi-Biennial Oscillation- (QBO) modulated Brewer-Dobson circulation (BDC) ascent rates inferred from water vapor and CO measurements in the tropical lower stratosphere (Minschwaner et al. 2016).

The stratospheric aerosol optical depth (sAOD) time series (1999–present) derived from MLSOL, the NOAA lidar, Global Space-based Stratospheric Aerosol Climatology (GloSSAC; zonal mean at 17.5°N ± 2.5°), and Ozone Mapping and Profiler Suite/Limb Profiler (OMPS/LP; ±1° latitude, ±12.5° longitude), is shown in Fig. SB2.4b. With the exception of a few points, all datasets remain within 10% of each other, well within measurement uncertainties. The time series is characterized by a quiescent period before 2005, a period of moderate volcanic activity between 2005 and 2013, and another period of low aerosol loading between 2013 and 2017 (Chouza et al. 2020), also observed at other Northern Hemisphere (NH) sites (Khaykin et al. 2017). The background level during that time is noticeably higher than that in the pre-2005 quiescent period. But most importantly, the time series is strongly disturbed in the summer of 2019 by the Raikoke eruption, with sAOD reaching 0.015, a level not reached at this latitude since 1995, i.e., the post-Pinatubo area. Chouza et al. (2020) showed that the Raikoke plume ascended rapidly into the mid-stratosphere, reaching an altitude of 27 km within two months. During that period, the main plume transited gradually from 55°N to 19°N and circled Earth three times. A strong extinction signature is noticeable at 27 km on the MLSOL extinction time series (Fig. SB2.4a).

Figure SB2.5a shows the sAOD derived from GloSSAC as a function of time and latitude since the post-Pinatubo era. Fig. SB2.5b shows the sAOD derived from OMPS/LP. The signatures of Kelut and Calbuco eruptions are visible in the southern tropics and midlatitudes in 2014 and 2015, respectively. The signature of the 2017 Pacific Northwest wildfires is visible at high and midlatitudes of the NH. The signature of the Aoba eruption extends in the SH in late 2018. But the most prominent feature is the very large signature of the Raikoke eruption, which yields an sAOD larger than 0.025 for at least four to five months. The second most prominent feature is the large signature of the Australian fires in late 2019 (see Sidebar 7.6), with values of sAOD exceeding 0.025 for several weeks. The Ulawun eruption also caused high sAOD values in the tropics starting in mid-2019. Altogether, these major events have caused sAOD to exceed 0.012 for several months in 2019 at almost all latitudes between 60°S and 90°N, simultaneously, a level of global aerosol loading unseen since 1994.

Although the occurrence and frequency of large volcanic eruptions remain random, there is a concern that favorable conditions (e.g., increase of surface temperature or drought) may lead to an increase in the occurrence and strength of pyrocumulonimbus events and its associated stratospheric aerosol injection (Peterson et al. 2018). Early estimates of the 2019/20 Australian wildfires total mass injected in the stratosphere point to the equivalent of a mid-size, possibly larger, volcanic eruption (see Sidebar 7.6). Although the composition of fire-type and volcanic-type aerosols is different, an increase in the strength and/or frequency of aerosol injection into the stratosphere may have an impact on climate and ozone that is yet to be quantified and understood. The continuation of key stratospheric aerosol measurements such as those described here is undoubtedly of crucial importance.

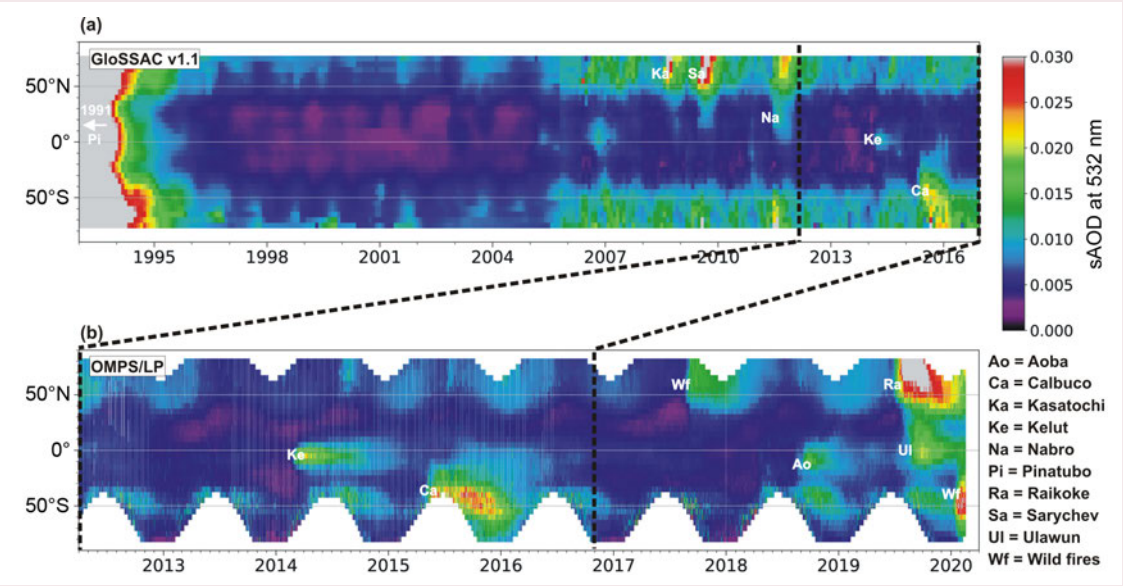

Fig. SB2.5. Time–latitude 2-D contour of the monthly mean sAOD derived from (a) GloSSAC and (b) OMPS/LP. Significant volcanic and biomass burning events are annotated by white letters.

h. Land surface properties

1) Land surface albedo dynamics—G. Duveiller, N. Gobron, and B. Pinty

Albedo is the fraction of shortwave radiation reflected by the surface and depends on a number of surface attributes such as snow cover, vegetation cover, and soil moisture among others. The year 2019 exhibited large regional contrasts in terms of land surface albedo in the visible part of the spectrum (see Plate 2.1ac), with the Northern Hemisphere (NH) overall darker (i.e., less reflective) and the Southern Hemisphere (SH) brighter that the baseline period 2003–10. Strong negative anomalies in visible albedo (on the order of –30%) were especially noticeable in central and eastern Europe. Similarly, high negative values were observed in the Caucasus and the Middle East; in eastern Asia (western China and Mongolia, Korea, and Japan); northwestern America (Alaska, Yukon, and Northwest Territories); eastern United States; and parts of Argentina and Chile. Milder negative anomalies (–10%) were found in Canada's Baffin Island, Mexico, much of northern South America, central Africa, and India. Large positive anomalies (up to +30%) were found in North America, in the Himalayas and eastern China, in eastern Australia, southern Africa, and sporadically in South America. The near-infrared anomalies follow the same general patterns as for the visible albedo but with moderate amplitudes (see Plate 2.1ad) and a relative tendency toward brightening.

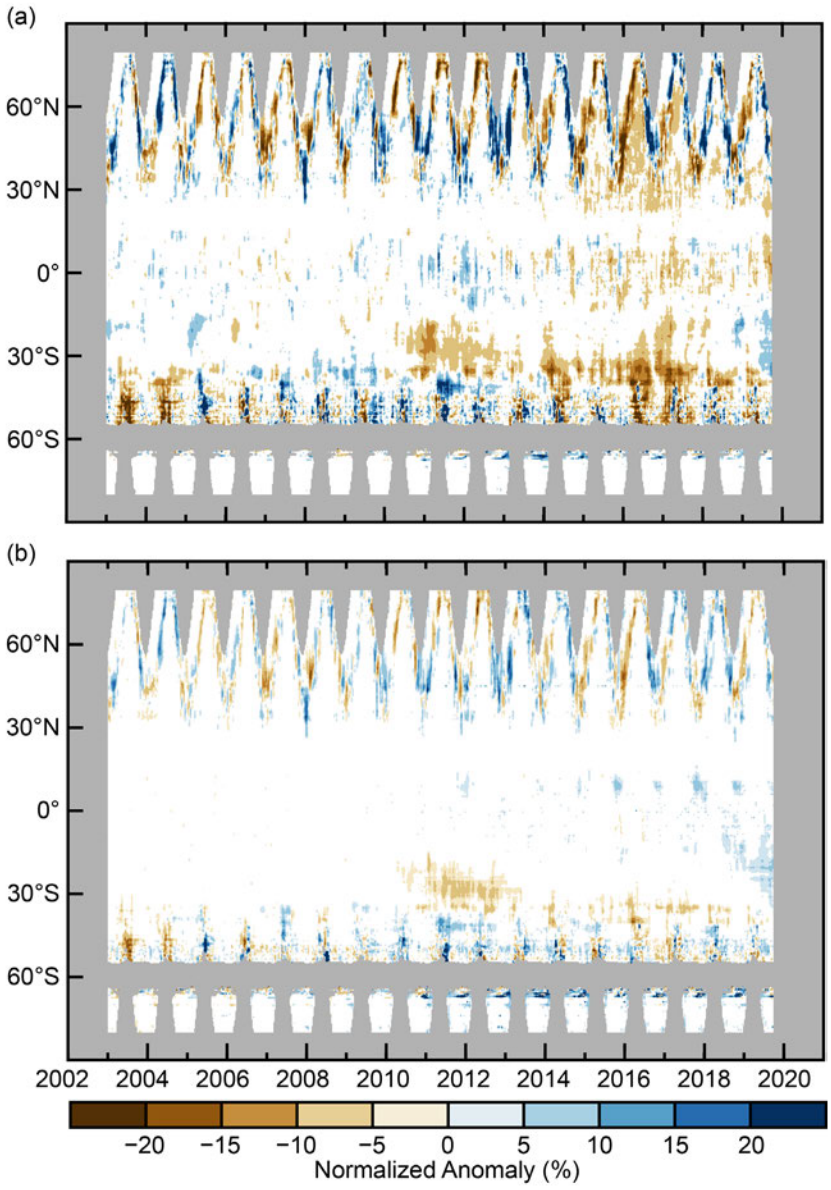

Fig. 2.63. Zonally averaged surface albedo anomalies (%; 2003–10 base period) in (a) visible and (b) near-infrared broadband.

The large albedo anomalies in northern latitudes largely follow those of snow cover. With the exception of January, Europe experienced much less snow cover than usual in both the early and late months of 2019 (see section 2c2 for an overall hemispheric and continental summary), resulting in an overall darker surface than the baseline. Northeastern China, Korea, and Mongolia similarly saw much reduced snow cover during the beginning of the year with respect to the 2003–10 baseline, which was not compensated by above-average snow cover in October–December. On the contrary, large areas of North America were more extensively covered with snow than usual in early and late 2019, which translated to brighter surfaces over these areas (section 2c2). The same is true for the Tibetan Plateau and neighboring areas. The fact that the northernmost latitudes were less extensively covered with snow than usual from May to June probably explains the darker surfaces in various areas nearer to the North Pole (Alaska, Baffin Island, and the northern tip of Siberia).

For regions not affected by snow cover, the main driver affecting land albedo is the relative vigor and health of vegetation, which itself largely depends on water availability. The drought that led to the disastrous fire season in Australia during late 2019 and early 2020 (see Sidebar 7.6) is responsible for brightening the surface, while the potential darkening effect of the fires is not significant enough to be observed in the yearly averaged data. Southern Africa has also seen clear reductions in soil moisture (section 2d10) and vegetation photosynthesis activity (section 2h2) during 2019, resulting in a relative brightening of the surfaces. India and China have seen significant trends in greening over the recent years due to intensified agriculture, translating to a reduction of surface visible albedo (Chen et al. 2019). In Europe, the strong summer drought (section 2d11) may have brightened the surface, partly by accelerating the end of the season (see Fig. 2.69d), but this was insufficient to counter the strong overall darkening effect generated by the reduction of snow cover in the cold months.

The separate contribution of snow occurrence and vegetation cover to albedo anomalies can be represented in a multiannual perspective using latitudinal averages for the entire record (Fig. 2.63). The effect of snow cover in the NH follows a clear seasonal cycle that is in phase between the visible and the near-infrared parts of the spectrum, and for which there is no clear trend. Aside from that, the rest of the world shows a slight overall negative trend in visible albedo and a lightly rising trend in near-infrared, which is consistent with the enhanced greening observed in the fraction of absorbed photosynthetically active radiation (FAPAR) estimates (section 2h2). The year 2019 does stand out by showing a contrasting pattern between North and South, respectively darker and brighter than the baseline (which is again consistent with the FAPAR anomalies in 2019). The global average shows a higher albedo in the SH for both the visible and near-infrared albedo, while the NH is slightly brighter in the near-infrared and darker in the visible (Fig. 2.64).

The albedo anomalies are calculated based on the NASA Collection 6 MCD43C3 products derived from satellite observations of the Moderate Resolution Imaging Spectroradiometer (MODIS) instrument on-board of the *Terra* and *Aqua* platforms (Schaaf et al. 2002; Schaaf and Wang 2015). The retrieval algorithm delivers visible albedo (0.3–0.7 nm) and near-infrared albedo (0.7–5.0 nm) values, in addition to both black-sky albedo and white-sky albedo values, the latter estimates of which are used in this report. The anomalies are calculated at a 10-daily frequency, based on the 2003–10 reference period.

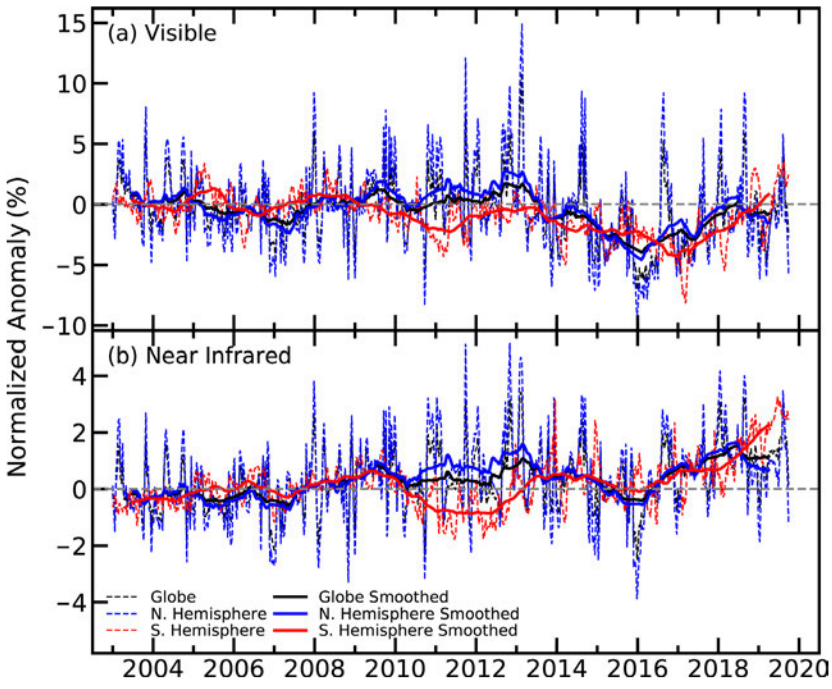

Fig. 2.64. Global and bi-hemispherical averaged surface albedo (%; 2003–10 base period) in (a) visible and (b) near-infrared broadband.

2) Terrestrial vegetation dynamics—N. Gobron

Fraction of absorbed photosynthetically active radiation (FAPAR) anomalies exhibited significant regional variations in vegetation conditions worldwide in 2019 (Plate 2.1ae). The greatest negative anomalies (brown: not favorable for vegetation) were observed in Australia, southern Africa, Kostanay (northern Kazakhstan), and eastern Russia (from Krasnoyarsk eastward around 60°N). Local negative anomalies affected northern China, Iowa and Wisconsin (United States), Bahia State (Brazil), Bolivia, La Pampa (Argentina), and Kenya. The greatest positive anomaly (green) was again observed in eastern China (as during the last four years) as well as northern India (Rajasthan, Uttar Pradesh, and Punjab), Bangladesh, Syria, and northern Iraq. To a lesser magnitude, the entire central region of the African continent and the region surrounding the Black Hills (South Dakota, United States) also had positive deviations.

The strongest negative annual anomaly, with a maximum absolute value of 0.15, occurred in Australia, possibly due to the strongly positive Indian Ocean dipole (IOD; section 4h) that influenced severe extreme weather events. This year was the warmest and driest year on record there, which implied drought, heat waves, and devastating bushfires. Over Botswana, Namibia, Zambia, and southern Mozambique, the negative anomalies were due to very dry conditions (section 2d12). Dry conditions and high temperatures from January to June over Kenya resulted in negative annual anomalies.

In the northern part of Kazakhstan and eastern Russia, the hot and dry climatic conditions hindered vegetation during the growing season (spring), which strongly affected the annual anomaly. Bad weather conditions with heavy spring rains in Wisconsin in the United States, and some adjoining regions delayed planting and affected crops. High temperatures associated with SH winter rainfall deficits had significant negative regional impacts on vegetated conditions such as over Bahia State (Brazil), Bolivia, and Argentina.

Terrestrial photosynthesis was again enhanced over eastern China with vegetation growth in 2019, similar to 2017 and 2018 (Gobron 2018, 2019) due to important changes in the overall land use (Chen et al. 2019). In addition, northern Turkey got an increase of vegetation activity for the last two years. Late in the year, the central region of the African continent had high positive anomalies, due to high temperatures and heavy rainfall that impacted the annual results.

Figure 2.65 displays the zonal average anomalies from 1998 to 2019 compared to the 1998–2010 base period. Strong seasonal deviations include mainly positive anomalies north of 20°N after 2014. Negative anomalies from 2002 to 2014 affected the SH, except in 2010–12. In contrast to the positive anomalies around 30°S from 2014 to 2017, anomalies turned negative again in 2018, with strongest values in 2019.

Figure 2.66 shows the global and bi-hemispheric anomalies, revealing more oscillations between the seasons in the SH with its smaller land area than in the NH. The NH had fewer negative events than the SH, and its plant activity increased from 2010 to 2017 and, after a short decline in late 2017/early 2018, increased again afterward. Analysis

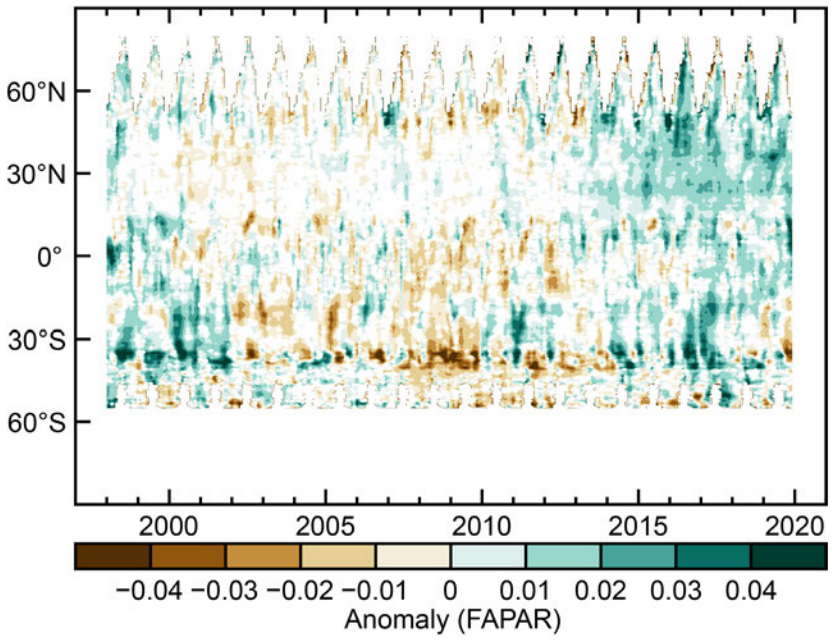

Fig. 2.65. Zonally averaged FAPAR anomalies for 1998–2019 (1998–2010 base period).

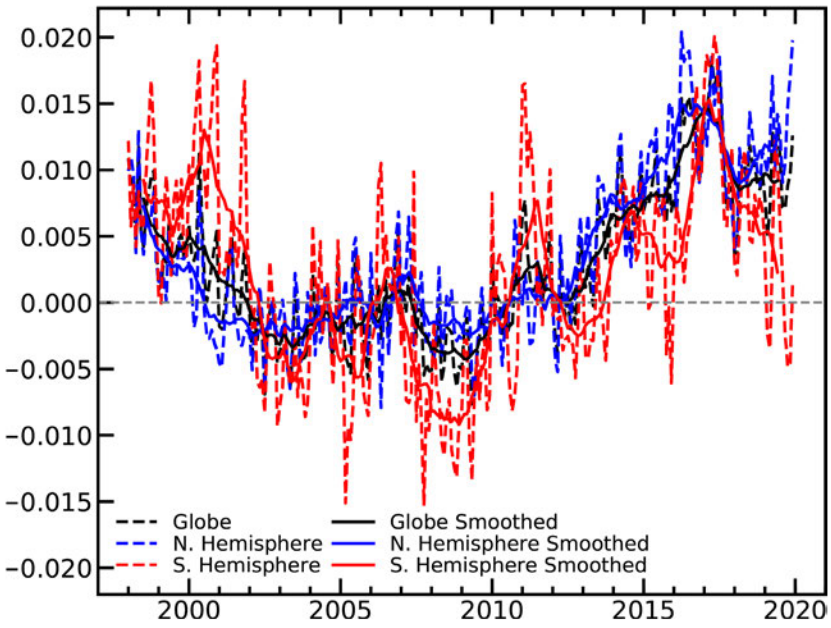

Fig. 2.66. Global (black lines), NH (blue), and SH (red) FAPAR anomalies for 1998–2019 (1998–2010 base period). Dotted lines denote each monthly period; solid lines indicate the six-month running averaged mean.

of SH data reveals two positive extreme peaks in 2000 and 2017, while extreme minimum events occurred in 2008–09. Following the decline from positive anomalies with negative values between 2002 and 2009, there has been an increase in positive values since 2011. Since 2017 the global anomalies have decreased but are still positive with 2019 equal to those in 2018; however, SH anomalies have decreased sharply since 2017.

Space-based measurements are essential for monitoring the activity of terrestrial plants worldwide. These observations are used to recover FAPAR, an essential climate variable (as defined by GCOS [2016]). The 2019 analysis merged 22 years of global FAPAR products based on three optical sensors from 1998 to 2019 (Gobron et al. 2010; Pinty et al. 2011; Gobron and Robustelli 2013; the base period is 1998–2010). Comparisons between each dataset and with multiple surrogates using ground measurements provide an estimate of the uncertainties and biases. Given the biases between the various sensor products, this long-term global dataset presents an estimated average uncertainty close to 5%–10%.

3) Biomass burning—J. W. Kaiser, G. R. van der Werf, and I. Hüser

During 2019, anomalously high vegetation fire emissions in several forested regions of Indonesia, Russia, Australia, Brazil, and Bolivia (Plate 2.1af) compensated the long-term global downward trend in emissions from savanna regions. The global annual emission of 1836 TgC was 9% lower than the average for the reference period 2003–10 (Table 2.9). The emission in 2019 was, however, substantially increased compared to 2018 and 2017 with 1600 TgC and 1680 TgC, respectively. Despite the declining trend in savanna regions, upward trends related to climate change with more extreme fire weather and longer fire seasons are emerging in several regions. Biomass burning displays large interannual variability driven by fire weather and human behavior. Its global distribution in 2019 is shown in Fig. 2.67.

Indonesia experienced a relatively long dry spell in September, which led to above-average emissions (Fig. 2.68). Usually, such dry spells are associated with El Niño years, which was not the case in 2019. Rather, it was related to the strong positive IOD (see section 4h). Annual emissions in the larger tropical Asian region were dominated by fires in eastern Sumatra and southern Borneo, which elevated the emissions by 62% to the third-largest value (191 TgC) since at least 2003, with larger values of 425 TgC and 228 TgC in 2015 and 2006, respectively.

Strong fire activity in Siberia led to a 62% increase in emissions from the northern Asia region. Many fires during June–August burnt farther north than usual, which led to a new record of 27 TgC for fire emissions from the Arctic. The emissions have increased in every year since 2015 and were more than twice as high in 2019 than in any preceding year (Fig. 2.68).

In December 2019, the Australian states of New South Wales and Victoria experienced their highest monthly fire activity since at least 2003 (Fig. 2.68, Sidebar 7.6). Their annual emission of 29 TgC more than doubled the previous record of 13 TgC set in 2003 and made up almost all of the

Table 2.9. Annual continental-scale biomass burning budgets in terms of carbon emission (Tg C yr^{-1}) from GFASv1.4.

Time period		2003–10	2019	
Quantity in Tg C yr^{-1}	Latitude/ longitude	Mean value (range)	Value	Anomaly (percent)
Global		2010 (1828–2272)	1836	–174 (–9%)
North America	30°–75°N 190°–330°E	79 (63–109)	70	–9 (–12%)
Central America	0°–30°N 190°–330°E	88 (71–122)	106	+18 (+20%)
S. Hem. America	0°–60°S 190°–330°E	381 (214–473)	274	–107 (–28%)
Europe and Mediterranean	30°–75°N 330°–60°E	37 (29–62)	36	–1 (–2%)
N. Hem. Africa	0°–30°N 330°–60°E	419 (353–453)	296	–123 (–29%)
S. Hem. Africa	0°–35°S 330°–60°E	484 (444–528)	428	–56 (–12%)
Northern Asia	30°–75°N 60°–190°E	176 (99–418)	214	+38 (+21%)
South-East Asia	10°–30°N 60°–190°E	128 (107–150)	87	–41 (–32%)
Tropical Asia	10°N–10°S 60°–190°E	118 (38–228)	191	+73 (+62%)
Australia	10°–50°S 60°–190°E	99 (47–137)	133	+34 (+35%)

35% anomaly in fire emissions from all of Australia. The fires started in September, i.e., relatively early, were strongest in December, and continued into 2020. The extreme fire weather was linked to the strong positive IOD anomaly and record temperatures in Australia.

Substantial media attention was also given to fires burning in the Amazon. Significant positive anomalies occurred in Bolivia and the Brazilian states of Amazonas and Roraima (see Plate 2.1af), although south of the equator there was an overall strong negative anomaly of –28% compared to the 2003–10 reference period. This period was characterized by high deforestation and drought years in Brazil. After 2010, emissions dropped significantly (Fig. 2.68), and emissions in 2019 were still in the typical range of its decade, albeit at the upper limit. An increase of deforestation in 2019 was reported by the PRODES program of the Brazilian space agency INPE (http://terrabrasilis.dpi.inpe.br/app/dashboard/deforestation/biomes/legal_amazon/rates). Whether 2019 marked a

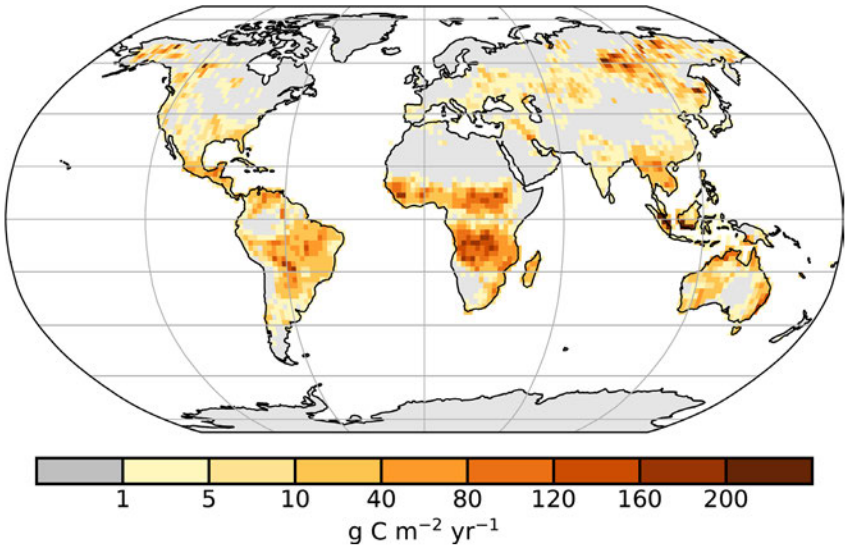

Fig. 2.67. Global map of fire activity (g C m^{-2} yr^{-1}) in 2019 in terms of carbon consumption. (Source: GFASv1.4.)

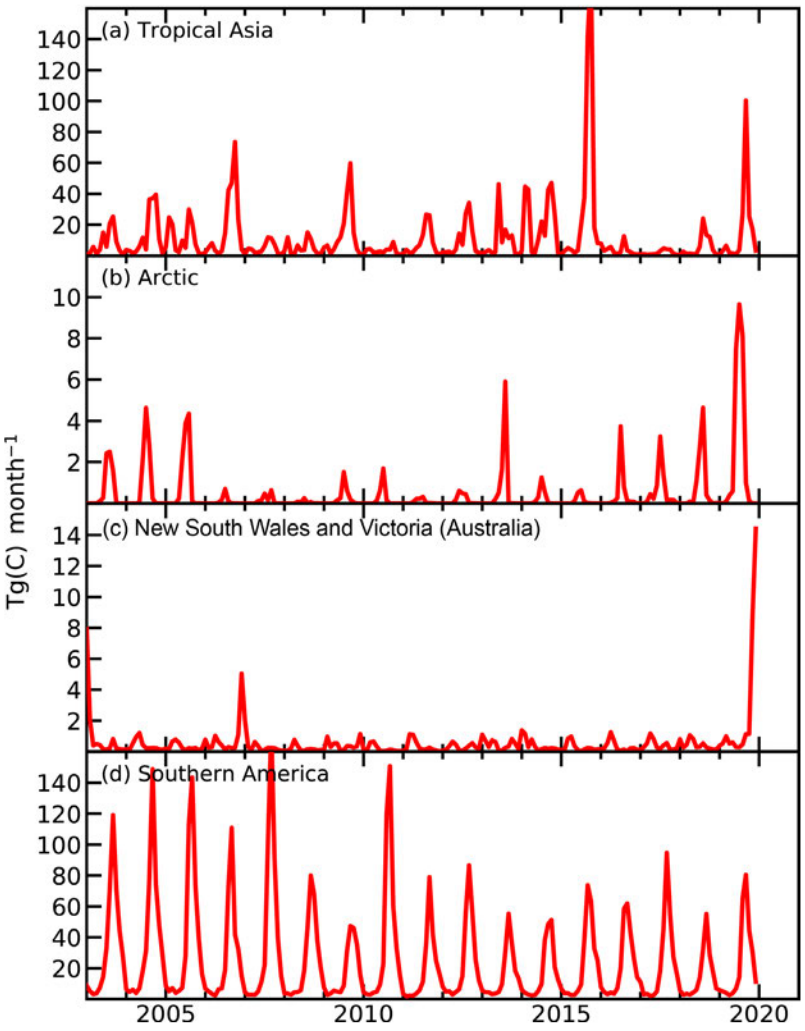

Fig. 2.68. Time series of monthly open biomass burning in (a) tropical Asia, (b) the Arctic, (c) New South Wales and Victoria, Australia, and (d) Southern hemispheric America. The Arctic is bounded by the Arctic Circle (66.5°N); the definitions of the other regions are provided in Table 2.9. (Source: GFASv1.4.)

corresponding reversal of the decreasing long-term trend remains to be seen.

The established long-term downward trend related to changes in land use in frequently burning savannas (Andela et al. 2017), in combination with a delay in the start of the fire season in sub-Saharan Africa, led to a 29% decrease (123 TgC) in fire emissions from NH Africa. Fires here normally burn in December and January but started weeks later related to wet conditions that were associated with the strong positive anomaly of the IOD.

The fire emission estimates have been derived from the Global Fire Assimilation System (GFAS; Kaiser et al. 2012, 2017), which uses satellite data of active fire detections and its intensity and is calibrated against the Global Fire Emissions Database (van der Werf et al. 2017). Here, vegetation fire activity is reported in terms of carbon emissions. Most biomass is released as CO_2, but substantial amounts of other gases and aerosols are emitted as well. Most of the carbon released into the atmosphere is taken up again by vegetation regrowth. However, tropical rain forests and peat lost to fires regrow on time scales longer than a few hundred years or not at all. Their emissions are, therefore, practically irreversible. Given the large spatio-temporal variability in fire activity and the difficulty to constrain those with ground measurements, emission estimates are notoriously uncertain. The presented estimates of relative anomalies in entire regions are more reliable because they are derived from consistent observations by NASA's two satellite-based MODIS instruments. The launch dates of the satellites carrying these instruments restrict the GFAS dataset to the period starting in 2003.

4) Phenology of primary producers—D. L. Hemming, J. Garforth, T. Park, A. D. Richardson, T. Rutishäuser, T. H. Sparks, S. J. Thackeray, and R. Myneni

Climate and nature are mutually dependent. This is visible from global to organism scales by phenological indicators—events in nature (Demarée and Rutishäuser 2011). Here, the timing of NH spring and autumn events of primary producers (terrestrial vegetation and lake plankton) is compared, utilizing records that reach across spatial scales from satellite remote sensing to site-level monitoring.

For 2019, the satellite-derived (MODIS) normalized difference vegetation index (NDVI; Park et al. 2016) revealed the earliest average start of season since the beginning of the record in 2000 (SOSM, 4.3 days) and a later-than-average end of season (EOSM , 2.4 days) across the NH (>30°N),

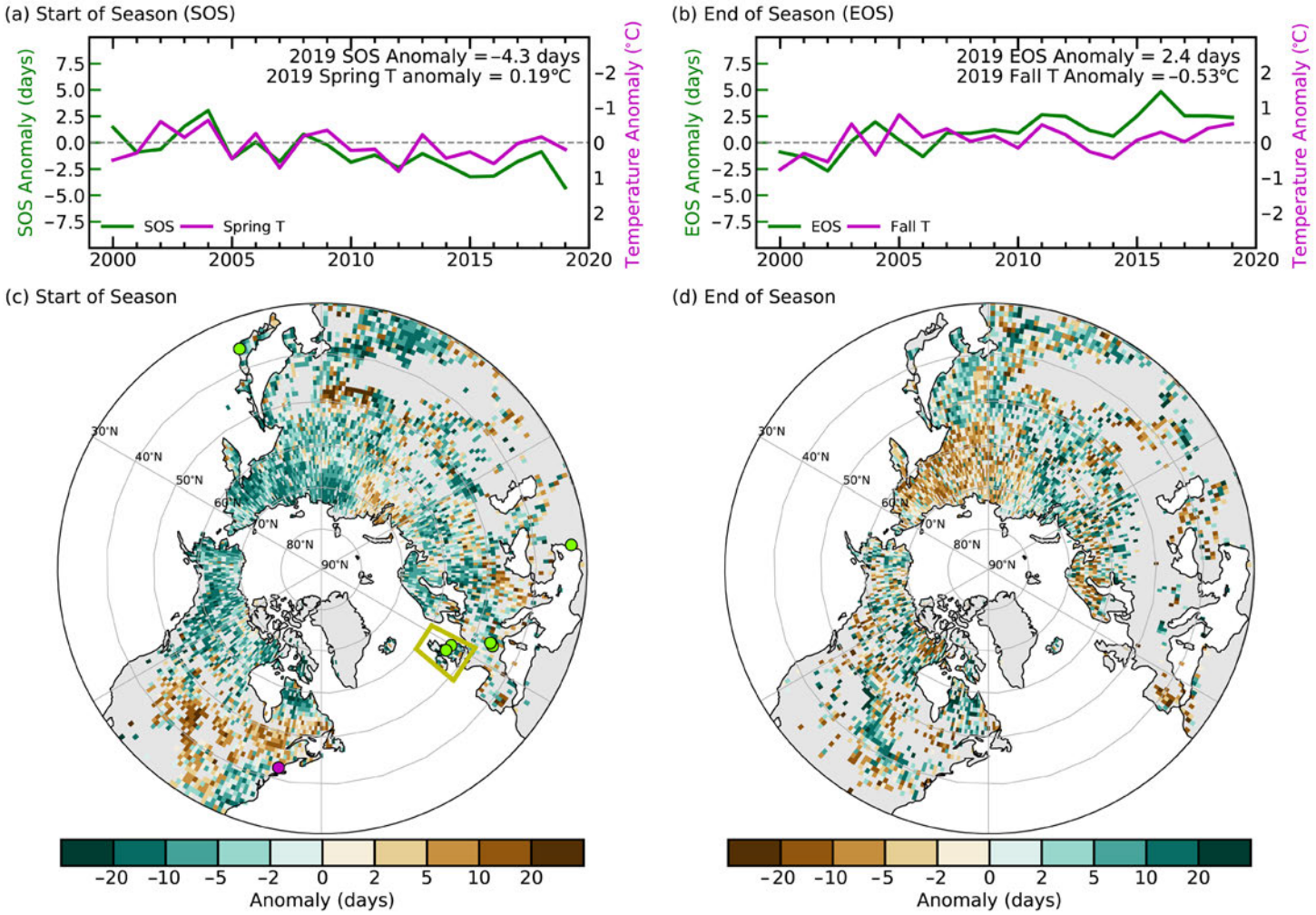

Fig. 2.69. (a) Time series of area mean anomalies (days relative to 2000–09 baseline) in MODIS NDVI-based vegetation growing season onset (SOS; purple) and MERRA-2 spring (Mar–May, green) temperature for NH (> 30°N). (b) Same as (a) but for end of growing season (EOS) and autumn (Sep–Nov) temperature. Note temperature scale reversal in panel (b). Spatial pattern of (c) SOS and (d) EOS anomaly in 2019 with respect to the baseline. Note the color bar reversal in (d) to highlight the longer growing season as green. Colored circles and box in (c) identify the location of sites shown in Figs. 2.70 and 2.71: Harvard Forest PhenoCam site (pink circle), UK phenology network (yellow box), lake phytoplankton NH monitoring sites (green circles).

relative to the 2000–09 baseline (SOS = day of year [DOY] 137, 17 May; and EOS = DOY 283, 10 October; Figs. 2.69a,b). This resulted in an 8-day longer growing season, relative to the baseline (161 days, estimated for all NH pixels and averaged over the baseline). Overall, about 65% and 56% of the NH region showed earlier SOS_M and later EOS_M in 2019, respectively (Figs. 2.69c,d). Regionally, earlier SOS_M occurred across northwestern North America (NA) and most of Eurasia, and later SOS_M occurred over central and eastern NA. A contrasting pattern of earlier and later EOS_M was observed in eastern and western Eurasia, whereas EOS_M in NA was spatially heterogeneous. Interannual variations in SOS_M and EOS_M correlate with changes in spring and autumn temperatures from MERRA-2 reanalysis (Gelaro et al. 2017). For 2019, SOSM and EOS_M are broadly consistent with spatial temperature patterns noted in section 2b of this report.

Two case studies for ground-based phenology observations are compared with the satellite data. PhenoCam data across NA (Richardson et al. 2018a) show similar spatial and temporal patterns to satellite-derived phenology data (Zhang et al. 2018; Richardson et al. 2018b), although the agreement tends to be better in spring than autumn (Melaas et al. 2016; Moon et al. 2019). Here, we compare site PhenoCam estimates for start of season (SOS_{PC}) and end of season (EOS_{PC})

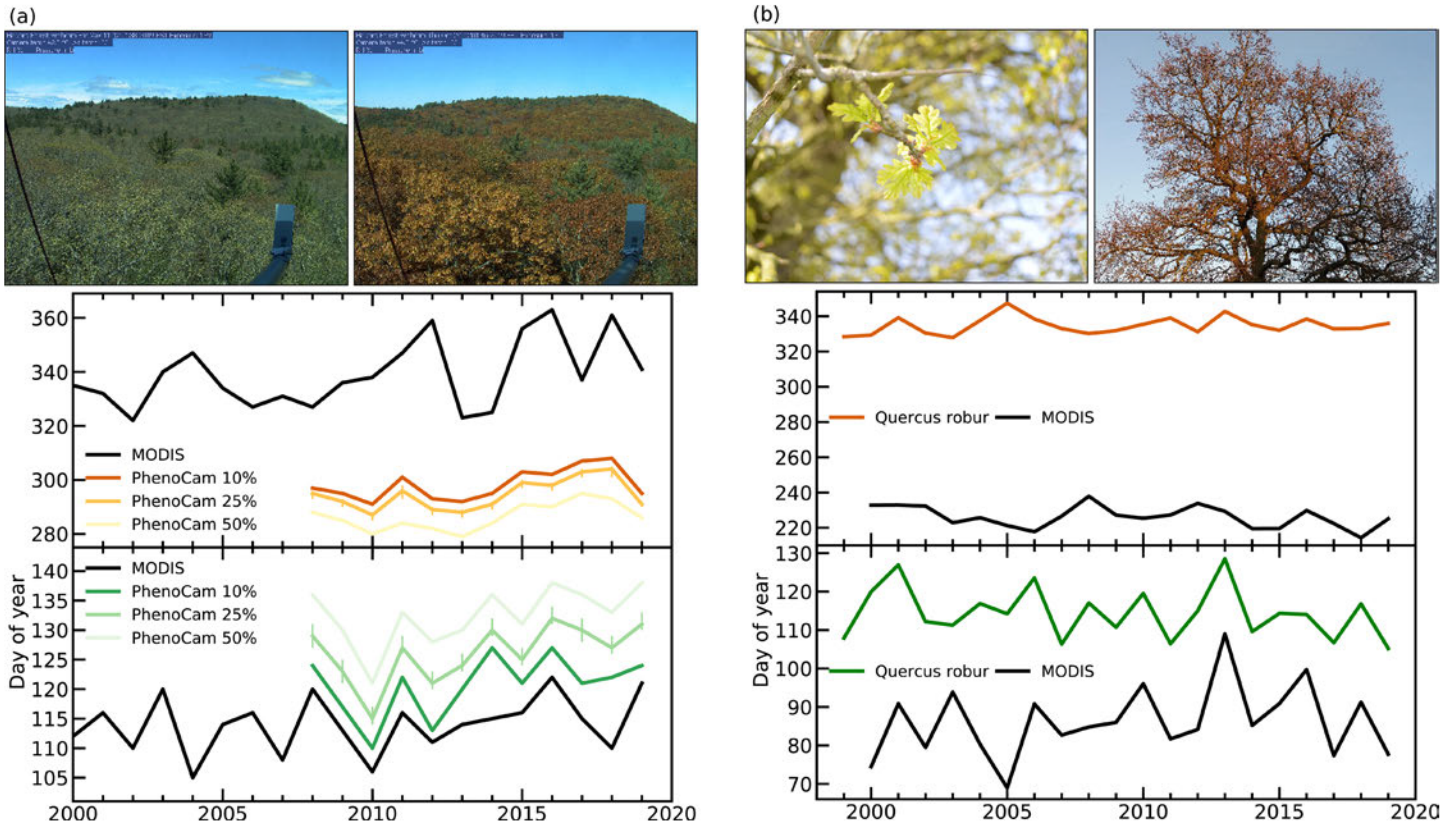

Fig. 2.70. Day of year (DOY) of spring and autumn vegetation phenology indicators and associated 2019 images for (a) Harvard Forest, Massachusetts, United States, SOS (green, bottom) and EOS (orange, top) days derived from PhenoCam and MODIS remote sensing (black), and (b) UK mean oak (*Quercus robur*) "first leaf" (bottom, green), "bare tree" (top, orange), and MODIS (black).

at Harvard Forest, a deciduous forest in Massachusetts (United States) with the same indicators derived from MODIS (Figs. 2.70a,b). SOS_{PC} and SOS_{M} are strongly correlated (r = 0.83, n = 12), although SOSPC is later by 11 ± 3 days, relative to SOS_{M} (Fig. 2.70a). The correlation between EOS_{PC} and EOS_{M} is weaker (r = 0.46), and EOS_{PC} is 48 ± 12 days earlier on average relative to EOS_{M} (Fig. 2.70b). In 2019, SOS_{PC} for Harvard Forest (DOY 131, 11 May, ± 2 days) was four days later relative to 2018 (DOY 127, 7 May, ± 2 days), and EOS_{PC} (DOY 291, 18 October, ± 1 days) was 13 days earlier relative to 2018 (DOY 304, 31 October, ± 2 days). The MODIS changes for this site were more extreme: SOS_{M} was 11 days later and EOS_{M} 20 days earlier in 2019 relative to 2018 (Figs. 2.70a,b). PhenoCam-derived total growing season length in 2019 was more than two weeks shorter than 2018, mostly because of the earlier EOS. This is the shortest growing season observed at Harvard Forest in the 12-year PhenoCam record.

Across the United Kingdom (UK), mean dates of oak (*Quercus robur*) "first leaf" and "bare tree" (indicators of start and end of season) recorded by citizen scientists have been collated by the Woodland Trust since 1999. Over the 2000–09 baseline, the mean first leaf and bare tree dates were 26 April (DOY 116) and 30 November (DOY 334), respectively, giving a 218-day season length (Figs. 2.70b). Both events are strongly influenced by prevailing temperature; first leaf advances by about six days for every 1°C increase in mean February–April temperature, and bare tree dates are delayed by about three days for every 1°C increase in October temperature. In 2019, the very warm spring resulted in mean first leaf nearly 11 days earlier than the baseline. In contrast, October temperature was similar to recent years and bare dates were delayed by about one day compared to the baseline. The net result was an "oak season" 12 days longer than the 10-year mean. These results are qualitatively comparable with UK mean MODIS NDVI SOS and EOS anomalies.

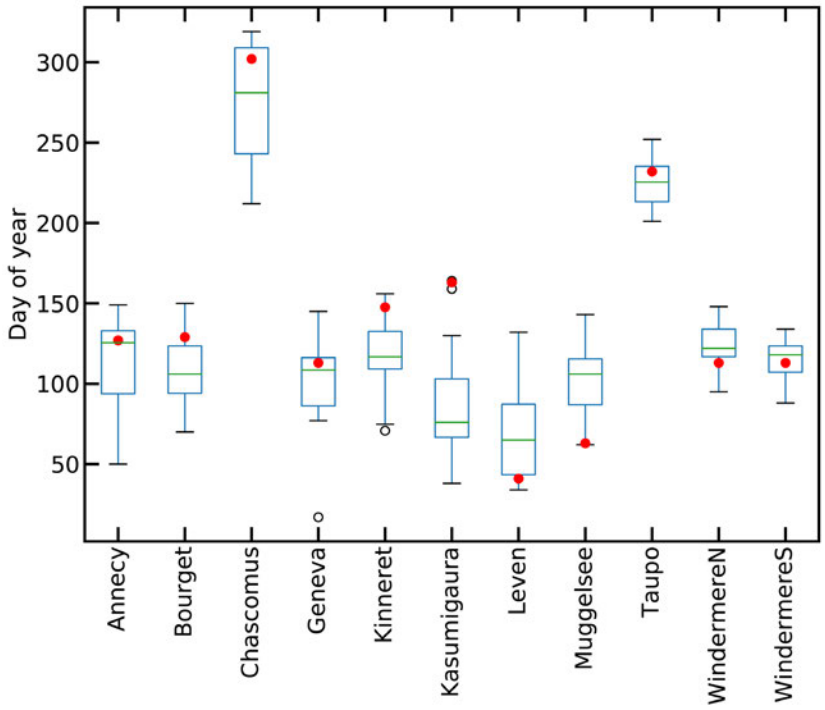

Fig. 2.71. Box-whisker plot showing the DOY of mean (green line), 50th (box), 90th (whiskers), and 99th (black open circles) percentiles of spring phytoplankton peak for 2000–10, and the 2019 mean day (red circles) for nine global lake basins: Annecy and Bourget (France), Chascomus (Argentina), Geneva (France-Switzerland), Kinneret (Israel), Kasumigaura (Japan), Loch Leven (UK), Muggelsee (Germany), Taupo (New Zealand), and Windermere north and south basins (UK).

Long-term (fortnightly-monthly) monitoring data on lake water concentrations of the photosynthetic pigment chlorophyll-*a* can be used to derive the seasonality of phytoplankton growth and the timing of the spring phytoplankton peak in lake ecosystems (Winder and Cloern 2010; Thackeray et al. 2013). We present such data from 11 lake basins (Fig. 2.71): Lakes Annecy and Bourget (France), Chascomus (Argentina), Geneva (France-Switzerland), Kinneret (Israel), Kasumigaura (Japan), Loch Leven (UK), Müggelsee (Germany), Taupo (New Zealand), and the north and south basins of Windermere (UK). During the 2000–10 baseline, the mean day of year of the spring bloom in the nine NH basins ranged from 76 (17 March, Loch Leven) to 122 (2 May, Windermere North Basin). In lakes Chascomus and Taupo, in the SH, the corresponding means were 274 (1 October) and 222 (10 August), respectively. In 2019, the day of year of the spring peak was later than the base period in eight lake basins (by 1 to 82 days), but earlier for Müggelsee, Loch Leven, and Windermere North Basin (by 37, 35, and 9 days, respectively). This site-based variability suggests the agency of additional factors, such as nutrient availability (Thackeray et al. 2008), that interact with climate to influence seasonal ecosystem behavior.

Acknowledgments

2a (Overview)

Robert Dunn and Kate Willett acknowledge support from the Joint BEIS/Defra Met Office Hadley Centre Climate Programme under (GA01101).

We thank our internal reviewers, David Parker, John Kennedy, Roger Saunders, Mark McCarthy, and Christoforos Tsamalis for their detailed suggestions.

We also thank the following authors for providing data included at multiple points in this chapter: Gil Compo and Cathy Smith, 20CRv3; Mike Bosilovich, MERRA2; Julien Nicholas, ERA5; and Atsushi Goto, JRA-55 data

2b2 (Lake Temperature)

Lake surface water temperatures from satellite data have been generated within the GloboLakes project funded by the UK National Environment Research Council (NE/J023345/2) with extensions funded by the EU Copernicus Climate Change Service (C3S) programme. Lake temperature data from Baikal was supported by grant of Foundation for support of applied ecological studies (https://baikalfoundation.ru/project/tochka-1/). Data from the Swedish Lake Vättern were received from the Lake Vättern's Society for Water Conservation. Collection of data from Loch Leven, Scotland, was supported by award number NE/R016429/1 as part of the UK-SCaPE programme, which is delivering UK National Capability.

2b3 (Land and marine temperature extremes)

Robert Dunn acknowledges support from the Joint BEIS/Defra Met Office Hadley Centre Climate Programme under (GA01101).

Research funding for R. W. Schlegel was provided by the Ocean Frontier Institute, through an award from the Canada First Research Excellence Fund.

2c1 (Permafrost thermal state)

PERMOS is financially supported by MeteoSwiss in the framework of GCOS Switzerland, the Federal Office for the Environment and the Swiss Academy of Sciences and acknowledges the important contribution of the partner institutions and principal investigators. The French Network PermaFRANCE is financially supported by Observatoire des Sciences de l'Univers Grenoble (OSUG) and the French Research Infrastructure OZCAR.

2c2 (Northern Hemisphere snow cover extent)

This work is funded in part by NOAA's Climate Data Record (CDR) Program located in Asheville, NC, at the National Centers for Environmental Information (NCEI).

Sidebar 2.1 (Lake Ice)

We thank John Magnuson, Kevin Blagrave, Nikolay Granin, Johanna Korhonen, Lars Rudstam, and Gesa Weyhenmeyer for providing updates to in situ lake ice phenology records. Funding to Sapna Sharma was provided by the Natural Sciences and Engineering Research Council Discovery Grant. R. Iestyn Woolway received funding from the European Union's Horizon 2020 research and innovation programme under the Marie Skłodowska-Curie grant agreement No. 791812.

2d1 (Surface humidity)

Kate Willett was supported by the Met Office Hadley Centre Climate Programme funded by BEIS and Defra. Adrian Simmons was supported by the Copernicus Climate Change Service implemented by ECMWF on behalf of the European Commission. The NOAA-CIRES-DOE Twentieth Century Reanalysis Project version 3 used resources of the National Energy Research Scientific Computing Center managed by Lawrence Berkeley National Laboratory, which is supported by the Office of Science of the U.S. Department of Energy under Contract No. DE-AC02-05CH11231 and used resources of NOAA's Remotely Deployed High Performance Computing Systems. Support for the Twentieth Century Reanalysis Project version 3 dataset is provided by the U.S. Department of Energy, Office of Science Biological and Environmental Research (BER), by the National

Oceanic and Atmospheric Administration Climate Program Office, and by the NOAA Earth System Research Laboratory Physical Sciences Division

2d5 (Land surface precipitation extremes)

Stephen Blenkinsop is funded by the U.K. Natural Environment Research Council FUTURE-STORMS project under grant number NE/R01079X/1. The National Center for Atmospheric Research is supported by the National Science Foundation.

2d6 (Lake water levels)

B. M. Kraemer received support from the German Research Foundation through the LimnoScenES project (AD 91/22-1). This work benefited from B. M. Kraemer's participation in the Global Lake Ecological Observatory Network (GLEON).

2d8 (River discharge and runoff)

Hyungjun Kim was supported by the Japan Society for the Promotion of Science KAKENHI (16H06291 and 18KK0117).

2d10 (Soil moisture)

The ESA CCI SM datasets and the authors were supported by ESA's Climate Change Initiative for Soil Moisture (Contract No. 4000104814/11/I-NB and 4000112226/14/I-NB). We would also like to thank support from the Copernicus Climate Change Service implemented by ECMWF.

2d11 Land evaporation

D. G. Miralles acknowledges support from the European Research Council (ERC) under grant agreement no. 715254 (DRY–2–DRY), and the Belgian Science Policy Office (BELSPO) in the frame of the STEREO III program projects ET–Sense (SR/02/377) and ALBERI (SR/00/373).

2d12 (Monitoring global drought using the self-calibrating Palmer Drought Severity Index)

Tim Osborn received funding from UK NERC (NE/P006809/1). Ian Harris received funding from the UK National Centre for Atmospheric Science (NCAS).

2e2 (Land and ocean surface winds)

The NOAA-CIRES-DOE Twentieth Century Reanalysis Project version 3 used resources of the National Energy Research Scientific Computing Center managed by Lawrence Berkeley National Laboratory, which is supported by the Office of Science of the U.S. Department of Energy under Contract No. DE-AC02-05CH11231 and used resources of NOAA's Remotely Deployed High Performance Computing Systems. Support for the Twentieth Century Reanalysis Project version 3 dataset is provided by the U.S. Department of Energy, Office of Science Biological and Environmental Research (BER), by the National Oceanic and Atmospheric Administration Climate Program Office, and by the NOAA Earth System Research Laboratory Physical Sciences Division

2f1 (Earth radiation budget at top of atmosphere)

This research has been supported by the NASA CERES project. The NASA Langley Atmospheric Sciences Data Center processed the instantaneous Single Scanner Footprint (SSF) data used as input to EBAF Ed4.1 and processed the FLASHFlux TISA version 3C.

2g3 (Aerosols)

The CAMS reanalysis has been produced by the Copernicus Atmosphere Monitoring Services (CAMS), which is a program funded by the European Union. The European Centre for Medium-Range Weather Forecast (ECMWF) operates CAMS on behalf of the European Commission. Melanie Ades, Olivier Boucher, Zak Kipling and Samuel Rémy are funded by CAMS.

2g4 (Stratospheric ozone)

Carlo Arosio, Melanie Coldewey-Egbers, Daan Hubert, Diego Loyola, Victoria Sofieva, Alexei Rozanov, and Mark Weber are grateful to ESA's Climate Change Initiative Ozone project and to the EU Copernicus Climate Change Service 312b Lot4 Ozone project for supporting the generation and extension of the GTO-ECV total ozone and SAGE-CCI-OMPS data records. Stacey M. Frith is supported by the NASA Long Term Measurement of Ozone program WBS 479717. Lucien Froidevaux's contribution, with the assistance of Ryan Fuller, was performed at the Jet Propulsion Laboratory, California Institute of Technology, under contract with NASA. Daan Hubert acknowledges the partial support by the EU/ERC Horizon 2020 project GAIA-CLIM.

2g5 (Stratospheric water vapor)

The authors would like to thank NASA's Upper Atmosphere Composition Observations program and NOAA's Climate Program Office for funding that helps sustain the frost point hygrometer soundings at Boulder, Lauder, Hilo, and Costa Rica.

Sidebar 2.2 (Stratospheric Aerosols)

This research was in part carried out at the Jet Propulsion Laboratory, California Institute of Technology, under a contract with the National Aeronautics and Space Administration, and by the National Oceanic and Atmospheric Administration Global Monitoring Laboratory. G. Taha's work is supported by NASA grant number 80NSSC18K0847.

2h1 (Land surface albedo dynamics)

The authors thank Monica Robustelli for her technical support.

2h2 (Terrestrial vegetation dynamics)

The author thanks Monica Robustelli for her technical support and the providers of the remote-sensing dataset needed to perform this research, i.e., the SeaWiFS Project (Code 970.2) and the Goddard Earth Sciences Data and Information Services Center/Distributed Active Archive Center (Code 902) at the Goddard Space Flight Center, Greenbelt, MD. MERIS products were processed at the Grid On Demand facility of European Space Agency (ESA/ESRIN) using JRC software code.

2h3 (Biomass burning)

The GFASv1.4 dataset was developed by the GFAS-CLIM project, funded by the German Bundesministerium für Wirtschaft und Energie (BMWi/DLR FKZ 50EE1543).

2h4 (Phenology)

Debbie Hemming acknowledges support from the Met Office Hadley Centre Climate Programme funded by BEIS and Defra, and thanks all co-authors for their interesting and helpful contributions, and Robert Dunn for his expertise finalizing the figures for this section. Taejin Park acknowledges support from the NASA Earth Science Directorate (grants NNX16AO34H and 80NSSC18K0173-CMS). Andrew Richardson acknowledges support from the National Science Foundation through the Macrosystems Biology (award 1702697) and LTER (award 1832210) programs. Nature's Calendar thanks all of its volunteer recorders, without whom it could not function. Stephen Thackeray thanks Heidrun Feuchtmayr, Mitzi De Ville, Ben James, Ellie Mackay, Mike Clarke, Bev Dodd, Anne Dobel, Laurence Carvalho, Piet Verburg, Orlane Anneville, Tamar Zohary, Nadia Diovisalvi, Leonardo Lagomarsino, Shin-ichiro Matsuzaki, Rita Adrian, and Daniel Langenhaun for collecting and providing lake chlorophyll-a data. Windermere data collection was supported by the Natural Environment Research Council award number NE/R016429/1 as part of the UK-SCaPE programme delivering National Capability.

Appendix 1: Acronyms

20CRv3	20th Greenhouse Gas Index
ALT	active layer thickness
AMSRE and AMSRE2	Advanced Microwave Scanning Radiometer
AO	Arctic Oscillation
AOD	aerosol optical depth
ASMA	Asian summer monsoon anticyclone
ATSR	Along Track Scanning Radiometer
AVHRR	Advanced Very High Resolution Radiometers
BDC	Brewer-Dobson circulation
CALIPSO	Cloud-Aerosol Lidar and Infrared Pathfinder Satellite Observation
CAMS	Copernicus Atmosphere Monitoring Service
CAMSRA	CAMS reanalysis
CCMI	Chemistry-Climate Model Initiative
CERES	Clouds and the Earth's Radiant Energy System
CH_3CCl_3	methyl chloroform
CH_4	methane
CLARA-A2	cloud, albedo and surface radiation dataset
CLOUD_CCI	Cloud Climate Change Initiative
CO	carbon monoxide
CO_2	carbon dioxide
CPT	cold-point temperature
EBAF	Energy Balanced And Filled
ECMWF	European Centre for Medium-Range Weather Forecasts
EESC	equivalent effective stratospheric chlorine
ELSE	Ensemble Land State Estimator
ENSO	El Niño–Southern Oscillation
EOS	Earth Observing System
EOS	end of season
ERA5	European Centre for Medium-Range Forecasts Reanalysis version 5
ERB	Earth's radiation budget
ESA CCI SM	European Space Agency Climate Change Initiative for Soil Moisture
ET	evapotranspiration
ETCCDI	Expert Team on Climate Change Detection and Indices
FAPAR	Fraction of absorbed photosynthetically active radiation
FLASHFlux	Fast Longwave and Shortwave Radiative Fluxes
GFAS	Global Fire Assimilation System
GHCN	Global Historical Climatology Network
GISS	Goddard Institute for Space Studies
GLEAM	Global Land Evaporation Amsterdam Model
GLoSSAC	Global Space-based Stratospheric Aerosol Climatology
GNSS	Global Navigation Satellite System
GPCC	Global Precipitation Climatology Centre
GPCP	Global Precipitation Climatology Project
GPS-RO	Global Positioning System–Radio Occultation

GRACE	Gravity Recovery and Climate Experiment
GRACE-FO	GRACE Follow On
G-REALM	Global Reservoir and Lake Monitoring
GrIS	Greenland ice sheet
GTN-P	Global Terrestrial Network for Permafrost
H_2O	water
HIRS	High Resolution Infrared Sounder
IFS	Integrated Forecasting System
IOD	Indian Ocean dipole
JAS	July, August, September
JJA	June, July, August
JPL	Jet Propulsion Laboratory
JRA-55	Japanese global atmospheric reanalysis
LLGHGs	long-lived greenhouse gases
LST	lower stratospheric temperature
LSWT	lake surface water temperature
LTT	lower tropospheric temperature
MACC	Monitoring Atmospheric Composition and Climate
MHW	marine heat wave
MISR	Multi-angle Imaging SpectroRadiometer
MLO	Mauna Loa (Hawaii)
MLS	Microwave Limb Sounder
MLSOL	Mauna Loa Stratospheric Ozone Lidar
MODIS C6	Moderate Resolution Imaging Spectroradiometer Collection 6
MOPITT	Measurement of Pollution in the Troposphere
MSLP	mean sea level pressure
N_2O	nitrous oxide
NA	North America
NAO	North Atlantic Oscillation
NDACC	Network for the Detection of Atmospheric Composition Change
NDVI	normalized difference vegetation index
NH	Northern Hemisphere
O_3	ozone
OCS	carbonyl sulfide
ODS	ozone depleting substance
OH	hydroxyl
OLR	outgoing longwave radiation
OMI	Ozone Monitoring Instrument
OMPS/LP	Ozone Mapping and Profiler Suite/Limb Profiler
ONI	Oceanic Niño Index
PATMOS-x/AVHRR	Pathfinder Atmospheres Extended/Advanced Very High Resolution Radiometer
PDO	Pacific Decadal Oscillation
POES	Polar Operational Environmental Satellites
ppb	parts per billion
ppm	parts per million
QBO	Quasi-Biennial Oscillation

QTP	Qinghai-Tibetan Plateau
RFaci	radiative forcing resulting from aerosol–cloud interactions
RFari	radiative forcing resulting from aerosol–radiation
RSS	Remote Sensing Systems
RSW	reflected shortwave
sAOD	stratospheric aerosol optical depth
SatCORPS	satellite cloud and radiative property retrieval system
SCE	snow cover extent
scPDSI	self-calibrating Palmer Drought Severity Index
SH	Southern Hemisphere
SO_2	sulfur dioxide
SOI	Southern Oscillation Index
SORCE	Solar Radiation and Climate Experiment
SOS	start of season
SPO	South Pole Observatory
SSM/I	Special Sensor Microwave/Imager
SSMIS	Special Sensor Microwave Imager/Sounder
SST	sea surface temperature
SSU	Stratospheric Sounding Unit
SSW	sudden stratospheric warming
SWV	stratospheric water vapor
TCCON	Total Carbon Column Observing Network
TCWV	total column water vapor
TMI	Tropical Rainfall Measuring Mission Microwave Imager
TOA	top of the atmosphere
TSI	total solar irradiance
TTL	tropical tropopause layer
TTT	tropical trophospheric temperature
TWS	terrestrial water storage
UTH	upper troposphere (relative) humidity
UV	ultraviolet
WGMS	World Glacier Monitoring Service
WMO	World Meteorological Organization
ZAA	zero annual amplitude

Appendix 2: Supplemental Material

2b1 Surface air temperature

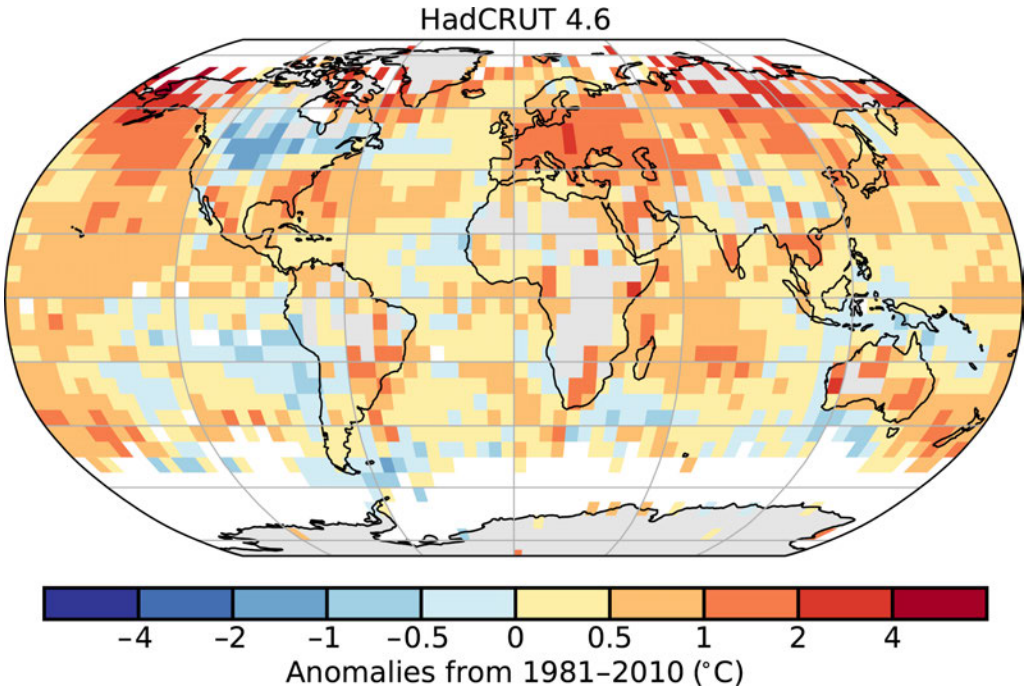

Fig. A2.1. Global land and ocean surface annual temperature anomalies for 2019 (°C; 1981–2010 base period). (Source: HadCRUT4.)

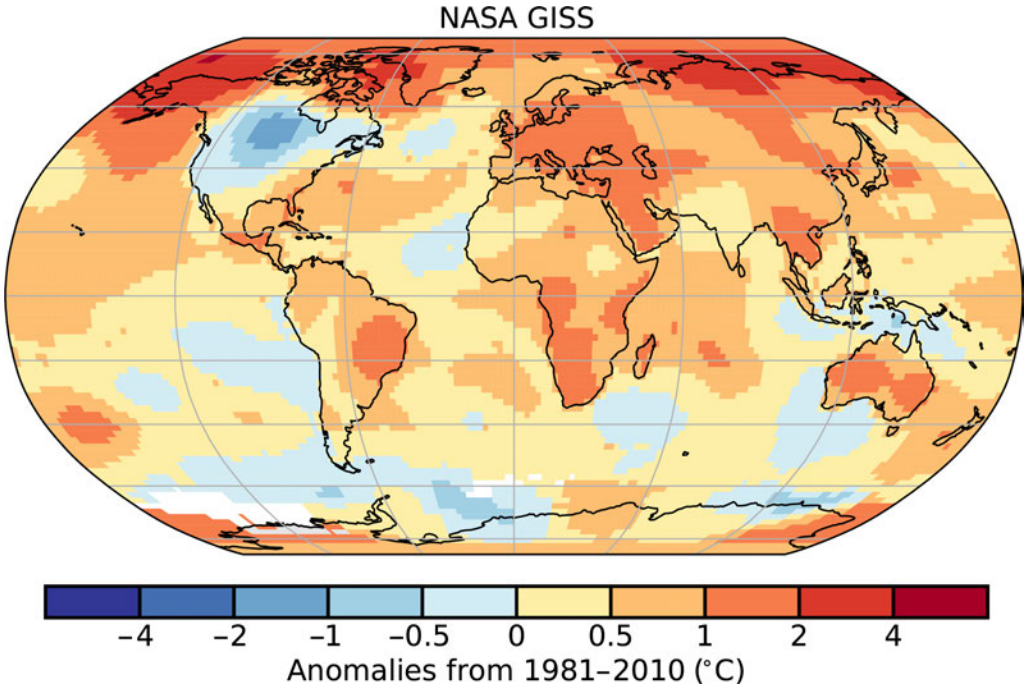

Fig. A2.2. Global land and ocean surface annual temperature anomalies for 2019 (°C; 1981–2010 base period). (Source: NASA GISTEMP.)

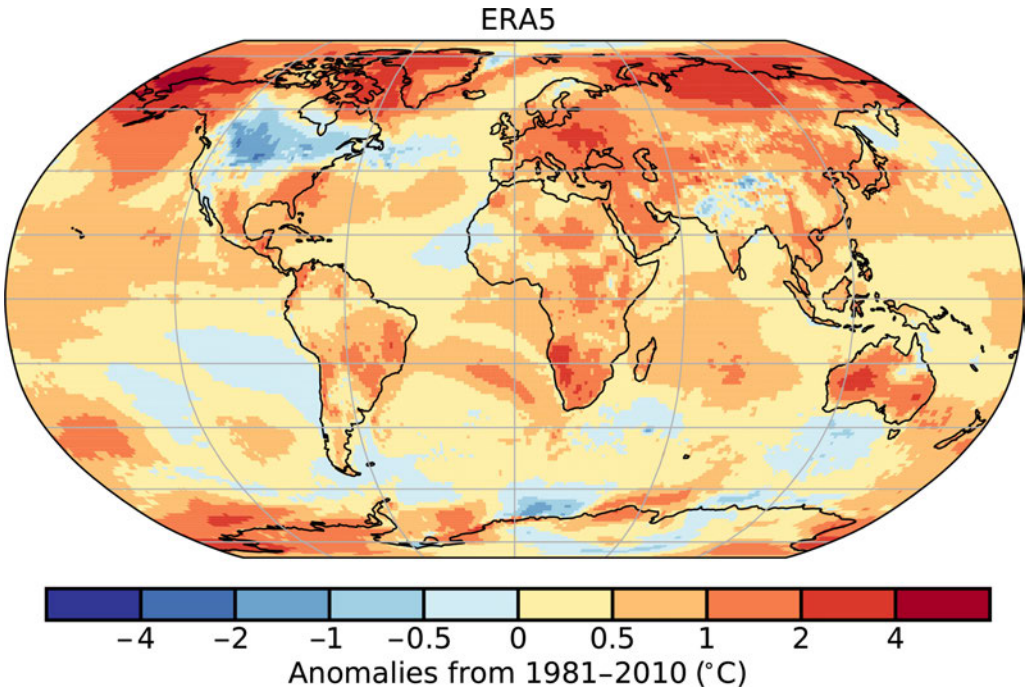

Fig. A2.3. Global land and ocean surface annual temperature anomalies for 2019 (°C; 1981–2010 base period). (Source: ERA5.)

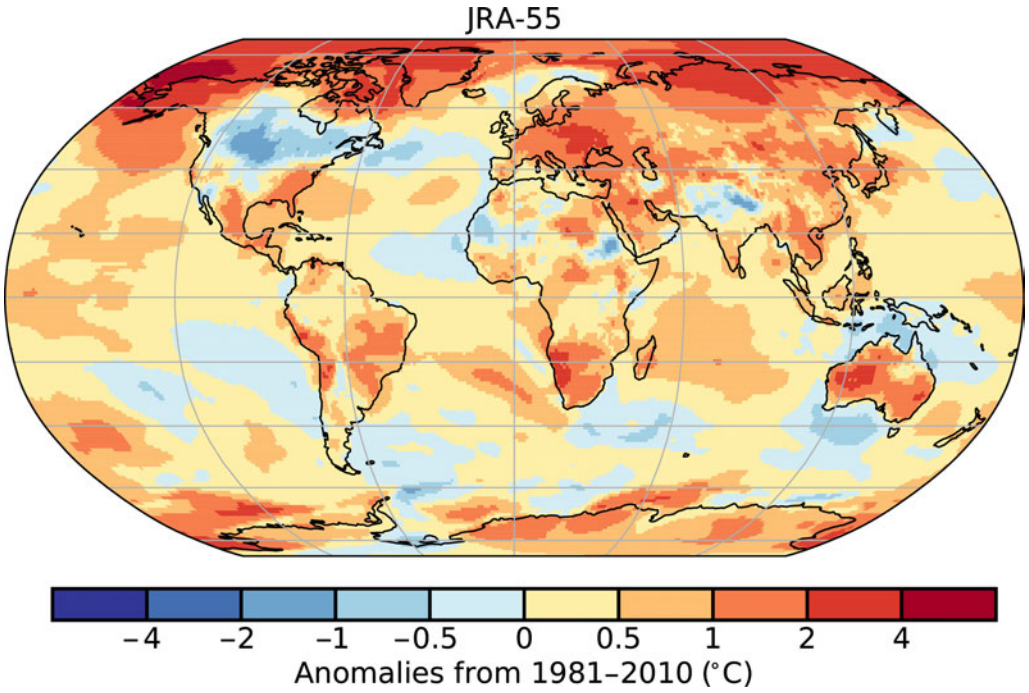

Fig. A2.4. Global land and ocean surface annual temperature anomalies for 2019 (°C; 1981–2010 base period). (Source: JRA-55.)

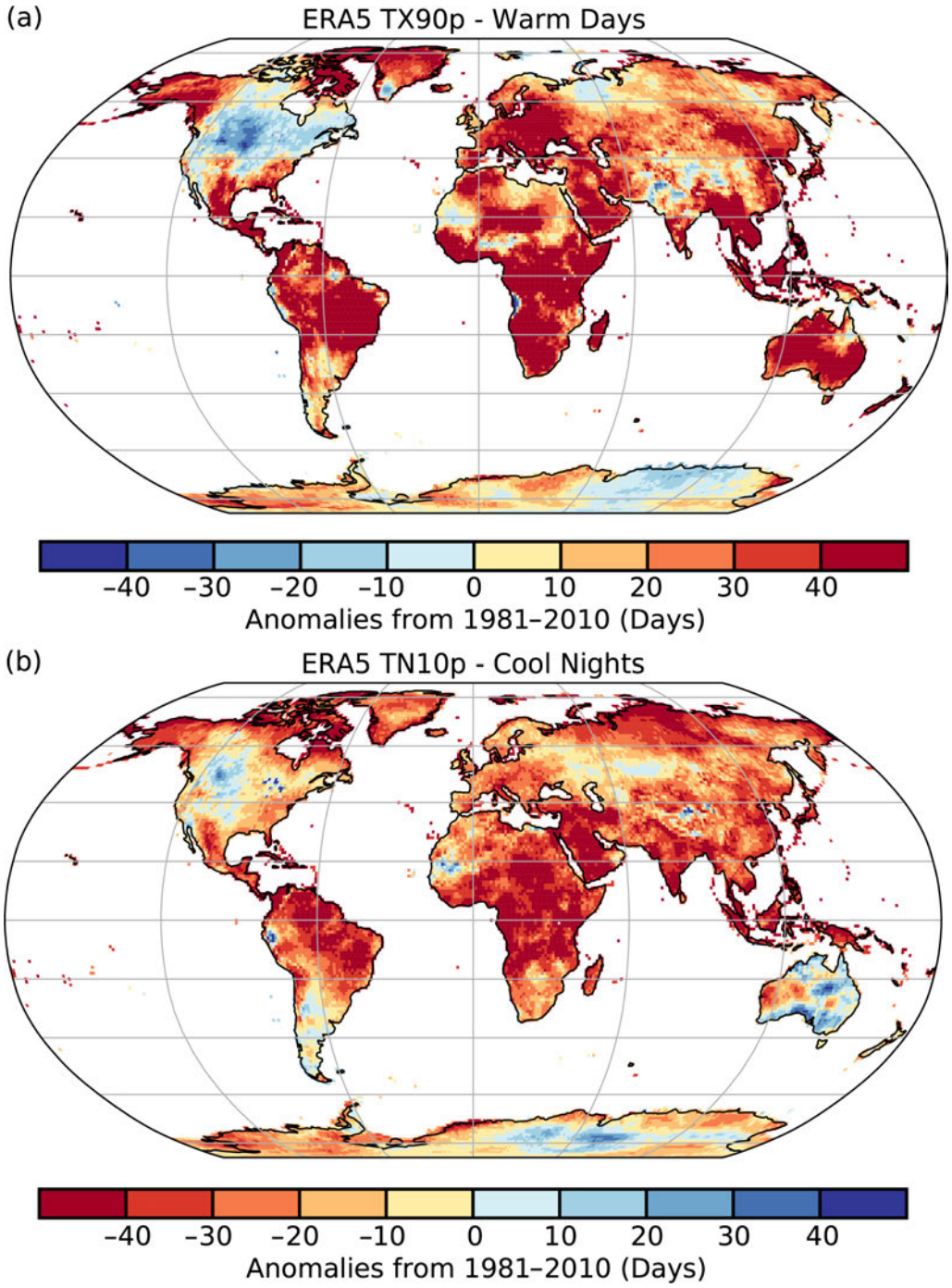

Fig. A2.5. (a) warm day threshold exceedance (TX90p), (b) cool night threshold exceedance (TN10p) in 2019. (Source: ERA5.)

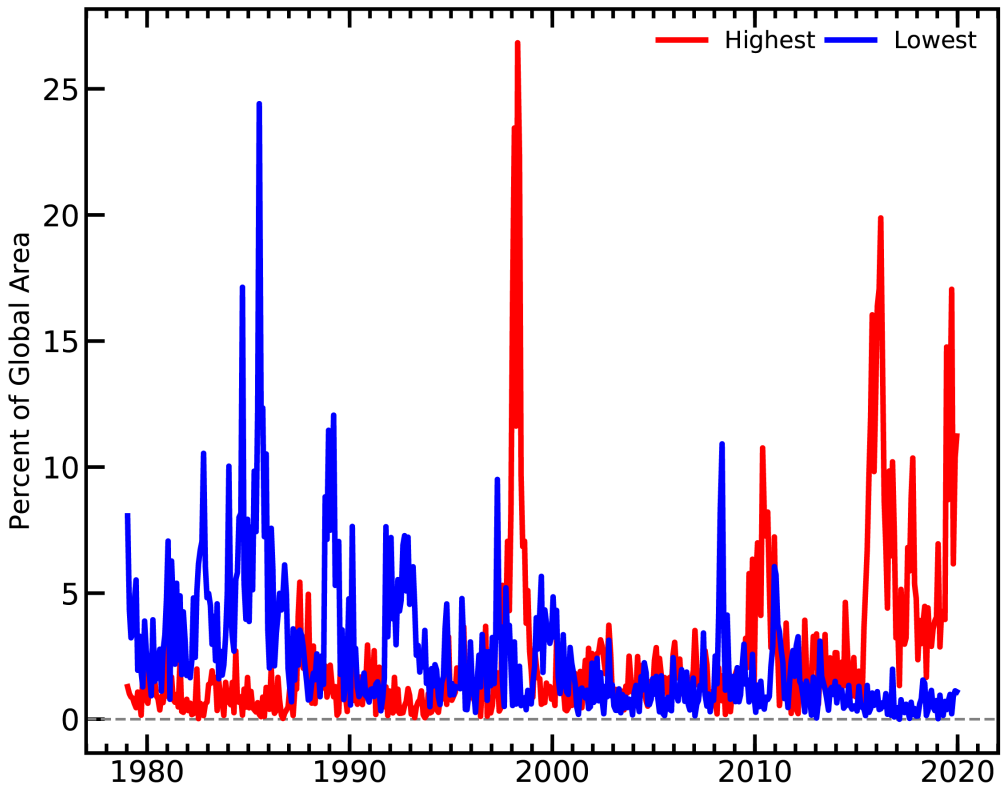

Fig. A2.6. Average area of highest (red) (blue) and lowest temperatures by month for the 41 years of observations in ERA5, RSS, and UAH datasets. This is an update of the figure from SotC 2018 (Christy et. al. 2019).

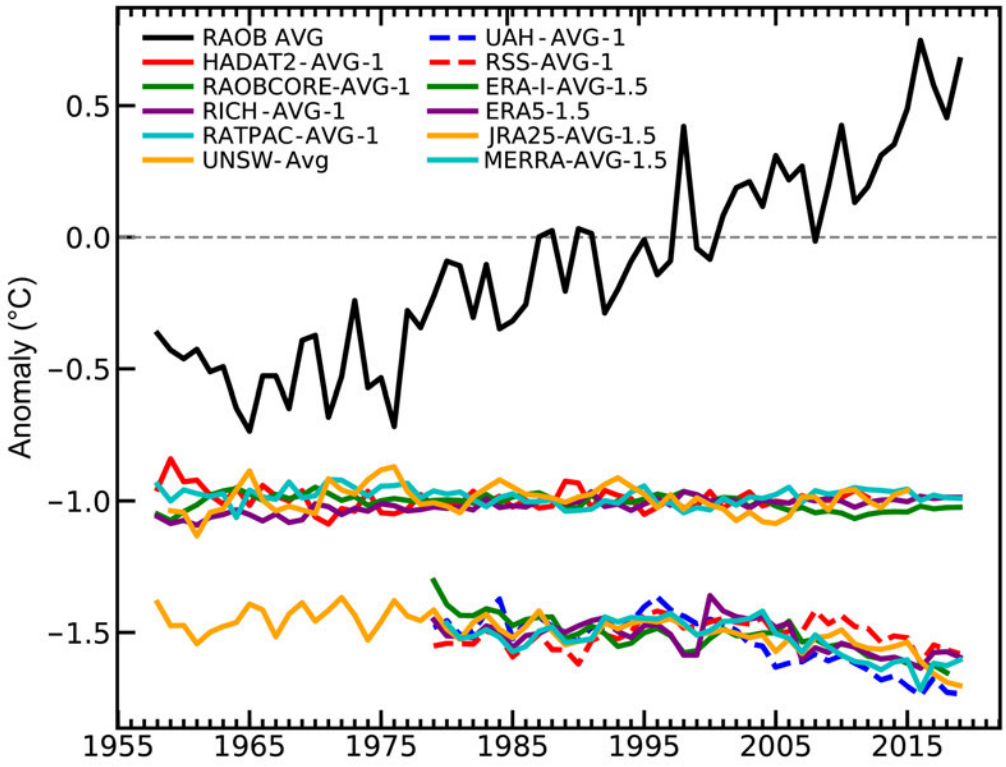

Fig. A2.7. (Top) Time series of annual anomalies of global lower tropospheric temperature (°C)from radiosonde datasets only. (Middle) Differences of individual radiosonde datasets (at –1.0°C axis) versus the radiosonde average. (Bottom) Differences relative to the radiosonde average (top) for satellite and reanalyses (at –1.5°C axis). As noted in the text, those datasets that are not exclusively radiosondes (bottom) show decreasing values after 2009 possibly related to spurious warming in the radiosondes as a consequence of a change in the software processing system at many of the stations.

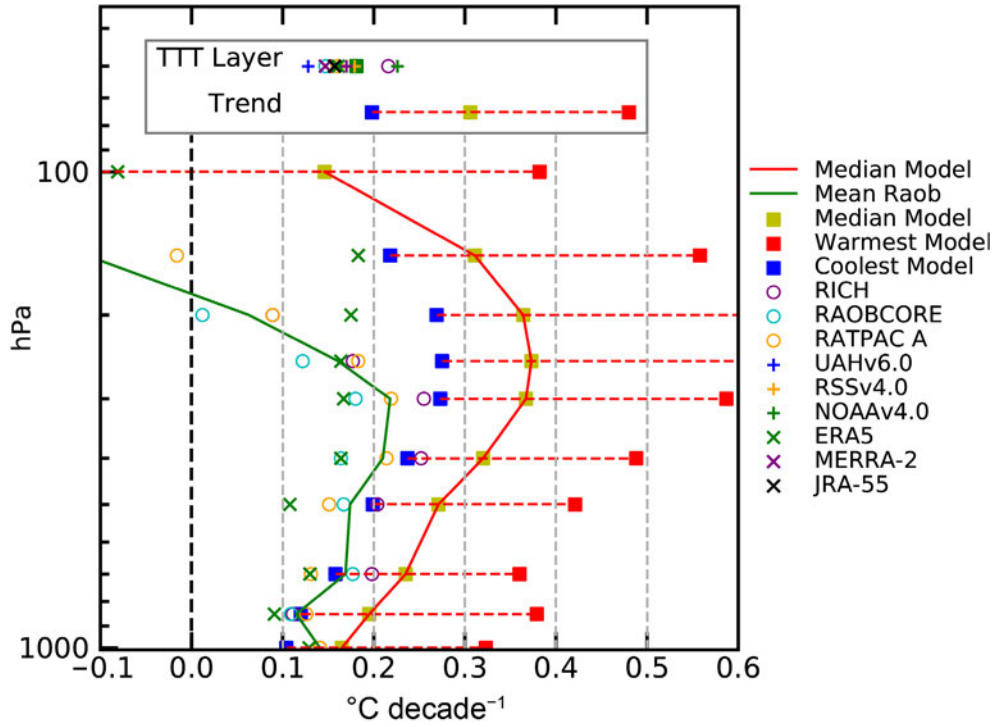

Fig. A2.8. Update of tropical temperature (TTT) trend comparisons (1979–2019) from SotC 2016 (Christy 2017) between observational datasets and the Climate Model Intercomparison Project version 6 (CMIP-6). The trend values for each pressure level are shown from 1000 to 100 hPa with central values represented by the green (mean radiosondes) and red (median model) lines. The upper box provides the trends for the average of the bulk atmospheric layer TTT as described in the text. The model time series are constructed with historical forcings from 1850 to 2014 and after 2014 with forcing scenario ssp245. The 30 CMIP-6 models used are ACCESS-CM2, ACCESS-ESM1-5, AWI-CM-1-1-MR, BCC-CSM2-MR, CanESM5 (warmest), CanESM5-OE, CESM2, CESM2-WACCM, CNRM-CM6-1, CNRM-ESM2, EC-EARTH3, EC-EARTH3-VEG, FGOALS, FIO, GFDL-CM4, GFDL-ESM, GISS-E2-1-G, HadGEM, INM-CM4-8, INM-CM5-0, IPSL-CM6A-LR, MCM-UA, MIROC6, MIROC6-2L MPI-ESM1-2-HR, MPI-ESM1-2-LR, MRI-ESM2-0 (coolest), NESM, NorESM2-LM, and UKESM1-0-LL.

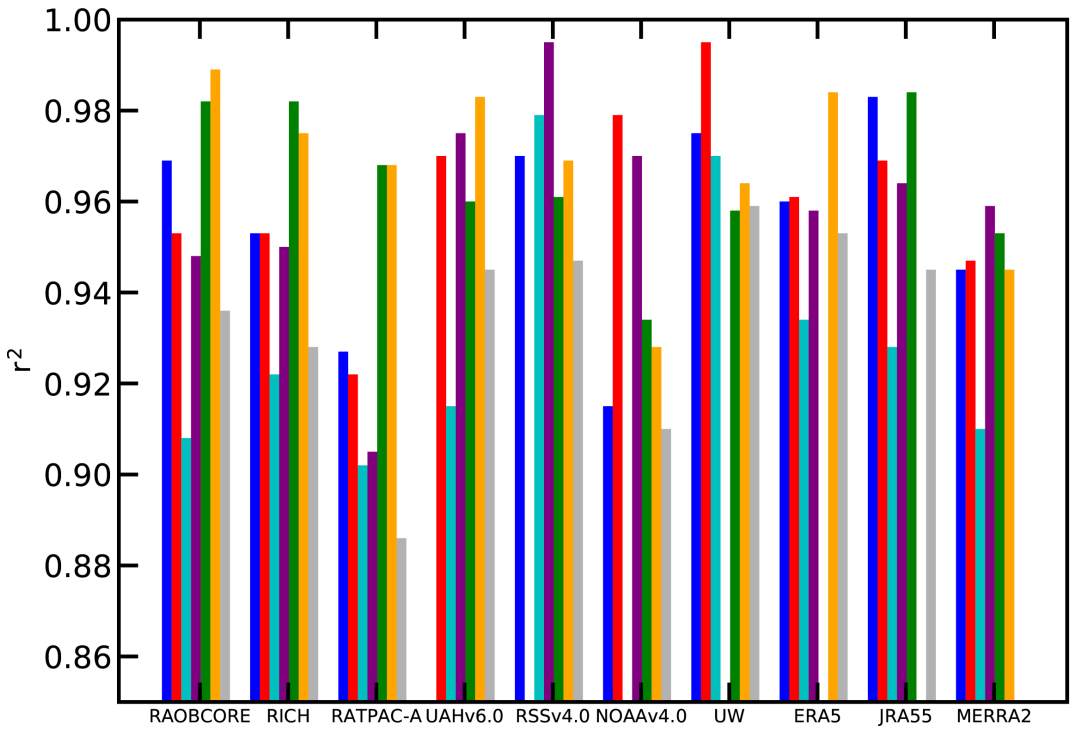

Fig. A2.9. Paired intercomparisons of the datasets utilized here for the tropical TTT metric, calculating the extent to which the identified paired datasets agree in terms of common variance (r^2).

Table A2.1. Comparison of decadal trend values (°C decade^{-1}) between observations and CMIP-6 climate model simulations. (See Fig. A2.8)

Area		Global	Global	Tropical	Tropical
Layer		LTT	LTT	TTT	TTT
Start year		1958	1979	1958	1979
Median	Observations	+0.18	+0.18	+0.16	+0.16
Median	CMIP6 (30 models)	+0.20	+0.29	+0.22	+0.32

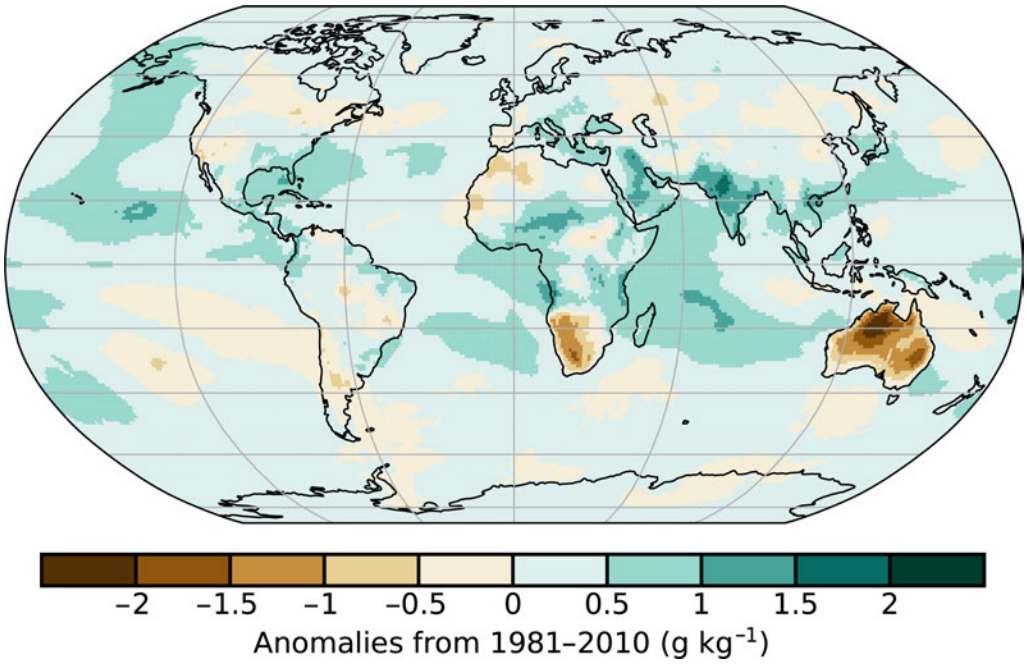

Fig. A2.10. Surface specific humidity anomalies for 2019. (Source: ERA5.)

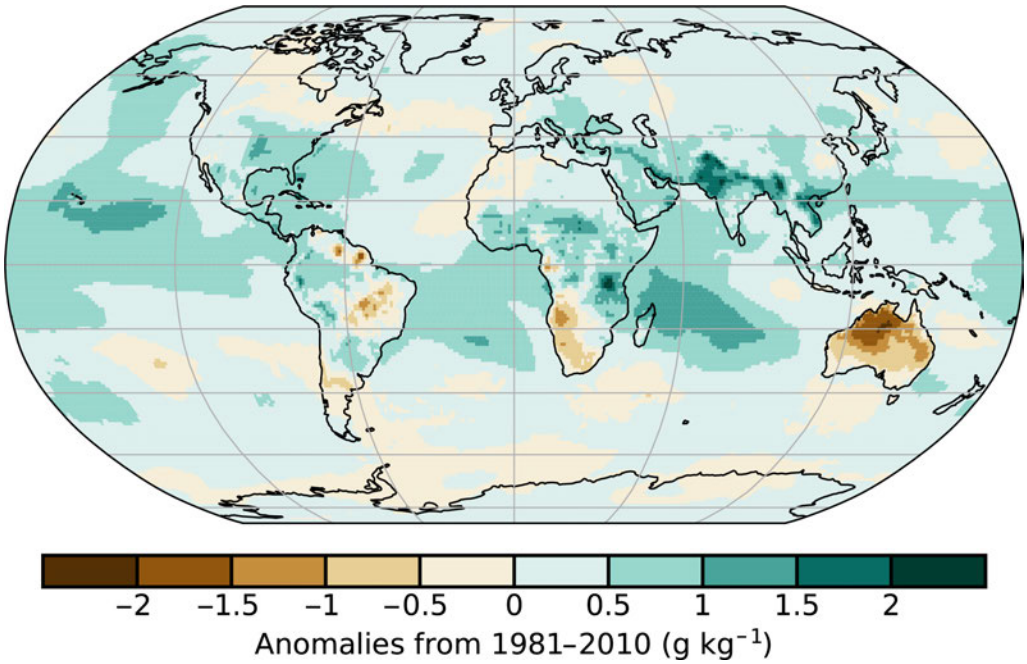

Fig. A2.11. Surface specific humidity anomalies for 2019. (Source: MERRA-2.)

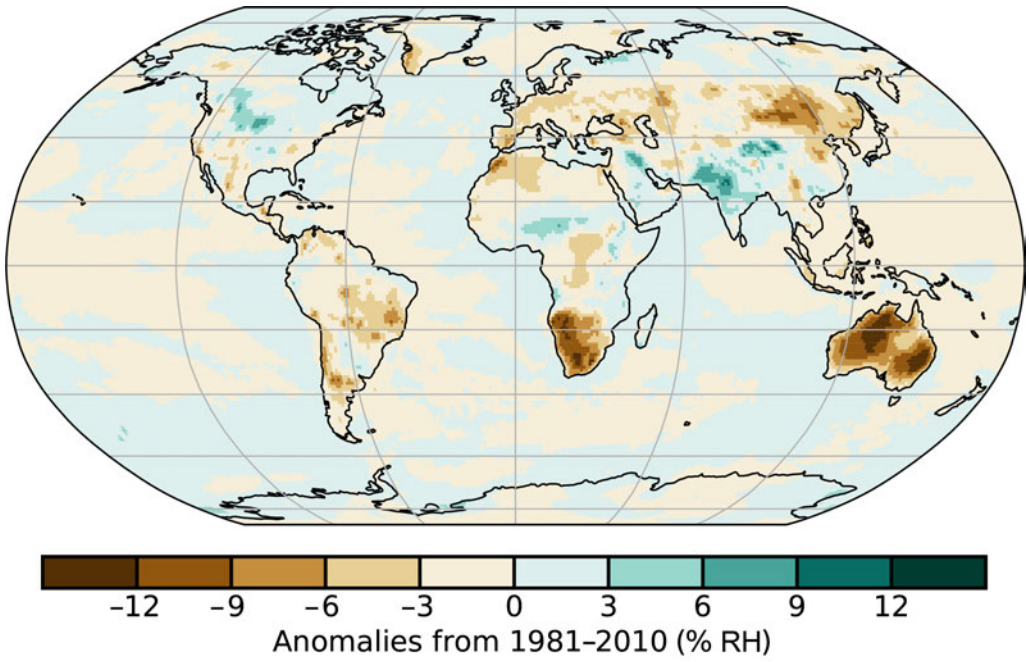

Fig. A2.12. Surface relative humidity anomalies for 2019. (Source: ERA5.)

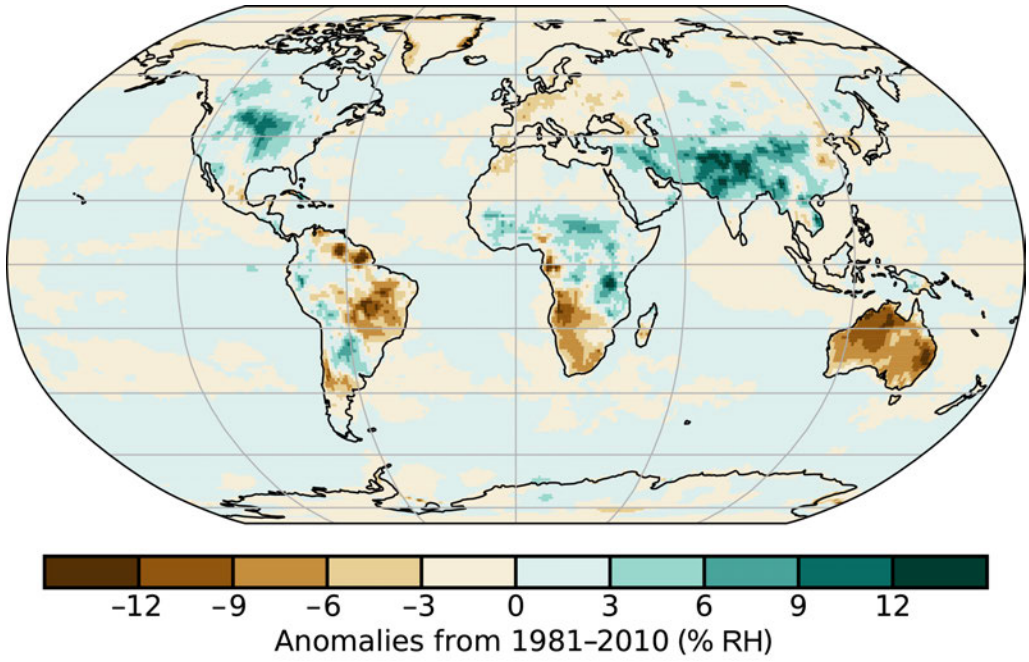

Fig. A2.13. Surface relative humidity anomalies for 2019. (Source: MERRA-2.)

2d2 Total column water vapor

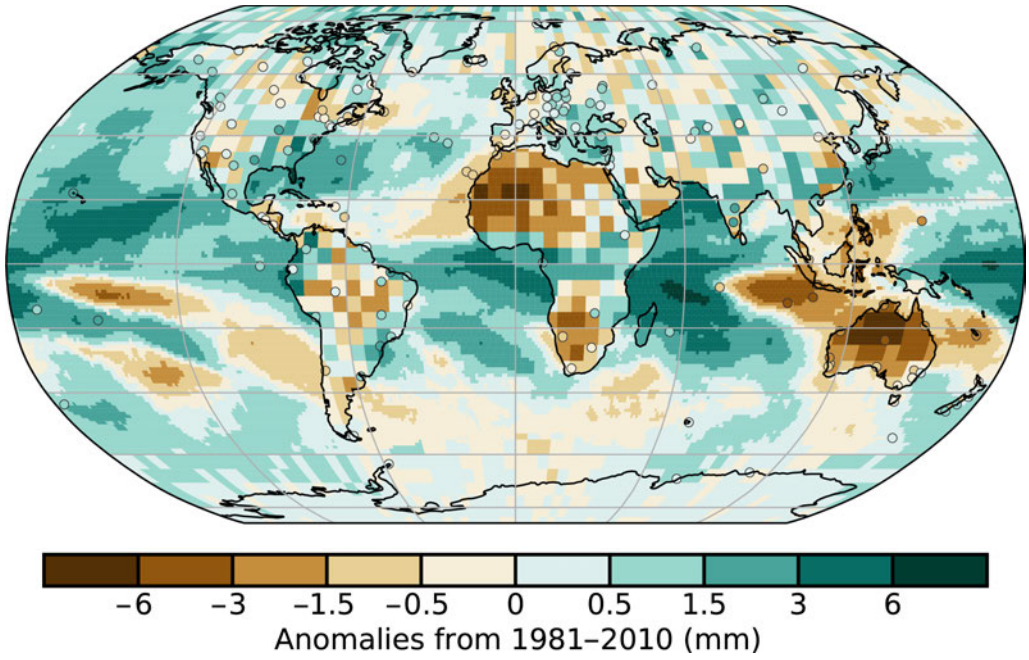

Fig. A2.14. Total column water vapor anomalies for 2019 relative to a 1981–2010 base period. Over the oceans, the data are from COSMIC, GPS RO, and satellite radiometers, and from COSMIC and GPS RO over land.

2d3 Upper tropospheric humidity

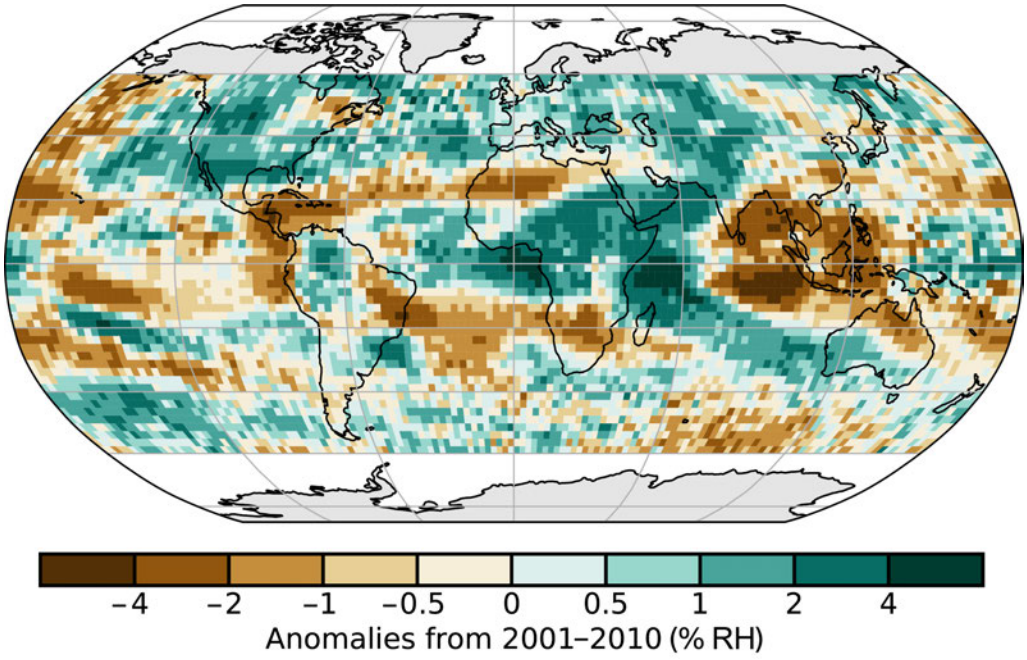

Fig. A2.15. Annual average upper tropospheric humidity anomalies anomaly map for 2019 relative to the 2001–10 climatology based on the HIRS dataset.

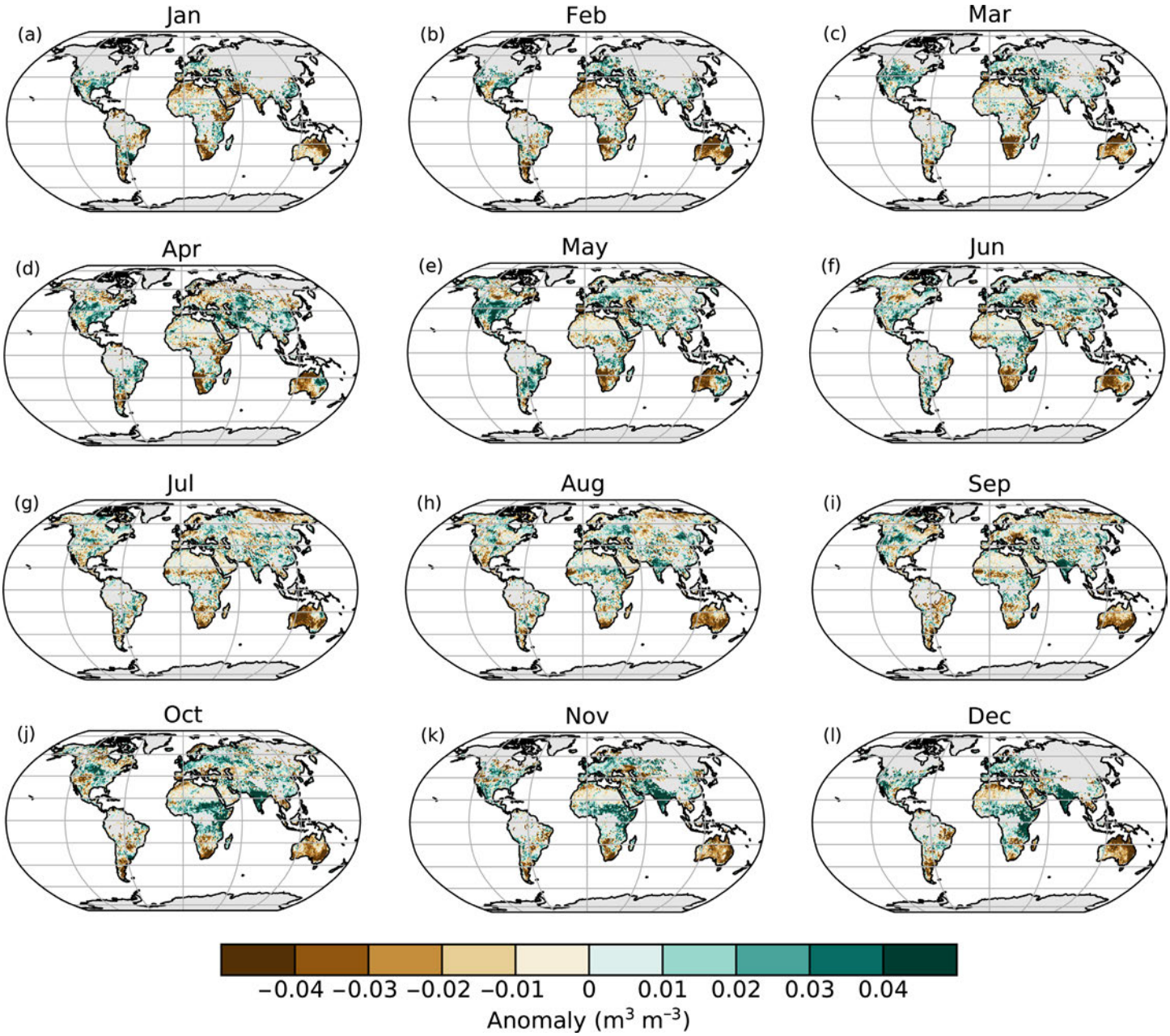

Fig. A2.16. Monthly soil moisture anomalies for 2019 (base period: 1991–2010). Data were masked as missing where retrievals are either not possible or of very low quality (dense forests, frozen soil, snow, ice, etc.). (Source: ESA CCI Soil Moisture.)

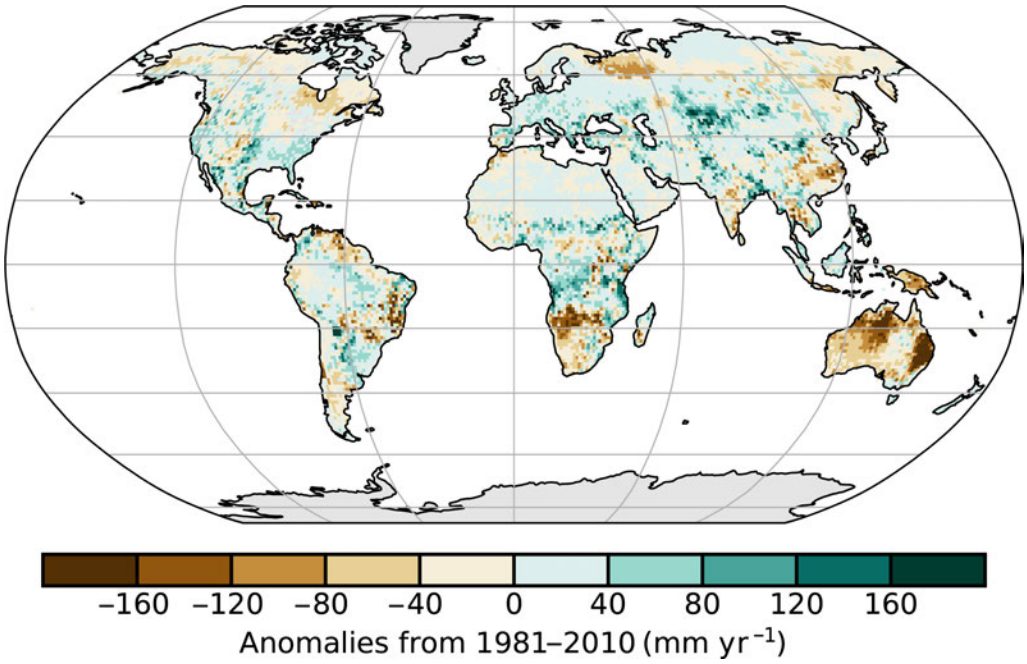

Fig A2.17. Plant transpiration anomalies (mm yr^{-1}). (Source: GLEAM.)

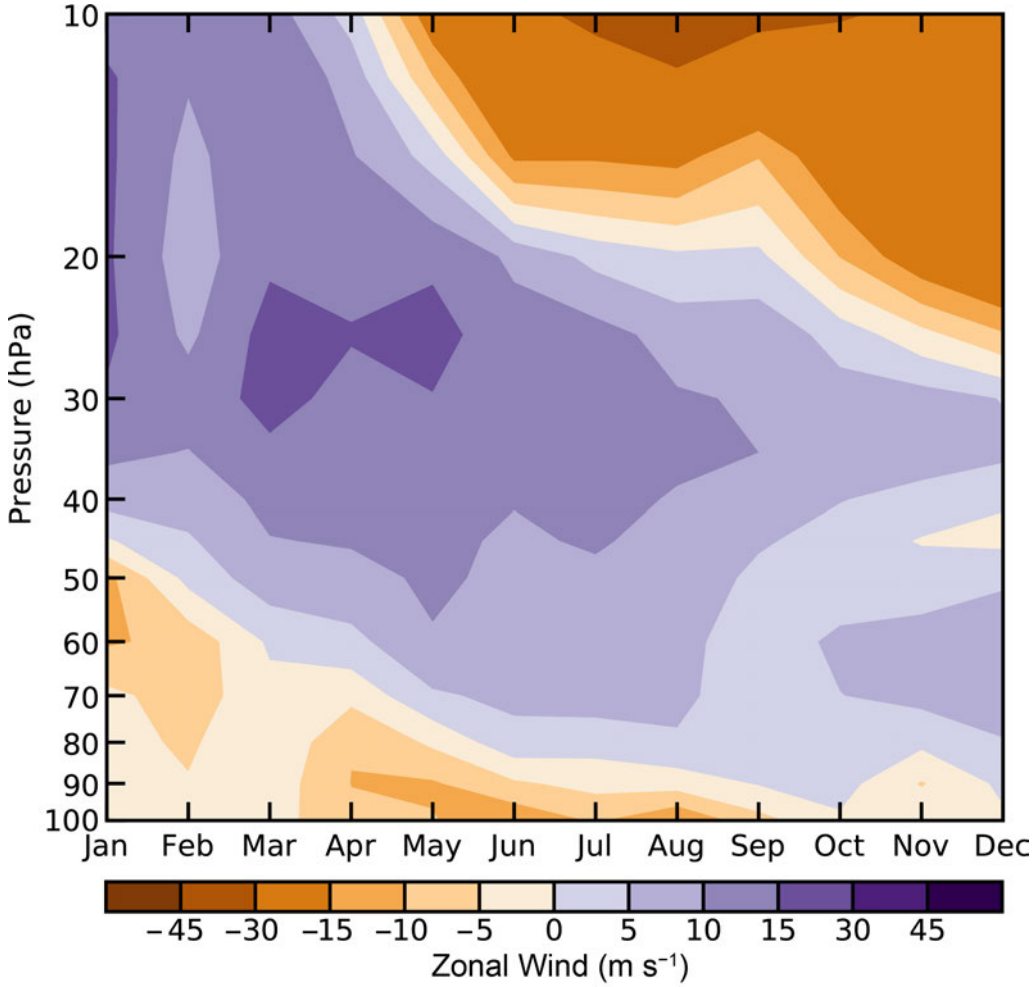

Fig. A2.18. Stratospheric monthly mean zonal winds over Singapore in 2019. Purple depicts westerly, brown easterly wind.

References

Adler, R., and Coauthors, 2018: The Global Precipitation Climatology Project (GPCP) monthly analysis (new version 2.3) and a review of 2017 global precipitation. *Atmosphere*, **9**, 138, https://doi.org/10.3390/atmos9040138.

Adrian, R., and T. Hintze, 2000: Effects of winter air temperature on the ice phenology of the Müggelsee (Berlin, Germany). *SIL Proc.*, **27**, 2808–2811, https://doi.org/10.1080/03680770.1998.11898178.

Allan, R. J., and R. D. D'Arrigo, 1999: 'Persistent' ENSO sequences: How unusual was the 1990–1995 El Niño? *Holocene*, **9**, 101–118, https://doi.org/10.1191/095968399669125102.

——, and T. Ansell, 2006: A new globally complete monthly historical gridded mean sea level pressure dataset (HadSLP2): 1850–2004. *J. Climate*, **19**, 5816–5842, https://doi.org/10.1175/JCLI3937.1.

——, J. A. Lindesay, and D. E. Parker, 1996: El Niño Southern Oscillation and Climatic Variability. CSIRO Publishing, 405 pp.

——, J. Gergis, and R. D. D'Arrigo, 2019: Placing the 2014–2016 'protracted' El Niño episode into a long-term context. *Holocene*, **30**, 90–105, https://doi.org/10.1177/0959683619875788.

Allan, R. P., K. P. Shine, A. Slingo, and J. A. Pamment, 1999: The dependence of clear-sky outgoing longwave radiation on surface temperature and relative humidity. *Quart. J. Roy. Meteor. Soc.*, **125**, 2103–2126, https://doi.org/10.1002/qj.49712555809.

Anabalón, A., and A. Sharma, 2017: On the divergence of potential and actual evapotranspiration trends: An assessment across alternate global datasets. *Earth's Future*, **5**, 905–917, https://doi.org/10.1002/2016EF000499.

Andela, N., and Coauthors, 2017: A human-driven decline in global burned area. *Science*, **356**, 1356–1362, https://doi.org/10.1126/science.aal4108.

Andersson, S. M., B. G. Martinsson, J.-P. Vernier, J. Friberg, C. A. M. Brenninkmeijer, M. Hermann, P. F. J. van Velthoven, and A. Zahn, 2015: Significant radiative impact of volcanic aerosol in the lowermost stratosphere. *Nat. Commun.*, **6**, 7692, https://doi.org/10.1038/ncomms8692.

Aquila, V., L. D. Oman, R. Stolarski, A. R. Douglass, and P. A. Newman, 2013: The response of ozone and nitrogen dioxide to the eruption of Mt. Pinatubo at southern and northern midlatitudes. *J. Atmos. Sci.*, **70**, 894–900, https://doi.org/10.1175/JAS-D-12-0143.1.

Arguez, A., S. Hurley, A. Inamdar, L. Mahoney, A. Sanchez-Lugo, and L. Yang, 2020: Should we expect each year in the next decade (2019–2028) to be ranked among the top 10 warmest years globally? *Bull. Amer. Meteor. Soc.*, **101**, E655–E663, https://doi.org/10.1175/BAMS-D-19-0215.1.

Arosio, C., A. Rozanov, E. Malinina, M. Weber, and J. P. Burrows, 2019: Merging of ozone profiles from SCIAMACHY, OMPS and SAGE II observations to study stratospheric ozone changes. *Atmos. Meas. Tech.*, **12**, 2423–2444, https://doi.org/10.5194/amt-12-2423-2019.

Arp, C. D., B. M. Jones, and G. Gross, 2013: Recent lake ice-out phenology within and among lake districts of Alaska, U.S.A. *Limnol. Oceanogr.*, **58**, 2013–2028, https://doi.org/10.4319/lo.2013.58.6.2013.

Ashok, K., Z. Guan, and T. Yamagata, 2003: Influence of the Indian Ocean Dipole on the Australian winter rainfall. *Geophys. Res. Lett.*, **30**, 1821, https://doi.org/10.1029/2003gl017926.

Azorin-Molina, C., J. A. Guijarro-Pastor, T. R. McVicar, S. M. Vicente-Serrano, D. Chen, S. Jerez, and F. Espirito-Santo, 2016: Trends of daily peak wind gusts in Spain and Portugal, 1961–2014. *J. Geophys. Res. Atmos.*, **121**, 1059–1078, https://doi.org/10.1002/2015jd024485.

——, S. Rehman, J. A. Guijarro, T. R. McVicar, L. Minola, D. Chen, and S. M. Vicente-Serrano, 2018a: Recent trends in wind speed across Saudi Arabia, 1978–2013: A break in the stilling. *Int. J. Climatol.*, **38**, e966–e984, https://doi.org/10.1002/joc.5423.

——, J. Asin, T. R. McVicar, L. Minola, J. I. Lopez-Moreno, S. M. Vicente-Serrano, and D. Chen, 2018b: Evaluating anemometer drift: A statistical approach to correct biases in wind speed measurement. *Atmos. Res.*, **203**, 175–188, https://doi.org/10.1016/j.atmosres.2017.12.010.

——, R. J. H. Dunn, C. A. Mears, P. Berrisford, T. R. McVicar, and J. P. Nicolas, 2019: Surface winds [in "State of the Climate in 2018"]. *Bull. Amer. Meteor. Soc.*, **100** (9), S43–S45, https://doi.org/10.1175/2019BAMSStateoftheClimate.1.

Ball, W. T., and Coauthors, 2018: Evidence for a continuous decline in lower stratospheric ozone offsetting ozone layer recovery. *Atmos. Chem. Phys.*, **18**, 1379–1394, https://doi.org/10.5194/acp-18-1379-2018.

Balsamo, G., R. Salgado, E. Dutra, S. Boussetta, T. Stockdale, and M. Potes, 2012: On the contribution of lakes in predicting near-surface temperature in a global weather forecasting model. *Tellus*, **64A**, 15829, https://doi.org/10.3402/tellusa.v64i0.15829.

Bândă, N., M. Krol, M. van Weele, T. van Noije, and T. Röckmann, 2013: Analysis of global methane changes after the 1991 Pinatubo volcanic eruption. *Atmos. Chem. Phys.*, **13**, 2267–2281, https://doi.org/10.5194/acp-13-2267-2013.

Banzon, V., T. M. Smith, T. M. Chin, C. Liu, and W. Hankins, 2016: A long-term record of blended satellite and in situ sea-surface temperature for climate monitoring, modeling and environmental studies. *Earth Syst. Sci. Data*, **8**, 165–176, https://doi.org/10.5194/essd-8-165-2016.

——, ——, M. Steele, B. Huang, and H. M. Zhang, 2020: Improved estimation of proxy sea surface temperature in the Arctic. *J. Atmos. Oceanic Technol.*, **37**, 341–349, https://doi.org/10.1175/JTECH-D-19-0177.1.

Barichivich, J., T. J. Osborn, I. Harris, G. van der Schrier, and P. D. Jones, 2019: Drought [in "State of the Climate in 2018"]. *Bull. Amer. Meteor. Soc.*, **100** (9), S39–S40, https://doi.org/10.1175/2019BAMSStateoftheClimate.1.

Barnes, E. A., A. M. Fiore, and L. W. Horowitz, 2016: Detection of trends in surface ozone in the presence of climate variability. *J. Geophys. Res. Atmos.*, **121**, 6112–6129, https://doi.org/10.1002/2015jd024397.

Barnes, J. E., and D. J. Hofmann, 1997: Lidar measurements of stratospheric aerosol over Mauna Loa Observatory. *Geophys. Res. Lett.*, **24**, 1923–1926, https://doi.org/10.1029/97GL01943.Becker, A., P. Finger, A. Meyer-Christoffer, B. Rudolf, K. Schamm, U. Schneider, and M. Ziese, 2013: A description of the global land-surface precipitation data products of the Global Precipitation Climatology Centre with sample applications including centennial (trend) analysis from 1901–present. *Earth Syst. Sci. Data*, **5**, 71–99, https://doi.org/10.5194/essd-5-71-2013.

Bellouin, N., and Coauthors, 2020: Radiative forcing of climate change from the Copernicus reanalysis of atmospheric composition. *Earth Syst. Sci. Data Discuss.*, https://doi.org/10.5194/essd-2019-251.

Benson, B., J. Magnuson, and S. Sharma, 2000: Global lake and river ice phenology database, version 1. National Snow and Ice Data Center, accessed 20 January 2020, https://doi.org/10.7265/N5W66HP8.

Berry, D. I., and E. C. Kent, 2009: A new air-sea interaction gridded dataset from ICOADS with uncertainty estimates. *Bull. Amer. Meteor. Soc.*, **90**, 645–656, https://doi.org/10.1175/2008BAMS2639.1.

——, and ——, 2011: Air–sea fluxes from ICOADS: The construction of a new gridded dataset with uncertainty estimates. *Int. J. Climatol.*, **31**, 987–1001, https://doi.org/10.1002/joc.2059.

Betts, R. A., C. D. Jones, J. R. Knight, R. F. Keeling, and J. J. Kennedy, 2016: El Niño and a record CO2 rise. *Nat. Climate Change*, **6**, 806–810, https://doi.org/10.1038/nclimate3063.

Beusen, A. H. W., A. F. Bouwman, L. P. H. Van Beek, J. M. Mogollón, and J. J. Middelburg, 2016: Global riverine N and P transport to ocean increased during the 20th century despite increased retention along the aquatic continuum. *Biogeosciences*, **13**, 2441–2451, https://doi.org/10.5194/bg-13-2441-2016.

Biskaborn, B. K., and Coauthors, 2019: Permafrost is warming at a global scale. *Nat. Commun.*, **10**, 264, https://doi.org/10.1038/s41467-018-08240-4.

Bock, O., 2019: Global GNSS IWV data at 436 stations over the 1994-2018 period. AERIS, accessed 7 July 2020, https://doi.org/10.25326/18.

——, and A. C. Parracho, 2019: Consistency and representativeness of integrated water vapour from ground-based GPS observations and ERA-Interim reanalysis. *Atmos. Chem. Phys.*, **19**, 9453–9468, https://doi.org/10.5194/acp-19-9453-2019.

Bodhaine, B. A., B. G. Mendonca, J. M. Harris, and J. M. Miller, 1981: Seasonal variations in aerosols and atmospheric transmission at Mauna Loa Observatory. *J. Geophys. Res.*, **86**, 7395–7398, https://doi.org/10.1029/JC086iC08p07395.

BoM, 2020: Climate monitoring graphs. Australian Bureau of Meteorology. www.bom.gov.au/climate/enso/indices.shtml?bookmark=iod.

Brohan, P., J. J. Kennedy, I. Harris, S. F. Tett, and P. D. Jones, 2006: Uncertainty estimates in regional and global observed temperature changes: A new data set from 1850. *J. Geophys. Res.*, **111**, D12106, https://doi.org/10.1029/2005JD006548.

Brown, L. C., and C. R. Duguay, 2010: The response and role of ice cover in lake-climate interactions. *Prog. Phys. Geogr.*, **34**, 671–704, https://doi.org/10.1177/0309133310375653.

Brutsaert, W., 2017: Global land surface evaporation trend during the past half century: Corroboration by Clausius-Clapeyron scaling. *Adv. Water Resour.*, **106**, 3–5, https://doi.org/10.1016/j.advwatres.2016.08.014.

Buchard, V., A. M. da Silva, C. A. Randles, C. Colarco, R. Ferrare, J. Hair, C. Hostetler, J. Tackett, and D. Winker: Evaluation of the surface PM2.5 in version 1 of the NASA MERRA aerosol reanalysis over the United States. *Atmos. Environ.*, **125**, 100–111, https://doi.org/10.1016/j.atmosenv.2015.11.004.

Capotondi, A., and Coauthors, 2015: Understanding ENSO diversity. *Bull. Amer. Meteor. Soc.*, **96**, 921–938, https://doi.org/10.1175/BAMS-D-13-00117.1.

Carpenter, L. J., and J. S. Daniel, 2018: Scenarios and information for policy makers. Scientific Assessment of Ozone Depletion: 2018, Global Ozone Research and Monitoring Project Rep. 58, 6.1–6.69, https://ozone.unep.org/sites/default/files/2019-05/SAP-2018-Assessment-report.pdf.

Carrea, L., O. Embury, and C. J. Merchant, 2015: Datasets related to in-land water for limnology and remote sensing applications: Distance-to-land, distance-to-water, water-body identifier and lake-centre co-ordinates. *Geosci. Data J.*, **2**, 83–97, https://doi.org/10.1002/gdj3.32.

——, and Coauthors, 2019: Lake surface temperature [in "State of the Climate in 2018"]. *Bull. Amer. Meteor. Soc.*, **100** (9), S13–S14, https://doi.org/10.1175/2019BAMSStateoftheClimate.1.

Chandra, S., J. R. Ziemke, W. Min, and W. G. Read, 1998: Effects of 1997–1998 El Niño on tropospheric ozone and water vapor. *Geophys. Res. Lett.*, **25**, 3867–3870, https://doi.org/10.1029/98GL02695.

——, ——, B. N. Duncan, T. L. Diehl, N. Livesey, and L. Froidevaux, 2009: Effects of the 2006 El Niño on tropospheric ozone and carbon monoxide: Implications for dynamics and biomass burning. *Atmos. Chem. Phys.*, **9**, 4239–4249, https://doi.org/10.5194/acp-9-4239-2009.

Charlton, A. J., and L. M. Polvani, 2007: A new look at stratospheric sudden warmings. Part I. Climatology and modeling benchmarks. *J. Climate*, **20**, 449–469, https://doi.org/10.1175/JCLI3996.1.

Chen, C., and Coauthors, 2019: China and India lead in greening of the world through land-use management. *Nat. Sustain.*, **2**, 122–129, https://doi.org/10.1038/s41893-019-0220-7.

Chen, Z., P. K. Bhartia, R. Loughman, P. Colarco, and M. DeLand, 2018: Improvement of stratospheric aerosol extinction retrieval from OMPS/LP using a new aerosol model. *Atmos. Meas. Tech.*, **11**, 6495–6509, https://doi.org/10.5194/amt-11-6495-2018.

Cheng, G., and Coauthors, 2019: Characteristic, changes and impacts of permafrost on Qinghai-Tibet Plateau. *Chin. Sci. Bull.*, **64**, 2783–2795, https://doi.org/10.1360/TB-2019-0191.

Cheng, L., and Coauthors, 2017: Recent increases in terrestrial carbon uptake at little cost to the water cycle. *Nat. Commun.*, **8**, 110, https://doi.org/10.1038/s41467-017-00114-5.

Chipperfield, M. P., and Coauthors, 2018: On the cause of recent variations in lower stratospheric ozone. *Geophys. Res. Lett.*, **45**, 5718–5726, https://doi.org/10.1029/2018GL078071.

Chouza, F., T. Leblanc, J. Barnes, M. Brewer, P. Wang, and D. Koon, 2020: Long-term (1999-2019) variability of stratospheric aerosol over Mauna Loa, Hawaii, as seen by two co-located lidars and satellite measurements. *Atmos. Chem. Phys.*, **20**, 6821–6839, https://doi.org/10.5194/acp-20-6821-2020.

Christiansen, H. H., and Coauthors, 2010: The thermal state of permafrost in the nordic area during the international polar year 2007–2009. *Permafrost Periglacial Processes*, **21**, 156–181, https://doi.org/10.1002/ppp.687.

Christy, J. R., 2017: Lower tropospheric temperature [in "State of the Climate in 2016"]. *Bull. Amer. Meteor. Soc.*, **98** (8), S16–S17, https://doi.org/10.1175/2017BAMSStateoftheClimate.1.

——, and R. T. McNider, 2017: Satellite bulk tropospheric temperatures as a metric for climate sensitivity. *Asia-Pacific J. Atmos. Sci.*, **53**, 511–518, https://doi.org/10.1007/s13143-017-0070-z.

——, R. W. Spencer, W. D. Braswell, and R. Junod, 2018: Examination of space-based bulk atmospheric temperatures for climate research. *Int. J. Remote Sens.*, **39**, 3580–3607, https://doi.org/10.1080/01431161.2018.1444293.

——, S. Po-Chedley, C. Mears, and L. Haimberger, 2019: Lower tropospheric temperature [in "State of the Climate in 2018"]. *Bull. Amer. Meteor. Soc.*, **100** (8), S16–S17, https://doi.org/10.1175/2019BAMSStateoftheClimate.1.

Chung, E., B. Soden, and V. O. John, 2013: Intercalibrating microwave satellite observations for monitoring long-term variations in upper- and midtropospheric water vapor. *J. Atmos. Oceanic Technol.*, **30**, 2303–2319, https://doi.org/10.1175/JTECH-D-13-00001.1.

——, ——, X. Huang, L. Shi, and V. O. John, 2016: An assessment of the consistency between satellite measurements of upper tropospheric water vapor. *J. Geophys. Res. Atmos.*, **121**, 2874–2887, https://doi.org/10.1002/2015jd024496.

Cohen, Y., and Coauthors, 2018: Climatology and long-term evolution of ozone and carbon monoxide in the UTLS at northern mid-latitudes, as seen by IAGOS from 1995 to 2013. *Atmos. Chem. Phys.*, **18**, 5415–5453, https://doi.org/10.5194/acp-18-5415-2018.

Coldewey-Egbers, M., and Coauthors, 2015: The GOME-type Total Ozone Essential Climate Variable (GTO-ECV) data record from the ESA climate change initiative. *Atmos. Meas. Tech.*, **8**, 3923–3940, https://doi.org/10.5194/amt-8-3923-2015.

Cooper, O. R., and Coauthors, 2014: Global distribution and trends of tropospheric ozone: An observation-based review. *Elem. Sci. Anthropocene*, **2**, 29, http://doi.org/10.12952/journal.elementa.000029.

Crétaux, J.-F., R. Abarca-del-Río, M. Bergé-Nguyen, A. Arsen, V. Drolon, G. Clos, and P. Maisongrande, 2016: Lake volume monitoring from space. *Surv. Geophys.*, **37**, 269–305, https://doi.org/10.1007/s10712-016-9362-6.

Dankers, R., and Coauthors, 2014: First look at changes in flood hazard in the Inter-Sectoral Impact Model Intercomparison Project ensemble. *Proc. Natl. Acad. Sci. USA*, **111**, 3257–3261, https://doi.org/10.1073/pnas.1302078110.

Davidson, E. A., 2009: The contribution of manure and fertilizer nitrogen to atmospheric nitrous oxide since 1860. *Nat. Geosci.*, **2**, 659–662, https://doi.org/10.1038/ngeo608.

Dee, D. P., and Coauthors, 2011: The ERA-Interim reanalysis: Configuration and performance of the data assimilation system. *Quart. J. Roy. Meteor. Soc.*, **137**, 553–597, https://doi.org/10.1002/qj.828.

Deeter, M. N., and Coauthors, 2014: The MOPITT Version 6 product: Algorithm enhancements and validation. *Atmos. Meas. Tech.*, **7**, 3623–3632, https://doi.org/10.5194/amt-7-3623-2014.

Demarée, G., and T. Rutishauser, 2011: From "Periodical Observations" to "Anthochronology" and "Phenology" – The scientific debate between Adolphe Quetelet and Charles Morren on the origin of the word "Phenology". *Int. J. Biometeor.*, **55**, 753–761, https://doi.org/10.1007/s00484-011-0442-5.

Dessler, A. E., M. R. Schoeberl, T. Wang, S. M. Davis, K. H. Rosenlof, and J. P. Vernier, 2014: Variations of stratospheric water vapor over the past three decades. *J. Geophys. Res. Atmos.*, **119**, 12 588–12 598, https://doi.org/10.1002/2014JD021712.

Dewitte, S., D. Crommelynck, and A. Joukof, 2004: Total solar irradiance observations from DIARAD/VIRGO. *J. Geophys. Res.*, **109**, A02102, https://doi.org/10.1029/2002JA009694.

Dhomse, S. S., and Coauthors, 2018: Estimates of ozone return dates from Chemistry-Climate Model Initiative simulations. *Atmos. Chem. Phys.*, **18**, 8409–8438, https://doi.org/10.5194/acp-18-8409-2018.

Diallo, M., and Coauthors, 2018: Response of stratospheric water vapor and ozone to the unusual timing of El Niño and the QBO disruption in 2015–2016. *Atmos. Chem. Phys.*, **18**, 13 055–13 073, https://doi.org/10.5194/acp-18-13055-2018.

Di Girolamo, L., A. Menzies, G. Zhao, K. Mueller, C. Moroney, and D. J. Diner, 2010: MISR level 3 cloud fraction by altitude algorithm theoretical basis document. Jet Propulsion Laboratory Rep. JPL D-62358, 24 pp., https://pdfs.semanticscholar.org/afa4/b593c759d1ef451e9dc194028cd581f367b5.pdf.

Dlugokencky, E. J., L. P. Steele, P. M. Lang, and K. A. Masarie, 1994: The growth rate and distribution of atmospheric methane. *J. Geophys. Res.*, **99**, 17 021–17 043, https://doi.org/10.1029/94JD01245.

——, K. A. Masarie, P. M. Lang, and P. P. Tans, 1998: Continuing decline in the growth rate of the atmospheric methane burden. *Nature*, **393**, 447–450, https://doi.org/10.1038/30934.

——, E. G. Nisbet, R. Fisher, and D. Lowry, 2011: Global atmospheric methane: Budget, changes and dangers. *Philos. Trans. Roy. Soc.*, **369A**, 2058–2072, https://doi.org/10.1098/rsta.2010.0341.

Dolman, A. J., D. G. Miralles, and R. A. M. De Jeu, 2014: Fifty years since Monteith's 1965 seminal paper: The emergence of global ecohydrology. *Ecohydrology*, **7**, 897–902, https://doi.org/10.1002/eco.1505.

Donat, M., L. Alexander, H. Yang, I. Durre, R. Vose, and J. Caesar, 2013: Global land-based datasets for monitoring climatic extremes. *Bull. Amer. Meteor. Soc.*, **94**, 997–1006, https://doi.org/10.1175/BAMS-D-12-00109.1.Dorigo, W. A., and Coauthors, 2017: ESA CCI Soil Moisture for improved Earth system understanding: State-of-the art and future directions. *Remote Sens. Environ.*, **203**, 185–215, https://doi.org/10.1016/j.rse.2017.07.001.

——, and Coauthors, 2018: Soil moisture [in "State of the Climate in 2017"]. *Bull. Amer. Meteor. Soc.*, **99** (8), S150–S152, https://doi.org/10.1175/2018BAMSStateoftheClimate.1.

——, and Coauthors, 2017: Soil moisture [in "State of the Climate in 2016"]. *Bull. Amer. Meteor. Soc.*, **98** (8), S30–S32, https://doi.org/10.1175/2017BAMSStateoftheClimate.1.

Dunn, R. J. H., 2019: HadISD version 3: Monthly updates. Hadley Centre Tech. Note 103, 10 pp., www.metoffice.gov.uk/research/library-and-archive/publications/science/climate-science-technical-notes.

——, K. M. Willett, D. E. Parker, and L. Mitchell, 2016: Expanding HadISD: Quality-controlled, sub-daily station data from 1931. *Geosci. Instrum. Methods Data Syst.*, **5**, 473–491, https://doi.org/10.5194/gi-5-473-2016.

——, and Coauthors, 2020: Development of an updated global land in-situ-based dataset of temperature and precipitation extremes: HadEX3. *J. Geophys. Res. Atmos.*, https://doi.org/10.1029/2019JD032263, in press.

Dussaillant, I., and Coauthors, 2019: Two decades of glacier mass loss along the Andes. *Nat. Geosci.*, **12**, 802–808, https://doi.org/10.1038/s41561-019-0432-5.

Dutra, E., and Coauthors, 2010: An offline study of the impact of lakes on the performance of the ECMWF surface scheme. *Boreal Environ. Res.*, **15**, 100–112.

Dutton, E. G., 1992: A coherence between the QBO and the amplitude of the Mauna Loa atmospheric transmission annual cycle. *Int. J. Climatol.*, **12**, 383–396, https://doi.org/10.1002/joc.3370120406.

——, and B. A. Bodhaine, 2001: Solar irradiance anomalies caused by clear-sky transmission variations above Mauna Loa: 1958–1999. *J. Climate*, **14**, 3255–3262, https://doi.org/10.1175/1520-0442(2001)014<3255:siacbc>2.0.co;2.

——, J. J. Deluisi, and A. P. Austring, 1985: Interpretation of Mauna Loa atmospheric transmission relative to aerosols, using photometric precipitable water amounts. *J. Atmos. Chem.*, **3**, 53–68, https://doi.org/10.1007/BF00049368.

Ebita, A., and Coauthors, 2011: The Japanese 55-year reanalysis "JRA-55": An interim report. *SOLA*, **7**, 149–152, https://doi.org/10.2151/sola.2011-038.

ECMWF, 2018: Part IV: Physical processes. IFS Documentation CY45R1, ECMWF, 223 pp., www.ecmwf.int/node/18714.

Ellis, H. T., and R. F. Pueschel, 1971: Solar radiation: Absence of air pollution trends at Mauna Loa. *Science*, **172**, 845–846, https://doi.org/10.1126/science.172.3985.845.

Engel, A., and M. Rigby, 2018: Update on ozone-depleting substances (ODSs) and other gases of interest to the Montreal protocol. Scientific Assessment of Ozone Depletion: 2018, Global Ozone Research and Monitoring Project Rep. 58, 1.1–1.66, https://ozone.unep.org/sites/default/files/2019-05/SAP-2018-Assessment-report.pdf.

Etheridge, D. M., L. P. Steele, R. L. Langenfelds, R. J. Francey, J. M. Barnola, and V. I. Morgan, 1996: Natural and anthropogenic changes in atmospheric CO2 over the last 1000 years from air in Antarctic ice and firn. *J. Geophys. Res.*, **101**, 4115–4128, https://doi.org/10.1029/95JD03410.

Eyring, V., and Coauthors, 2013: Long-term ozone changes and associated climate impacts in CMIP5 simulations. *J. Geophys. Res. Atmos.*, **118**, 5029–5060, https://doi.org/10.1002/jgrd.50316.

Fioletov, V. E., G. E. Bodeker, A. J. Miller, R. D. McPeters, and R. Stolarski, 2002: Global and zonal total ozone variations estimated from ground-based and satellite measurements: 1964–2000. *J. Geophys. Res.*, **107**, 4647, https://doi.org/10.1029/2001JD001350.

——, and Coauthors, 2008: The performance of the ground-based total ozone network assessed using satellite data. *J. Geophys. Res.*, **113**, D14313, https://doi.org/10.1029/2008JD009809.

Fisher, J. B., and Coauthors, 2017: The future of evapotranspiration: Global requirements for ecosystem functioning, carbon and climate feedbacks, agricultural management, and water resources. *Water Resour. Res.*, **53**, 2618–2626, https://doi.org/10.1002/2016WR020175.

Flemming, J., and A. Inness, 2018: Carbon monoxide [in "State of the Climate in 2018"]. *Bull. Amer. Meteor. Soc.*, **100** (9), S181–S185, https://doi.org/10.1175/2019BAMSStateoftheClimate.1.

——, and Coauthors, 2017: The CAMS interim reanalysis of carbon monoxide, ozone and aerosol for 2003–2015. *Atmos. Chem. Phys.*, **17**, 1945–1983, https://doi.org/10.5194/acp-17-1945-2017.

Fleming, Z. L., and Coauthors, 2018: Tropospheric ozone assessment report: Present-day ozone distribution and trends relevant to human health. *Elem. Sci. Anthropocene*, **6**, 12, https://doi.org/10.1525/elementa.273.

Floodlist, 2019: Afghanistan–More flash floods leave 24 dead, houses destroyed. Floodlist, accessed 11 February 2020, http://floodlist.com/asia/afghanistan-flash-floods-may-2019.

Foster, G., and S. Rahmstorf, 2011: Global temperature evolution 1979–2010. *Environ. Res. Lett.*, **6**, 044022, https://doi.org/10.1088/1748-9326/6/4/044022.

Franco, B., and Coauthors, 2016: Evaluating ethane and methane emissions associated with the development of oil and natural gas extraction in North America. *Environ. Res. Lett.*, **11**, 044010. https://doi.org/10.1088/1748-9326/11/4/044010.

Freychet, N., S. F. B. Tett, Z. Yan, and Z. Li, 2020: Underestimated change of wet-bulb temperatures over East and South China. *Geophys. Res. Lett.*, **47**, e2019GL086140, https://doi.org/10.1029/2019GL086140.

Friedlingstein, P., and Coauthors, 2019: Global carbon budget 2019. *Earth Syst. Sci. Data*, **11**, 1783–1838, https://doi.org/10.5194/essd-11-1783-2019.

Frith, S. M., N. A. Kramarova, R. S. Stolarski, R. D. McPeters, P. K. Bhartia, and G. J. Labow, 2014: Recent changes in total column ozone based on the SBUV Version 8.6 Merged Ozone Data Set. *J. Geophys. Res. Atmos.*, **119**, 9735–9751, https://doi.org/10.1002/2014jd021889.

——, R. S. Stolarski, N. A. Kramarova, and R. D. McPeters, 2017: Estimating uncertainties in the SBUV Version 8.6 merged profile ozone data set. *Atmos. Chem. Phys.*, **17**, 14695–14707, https://doi.org/10.5194/acp-17-14695-2017.

Garane, K., and Coauthors, 2018: Quality assessment of the Ozone_cci Climate Research Data Package (release 2017): 1. Ground-based validation of total ozone column data products. *Atmos. Meas. Tech.*, **11**, 1385–1402, https://doi.org/10.5194/amt-11-1385-2018.

Garfinkel, C. I., A. Gordon, L. D. Oman, F. Li, S. Davis, and S. Pawson, 2018: Nonlinear response of tropical lower-stratospheric temperature and water vapor to ENSO. *Atmos. Chem. Phys.*, **18**, 4597–4615, https://doi.org/10.5194/acp-18-4597-2018.

Garreaud, R. D., and Coauthors, 2017: The 2010–2015 megadrought in central Chile: Impacts on regional hydroclimate and vegetation. *Hydrol. Earth Syst. Sci.*, **21**, 6307–6327, https://doi.org/10.5194/hess-21-6307-2017.

Gaubert, B., and Coauthors, 2017: Chemical feedback from decreasing carbon monoxide emissions. *Geophys. Res. Lett.*, **44**, 9985–9995, https://doi.org/10.1002/2017GL074987.

Gaudel, A., and Coauthors, 2018: Tropospheric ozone assessment report: Present-day distribution and trends of tropospheric ozone relevant to climate and global atmospheric chemistry model evaluation. *Elem. Sci. Anthropocene*, **6**, 39, http://doi.org/10.1525/elementa.291.

GCOS, 2016: The global observing system for climate: Implementation needs. Tech. Rep. GCOS-200, 341 pp., https://library.wmo.int/doc_num.php?explnum_id=3417.

Gelaro, R., and Coauthors, 2017: The Modern-Era Retrospective Analysis for Research and Applications, version 2 (MERRA-2). *J. Climate*, **30**, 5419–5454, https://doi.org/10.1175/JCLI-D-16-0758.1.

Gleason, K. L., J. H. Lawrimore, D. H. Levinson, T. R. Karl, and D. J. Karoly, 2008: A revised U.S. climate extremes index. *J. Climate*, **21**, 2124–2137, https://doi.org/10.1175/2007JCLI1883.1.

Gobron, N., 2018: Terrestrial vegetation activity [in "State of the Climate in 2017"]. *Bull. Amer. Meteor. Soc.*, **99** (8), S62–S63, https://doi.org/10.1175/2018BAMSStateoftheClimate.1.

Gobron, N., 2019: Terrestrial vegetation activity [in "State of the Climate in 2018"]. *Bull. Amer. Meteor. Soc.*, **100** (9), S63–S64, https://doi.org/10.1175/2019BAMSStateoftheClimate.1

——, and M. Robustelli, 2013: Monitoring the state of the global terrestrial surfaces. Proc. 2013 ESA Living Planet Symp., Edinburgh, United Kingdom, ESA, http://seom.esa.int/lps13/abstracts/850030.html.

——, A. S. Belward, B. Pinty, and W. Knorr, 2010: Monitoring biosphere vegetation 1998–2009. *Geophys. Res. Lett.*, **37**, L15402, https://doi.org/10.1029/2010gl043870.

Gruber, A., T. Scanlon, R. van der Schalie, W. Wagner, and W. Dorigo, 2019: Evolution of the ESA CCI Soil Moisture climate data records and their underlying merging methodology. *Earth Syst. Sci. Data*, **11**, 717–739, https://doi.org/10.5194/essd-11-717-2019.

Guo, S., G. J. S. Bluth, W. I. Rose, I. M. Watson, and A. J. Prata, 2004: Re-evaluation of SO2 release of the 15 June 1991 Pinatubo eruption using ultraviolet and infrared satellite sensors. *Geochem. Geophys. Geosyst.*, **5**, Q04001, https://doi.org/10.1029/2003GC000654.

Haimberger, L., C. Tavolato, and S. Sperka, 2012: Homogenization of the Global Radiosonde Temperature dataset through combined comparison with reanalysis background series and neighboring stations. *J. Climate*, **25**, 8108–8131, https://doi.org/10.1175/JCLI-D-11-00668.1.

Hall, B. D., S. A. Montzka, G. Dutton, B. R. Miller, and J. W. Elkins, 2019: Ozone-depleting substances [in "State of the Climate in 2018"]. *Bull. Amer. Meteor. Soc.*, **100** (9), S50–S52, https://doi.org/10.1175/2019BAMSStateoftheClimate.1.

Hansen, J., R. Ruedy, M. Sato, and K. Lo, 2010: Global surface temperature change. *Rev. Geophys.*, **48**, RG4004, https://doi.org/10.1029/2010RG000345.

Harris, I., T. J. Osborn, P. D. Jones, and D. H. Lister, 2020: Version 4 of the CRU TS monthly high-resolution gridded multivariate climate dataset. *Sci. Data*, **7**, 109, https://doi.org/10.1038/s41597-020-0453-3.

Hartmann, D. L., and Coauthors, 2013: Observations: Atmosphere and surface. Climate Change 2013: The Physical Science Basis, T. F. Stocker et al., Eds., Cambridge University Press, 159–254.

Hausmann, P., R. Sussmann, and D. Smale, 2016: Contribution of oil and natural gas production to renewed increase in atmospheric methane (2007–2014): Top-down estimate from ethane and methane column observations. *Atmos. Chem. Phys.*, **16**, 3227–3244, https://doi.org/10.5194/acp-16-3227-2016.

Heidinger, A. K., M. J. Foster, A. Walther, and X. Zhao, 2013: The pathfinder atmospheres-extended AVHRR climate dataset. *Bull. Amer. Meteor. Soc.*, **95**, 909–922, https://doi.org/10.1175/BAMS-D-12-00246.1.

Held, I. M., and B. J. Soden, 2000: Water vapor feedback and global warming. *Annu. Rev. Energy Environ.*, **25**, 441–475, https://doi.org/10.1146/annurev.energy.25.1.441.

Helmig, D., and Coauthors, 2016: Reversal of global atmospheric ethane and propane trends largely due to US oil and natural gas production. *Nat. Geosci.*, **9**, 490–495, https://doi.org/10.1038/ngeo2721.

Hersbach, H., and Coauthors, 2020: The ERA5 global reanalysis. *Quart. J. Roy. Meteor. Soc.*, https://doi.org/10.1002/qj.3803, accepted.

Hirabayashi, Y., R. Maendran, S. Koirala, L. Konoshima, D. Yamazaki, S. Watanabe, H. Kim, and S. Kanae, 2013: Global flood risk under climate change. *Nat. Climate Change*, **3**, 816–821, https://doi.org/10.1038/nclimate1911.

Ho, S.-P., Y.-H. Kuo, W. Schreiner, and X. Zhou, 2010a: Using SI-traceable global positioning system radio occultation measurements for climate monitoring [In "States of the Climate in 2009]. *Bull. Amer. Meteor. Soc.*, **91** (7), S36–S37.

——, X. Zhou, Y.-H. Kuo, D. Hunt, and J.-H. Wang, 2010b: Global evaluation of radiosonde water vapor systematic biases using GPS radio occultation from COSMIC and ECMWF analysis. *Remote Sens.*, **2**, 1320–1330, https://doi.org/10.3390/rs2051320.

——, and Coauthors, 2020: The COSMIC/FORMOSAT-3 radio occultation mission after 12 years: Accomplishments, remaining challenges, and potential impacts of COSMIC-2. *Bull. Amer. Meteor. Soc.*, **101,** E1107–E1136, https://doi.org/10.1175/BAMS-D-18-0290.1.

Hobday, A. J., and Coauthors, 2016: A hierarchical approach to defining marine heatwaves. *Prog. Oceanogr.*, **141**, 227–238, https://doi.org/10.1016/j.pocean.2015.12.014.

——, and Coauthors, 2018: Categorizing and naming marine heatwaves. *Oceanography*, **31**, 162–173, https://doi.org/10.5670/oceanog.2018.205.

Hock, R., and Coauthors, 2020: High mountain areas. IPCC Special Report on the Ocean and Cryosphere in a Changing Climate, H.-O. Pörtner et al., Eds., IPCC, in press.

Hofmann, D., J. Barnes, M. O'Neill, M. Trudeau, and R. Neely, 2009: Increase in background stratospheric aerosol observed with lidar at Mauna Loa Observatory and Boulder, Colorado. *Geophys. Res. Lett.*, **36**, L15808, https://doi.org/10.1029/2009GL039008.

——, and S. Solomon, 1989: Ozone destruction through heterogeneous chemistry following the eruption of El Chichon. *J. Geophys. Res.*, **94**, 5029–5041, https://doi.org/10.1029/JD094iD04p05029.

——, J. H. Butler, E. J. Dlugokencky, J. W. Elkins, K. Masarie, S. A. Montzka, and P. Tans, 2006: The role of carbon dioxide in climate forcing from 1979 to 2004: Introduction of the annual greenhouse gas index. *Tellus*, **58B**, 614–619, https://doi.org/10.1111/j.1600-0889.2006.00201.x.

Hu, L., and Coauthors, 2019: Enhanced North American carbon uptake associated with El Niño. *Sci. Adv.*, **5**, eaaw0076, https://doi.org/10.1126/sciadv.aaw0076.

Huang, C.-Y., W.-H. Teng, S.-P. Ho, and Y.-H. Kuo, 2013: Global variation of COSMIC precipitable water over land: Comparisons with ground-based GPS measurements and NCEP reanalyses. *Geophys. Res. Lett.*, **40**, 5327–5331, https://doi.org/10.1002/grl.50885.

Huntington, T. G., 2006: Evidence for intensification of the global water cycle: Review and synthesis. *J. Hydrol.*, **319**, 83–95, https://doi.org/10.1016/j.jhydrol.2005.07.003.

Hurst, D. F., and Coauthors, 2016: Recent divergences in stratospheric water vapor measurements by frost point hygrometers and the Aura Microwave Limb Sounder. *Atmos. Meas. Tech.*, **9**, 4447–4457, https://doi.org/10.5194/amt-9-4447-2016.

Iacono, M. J., and C. Azorin-Molina, 2014: Long-term declining trends in historical wind measurements at the Blue Hill Meteorological Observatory, 1885–2013. 2014 Fall Meeting, San Francisco, CA, Amer. Geophys. Union, Abstract A23C-3241.

Inness, A., and Coauthors, 2013: The MACC reanalysis: An 8-year data set of atmospheric composition. *Atmos. Chem. Phys.*, **13**, 4073–4109, https://doi.org/10.5194/acp-13-4073-2013.

——, and Coauthors, 2019: The CAMS reanalysis of atmospheric composition. *Atmos. Chem. Phys.*, **19**, 3515–3556, https://doi.org/10.5194/acp-19-3515-2019.

IPCC, 2013: Climate Change 2013: The Physical Science Basis. Cambridge University Press, 1535 pp.

Isaksen, K., J. L. Sollid, P. Holmlund, and C. Harris, 2007: Recent warming of mountain permafrost in Svalbard and Scandinavia. *J. Geophys. Res.*, **112**, F02S04, https://doi.org/10.1029/2006JF000522.

Jiménez, C., B. Martens, D. M. Miralles, J. B. Fisher, H. E. Beck, and D. Fernández-Prieto, 2018: Exploring the merging of the global land evaporation WACMOS-ET products based on local tower measurements. *Hydrol. Earth Syst. Sci.*, **22**, 4513–4533, https://doi.org/10.5194/hess-22-4513-2018.

Jiménez-Muñoz, J. C., C. Mattar, J. Barichivich, A. Santamaría-Artigas, K. Takahashi, Y. Malhi, J. A. Sobrino, and G. van der Schrier, 2016: Record-breaking warming and extreme drought in the Amazon rainforest during the course of El Niño 2015–2016. *Sci. Rep.*, **6**, 33130, https://doi.org/10.1038/srep33130.

John, V. O., and B. J. Soden, 2007: Temperature and humidity biases in global climate models and their impact on climate feedbacks. *Geophys. Res. Lett.*, **34**, L18704, https://doi.org/10.1029/2007GL030429.

——, G. Holl, R. P. Allan, S. A. Buehler, D. E. Parker, and B. J. Soden, 2011: Clear-sky biases in satellite infra-red estimates of upper tropospheric humidity and its trends. *J. Geophys. Res.*, **116**, D14108, https://doi.org/10.1029/2010JD015355.

Jones, P. D., D. H. Lister, T. J. Osborn, C. Harpham, M. Salmon, and C. P. Morice, 2012: Hemispheric and large-scale land surface air temperature variations: An extensive revision and an update to 2010. *J. Geophys. Res.*, **117**, D05127, https://doi.org/10.1029/2011JD017139.

Kaiser, J. W., and Coauthors, 2012: Biomass burning emissions estimated with a global fire assimilation system based on observed fire radiative power. *Biogeosciences*, **9**, 527–554, https://doi.org/10.5194/bg-9-527-2012.

——, W. Xu, A. Heil, T. Nikonovas, I. Hüser, and M. J. Wooster, 2017: How to use SEVIRI fire radiative power in the Copernicus Atmosphere Monitoring Service. 2017 EUMETSAT Meteorological Satellite Conf., Rome, Italy, EUMETSAT, www.eumetsat.int/website/home/News/ConferencesandEvents/DAT_3212307.html.

Kaplan, A., 2011: Patterns and indices of climate variability [in "State of the Climate in 2010"]. *Bull. Amer. Meteor. Soc.*, **92** (6), S20–S25, https://doi.org/10.1175/1520-0477-92.6.S1.

Karlsson, K.-G., and Coauthors, 2017: CLARA-A2: The second edition of the CM SAF cloud and radiation data record from 34 years of global AVHRR data. *Atmos. Chem. Phys.*, **17**, 5809–5828, https://doi.org/10.5194/acp-17-5809-2017.

Karpechko, A. Y., and A. C. Maycock, 2018: Stratospheric ozone changes and climate. Scientific Assessment of Ozone Depletion: 2018, Global Ozone Research and Monitoring Project Rep. 58, 5.1–5.50, https://ozone.unep.org/sites/default/files/2019-05/SAP-2018-Assessment-report.pdf.

Karplus, V. J., S. Zhang, and D. Almond, 2018: Quantifying coal power plant responses to tighter SO2 emissions standards in China. *Proc. Natl. Acad. Sci. USA*, **115**, 7004–7009, https://doi.org/10.1073/pnas.1800605115.

Kennedy, J. J., and Coauthors, 2010: How do we know the world has warmed [in "State of the Climate in 2009"]? *Bull. Amer. Meteor. Soc.*, **91** (7), S26–S27, https://doi.org/10.1175/BAMS-91-7-StateoftheClimate.

——, N. A. Rayner, R. O. Smith, M. Saunby, and D. E. Parker, 2011a: Reassessing biases and other uncertainties in sea surface temperature observations measured in situ since 1850: 1. Measurement and sampling uncertainties. *J. Geophys. Res.*, **116**, D14103, https://doi.org/10.1029/2010JD015218.

——, N. A. Rayner, R. O. Smith, M. Saunby, and D. E. Parker, 2011b: Reassessing biases and other uncertainties in sea surface temperature observations measured in situ since 1850: 2. Biases and homogenization. *J. Geophys. Res.*, **116**, D14104, https://doi.org/10.1029/2010JD015220.

Khaykin, S. M., and Coauthors, 2017: Variability and evolution of the midlatitude stratospheric aerosol budget from 22 years of ground-based lidar and satellite observations. *Atmos. Chem. Phys.*, **17**, 1829–1845, https://doi.org/10.5194/acp-17-1829-2017.

——, S. Godin-Beekmann, A. Hauchecorne, J. Pelon, F. Ravetta, and P. Keckhut, 2018: Stratospheric smoke with unprecedentedly high backscatter observed by lidars above southern France. *Geophys. Res. Lett.*, **45**, 1639–1646, https://doi.org/10.1002/2017GL076763.

Kim, H., 2017: River discharge [in "State of the Climate in 2016"]. *Bull. Amer. Meteor. Soc.*, **98** (8), S28–S30, https://doi.org/10.1175/2017BAMSStateoftheClimate.1.

——, 2018: River discharge and runoff [in "State of the Climate in 2017"]. *Bull. Amer. Meteor. Soc.*, **99** (8), S33–S34, https://doi.org/10.1175/2018BAMSStateoftheClimate.1.

——, 2019: River discharge and runoff [in "State of the Climate in 2018"]. *Bull. Amer. Meteor. Soc.*, **100** (9), S35–S36, https://doi.org/10.1175/2019BAMSStateoftheClimate.1

——, P. J.-F. Yeh, T. Oki, and S. Kanae, 2009: Role of rivers in the seasonal variations of terrestrial water storage over global basins. *Geophys. Res. Lett.*, **36**, L17402, https://doi.org/10.1029/2009GL039006.

Kim, J., and K. Paik, 2015: Recent recovery of surface wind speed after decadal decrease: A focus on South Korea. *Climate Dyn.*, **45**, 1699–1712, https://doi.org/10.1007/s00382-015-2546-9.

King, O., A. Bhattacharya, R. Bhambri, and T. Bolch, 2019: Glacial lakes exacerbate Himalayan glacier mass loss. *Sci. Rep.*, **9**, 18145, https://doi.org/10.1038/s41598-019-53733-x.

Kjøllmoen, B., L. Andreassen, H. Elvehøy, and M. Jackson, 2019: Glaciological investigations in Norway 2018. NVE Rep. 46-2019, 84 pp., http://publikasjoner.nve.no/rapport/2019/rapport2019_46.pdf.

Klein Tank, A. M. G., and Coauthors, 2002: Daily dataset of 20th-century surface air temperature and precipitation series for the European Climate Assessment. *Int. J. Climatol.*, **22**, 1441–1453, https://doi.org/10.1002/joc.773.

Kobayashi, S., and Coauthors, 2015: The JRA-55 reanalysis: General specifications and basic characteristics. *J. Meteor. Soc. Japan*, **93**, 5–48, https://doi.org/10.2151/jmsj.2015-001.

Kopp, G., and J. L. Lean, 2011: A new, lower value of total solar irradiance: Evidence and climate significance. *Geophys. Res. Lett.*, **38**, L01706, https://doi.org/10.1029/2010GL045777.

Kratz, D. P., P. W. Stackhouse Jr., S. K. Gupta, A. C. Wilber, P. Sawaengphokhai, and G. R. McGarragh, 2014: The Fast Longwave and Shortwave Flux (FLASHFlux) data product: Single Scanner Footprint Fluxes. *J. Appl. Meteor. Climatol.*, **53**, 1059–1079, https://doi.org/10.1175/JAMC-D-13-061.1.

Lan, X., and Coauthors, 2019: Long-term measurements show little evidence for large increases in total us methane emissions over the past decade. *Geophys. Res. Lett.*, **46**, 4991–4999, https://doi.org/10.1029/2018GL081731.

Lee, H.-T., and NOAA CDR Program, 2011: NOAA Climate Data Record (CDR) of monthly outgoing longwave radiation (OLR), version 2.2-1. NOAA National Climatic Data Center, accessed 23 January 2020, https://doi.org/10.7289/V5222RQP.

Lenssen, N., G. Schmidt, J. Hansen, M. Menne, A. Persin, R. Ruedy, and D. Zyss, 2019: Improvements in the GISTEMP uncertainty model. *J. Geophys. Res. Atmos.*, **124**, 6307–6326, https://doi.org/10.1029/2018jd029522.

Levy, R. C., S. Mattoo, L. A. Munchak, L. A. Remer, A. M. Sayer, F. Patadia, and N. C. Hsu, 2013: The Collection 6 MODIS aerosol products over land and ocean. *Atmos. Meas. Tech.*, **6**, 2989–3034, https://doi.org/10.5194/amt-6-2989-2013.

L'Heureux, M. L., and Coauthors, 2017: Observing and predicting the 2015/16 El Niño. *Bull. Amer. Meteor. Soc.*, **98**, 1363–1382, https://doi.org/10.1175/BAMS-D-16-0009.1.

Li, B., M. Rodell, and J. S. Famiglietti, 2015: Groundwater variability across temporal and spatial scales in the central and northeastern U.S. *J. Hydrol.*, **525**, 769–780, https://doi.org/10.1016/j.jhydrol.2015.04.033.

——, and Coauthors, 2019: Global GRACE data assimilation for groundwater and drought monitoring: Advances and challenges. *Water Resour. Res.*, **55**, 7564–7586, https://doi.org/10.1029/2018WR024618.

Lieb, G. K., and A. Kellerer-Pirklbauer, 2019: Gletscherbericht 2017/18 Sammelbericht über die Gletschermessungen des Österreichischen Alpenvereins im Jahre 2018. Letzter Bericht: Bergauf 2/2018, Jg. 73 (143), 20–29, www.alpenverein.at/portal_wAssets/docs/service/presse/2019/gletscherbericht/Gletscherbericht_2_19.pdf.

Lim, E., H. H. Hendon, G. Boschat, D. Hudson, D. W. J. Thompson, A. J. Dowdy, and J. M. Arblaster, 2019: Australian hot and dry extremes induced by weakenings of the stratospheric polar vortex. *Nat. Geosci.*, **12**, 896–901, https://doi.org/10.1038/s41561-019-0456-x.

Lin, M., L. W. Horowitz, S. J. Oltmans, A. M. Fiore, and S. Fan, 2014: Tropospheric ozone trends at Mauna Loa Observatory tied to decadal climate variability. *Nat. Geosci.*, **7**, 136–143, https://doi.org/10.1038/ngeo2066.

——, ——, R. Payton, A. M. Fiore, and G. Tonnesen, 2017: US surface ozone trends and extremes from 1980 to 2014: Quantifying the roles of rising Asian emissions, domestic controls, wildfires, and climate. *Atmos. Chem. Phys.*, **17**, 2943–2970, https://doi.org/10.5194/acp-17-2943-2017.

Liu, Y., and Coauthors, 2015: Agriculture intensifies soil moisture decline in Northern China. *Sci. Rep.*, **5**, 11 261, https://doi.org/10.1038/srep11261.

Loeb, N. G., B. A. Wielicki, D. R. Doelling, G. L. Smith, D. F. Keyes, S. Kato, N. Manalo-Smith, and T. Wong, 2009: Toward optimal closure of the Earth's top-of-atmosphere radiation budget. *J. Climate*, **22**, 748–766, https://doi.org/10.1175/2008JCLI2637.1.

——, S. Kato, W. Su, T. Wong, F. Rose, D. R. Doelling, and J. Norris, 2012: Advances in understanding top-of-atmosphere radiation variability from satellite observations. *Surv. Geophys.*, **33**, 359–385, https://doi.org/10.1007/s10712-012-9175-1.

——, and Coauthors, 2018: Clouds and the Earth's Radiant Energy System (CERES) Energy Balanced and Filled (EBAF) top-of-atmosphere (TOA) Edition-4.0 data product. *J. Climate*, **31**, 895–918, https://doi.org/10.1175/JCLI-D-17-0208.1.

Lu, X., and Coauthors, 2018: Severe surface ozone pollution in China: A global perspective. *Environ. Sci. Technol. Lett.*, **5**, 487–494, https://doi.org/10.1021/acs.estlett.8b00366.

——, and Coauthors, 2019: Surface and tropospheric ozone trends in the Southern Hemisphere since 1990: Possible linkages to poleward expansion of the Hadley Circulation. *Sci. Bull.*, **64**, 400–409, https://doi.org/10.1016/j.scib.2018.12.021.

MacCallum, S. N., and C. J. Merchant, 2012: Surface water temperature observations of large lakes by optimal estimation. *Can. J. Remote Sens.*, **38**, 25–45, https://doi.org/10.5589/m12-010.

MacFarling Meure, C., D. Etheridge, C. Trudinger, P. Steele, R. Langenfelds, T. van Ommen, A. Smith, and J. Elkins, 2006: Law Dome CO2, CH4 and N2O ice core records extended to 2000 years BP. *Geophys. Res. Lett.*, **33**, L14810, https://doi.org/10.1029/2006GL026152.

Madakumbura, D. G., H. Kim, N. Utsumi, H. Shiogama, E. M. Fischer, Ø. Seland, J. F. Scinocca, D. M. Mitchell, Y. Hirabayashi, and T. Oki, 2019: Event-to-event intensification of the hydrologic cycle in 1.5°C and 2°C warmer worlds. *Sci. Rep.*, **9**, 3483, https://doi.org/10.1038/s41598-019-39936-2.

Magnin, F., P. Deline, L. Ravanel, J. Noetzli, and P. Pogliotti, 2015: Thermal characteristics of permafrost in the steep alpine rock walls of the Aiguille du Midi (Mont Blanc Massif, 3842 m a.s.l). *Cryosphere*, **9**, 109–121, https://doi.org/10.5194/tc-9-109-2015.

Magnuson, J. J., and Coauthors, 2000: Historical trends in lake and river ice cover in the Northern Hemisphere. *Science*, **289**, 1743–1746, https://doi.org/10.1126/science.289.5485.1743.

Manabe, S., and R. Wetherald, 1967: Thermal equilibrium of the atmosphere with a given distribution of relative humidity. *J. Atmos. Sci.*, **24**, 241–259, https://doi.org/10.1175/1520-0469(1967)024<0241:TEOTAW>2.0.CO;2.

Martens, B., and Coauthors, 2017: GLEAM v3: Satellite-based land evaporation and root-zone soil moisture. *Geosci. Model Dev.*, **10**, 1903–1925, https://doi.org/10.5194/gmd-10-1903-2017.

——, W. Waegeman, W. A. Dorigo, N. E. C. Verhoest, and D. G. Miralles, 2018: Terrestrial evaporation response to modes of climate variability. *npj Climate Atmos. Sci.*, **1**, 43, https://doi.org/10.1038/s41612-018-0053-5.

Maycock, A. C., and Coauthors, 2018: Revisiting the mystery of recent stratospheric temperature trends. *Geophys. Res. Lett.*, **45**, 9919–9933, https://doi.org/10.1029/2018GL078035.

McCabe, A., A. Ershadi, C. Jimenez, D. G. Miralles, D. Michel, and E. F. Wood, 2016: The GEWEX LandFlux project: Evaluation of model evaporation using tower-based and globally-gridded forcing data. *Geosci. Model Dev.*, **9**, 283–305, https://doi.org/10.5194/gmd-9-283-2016.

——, and Coauthors, 2017: The future of Earth observation in hydrology. *Hydrol. Earth Syst. Sci.*, **21**, 3879–3914, https://doi.org/10.5194/hess-21-3879-2017.

——, D. G. Miralles, T. R. H. Holmes, and J. B. Fisher, 2019: Advances in the remote sensing of terrestrial evaporation. *Remote Sens.*, **11**, 1138, https://doi.org/10.3390/rs11091138.

McDermid, I. S., T. D. Walsh, A. Deslis, and M. L. White, 1995: Optical-systems design for a stratospheric lidar system. *Appl. Opt.*, **34**, 6201–6210, https://doi.org/10.1364/AO.34.006201.

McKitrick, R., and J. R. Christy, 2018: A test of the tropical 200- to 300-hPa warming rate in climate models. *Earth Space Sci.*, **5**, 529–536, https://doi.org/10.1029/2018ea000401.

McVicar, T. R., R. Vautard, J.-N. Thépaut, P. Berrisford, and R. J. H. Dunn, 2013: Surface winds [in "State of the Climate in 2012"]. *Bull. Amer. Meteor. Soc.*, **94** (8), S27–S29, https://doi.org/10.1175/2013BAMSStateoftheClimate.1.

Mears, C., D. K. Smith, L. Ricciardulli, J. Wang, H. Huelsing, and F. J. Wentz, 2018: Construction and uncertainty estimation of a satellite-derived total precipitable water data record over the world's oceans. *Earth Space Sci.*, **5**, 197–210, https://doi.org/10.1002/2018EA000363.

——, and F. J. Wentz, 2016: Sensitivity of satellite-derived tropospheric temperature trends to the diurnal cycle adjustment. *J. Climate*, **29**, 3629–3646, https://doi.org/10.1175/JCLI-D-15-0744.1.

Melaas, E. K., D. Sulla-Menashe, J. M. Gray, T. A. Black, T. H. Morin, A. D. Richardson, and M. A. Friedl, 2016: Multisite analysis of land surface phenology in North American temperate and boreal deciduous forests from Landsat. *Remote Sens. Environ.*, **186**, 452–464, https://doi.org/10.1016/j.rse.2016.09.014.

Menne, M. J., I. Durre, R. S. Vose, B. E. Gleason, and T. G. Houston, 2012: An overview of the global historical climatology network-daily database. *J. Atmos. Oceanic Technol.*, **29**, 897–910, https://doi.org/10.1175/JTECH-D-11-00103.1.

Menzel, W. P., R. A. Frey, E. E. Borbas, B. A. Baum, G. Cureton, and N. Bearson, 2016: Reprocessing of HIRS satellite measurements from 1980 to 2015: Development toward a consistent decadal cloud record. *J. Appl. Meteor. Climatol.*, **55**, 2397–2410, https://doi.org/10.1175/JAMC-D-16-0129.1.

Meredith, M., and Coauthors, 2020: Polar regions. IPCC Special Report on the Ocean and Cryosphere in a Changing Climate, H.-O. Pörtner et al., Eds., IPCC, in press.

Miller, B. R., and Coauthors, 2010: HFC-23 (CHF3) emission trend response to HCFC-22 (CHClF2) production and recent HFC-23 emission abatement measures. *Atmos. Chem. Phys.*, **10**, 7875–7890, https://doi.org/10.5194/acp-10-7875-2010.

Mills, G., and Coauthors, 2018: Tropospheric ozone assessment report: Present-day tropospheric ozone distribution and trends relevant to vegetation. *Elem. Sci. Anthropocene*, **6**, 47, https://doi.org/10.1525/elementa.302.

Minnis, P., and Coauthors, 2008: Cloud detection in nonpolar regions for CERES using TRMM VIRS and Terra and Aqua MODIS data. *IEEE Trans. Geosci. Remote Sens.*, **46**, 3857–3884, https://doi.org/10.1109/TGRS.2008.2001351.

——, K. Bedka, Q. Trepte, C. R. Yost, S. T. Bedka, B. Scarino, K. Khlopenkov, and M. M. Khaiyer, 2016: A consistent long-term cloud and clear-sky radiation property dataset from the Advanced Very High Resolution Radiometer (AVHRR). Climate Algorithm Theoretical Basis Doc. CDRP-ATBD-0826, NOAA, 159 pp., www.ncdc.noaa.gov/sites/default/files/cdr-documentation/CDRP-ATBD-0826%20AVHRR%20Cloud%20Properties%20-%20NASA%20C-ATBD%20(01B-30b)%20(DSR-1051).pdf.

Minschwaner, K., H. Su, and J. H. Jiang, 2016: The upward branch of the Brewer-Dobson circulation quantified by tropical stratospheric water vapor and carbon monoxide measurements from the Aura Microwave Limb Sounder. *J. Geophys. Res. Atmos.*, **121**, 2790–2804, https://doi.org/10.1002/2015jd023961.

Miralles, D. G., T. R. H. Holmes, R. A. M. De Jeu, J. H. Gash, A. G. C. A. Meesters, and A. J. Dolman, 2011: Global land-surface evaporation estimated from satellite-based observations. *Hydrol. Earth Syst. Sci.*, **15**, 453–469, https://doi.org/10.5194/hess-15-453-2011.

——, and Coauthors, 2014: El Niño–La Niña cycle and recent trends in continental evaporation. *Nat. Climate Change*, **4**, 122–126, https://doi.org/10.1038/nclimate2068.

——, and Coauthors, 2016: The WACMOS-ET project – Part II: Evaluation of global terrestrial evaporation data sets. *Hydrol. Earth Syst. Sci.*, **20**, 823–842, https://doi.org/10.5194/hess-20-823-2016.

— P. Gentine, S. I. Seneviratne, and A. J. Teuling, 2019: Land-atmospheric feedbacks during droughts and heatwaves: State of the science and current challenges. *Ann. New York Acad. Sci.*, **1436**, 19–35, https://doi.org/10.1111/nyas.13912.

Mironov, D., 2008: Parameterization of lakes in numerical weather prediction. Part 1: Description of a lake mode. COSMO Tech. Rep. 11, 47 pp., www.cosmo-model.org/content/model/documentation/techReports/docs/techReport11.pdf.

——, and Coauthors, 2010: Implementation of the lake parameterisation scheme FLake into the numerical weather prediction model COSMO. *Boreal Environ. Res.*, **15**, 218–230.

Mitchell, J. M. J., 1971: The effect of atmospheric aerosols on climate with special reference to temperature near the Earth's surface. *J. Appl. Meteor.*, **10**, 703–714, https://doi.org/10.1175/1520-0450(1971)010<0703:TEOAAO>2.0.CO;2.

Miyazaki, K., H. J. Eskes, and K. Sudo, 2015: A tropospheric chemistry reanalysis for the years 2005–2012 based on an assimilation of OMI, MLS, TES, and MOPITT satellite data. *Atmos. Chem. Phys.*, **15**, 8315–8348, https://doi.org/10.5194/acp-15-8315-2015.

Mollaret, C., C. Hilbich, C. Pellet, A. Flores-Orozco, R. Delaloye, and C. Hauck, 2019: Mountain permafrost degradation documented through a network of permanent electrical resistivity tomography sites. *Cryosphere*, **13**, 2557–2578, https://doi.org/10.5194/tc-13-2557-2019.

Monks, P. S., and Coauthors, 2015: Tropospheric ozone and its precursors from the urban to the global scale from air quality to short-lived climate forcer. *Atmos. Chem. Phys.*, **15**, 8889–8973, https://doi.org/10.5194/acp-15-8889-2015.

Montzka, S. A., J. H. Butler, R. C. Myers, T. M. Thompson, T. H. Swanson, A. D. Clarke, L. T. Lock, and J. W. Elkins, 1996: Decline in the tropospheric abundance of halogen from halocarbons: Implications for stratospheric ozone depletion. *Science*, **272**, 1318–1322, https://doi.org/10.1126/science.272.5266.1318.

——, and Coauthors, 2018a: An unexpected and persistent increase in global emissions of ozone-depleting CFC-11. *Nature*, **557**, 413–417, https://doi.org/10.1038/s41586-018-0106-2.

——, and Coauthors, 2018b: Hydrofluorocarbons (HFCs). Scientific Assessment of Ozone Depletion: 2018, Global Ozone Research and Monitoring Project Rep. 58, 2.1–2.47, https://ozone.unep.org/sites/default/files/2019-05/SAP-2018-Assessment-report.pdf.

Moon, M., X. Zhang, G. M. Henebry, L. Liu, J. M. Gray, E. K. Melaas, and M. A. Friedl, 2019: Long-term continuity in land surface phenology measurements: A comparative assessment of the MODIS land cover dynamics and VIIRS land surface phenology products. *Remote Sens. Environ.*, **226**, 74–92, https://doi.org/10.1016/j.rse.2019.03.034.

Morgenstern, O., and Coauthors, 2017: Review of the global models used within phase 1 of the Chemistry–Climate Model Initiative (CCMI). *Geosci. Model Dev.*, **10**, 639–671, https://doi.org/10.5194/gmd-10-639-2017.

Morice, C. P., J. J. Kennedy, N. A. Rayner, and P. D. Jones, 2012: Quantifying uncertainties in global and regional temperature change using an ensemble of observational estimates: The HadCRUT4 dataset. *J. Geophys. Res.*, **117**, D08101, https://doi.org/10.1029/2011JD017187.

Mühle, J., and Coauthors, 2010: Perfluorocarbons in the global atmosphere: Tetrafluoromethane, hexafluoroethane, and octafluoropropane. *Atmos. Chem. Phys.*, **10**, 5145–5164, https://doi.org/10.5194/acp-10-5145-2010.

Myhre, G., and Coauthors, 2013: Anthropogenic and natural radiative forcing. Climate Change 2013: The Physical Science Basis, T. F. Stocker et al., Eds., Cambridge University Press, 659–740.

Neu, J., T. Flury, G. L. Manney, M. L. Santee, N. J. Livesey, and J. Worden, 2014: Tropospheric ozone variations governed by changes in stratospheric circulation. *Nat. Geosci.*, **7**, 340–344, https://doi.org/10.1038/ngeo2138.

Newman, M., A. T. Wittenberg, L. Cheng, G. P. Compo, and C. A. Smith, 2018: The extreme 2015/16 El Niño, in the context of historical climate variability and change. *Bull. Amer. Meteor. Soc.*, **99** (1), S16–S20, https://doi.org/10.1175/BAMS-D-17-0116.1.

Newman, P. A., J. S. Daniel, D. W. Waugh, and E. R. Nash, 2007: A new formulation of equivalent effective stratospheric chlorine (EESC). *Atmos. Chem. Phys.*, **7**, 4537–4552, https://doi.org/10.5194/acp-7-4537-2007.

Nisbet, E. G., and Coauthors, 2019: Very strong atmospheric methane growth in the 4 years 2014–2017: Implications for the Paris Agreement. *Global Biogeochem. Cycles*, **33**, 318–342, https://doi.org/10.1029/2018GB006009.

Noetzli, J., and Coauthors, 2018: Permafrost thermal state [in "State of the Climate in 2017"]. *Bull. Amer. Meteor. Soc.*, **99** (8), S20–S22, https://doi.org/10.1175/2018BAMSStateoftheClimate.1.

——, and Coauthors, 2019: Permafrost thermal state [in "State of the Climate in 2018"]. *Bull. Amer. Meteor. Soc.*, **100** (9), S21–S22, https://doi.org/10.1175/2019BAMSStateoftheClimate.1

Novelli, P. C., K. A. Masarie, P. M. Lang, B. D. Hall, R. C. Myers, and J. W. Elkins, 2003: Reanalysis of tropospheric CO trends: Effects of the 1997–1998 wildfires. *J. Geophys. Res.*, **108**, 4464, https://doi.org/10.1029/2002jd003031.

Olsen, M. A., G. L. Manney, and J. Liu, 2019: The ENSO and QBO impact on ozone variability and stratosphere-troposphere exchange relative to the subtropical jets. *J. Geophys. Res. Atmos.*, **124**, 7379–7392, https://doi.org/10.1029/2019jd030435.

O'Neel, S., and Coauthors, 2019: Reanalysis of the US Geological Survey Benchmark Glaciers: Long-term insight into climate forcing of glacier mass balance. *J. Glaciol.*, **65**, 850–866, https://doi.org/10.1017/jog.2019.66.

Otto, F. E. L., and Coauthors, 2018: Anthropogenic influence on the drivers of the Western Cape drought 2015–2017. *Environ. Res. Lett.*, **13**, 124010, https://doi.org/10.1088/1748-9326/aae9f9.

Palecki, M. A., and R. G. Barry, 1986: Freeze-up and break-up of lakes as an index of temperature changes during the transition seasons: A case study for Finland. *J. Climate Appl. Meteor.*, **25**, 893–902, https://doi.org/10.1175/1520-0450(1986)025<0893:FUABUO>2.0.CO;2.

Park, T., and Coauthors, 2016: Changes in growing season duration and productivity of northern vegetation inferred from long-term remote sensing data. *Environ. Res. Lett.*, **11**, 084001, https://doi.org/10.1088/1748-9326/11/8/084001.

Pelto, M., 2019: Exceptionally high 2018 equilibrium line altitude on Taku Glacier, Alaska. *Remote Sens.*, **11**, 2378, https://doi.org/10.3390/rs11202378.

PERMOS, 2019: Permafrost in Switzerland 2014/2015 to 2017/2018. Glaciological Rep. Permafrost 16-19, 104 pp., https://doi.org/10.13093/permos-rep-2019-16-19.

Peterson, D. A., J. R. Campbell, E. J. Hyer, M. D. Fromm, G. P. Kablick III, J. H. Cossuth, and M. T. DeLand, 2018: Wildfire-driven thunderstorms cause a volcano-like stratospheric injection of smoke. *npj Climate Atmos. Sci.*, **1**, 30, https://doi.org/10.1038/s41612-018-0039-3.

Peterson, T. C., and R. S. Vose, 1997: An overview of the Global Historical Climatology Network temperature database. *Bull. Amer. Meteor. Soc.*, **78**, 2837–2849, https://doi.org/10.1175/1520-0477(1997)078<2837:AOOTGH>2.0.CO;2.

Petrenko, V. V., and Coauthors, 2013: A 60 yr record of atmospheric carbon monoxide reconstructed from Greenland firn air. *Atmos. Chem. Phys.*, **13**, 7567–7585, https://doi.org/10.5194/acp-13-7567-2013.

Pétron, G., A. M. Crotwell, E. Dlugokencky, and J. W. Mund, 2019: Atmospheric carbon monoxide dry air mole fractions from the NOAA ESRL Carbon Cycle Cooperative Global Air Sampling Network, 1988-2018, version: 2019-08. NOAA, accessed 9 July 2020, https://doi.org/10.15138/33bv-s284.

Phillips, N., and B. Nogrady, 2020: The race to decipher how climate change influenced Australia's record fires. *Nature*, **577**, 610–612, https://doi.org/10.1038/d41586-020-00173-7.

Pinty, B., and Coauthors, 2011: Exploiting the MODIS albedos with the Two-stream Inversion Package (JRC-TIP): 2. Fractions of transmitted and absorbed fluxes in the vegetation and soil layers. *J. Geophys. Res.*, **116**, D09106, https://doi.org/10.1029/2010jd015373.

Platnick, S., P. Hubanks, K. Meyer, and M. D. King, 2015: MODIS atmosphere L3 monthly product (08_L3). NASA MODIS Adaptive Processing System, Goddard Space Flight Center, https://doi.org/10.5067/MODIS/MOD08_M3.006.

Po-Chedley, S., T. J. Thorsen, and Q. Fu, 2015: Removing diurnal cycle contamination in satellite-derived tropospheric temperatures: Understanding tropical tropospheric trend discrepancies. *J. Climate*, **28**, 2274–2290, https://doi.org/10.1175/JCLI-D-13-00767.1.

Popp, T., and Coauthors, 2016: Development, production and evaluation of aerosol climate data records from European satellite observations (Aerosol_cci). *Remote Sens.*, **8**, 421, https://doi.org/10.3390/rs8050421.

Prather, M. J., C. D. Holmes, and J. Hsu, 2012: Reactive greenhouse gas scenarios: Systematic exploration of uncertainties and the role of atmospheric chemistry. *Geophys. Res. Lett.*, **39**, L09803, https://doi.org/10.1029/2012GL051440.

Ramon, J., L. Lledó, V. Torralba, A. Soret, and F. J. Doblas-Reyes, 2019: What global reanalysis best represents near-surface winds? *Quart. J. Roy. Meteor. Soc.*, **145**, 3236–3251, https://doi.org/10.1002/qj.3616.

Randel, W. J., and J. B. Cobb, 1994: Coherent variations of monthly mean total ozone and lower stratospheric temperature. *J. Geophys. Res.*, **99**, 5433–5447, https://doi.org/10.1029/93jd03454.

——, A. K. Smith, F. Wu, C.-Z. Zou, and H. Qian, 2016: Stratospheric temperature trends over 1979-2015 derived from combined SSU, MLS and SABER satellite observations. *J. Climate*, **29**, 4843–4859, https://doi.org/10.1175/JCLI-D-15-0629.1.

Ravishankara, A. R., J. S. Daniel, and R. W. Portmann, 2009: Nitrous oxide (N2O): The dominant ozone-depleting substance emitted in the 21st century. *Science*, **326**, 123–125, https://doi.org/10.1126/science.1176985.

Ray, E. A., F. L. Moore, J. W. Elkins, K. H. Rosenlof, J. C. Laube, T. Röckmann, D. R. Marsh, and A. E. Andrews, 2017: Quantification of the SF6 lifetime based on mesospheric loss measured in the stratospheric polar vortex. *J. Geophys. Res. Atmos.*, **122**, 4626–4638, https://doi.org/10.1002/2016jd026198.

——, and Coauthors, 2020: The influence of the stratospheric Quasi-Biennial Oscillation on trace gas levels at the Earth's surface. *Nat. Geosci.*, **13**, 22–27, https://doi.org/10.1038/s41561-019-0507-3.

Richardson, A. D., and Coauthors, 2018a: Tracking vegetation phenology across diverse North American biomes using PhenoCam imagery. *Sci. Data*, **5**, 180028, https://doi.org/10.1038/sdata.2018.28.

——, K. Hufkens, T. Milliman, and S. Frolking, 2018b: Intercomparison of phenological transition dates derived from the PhenoCam Dataset V1.0 and MODIS satellite remote sensing. *Sci. Rep.*, **8**, 5679, https://doi.org/10.1038/s41598-018-23804-6.

Rigby, M., and Coauthors, 2019: Increase in CFC-11 emissions from eastern China based on atmospheric observations. *Nature*, **569**, 546–550, https://doi.org/10.1038/s41586-019-1193-4.

Robock, A., 2000: Volcanic eruptions and climate. *Rev. Geophys.*, **38**, 191–219, https://doi.org/10.1029/1998RG000054.

Roderick, M. L., L. D. Rotstayn, G. D. Farquhar, and M. T. Hobbins, 2007: On the attribution of changing pan evaporation. *Geophys. Res. Lett.*, **34**, L17403, https://doi.org/10.1029/2007GL031166.

Romanovsky, V. E., and Coauthors, 2010: Thermal state of permafrost in Russia. *Permafrost Periglacial Processes*, **21**, 136–155, https://doi.org/10.1002/ppp.683.

Sánchez-Lugo, A., C. Morice, P. Berrisford, and A. Argüez, 2017: Global surface temperatures [in "State of the Climate in 2016"]. *Bull. Amer. Meteor. Soc.*, **98** (8), S11–S13, https://doi.org/10.1175/2017BAMSStateoftheClimate.1.

Santer, B. D., S. Solomon, F. J. Wentz, Q. Fu, S. Po-Chedley, C. Mears, J. F. Painter, and C. Bonfils, 2017: Tropospheric warming over the past two decades. *Sci. Rep.*, **7**, 2336, https://doi.org/10.1038/s41598-017-02520-7.

Santoso, A., and Coauthors, 2019: Dynamics and predictability of the El Niño–Southern Oscillation: An Australian perspective on progress and challenges. *Bull. Amer. Meteor. Soc.*, **100**, 403–420, https://doi.org/10.1175/BAMS-D-18-0057.1.

Satheesh, S. K., and Coauthors, 2017: Variability of atmospheric aerosols over India. Observed Climate Variability and Change over the Indian Region, M. Rajeevan and S. Nayak, Eds., Springer, 221–248, https://doi.org/10.1007/978-981-10-2531-0_13.

Saunois, M., and Coauthors, 2016: The global methane budget 2000-2012. *Earth Syst. Sci. Data*, **8**, 697–751, https://doi.org/10.5194/essd-8-697-2016.

Scanlon, T., and Coauthors, 2019: Soil moisture [in "State of the Climate in 2018"]. *Bull. Amer. Meteor. Soc.*, **100** (9), S38–S39, https://doi.org/10.1175/2019BAMSStateoftheClimate.1.

Schaaf, C. B., and Z. Wang, 2015: MCD43C3 MODIS/Terra+Aqua BRDF/Albedo Albedo Daily L3 Global 0.05Deg CMG. NASA EOSDIS Land Processes DAAC, accessed 1 February 2020, https://doi.org/10.5067/MODIS/MCD43C3.006.

——, and Coauthors, 2002: First operational BRDF, albedo nadir reflectance products from MODIS. *Remote Sens. Environ.*, **83**, 135–148, https://doi.org/10.1016/S0034-4257(02)00091-3.Schaefer, H., and Coauthors, 2016: A 21st-century shift from fossil-fuel to biogenic methane emissions indicated by 13CH4. *Science*, **352**, 80–84, https://doi.org/10.1126/science.aad2705.

Schamm, K., M. Ziese, A. Becker, P. Finger, A. Meyer-Christoffer, B. Rudolf, and U. Schneider, 2013: GPCC first guess daily product at 1.0°: Near real-time first guess daily land-surface precipitation from rain-gauges based on SYNOP data. Deutscher Wetterdienst, accessed 12 February 2020, https://doi.org/10.5676/DWD_GPCC/FG_D_100.

Schewe, J., and Coauthors, 2014: Multi-model assessment of water scarcity under climate change. *Proc. Natl. Acad. Sci.*, **111**, 3245–3250, https://doi.org/10.1073/pnas.1222460110.

Schneider, U., A. Becker, P. Finger, A. Meyer-Christoffer, M. Ziese, 2018: GPCC Monitoring product: Near real-time monthly land-surface precipitation from rain-gauges based on SYNOP and CLIMAT data. Deutscher Wetterdienst, accessed 4 March 2020, http://doi.org/10.5676/DWD_GPCC/MP_M_V6_100.

Schoeberl, M. R., R. S. Stolarski, and A. J. Krueger, 1989: The 1988 Antarctic ozone depletion: Comparison with previous year depletions. *Geophys. Res. Lett.*, **16**, 377–380, https://doi.org/10.1029/GL016i005p00377.

Schwietzke, S., and Coauthors, 2016: Upward revision of global fossil fuel methane emissions based on isotope database. *Nature*, **538**, 88–91, https://doi.org/10.1038/nature19797.

Seager, R., T. J. Osborn, Y. Kushnir, I. R. Simpson, J. Nakamura, and H. Liu, 2019: Climate variability and change of Mediterranean-type climates. *J. Climate*, **32**, 2887–2915, https://doi.org/10.1175/JCLI-D-18-0472.1.

Sharma, S., J. J. Magnuson, R. D. Batt, L. A. Winslow, J. Korhonen, and Y. Aono, 2016: Direct observations of ice seasonality reveal changes in climate over the past 320-570 years. *Sci. Rep.*, **6**, 25061, https://doi.org/10.1038/srep25061.

Shi, L., and J. J. Bates, 2011: Three decades of intersatellite-calibrated high-resolution infrared radiation sounder upper tropospheric water vapor. *J. Geophys. Res.*, **116**, D04108, https://doi.org/10.1029/2010JD014847.

Sinnhuber, B.-M., M. Weber, A. Amankwah, and J. P. Burrows, 2003: Total ozone during the unusual Antarctic winter of 2002. *Geophys. Res. Lett.*, **30**, 1580, https://doi.org/10.1029/2002GL016798.

Slivinski, L. C., and Coauthors, 2019: Towards a more reliable historical reanalysis: Improvements for version 3 of the twentieth century reanalysis system. *Quart. J. Roy. Meteor. Soc.*, **145**, 2876–2908, https://doi.org/10.1002/qj.3598.

Solomon, S., D. J. Ivy, D. Kinnison, M. J. Mills, R. R. Neely, and A. Schmidt, 2016: Emergence of healing in the Antarctic ozone layer. *Science*, **353**, 269–274, https://doi.org/10.1126/science.aae0061.

SPARC/IO3C/GAW, 2019: SPARC/IO3C/GAW report on long-term ozone trends and uncertainties in the stratosphere. SPARC Rep. 9, WCRP-17/2018, GAW Rep. 241, 102 pp., https://doi.org/10.17874/f899e57a20b.

Stackhouse, P. W., T. Wong, D. P. Kratz, P. Sawaengphokhai, A. C. Wiber, S. K. Gupta, and N. G. Loeb, 2016: Earth radiation budget at top-of-atmosphere [in "State of the Climate in 2015"]. *Bull. Amer. Meteor. Soc.*, **97** (8), S41–S43, https://doi.org/10.1175/2016BAMSStateoftheClimate.1.

Steinbrecht, W., and Coauthors, 2017: An update on ozone profile trends for the period 2000 to 2016. *Atmos. Chem. Phys.*, **17**, 10675–10690, https://doi.org/10.5194/acp-17-10675-2017.

Stengel, M., and Coauthors, 2017: Cloud property datasets retrieved from AVHRR, MODIS, AATSR and MERIS in the framework of the Cloud_cci project. *Earth Syst. Sci. Data*, **9**, 881–904, https://doi.org/10.5194/essd-9-881-2017.

Strode, S. A., J. R. Ziemke, L. D. Oman, L. N. Lamsal, M. A. Olsen, and J. Liu, 2019: Global changes in the diurnal cycle of surface ozone. *Atmos. Environ.*, **199**, 323–333, https://doi.org/10.1016/j.atmosenv.2018.11.028.

Stubenrauch, C., and Coauthors, 2012: Assessment of global cloud datasets from satellites. World Climate Research Programme Rep. 23/2012, 175 pp., www.wcrp-climate.org/documents/GEWEX_ Cloud_Assessment_2012.pdf.

Sun, W., P. Hess, and B. Tian, 2014: The response of the equatorial tropospheric ozone to the Madden-Julian Oscillation in TES satellite observations and CAM-chem model simulation. *Atmos. Chem. Phys.*, **14**, 11775–11790, https://doi.org/10.5194/acp-14-11775-2014.

Sun, Z., L. Zhao, G. Hu, Y. Qiao, E. Du, D. Zou, and C. Xie, 2020: Modeling permafrost changes on the Qinghai–Tibetan plateau from 1966 to 2100: A case study from two boreholes along the Qinghai–Tibet engineering corridor. *Permafrost Periglacial Processes*, **31**, 156–171, https://doi.org/10.1002/ppp.2022.

Susskind, J., G. Molnar, L. Iredell, and N. G. Loeb, 2012: Interannual variability of outgoing longwave radiation as observed by AIRS and CERES. *J. Geophys. Res.*, **117**, D23107, https://doi.org/10.1029/2012JD017997.

Tans, P., 2009: An accounting of the observed increase in oceanic and atmospheric CO2 and an outlook for the future. *Oceanography*, **22**, 26–35, https://doi.org/10.5670/oceanog.2009.94.

Tapley, B. D., S. Bettadpur, J. C. Ries, P. F. Thompson, and M. M. Watkins, 2004: GRACE measurements of mass variability in the Earth system. *Science*, **305**, 503–505, https://doi.org/10.1126/science.1099192.

Tarasick, D. W., and Coauthors, 2019: Tropospheric ozone assessment report: Tropospheric ozone from 1877 to 2016, observed levels, trends and uncertainties. *Elem. Sci. Anthropocene*, **7**, 39, https://doi.org/10.1525/elementa.376.

Teng, W.-H., C.-Y. Huang, S.-P. Ho, Y.-H. Kuo, and X.-J. Zhou, 2013: Characteristics of global precipitable water in ENSO events revealed by COSMIC measurements. *J. Geophys. Res. Atmos.*, **118**, 8411–8425, https://doi.org/10.1002/jgrd.50371.

Teuling, A. J., and Coauthors, 2013: Evapotranspiration amplifies European summer drought. *Geophys. Res. Lett.*, **40**, 2071–2075, https://doi.org/10.1002/grl.50495.

Thackeray, S. J., I. D. Jones, and S. C. Maberly, 2008: Long-term change in the phenology of spring phytoplankton: Species-specific responses to nutrient enrichment and climatic change. *J. Ecol.*, **96**, 523–535, https://doi.org/10.1111/j.1365-2745.2008.01355.x.

——, P. A. Henrys, H. Feuchtmayr, I. D. Jones, S. C. Maberly, and I. J. Winfield, 2013: Food web de-synchronization in England's largest lake: An assessment based on multiple phenological metrics. *Global Change Biol.*, **19**, 3568–3580, https://doi.org/10.1111/gcb.12326.

Thomason, L. W., and Coauthors, 2018: A global space-based stratospheric aerosol climatology: 1979–2016. *Earth Syst. Sci. Data*, **10**, 469–492, https://doi.org/10.5194/essd-10-469-2018.

Thompson, D. W. J., J. M. Wallace, P. D. Jones, and J. J. Kennedy, 2009: Identifying signatures of natural climate variability in time series of global-mean surface temperature: Methodology and insights. *J. Climate*, **22**, 6120–6141, https://doi.org/10.1175/2009JCLI3089.1.

Thompson, R. L., and Coauthors, 2019: Acceleration of global N2O emissions seen from two decades of atmospheric inversion. *Nat. Climate Change*, **9**, 993–998, https://doi.org/10.1038/s41558-019-0613-7.

Timmermann, A., and Coauthors, 2018: El Niño–Southern Oscillation complexity. *Nature*, **559**, 535–545, https://doi.org/10.1038/s41586-018-0252-6.

Tivig, M., V. Grützun, V. O. John, and S. A. Buehler, 2020: Trends in upper-tropospheric humidity: Expansion of the subtropical dry zones? *J. Climate*, **33**, 2149–2161, https://doi.org/10.1175/JCLI-D-19-0046.1.

Tokuda, D., H. Kim, D. Yamazaki, and T. Oki, 2019: Development of a global river water temperature model considering fluvial dynamics and seasonal freeze-thaw cycle. *Water Resour. Res.*, **55**, 1366–1383, https://doi.org/10.1029/2018WR023083.

Torralba, V., F. J. Doblas-Reyes, and N. Gonzalez-Reviriegol, 2017: Uncertainty in recent near-surface wind speed trends: A global reanalysis intercomparison. *Environ. Res. Lett.*, **12**, 114019, https://doi.org/10.1088/1748-9326/aa8a58.

Trepte, C. R., and M. H. Hitchman, 1992: Tropical stratospheric circulation deduced from satellite aerosol data. *Nature*, **355**, 626–628, https://doi.org/10.1038/355626a0.

Trepte, Q. Z., P. Minnis, C. R. Trepte, S. Sun-Mack, and R. Brown, 2010: Improved cloud detection in CERES Edition 3 algorithm and comparison with the CALIPSO Vertical Feature Mask. 13th Conf. on Atmospheric Radiation and Cloud Physics, Portland, OR, Amer. Meteor. Soc., JP1.32, https://ams.confex.com/ams/13CldPhy13AtRad/webprogram/Paper171785.html.

Ummenhofer, C. C., M. H. England, P. C. McIntosh, G. A. Meyers, M. J. Pook, J. S. Risbey, A. S. Gupta, and A. S. Taschetto, 2009: What causes southeast Australia's worst droughts? *Geophys. Res. Lett.*, **36**, L04706, https://doi.org/10.1029/2008GL036801.

van der A, R. J., M. A. F. Allaart, and H. J. Eskes, 2015: Extended and refined multi sensor reanalysis of total ozone for the period 1970–2012. *Atmos. Meas. Tech.*, **8**, 3021–3035, https://doi.org/10.5194/amt-8-3021-2015.

van der Schrier, G., J. Barichivich, K. R. Briffa, and P. D. Jones, 2013: A scPDSI-based global dataset of dry and wet spells for 1901-2009. *J. Geophys. Res. Atmos.*, **118**, 4025–4048, https://doi.org/10.1002/jgrd.50355.

van der Werf, G. R., and Coauthors, 2017: Global fire emissions estimates during 1997–2016. *Earth Syst. Sci. Data*, **9**, 697–720, https://doi.org/10.5194/essd-9-697-2017.

Vautard, R., J. Cattiaux, P. Yiou, J. N. Thépaut, and P. Ciais, 2010: Northern Hemisphere atmospheric stilling partly attributed to an increase in surface roughness. *Nat. Geosci.*, **3**, 756–761, https://doi.org/10.1038/ngeo979.

Vernier, J. P., J.-P. Pommereau, L. W. Thomason, J. Pelon, A. Garnier, T. Deshler, J. Jumelet, and J. K. Nielsen, 2011a: Overshooting of clean tropospheric air in the tropical lower stratosphere as seen by the CALIPSO lidar. *Atmos. Chem. Phys.*, **11**, 9683–9696, https://doi.org/10.5194/acp-11-9683-2011.

——, and Coauthors, 2011b: Major influence of tropical volcanic eruptions on the stratospheric aerosol layer during the last decade. *Geophys. Res. Lett.*, **38**, L12807, https://doi.org/10.1029/2011gl047563.——, and Coauthors, 2013: An advanced system to monitor the 3D structure of diffuse volcanic ash clouds. *J. Appl. Meteor. Climatol.*, **52**, 2125–2138, https://doi.org/10.1175/JAMC-D-12-0279.1.

Vose, R. S., R. Adler, G. Gu, A. Becker, X. Yin, and M. Bosilovich, 2019: Precipitation [in "State of the Climate in 2018"]. *Bull. Amer. Meteor. Soc.*, **100** (9), S29–S30, https://doi.org/10.1175/2019BAMSStateoftheClimate.1.

Wang, C., C. Deser, J. Y. Yu, P. DiNezio, and A. Clement, 2017: El Niño and Southern Oscillation (ENSO): A review. Coral Reefs of the Eastern Tropical Pacific, P. Glynn, D. Manzello, and I. Enochs, Eds., Vol. 8, Coral Reefs of the World, Springer, 85–106, https://doi.org/10.1007/978-94-017-7499-4_4.

Weatherhead, E. C., and Coauthors, 1998: Factors affecting the detection of trends: Statistical considerations and applications to environmental data. *J. Geophys. Res.*, **103**, 17 149–17 161, https://doi.org/10.1029/98JD00995.

Weber, M., S. Dikty, J. P. Burrows, H. Garny, M. Dameris, A. Kubin, J. Abalichin, and U. Langematz, 2011: The Brewer-Dobson circulation and total ozone from seasonal to decadal time scales. *Atmos. Chem. Phys.*, **11**, 11 221–11 235, https://doi.org/10.5194/acp-11-11221-2011.

——, M. Coldewey-Egbers, V. E. Fioletov, S. M. Frith, J. D. Wild, J. P. Burrows, C. S. Long, and D. Loyola, 2018: Total ozone trends from 1979 to 2016 derived from five merged observational datasets – The emergence into ozone recovery. *Atmos. Chem. Phys.*, **18**, 2097–2117, https://doi.org/10.5194/acp-18-2097-2018.

Wells, N., S. Goddard, and M. J. Hayes, 2004: A self-calibrating palmer drought severity index. *J. Climate*, **17**, 2335–2351, https://doi.org/10.1175/1520-0442(2004)017<2335:ASPDSI>2.0.CO;2.

Wentz, F. J., 1997: A well calibrated ocean algorithm for special sensor microwave/imager. *J. Geophys. Res. Oceans*, **102**, 8703–8718, https://doi.org/10.1029/96JC01751.

——, 2015: A 17-year climate record of environmental parameters derived from the Tropical Rainfall Measuring Mission (TRMM) microwave imager. *J. Climate*, **28**, 6882–6902, https://doi.org/10.1175/JCLI-D-15-0155.1.

——, L. Ricciardulli, K. A. Hilburn, and C. A. Mears, 2007: How much more rain will global warming bring? *Science*, **317**, 233–235, https://doi.org/10.1126/science.1140746.

Weyhenmeyer, G. A., A. M. Meili, and D. M. Livingstone, 2004: Nonlinear temperature response of lake ice breakup. *Geophys. Res. Lett.*, **31**, L07203, https://doi.org/10.1029/2004GL019530.

WGMS, 2017: Global Glacier Change Bulletin 2. ICSU(WDS)/IUGG(IACS)/UNEP/UNESCO/WMO, World Glacier Monitoring Service, 244 pp., https://doi.org/10.5904/wgms-fog-2017-10.

Wielicki, B. A., B. R. Barkstrom, E. F. Harrison, R. B. Lee III, G. L. Smith, and J. E. Cooper, 1996: Clouds and the Earth's Radiant Energy System (CERES): An earth observing system experiment. *Bull. Amer. Meteor. Soc.*, **77**, 853–868, https://doi.org/10.1175/1520-0477(1996)077<0853:CATERE>2.0.CO;2.

——, and Coauthors, 1998: Clouds and the Earth's Radiant Energy System (CERES): Algorithm overview. *IEEE Trans. Geosci. Remote Sens.*, **36**, 1127–1141, https://doi.org/10.1109/36.701020.

Willett, K. M., C. N. Williams Jr., R. J. H. Dunn, P. W. Thorne, S. Bell, M. de Podesta, P. D. Jones, and D. E. Parker, 2013: HadISDH: An updated land surface specific humidity product for climate monitoring. *Climate Past*, **9**, 657–677, https://doi.org/10.5194/cp-9-657-2013.

——, R. J. H. Dunn, P. W. Thorne, S. Bell, M. de Podesta, D. E. Parker, P. D. Jones, and C. N. Williams Jr., 2014: HadISDH land surface multi-variable humidity and temperature record for climate monitoring. *Climate Past*, **10**, 1983–2006, https://doi.org/10.5194/cp-10-1983-2014.

——, D. I. Berry, M. Bosilovich, and A. Simmons, 2019a: Surface humidity [in "State of the Climate in 2018"]. *Bull. Amer. Meteor. Soc.*, **100** (9), 25–27, https://doi.org/10.1175/2019BAMSStateoftheClimate.1.

——, R. J. H. Dunn, J. Kennedy, and D. Berry, 2019b: Development of the HadISDH marine humidity climate monitoring dataset. *Earth Syst. Sci. Data Discuss.*, https://doi.org/10.5194/essd-2019-190.

Winder, M., and J. E. Cloern, 2010: The annual cycles of phytoplankton biomass. *Philos. Trans. Roy. Soc.*, **365B**, 3215–3226, https://doi.org/10.1098/rstb.2010.0125.

Winker, D. M., W. Hunt, and M. J. McGill, 2007: Initial performance assessment of CALIOP. *Geophys. Res. Lett.*, **34**, L19803, https://doi.org/10.1029/2007GL030135.

WMO, 2018: Scientific Assessment of Ozone Depletion: 2018. Global Ozone Research and Monitoring Project Rep. 58, 588 pp., https://ozone.unep.org/sites/default/files/2019-05/SAP-2018-Assessment-report.pdf.

——, 2019: July matched, and maybe broke, the record for the hottest month since analysis began. WMO, accessed 2 December 2020, https://public.wmo.int/en/media/news/july-matched-and-maybe-broke-record-hottest-month-analysis-began.

Wohland, J., N.-E. Omrani, D. Witthaut, and N.-S. Keenlyside, 2019: Inconsistent wind speed trends in current twentieth century reanalyses. *J. Geophys. Res. Atmos.*, **124**, 1931–1940, https://doi.org/10.1029/2018jd030083.

Woolway, R. I., and C. J. Merchant, 2018: Intralake heterogeneity of thermal responses to climate change: A study of large Northern Hemisphere lakes. *J. Geophys. Res. Atmos.*, **123**, 3087–3098, https://doi.org/10.1002/2017jd027661.

——, and Coauthors, 2017: Lake surface temperature [in "State of the Climate in 2016"]. *Bull. Amer. Meteor. Soc.*, **98** (8), S13–S14, https://doi.org/10.1175/2017BAMSStateoftheClimate.1.

——, and Coauthors, 2018: Lake surface temperature [in "State of the Climate in 2017"]. *Bull. Amer. Meteor. Soc.*, **99** (8), S13–S15, https://doi.org/10.1175/2018BAMSStateoftheClimate.1.Wylie, D. P., D. L. Jackson, W. P. Menzel, and J. J. Bates, 2005: Trends in global cloud cover in two decades of HIRS observations. *J. Climate*, **18**, 3021–3031, https://doi.org/10.1175/JCLI3461.1.

Worden, J. R., and Coauthors, 2017: Reduced biomass burning emissions reconcile conflicting estimates of the post-2006 atmospheric methane budget. *Nat. Commun.*, **8**, 2227, https://doi.org/10.1038/s41467-017-02246-0.

Young, I., and A. Ribal, 2019: Multiplatform evaluation of global trends in wind speed and wave height. *Science*, **364**, 548–552, https://doi.org/10.1126/science.aav9527.

Young, P. J., and Coauthors, 2013: Pre-industrial to end 21st century projections of tropospheric ozone from the Atmospheric Chemistry and Climate Model Inter-comparison Project (ACCMIP). *Atmos. Chem. Phys.*, **13**, 2063–2090, https://doi.org/10.5194/acp-13-2063-2013.

——, and Coauthors, 2018: Tropospheric ozone assessment report: Assessment of global-scale model performance for global and regional ozone distributions, variability, and trends. *Elem. Sci. Anthropocene*, **6**, 10, https://doi.org/10.1525/elementa.265.

Zemp, M., and Coauthors, 2019: Global glacier mass changes and their contributions to sea-level rise from 1961 to 2016. *Nature*, **568**, 382–386, https://doi.org/10.1038/s41586-019-1071-0.

Zeng, Z., and Coauthors, 2018: Global terrestrial stilling: Does Earth's greening play a role? *Environ. Res. Lett.*, **13**, 124013, https://doi.org/10.1088/1748-9326/aaea84.

——, and Coauthors, 2019: A reversal in global terrestrial stilling and its implications for wind energy production. *Nat. Climate Change*, **9**, 979–985, https://doi.org/10.1038/s41558-019-0622-6.

Zhang, H.-M., and Coauthors, 2019: Updated temperature data give a sharper view of climate trends. *Eos*, **100**, https://doi.org/10.1029/2019EO128229.

Zhang, R., S. Zhang, J. Luo, Y. Han, and J. Zhang, 2019: Analysis of near-surface wind speed change in China during 1958-2015. *Theor. Appl. Climatol.*, **137**, 2785–2801, https://doi.org/10.1007/s00704-019-02769-0.

Zhang, T., A. Hoell, J. Perlwitz, J. Eischeid, D. Murray, M. Hoerling, and T. Hamill, 2019: Towards probabilistic multivariate ENSO monitoring. *Geophys. Res. Lett.*, **46**, 10 532–10 540, https://doi.org/10.1029/2019gl083946.

Zhang, X.., L. Alexander, G. C. Hegerl, P. Jones, A. K. Tank, T. C. Peterson, B. Trewin, and F. W. Zwiers, 2011: Indices for monitoring changes in extremes based on daily temperature and precipitation data. *Wiley Interdiscip. Rev.: Climate Change*, **2**, 851–870, https://doi.org/10.1002/wcc.147.

Zhang, X.-Y., and Coauthors, 2018: Evaluation of land surface phenology from VIIRS data using time series of PhenoCam imagery. *Agric. For. Meteor.*, **256–257**, 137–149, https://doi.org/10.1016/j.agrformet.2018.03.003.

Zhang, Y., J. M. Wallace, and D. S. Battisti, 1997: ENSO-like interdecadal variability: 1900-93. *J. Climate*, **10**, 1004–1020, https://doi.org/10.1175/1520-0442(1997)010<1004:ELIV>2.0.CO;2.

Zhang, Yo., and Coauthors, 2016: Multi-decadal trends in global terrestrial evapotranspiration and its components. *Sci. Rep.*, **6**, 19 124, https://doi.org/10.1038/srep19124.

Zhang, Yu., O. R. Cooper, A. Gaudel, A. M. Thompson, P. Nédélec, S.-Y. Ogino, and J. J. West, 2016: Tropospheric ozone change from 1980 to 2010 dominated by equatorward redistribution of emissions. *Nat. Geosci.*, **9**, 875–879, https://doi.org/10.1038/ngeo2827.

Zhao, L., and Coauthors, 2019: Permafrost changes and its effects on hydrological processes on Qinghai-Tibet Plateau. *Bull. Chin. Acad. Sci.*, **34**, 1233–1246.

Ziemke, J. R., and O. R. Cooper, 2018: Tropospheric ozone [in "State of the Climate in 2017"]. *Bull. Amer. Meteor. Soc.*, **99** (8), S56–S59, https://doi.org/10.1175/2018BAMSStateoftheClimate.1.

——, A. R. Douglass, L. D. Oman, S. E. Strahan, and B. N. Duncan, 2015: Tropospheric ozone variability in the tropics from ENSO to MJO and shorter timescales. *Atmos. Chem. Phys.*, **15**, 8037–8049, https://doi.org/10.5194/acp-15-8037-2015.

——, and Coauthors, 2019: Trends in global tropospheric ozone inferred from a composite record of TOMS/OMI/MLS/OMPS satellite measurements and the MERRA-2 GMI simulation. *Atmos. Chem. Phys.*, 19, 3257–3269, https://doi.org/10.5194/acp-19-3257-2019.

Zou, C.-Z., and H. Qian, 2016: Stratospheric temperature climate data record from merged SSU and AMSU-A observations. *J. Atmos. Oceanic Technol.*, **33**, 1967–1984, https://doi.org/10.1175/JTECH-D-16-0018.1.